Regional to Interhemispheric Connectivity of the Atlantic Ocean Circulation

Dissertation submitted by:
Tobias Gereon Schulzki

for the degree
Doctor of Natural Science

at the
Faculty of Mathematics and Natural Sciences of the Christian-Albrechts-Universität zu Kiel

Kiel, 2023

Main Supervisor and First Examiner:	**Prof. Dr. Arne Biastoch** GEOMAR Helmholtz Centre for Ocean Research Kiel RD1 - Ocean Dynamics and Kiel University
Second Examiner:	**Prof. Dr. Peter Brandt** GEOMAR Helmholtz Centre for Ocean Research Kiel RD1 - Physical Oceanography and Kiel University
Additional Supervisors through ISOS:	**Prof. Dr. Joakim Kjellsson** GEOMAR Helmholtz Centre for Ocean Research Kiel RD1 - Maritime Meteorology
	Prof. Dr. Katja Matthes GEOMAR Helmholtz Centre for Ocean Research Kiel
Date of Submission:	**05.05.2023**
Date of Oral Examination:	**24.07.2023**
Approved for Publication:	**24.07.2023**
Signature of the Dean:	**Prof. Dr. Frank Kempken**

Abstract

Over 200 years ago, the idea emerged that explaining the temperature distribution in the Atlantic Ocean requires to understand how remote ocean regions are connected through the circulation of water. Connectivity is thus relevant for the distribution of physical sea water properties, but also for the mean strength and variability of the circulation itself, as well as for the spreading of marine organisms in an interdisciplinary context.

The large-scale Atlantic circulation is characterised by wind-driven horizontal gyres and the Atlantic Meridional Overturning Circulation (AMOC), which describes the circulation of water in the vertical plane. The AMOC is associated with an inflow of warm surface water into the South Atlantic, which is transported northward across the equator and further into subpolar latitudes. In the subpolar North Atlantic and Nordic Seas, surface buoyancy fluxes result in a transformation of light surface to dense deep water and sinking. At mid-depth, the more dense water is transported southward, predominantly, but not exclusively within the Deep Western Boundary Current (DWBC). Deep water formation at subpolar latitudes and the resulting cross-equatorial overturning structure are unique to the Atlantic and strongly contribute to a basin wide northward heat transport with major impacts on the climate of all countries surrounding the Atlantic.

Modelling the AMOC is of particular importance to complement sparse and relatively short direct measurements and to study the contribution of specific processes/regions to the mean AMOC and its variability. The AMOC is highly complex, comprising various local circulation systems and processes converting light surface water to dense deep water and vice versa. Furthermore, it is affected by surface wind forcing, buoyancy fluxes and mixing in the ocean. Therefore, modelling the AMOC has been a challenge for decades. In this thesis, several modelling objectives are pursued in order to gain new insights into the variability of the Atlantic Ocean circulation, and of the AMOC in particular. A new nested climate model configuration (FOCI-ATLAS10) is developed, which covers the entire Atlantic (including the Agulhas Current System and Drake Passage) with an eddying nest that is embedded in a coarse resolution global ocean and can be run flexibly in fully coupled, but also forced modes.

With the objective to improve the representation of past AMOC variability in models, it is studied whether a coupled model can be modified to simulate the correct timing of (AMOC) variability, while maintaining important ocean-atmosphere feedbacks that are largely suppressed in forced experiments. In this thesis, the capabilities and limitations of applying a partial coupling procedure are evaluated. In partial coupling mode, the ocean component of a coupled model is forced with reanalysed wind stress anomalies, while heat and freshwater fluxes are still interactively exchanged with the atmosphere component. The application of partial coupling in FOCI-ATLAS10 does not only provide potentially improved model simulations to study past AMOC variability, but also new insights into the basin wide impact of wind variability on the AMOC in an eddying model configuration. It is shown that partially coupled experiments are able to simulate the important ocean-atmosphere feedbacks needed to retain the stable AMOC of a fully coupled experiment. At the same time, they are highly correlated to a forced simulation that incorporates the same wind stress anomalies on timescales shorter than 5 years. This result also proves the dominance of wind-driven variability on sub-decadal timescales. On longer timescales, buoyancy fluxes in the subpolar North Atlantic become more important. As these buoyancy fluxes are not significantly impacted by assimilating wind stress anomalies only, partial coupling is less successful in reproducing the correct timing of AMOC variability on decadal timescales.

Due to its large nested domain, its capability to run in a coupled set-up and the comparably low computational cost (due to the nesting approach), the FOCI-ATLAS10 configuration is uniquely suited to address fundamental questions on AMOC variability also on climate timescales. In addition to local buoyancy flux variability in the North Atlantic, driven for example by the North Atlantic Oscillation, interhemispheric connectivity was hypothesised to strongly impact the AMOC strength on (multi-)decadal to millennial timescales. In this thesis, it is shown that changes of the Southern Ocean wind stress and Agulhas leakage lead to temperature and salinity anomalies that have a direct impact on the AMOC strength. Probably for the first time, it is possible to show such a connectivity in a coupled model configuration at basin wide eddying resolution. A perturbation experiment with 5 ensemble members of 120 years length each yields that a 30% increase in the Southern Ocean wind stress maximum results in a fast and sustained Agulhas leakage increase by 3.8 Sv (35%). Temperature and salinity anomalies introduced in the South Atlantic propagate north through a complex interplay of advection, mixing and local atmospheric responses. After anomalies have developed in the subpolar North Atlantic, the AMOC increases by 1.2 Sv (7%) after 80 years. Anomalous water mass transformation and anomalous vertical transport are found to be linked through anomalies in overflow density.

Furthermore, this thesis demonstrates how important AMOC pathways, and their interaction with eddies, shape physical and biophysical connectivity in the Atlantic Ocean on smaller, regional scales. In the context of regional connectivity, coupling to an atmosphere model and the large eddying domain of FOCI-ATLAS10 are less important, compared to the horizontal resolution itself. Therefore, simulations of the existing VIKING20X configuration, which provides a twice as high horizontal resolution in the respective regions of interest, are analysed. While interhemispheric connectivity through advection is shown to be important on climate timescales, it is unclear on which timescale regional connectivity through advection can result in coherent AMOC variability and which processes set this timescale. Addressing these questions is especially important for the interpretation of sparse AMOC measurements. Similar to the analysis of wind-driven AMOC variability in partially coupled experiments, it contributes to an improved understanding which mechanisms can result in local and basin-scale adjustments of the AMOC. It is shown that strong mesoscale variability along the deep western boundary of the subtropical North Atlantic acts to decorrelate volume transport variations in the DWBC at two sections of long term AMOC measurements. As a consequence, the DWBC does not contribute to the coherence of interannual AMOC variability, despite carrying the majority of the southward transport that connects the sections. A similar interaction between mean AMOC pathways, in particular the DWBC, and eddies is found to strongly impact the dispersal of marine organisms. As an example, it is shown that the interaction of currents, eddies and bathymetric constraints can strongly affect the connectivity of remote ecosystems in the Northwest Atlantic, including the wreck of RMS Titanic. The results presented in this thesis highlight the need for high resolution modelling to obtain realistic dispersal pathways and yields important information on biophysical connectivity, with implications for the resilience of marine species and possibly for political decisions on marine protection measures.

Overall, this thesis provides new insights into fundamental mechanisms that are responsible for variability of the Atlantic Ocean circulation, in particular of the AMOC. Based on several advancements in modelling, which proved to be highly useful for the purpose of this thesis and can be of benefit for future projects as well, it is demonstrated how interhemispheric connectivity contributes to AMOC changes on climate timescales. At the same time, the effect of wind-forcing and the interaction of individual AMOC pathways with eddies on regional scales are shown to be highly important to understand AMOC variability on sub-decadal timescales, with further implications on interdisciplinary research questions.

Zusammenfassung

Bereits seit mehr als 200 Jahren ist bekannt, dass die physikalischen Eigenschaften von Meerwasser im Atlantischen Ozean nicht allein durch lokale Einflüsse an der Ozeanöberflache erklärt werden können, sondern auch durch Meeresströmungen beeinflusst werden. Wie sich Wasser und seine Eigenschaften im Ozean ausbreiten und so teilweise weit entfernte Regionen miteinander verbinden ist nicht nur von Relevanz für physikalisch motivierte Fragestellungen, sondern auch in Bezug auf interdisziplinäre Forschung, im Speziellen für die Ausbreitung von Meereslebewesen. Die großskalige horizontale Zirkulation im Atlantik ist dominiert durch windgetriebene Wirbel, die sich über die gesamte Breite des Atlantiks erstrecken. Die vertikale Zirkulation ist charakterisiert durch die Atlantische Meriodionale Umwälzzirkulation (AMOC). Sie ist verbunden mit einem Einstrom von warmem Wasser in den oberflächennahen Schichten des Südatlantiks. Dieses Wasser wird über den Äquator hinweg in subpolare Breiten transportiert, wo das Oberflächenwasser, hauptsächlich durch den Verlust von Wärme an die Atmosphäre, dichter wird und absinkt. Das so gebildete Tiefenwasser strömt zurück nach Süden. Dies geschieht vor allem, aber nicht ausschließlich, im tiefen westlichen Randstrom. Die Bildung von Tiefenwasser in subpolaren Breiten und die daraus resultierende interhemisphärische Zirkulation sind nur im Atlantischen Ozean zu finden. Ebenfalls damit verbunden ist ein nach Norden gerichteter Wärmetransport über den gesamten Atlantik, welcher einen starken Einfluss auf das Klima und die Klimavariabilität in allen Anrainerstaaten hat.

Um die wenigen und verhältnismäßig kurzen Beobachtungen zu ergänzen und spezielle Prozesse und Regionen mit Einfluss auf die Variabilität der Zirkulation isoliert zu untersuchen, ist die Modellierung der AMOC von großer Bedeutung. Die AMOC ist hochgradig komplex. Sie umfasst lokale Strömungssysteme und eine Vielzahl von Prozessen zur Bildung von Tiefenwasser und dessen Rückkehr an die Oberfläche. Sie wird beeinflusst durch Wind und Dichteflüsse an der Ozeanoberfläche, sowie durch Vermischung in der Wassersäule. Dadurch ist die realitische Simulation der AMOC eine bereits seit Jahrzehnten bestehende Herausforderung. In der vorliegenden Arbeit werden verschiedene Modellentwicklungen vorangetrieben um neue Einsichten in die Variabilität der Strömung im Atlantik, insbesondere der AMOC, zu erlangen. Zentral dabei ist die Entwicklung einer neuen Modellkonfiguration (FOCI-ATLAS10). Diese simuliert den gesamten Atlantik in einem hochauflösenden Nest, welches in ein globales Modell mit grober horizontaler Auflösung eingebettet ist. Dadurch werden große Teile der wichtigen mesoskaligen Variabilität im Atlantik explizit simuliert, ohne den globalen Kontext zu verlieren. Diese Modellkonfiguration kann sowohl gekoppelt mit einem Atmosphärenmodell, als auch ungekoppelt, als reine Ozeankonfiguration, angetrieben durch beobachtete (reanalysierte) atmosphärische Felder genutzt werden.

Gekoppelte Modelle haben den Vorteil Rückkopplungen zwischen dem Ozean und der Atmosphäre explizit zu simulieren, was in ungekoppelten Experimenten nicht möglich ist und durch eine Modifikation der Frischwasserflüsse an der Oberfläche kompensiert werden muss. Sie sind jedoch nicht in der Lage die beobachtete zeitliche Entwicklung der Strömungen auf multi-dekadischen und kürzeren Zeitskalen zu reproduzieren. Aus diesem Grund wird in der vorliegenden Arbeit untersucht, wie ein gekoppeltes Modell (hier FOCI-ATLAS10) so erweitert werden kann, dass die zeitliche Entwicklung der großskaligen Zirkulation verbessert wird, ohne dabei Rückkopplungen zwischen dem Ozean und der Atmosphäre weitgehend zu unterdrücken. Dazu wird die Windschubspannung in der Ozeankomponente des gekoppelten Modells durch auf Reanalyseprodukten basierende Anomalien ersetzt, während Wärme- und Frischwasserflüsse weiterhin interaktiv mit der Atmosphäre ausgetauscht werden. Es wird gezeigt, dass solche partiell gekoppelten Experimente in einem Modell mit explizit simulierten mesoskaligen Wirbeln eine ähnliche Stabilität der AMOC aufweisen, wie ein voll gekoppeltes Experiment. Gleichzeitig sind Schwankungen der AMOC Stärke auf Zeitskalen kürzer als 5 Jahren hoch korreliert mit einem ungekoppelten Experiment, welches durch die gleichen Windanomalien angetrieben wird. Dies bestätigt einen starken Einfluss von Windvariabilität auf die

AMOC auf sub-dekadischen Zeitskalen. Auf längeren Zeitskalen, werden die Oberflächendichteflüsse im Nordatlantik zunehmend wichtiger. Es wird gezeigt, dass diese nicht signifikant durch Anomalien der Windschubspannung beeinflusst werden, sodass partiell gekoppelte Experimente die zeitliche Entwicklung der AMOC auf dekadischen Zeitskalen nur begrenzt reproduzieren können.

Durch die Panatlantische Ausdehnung der hochauflösenden Nestregion, welche das Agulhas Stromsystem und die Drakestraße umfasst, und die Möglichkeit gekoppelte Experimente mit vergleichsweise geringen Kosten durchzuführen, ist FOCI-ATLAS10 speziell dafür geeignet auch AMOC Schwankungen auf längeren Zeitskalen von Dekaden bis hin zu einem Jahrhundert zu untersuchen. Neben dem Einfluss von Dichteflüssen an der Oberfläche, welche oft in einen Zusammenhang mit der Nordatlantischen Oszillation (NAO) gebracht werden, könnte vor allem die Interaktion von Prozessen auf der Süd- und Nordhalbkugel von großer Bedeutung für die Schwankungen der AMOC auf diesen Zeitskalen sein. In der vorliegenden Arbeit wird gezeigt, dass Änderungen in den Westwinden der südlichen Hemisphäre und dem Einstrom aus dem Indischen Ozean durch das Agulhas Stromsystem zu Anomalien der Temperatur und des Salzgehaltes führen, welche einen direkten Einfluss auf die Stärke der AMOC haben. Wahrscheinlich zum ersten Mal war es möglich, einen solchen Zusammenhang in einer gekoppelten Modellkonfiguration mit explizit aufgelösten mesoskaligen Wirbeln nachzuweisen. Basierend auf einem Ensemble-Experiment, bestehend aus 5 Modellsimulationen mit um 30% verstärkter Windschubspannung im Südlichen Ozean, wird gezeigt, dass der Einstrom aus dem Indischen Ozean in den Südatlantik, im Vergleich zu einem Experiment mit unveränderter Windschubspannung, um 3.8 Sv (35%) zunimmt. Die damit verbundenen Salzgehalts- und Temperaturanomalien breiten sich in einem komplexen Zusammenspiel von Advektion, Vermischung und lokalen Änderungen der atmosphärischen Zirkulation in den Nordatlantik aus. Dies führt zu einer Verstärkung der Tiefenwasserbildung im Nordatlantik und resultiert in einer Zunahme der AMOC um 1.2 Sv (7%) nach circa 80 Jahren. Zudem wird gezeigt, dass Änderungen in der Wassermassentransformation und im vertikalen Transport durch das Absinken des aus dem Nordmeer in den Atlantik einströmenden Tiefenwassers verbunden sind.

Desweiteren werden in der vorliegenden Arbeit die Interaktionen wichtiger AMOC Pfade, vor allem des tiefen westlichen Randstroms, mit Wirbeln und deren Auswirkungen auf regionale Konnektivität untersucht. Das Zusammenspiel verschiedener Prozesse und Strömungsysteme auf regionalen Skalen hat nicht nur Einfluss auf die Zirkulation selbst, sondern darüber hinaus auch auf interdiszplinäre Fragestellungen. In diesem Zusammenhang ist die große Ausdehnung der hochauflösenden Nestregion in FOCI-ATLAS10 und die Möglichkeit zur Kopplung an ein Atmosphärenmodell von geringerer Bedeutung, als die horizontale Auflösung selbst. Aus diesem Grund wurde für die regionale Betrachtung die bereits existierende VIKING20X Konfiguration gewählt. Diese stellt eine doppelt so hohe Auflösung im Vergleich zu FOCI-ATLAS10 bereit. Wie in der vorliegenden Arbeit gezeigt wird, hat die Advektion von Anomalien aus dem Süd- in den Nordatlantik einen starken Einfluss auf multi-dekadische Schwankungen der AMOC. Es ist ebenfalls von großer Bedeutung zu untersuchen, welche Einflussfaktoren bestimmend dafür sind, auf welcher Zeitskala die Advektion von Anomalien kohärente regionale Schwankungen der AMOC hervorrufen kann und welche Prozesse diese Zeitskala festlegen. Wie auch die Untersuchung des Einflusses von Windvariabilität in partiell gekoppelten Experimenten, lässt dies Rückschlüsse darauf zu, welche Prozesse zu lokalen und beckenweiten Änderungen der AMOC beitragen können. Dieses hat vor allem Konsequenzen für die Interpretation von Messungen, die nur an wenigen Breitengraden durchgeführt werden. In dieser Arbeit wird gezeigt, dass Wirbel und Mäander die Kohärenz von Transportanomalien im tiefen westlichen Randstrom reduzieren. Dadurch trägt die Advektion im tiefen westlichen Randstrom nicht signifikant zu der Kohärenz von interannualen AMOC Schwankungen an zwei Breitegraden im subtropischen Nordatlantik bei, an denen die AMOC kontinuierlich gemessen wird.

Wie in dieser Arbeit beispielhaft anhand der Ausbreitung von Tiefseekorallen entlang des nordwest-atlantischen Kontinentalhangs demonstiert wird, hat die Interaktion der AMOC-Pfade, wie dem tiefen westlichen Randstrom, mit mesoskaligen Wirbeln ebenfalls einen starken Einfluss auf die Ausbreitung von Meereslebewesen. Das Zusammenspiel von starken mittleren Strömungen, mesoskaligen Wirbeln und der Bathymetrie hat wichtige Folgen für die Konnektivität von Ökosystemen und damit Konsequenzen für die Anpassungs- und Überlebensfähigkeit von

Meereslebewesen. Dies wiederum stellt eine wichtige Informationen für politische Entscheidungen über mögliche Unternehmungen zum Schutz der Artenvielfalt dar. Zudem verdeutlicht der gezeigte Einfluss der Mesoskala auf die Ausbreitungpfade von Meereslebewesen die große Bedeutung hochauflösender Modelle.

Insgesamt werden in der vorliegenden Arbeit neue Ergebnisse in Bezug auf fundamentale Fragen über die Zirkulation im Atlantik und deren Variabilität dargelegt. Basierend auf Fortschritten in der Modellierung, welche über diese Arbeit hinaus nützlich sein können, wird gezeigt, dass die Interaktion der Süd- und Nordhalbkugel essenziell für die Variabilität der Meerströmungen im Atlantik auf Zeitskalen von mehreren Dekaden bishin zu einem Jahrhundert ist. Gleichzeitig wird demonstriert, dass AMOC Schwankungen auf sub-dekadischer Zeitskala stark unter dem Einfluss von Windänderungen und der Interaktion von Wirbeln mit den Strömungspfaden der AMOC stehen, welche ebenfalls von großer Bedeutung für interdisplinäre Fragestellungen sind.

Contents

CHAPTER 1

Introduction

As early as 1798, Benjamin Thompson (later Count Rumford) suggested that mid-depth water in the tropical Atlantic likely originates from polar latitudes based on a limited number of equatorial temperature measurements (Richardson, 2008; Rumford, 1798). Thus, over 200 years ago, the concept emerged that certain locations can be linked to remote regions, spanning even hundreds of kilometres, through the circulation of water. Foundational research was carried out throughout the 19th and 20th centuries, continuously building up knowledge of the Atlantic circulation based on ship observations and theory. First ideas of the horizontal circulation in the Atlantic were based on data collected from merchant and naval ships. An early diagram of major near-surface currents, already including, for example, the Gulf Stream and North Atlantic Current, was published in 1832 by Jane Rodd and James Rennell (Richardson, 2008; Rennell, 1832). In 1921, the first visualisation to suggest a connectivity between the northern and southern hemisphere Atlantic was published by Carl Wilhelm A. Brennecke (Brennecke, 1921; Richardson, 2008). It showed a cross-equatorial northward flow near the surface and a southward return flow at depth. In 1987, Wallace Broecker introduced the global conveyor belt, a conceptual visualisation of a circulation system connecting all world oceans (Broecker, 1987). This concept gave rise to concerns about a shut-down of the interhemispheric circulation under global climate change (discussed for example in Lozier, 2010), which is essentially based on the assumption that once a single component of the system is stopped, the whole circulation is halted. With rising computing power at the end of the 20th century, numerical models became another important scientific tool to study the Atlantic circulation in addition to direct observations and theory. Extensive research has refined our view of the Atlantic circulation and it became clear that the circulation is not fully described by coherent currents (e.g. Wyrtki et al., 1976), or the conveyor belt concept (Broecker, 1991; Lozier, 2010). Especially the presence of mesoscale (spatial scales of roughly 10-100 km) processes and eddies adds an additional layer of complexity. Satellite observations and high resolution model simulations, showed the dominance of mesoscale eddies (vortices with a radius approximately in the mesoscale range) throughout most of the world oceans (e.g. Chelton et al., 2007, 2011; Smith et al., 2000). Advancements in observations, theory and modelling provided a deeper insight into the Atlantic Ocean circulation, but inevitably brought up further research questions. This includes questions about the impact of connectivity between remote regions on the variability of the large-scale Atlantic circulation. Connectivity refers to an exchange of information, energy, or matter between two remote locations. As implied by the term 'conveyor', the large-scale Atlantic circulation is associated with a cross equatorial transport of water and water mass properties (for example salinity and temperature), connecting the northern and southern hemispheres. Nevertheless, variability of this interhemispheric circulation is not coherent across the entire Atlantic, but dependent on various local and remote processes (e.g Bingham et al., 2007; Biastoch et al., 2008a). To better understand the relative importance and interaction of these processes on different spatial and temporal scales is not only relevant for the distribution of physical sea-water properties and the interpretation of sparse direct measurements, but connectivity between remote ocean regions may also allow to predict future changes of the circulation. Furthermore, connectivity is not only important with regard to physical questions. Biophysical connectivity, this is for example the exchange of larvae between remote ecosystems through the ocean's circulation, strongly impacts the growth, spread

and resilience of marine species (Gary et al., 2020; Cowen & Sponaugle, 2009). The importance to obtain deeper insights into biophysical connectivity goes beyond science, but can also inform political decisions on marine protection.

Physical and biophysical connectivity are closely related, because the same processes that govern physical exchanges between remote regions could also impact the dispersal of marine organisms. Understanding changes of the Atlantic large-scale circulation and their potential impact on marine organisms, as well as a better knowledge of ecosystem connectivity, are core objectives of the iAtlantic project (see Roberts et al., 2023) in which the research presented in this thesis was conducted.

Based on advancements in numerical ocean modelling and the combination of Eulerian and Lagrangian analysis techniques, this thesis answers fundamental questions about the variability and connectivity of the Atlantic Ocean circulation from regional to interhemispheric scales.

1.1 Atlantic Ocean Circulation

There are two main sources of energy that generate circulation in the ocean, the kinetic energy of winds blowing over the ocean's surface and potential energy associated with density differences caused by buoyancy, i.e. heat and freshwater, fluxes (Stocker, 2013). For the purpose of this thesis, the theoretical foundation of the purely wind-driven circulation is described first. Second, a detailed introduction into the concept of the Atlantic Meridional Overturning Circulation is provided, which is generated by both, wind and buoyancy forcing.

1.1.1 Fundamentals of the Wind-Driven Circulation

Ekman Transport

As winds blow over the ocean's surface they transfer momentum into the ocean, causing the water to move (Gill, 1982). The stress (force per area) applied to the surface layer of the ocean is transferred to the underlying fluid layers by drag. As a consequence, the impact of wind forcing can be described as a body force acting on a volume of water. The linearised momentum balance for a uniformly rotating, homogeneous fluid (equation 1.1), as derived by Gill (1982), describes that wind force (4) and a gradient in pressure (3) can cause an acceleration (1) of the flow, which is deflected to the right/left by the Coriolis force (2) once the fluid is moving:

$$\begin{aligned} \frac{\partial u}{\partial t} - fv &= -\frac{1}{\rho_0}\frac{\partial p'}{\partial x} + \frac{1}{\rho_0}\frac{\partial \tau_x}{\partial z} \\ \frac{\partial v}{\partial t} + fu &= -\frac{1}{\rho_0}\frac{\partial p'}{\partial y} + \frac{1}{\rho_0}\frac{\partial \tau_y}{\partial z} \\ (1) \quad (2) \qquad & (3) \qquad (4) \end{aligned} \tag{1.1}$$

ρ_0 is a constant reference density, p' the perturbation pressure, $\vec{u} = (u, v, w)$ the velocity vector and its components and $f = 2\Omega sin(\phi)$ the Coriolis parameter related to the earth's rotation. Ω is the angular speed of earth rotation and ϕ the latitude. $\vec{\tau} = (\tau_x, \tau_y)$ is the horizontal stress. t is time and x,y,z denote the three spatial dimensions.

For a steady flow the time derivatives (1) are zero and in the absence of wind-forcing there is a balance between the Coriolis force (2) and pressure gradient force (3). This is one of the most fundamental balances in oceanography and known as the geostrophic balance.

To understand the ocean's response to the applied wind stress, it is possible to split the equations into a geostrophic part (associated with a velocity caused by the pressure gradient) and an ageostrophic part (associated with a velocity caused by the wind force u_E,v_E). The geostrophic part describes the flow below the Ekman layer and for the ageostrophic part it is sufficient to only consider the Ekman layer, because the wind force is zero below. The ageostrophic part of the equation is:

$$\begin{aligned} -fv_E &= \frac{1}{\rho_0}\frac{\partial \tau_x}{\partial z} \\ fu_E &= \frac{1}{\rho_0}\frac{\partial \tau_y}{\partial z} \end{aligned} \tag{1.2}$$

This equation states that the Coriolis force associated with the part of the velocity that is not in geostrophic balance (left hand side), must be balanced by the frictional force (right hand side). At this point, it is useful to consider individual layers of fluid again (Gill, 1982). The wind stress ($\vec{\tau}_{wind}$) acts on the top of the surface layer. Motion of the surface layer itself exerts a stress on the underlying layer, which is smaller than the wind stress. The underlying layer exerts an equal and opposite stress on the bottom of the surface layer. The net frictional force generated by the wind and the layer below must be balanced by the Coriolis force. As the Coriolis force is always directed to the right (in the northern hemisphere, where $f > 0$) and the stress exerted from the layer beneath is always against the direction of motion, a balance is obtained when the velocity in the surface layer is directed in a 45° angle to the right of the wind stress vector (figure 1.1a). A similar balance can be obtained for all layers, resulting in a spiral known as the Ekman spiral (Ekman, 1905). The angle between the initial wind direction and the flow becomes larger with depth, but at the same time the velocity decreases. As the stress exerted on a layer of fluid decreases with the depth of this layer (distance from the ocean's surface), the stress eventually vanishes. This depth defines the so called Ekman layer and has a typical thickness of a few tens of meters (Marshall & Plumb, 2007).

Integration of equation 1.2 from the base of the Ekman layer (z_E) to the surface now yields the volume transport in the Ekman layer driven by the wind:

$$\begin{aligned} -f\int_{z_E}^{0} \rho_0 v_E dz &= [\tau_{x,z=0} - \tau_{x,z=z_E}] = \tau_{x,wind} \\ f\int_{z_E}^{0} \rho_0 u_E dz &= [\tau_{y,z=0} - \tau_{y,z=z_E}] = \tau_{y,wind} \\ \Rightarrow \vec{M_E} &= \frac{\vec{\tau}_{wind} \times \hat{k}}{f} \end{aligned} \tag{1.3}$$

The stress at the surface ($z = 0$) is the wind stress and based on the definition of the Ekman layer, the stress at the base of the Ekman layer $\vec{\tau}_{z=z_E}$ is zero. $\vec{M_E} = \int_{z_E}^{0} \rho_0 \vec{u}_E dz$ is the Ekman volume transport and $\hat{k}$ the vertical unit vector.

This equation states, that the integrated volume transport is directed in a right angle to the direction of the wind stress. This can be understood if the whole Ekman layer, not individual thin layers, are considered. In this case the Coriolis force, which is directed in a 90° angle to the velocity vector, must balance the force exerted by the wind. The concept of Ekman transport will appear throughout the introduction and is highly important to understand the impact of wind variability on the Atlantic Ocean circulation as presented in chapters 3 and 4 and also to understand the context of chapter 5.

Sverdrup Transport

As the winds don't blow in the same direction and with the same magnitude everywhere, the Ekman transport is not uniform. Following the atmospheric general circulation, with easterly trade winds in tropical latitudes, mid-latitude westerlies and polar easterlies, regions in the ocean develop where the Ekman transport converges, or diverges (Gill, 1982; Marshall & Plumb, 2007). This process generates high and low pressure areas in the ocean. Under the assumption that water is incompressible, the fundamental constraint that mass is conserved yields the continuity equation:

$$\nabla \cdot \vec{u} = \frac{\partial u}{\partial x} + \frac{\partial v}{\partial y} + \frac{\partial w}{\partial z} = 0 \tag{1.4}$$

$\nabla = (\frac{\partial}{\partial x}, \frac{\partial}{\partial y}, \frac{\partial}{\partial z})$ is a vector and called Nabla operator. In this context, the continuity equation states that a horizontally convergent/divergent flow must be balanced by a downward/upward vertical velocity at the bottom of the Ekman layer, called Ekman pumping/suction (Gill, 1982). Replacing the horizontal velocity components in equation 1.4 with u_E and v_E, vertical integration over the Ekman layer and equation 1.3 yield:

$$w_E = \frac{1}{\rho_0} \nabla_H \cdot \vec{M}_E = \frac{1}{\rho_0} \hat{k} \cdot \nabla \times (\frac{\vec{\tau}_{wind}}{f}) \tag{1.5}$$

This equation relates the vertical velocity at the base of the Ekman layer w_E to the horizontal divergence of the Ekman transport $\nabla_H \cdot \vec{M}_E$ and further to the curl of the wind stress divided by the Coriolis parameter. ∇_H the horizontal Nabla operator. Note that Ekman theory (see previous section) describes a local balance of forces, but here a larger domain is considered and in general the change of f with latitude must be considered.

As mentioned before, the flow below the Ekman layer is considered to be in geostrophic balance, so the question arises how the vertical velocities induced by Ekman suction/pumping are balanced below the Ekman layer (Marshall & Plumb, 2007). Taking the horizontal divergence of the geostrophic flow with $f = f(y)$, $\frac{\partial f}{\partial x} = 0$ and $\beta = \frac{\partial f}{\partial y}$ yields:

$$\nabla_H \cdot \vec{u}_g = \frac{\partial}{\partial x}(-\frac{1}{\rho_0 f}\frac{\partial p'}{\partial y}) + \frac{\partial}{\partial y}(\frac{1}{\rho_0 f}\frac{\partial p'}{\partial x}) = -(\frac{1}{\rho_0 f}\frac{\partial p'}{\partial x})\frac{\partial f}{\partial y}\frac{1}{f} = -\frac{\beta}{f} v_g \tag{1.6}$$

$\vec{u}_g = (u_g, v_g)$ is the velocity in geostrophic balance. This equation states that the change of the Coriolis parameter f in meridional direction gives rise to a divergence of the geostrophic flow. As $\beta > 0$ a northward geostrophic flow is convergent, while a southward flow is divergent. In the southern hemisphere, where f is negative, the opposite is true.

This allows the geostrophic flow below the Ekman layer to balance Ekman pumping/suction at the base of the Ekman layer, which is the fundamental idea of Sverdrup theory. Formally, the Sverdrup theory is concerned with the depth integrated, stationary flow (Gill, 1982). Starting from equation 1.1 the time derivatives are again zero.

Now cross-differentiation and the continuity equation (equation 1.4) yield an expression for the depth integrated meridional velocity V:

$$\beta V = \frac{1}{\rho_0}(\frac{\partial \tau_{y,wind}}{\partial x} - \frac{\partial \tau_{x,wind}}{\partial y}) = \frac{1}{\rho_0} \hat{k} \cdot \nabla \times \vec{\tau}_{wind} \tag{1.7}$$

This is equation relates the integrated meridional velocity to the curl of the wind stress and is called Sverdrup relation. The curl of the wind stress in turn is related to the Ekman pumping velocity (equation 1.5). Therefore the upper equation expresses that a positive wind stress curl (anti-clockwise rotation) causes Ekman divergence, which is balanced by a convergent northward geostrophic transport.

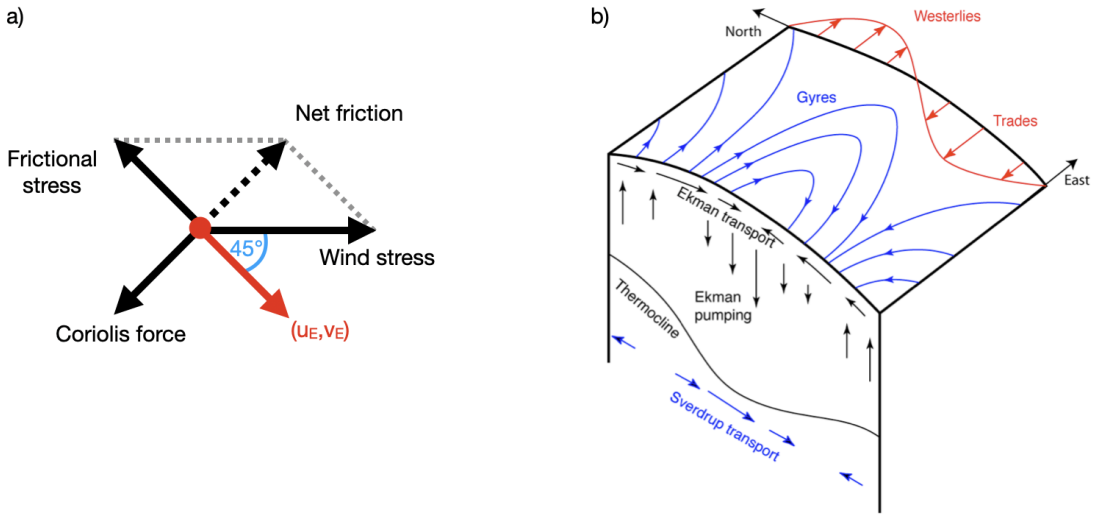

Figure 1.1: a) Balance of forces in a thin layer of fluid at the surface. b) Illustration of the circulation driven by surface winds based on Ekman and Sverdrup theory, taken from Talley et al. (2011).

A common representation of 1.7 is by defining the Sverdrup stream function (Ψ):

$$U = -\frac{\partial \Psi}{\partial y}; V = \frac{\partial \Psi}{\partial x}$$

$$(1.7) \Rightarrow \Psi(x,y) = \frac{1}{\rho_0 \beta} \int_{x_E}^{x} \hat{k} \cdot \nabla \times \vec{\tau}_{wind} dx \tag{1.8}$$

Analogously to the definition of V, U is the depth integrated zonal velocity. The stream function value at the western boundary provides the total meridional transport between the eastern (x_E) and western boundary of an ocean basin and is known as the Sverdrup transport.

The nature of the atmospheric general circulation, which itself is mostly caused by differential heating at the equator and poles on a rotating sphere, causes 3 large-scale gyres to emerge in the Atlantic Ocean (figure 1.2). The anti-clockwise Subpolar and South Atlantic Subtropical Gyres and the clockwise North Atlantic Subtropical Gyre. The Sverdrup theory can explain their sense of rotation, provides an estimate for their transports and has direct implications for the ocean response to changes in the wind-field (Marshall & Plumb, 2007). This will be discussed in more detail in chapters 3 and 4. Sverdrup theory is further related to the motivation for chapter 5. The circulation driven by wind stress forcing, based on Ekman and Sverdrup theory is summarised in figure 1.1b, taken from Talley et al. (2011).

Although the Sverdrup theory itself does not include western boundary currents, their existence follows from the need to balance the interior Sverdrup transport by an opposite transport along the western boundary. Further theoretical work was carried out by Henry Stommel and Walter Munk to explain the existence and characteristics of these currents in more detail. The basic assumptions made to derive the Sverdrup theory are not applicable for the narrow and fast western boundary currents. Lateral friction along the boundaries (Munk, 1950) or bottom friction (Stommel, 1948) must be considered to explain their dynamics and close the circulation at the western boundary. Both solutions yield an interior Sverdrup circulation closed by narrow western boundary currents. However, these theories are not explained in more detail here, because for the purpose of this thesis the fundamental ideas of Ekman and Sverdrup theory are most relevant.

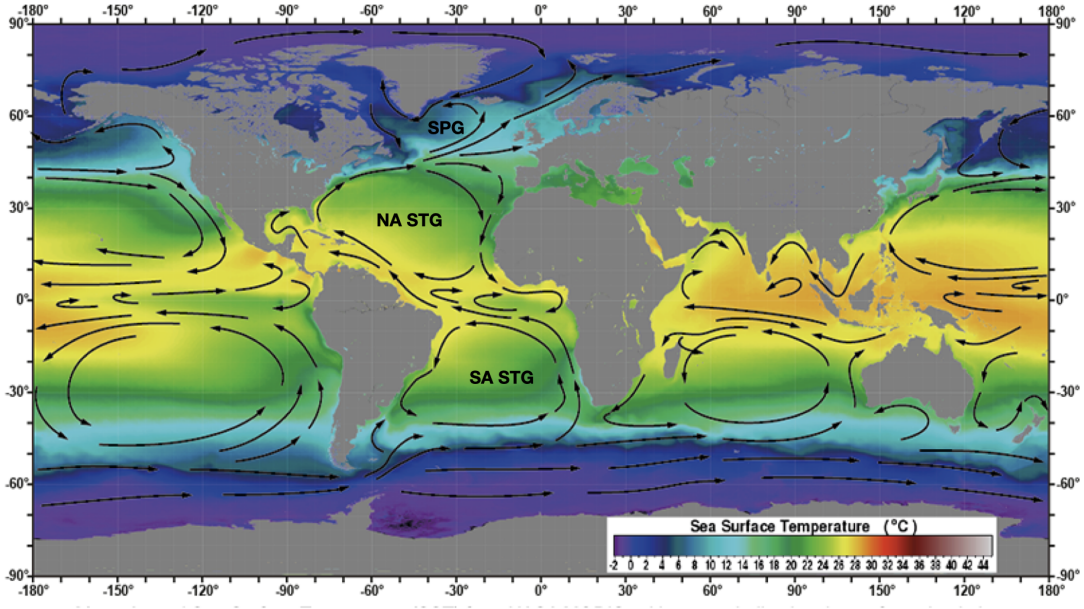

Figure 1.2: Schematic diagram of the surface ocean circulation, including the three large-scale gyres in the Atlantic Ocean: the Subpolar Gyre (SPG), North Atlantic Subtropical Gyre (NA STG) and South Atlantic Subtropical Gyre (SA STG). Colour shading shows the mean annual Sea Surface Temperature (SST) from satellite observations (NASA MODIS). The figure is adapted from `https://rapid.ac.uk/abc/bg/atlantic_conveyor.php` (11.04.2023).

1.1.2 Atlantic Meridional Overturning Circulation

While the fundamentals of the wind-driven theory can explain the existence of large-scale gyres in the ocean, they are not able to describe the full 3-dimensional circulation, especially the mid-depth and abyssal circulation (below approximately 1000 m depth). Therefore, this section is concerned with the circulation in the vertical plane, known as the overturning circulation. To understand this circulation and its variability, wind-driven theory is still important, but the effect of buoyancy forcing must be considered as well.

Definition and Direct Measurements

The Atlantic Meridional Overturning Circulation (AMOC) describes the zonally integrated meridional transport of water in the Atlantic Ocean (see blue arrows in figure 1.3; Lozier, 2012). It is characterised by a northward flow of warm water in the upper ocean. At mid-depth, water of North Atlantic origin, called North Atlantic Deep Water (NADW), is transported to the south. NADW itself is a composite of different water masses formed in the subpolar North Atlantic and Nordic Seas. The least dense component of this water mass, called Labrador Sea Water (LSW) is a result of deep winter convection in the Labrador and Irminger Seas (Marshall & Schott, 1999; de Jong et al., 2018). The deeper lying components are formed in Nordic Seas and overflow the shallow bathymetry of the Denmark Strait and Iceland-Scotland Ridge into the subpolar North Atlantic (Dickson & Brown, 1994). At abyssal depths, water formed on the Antarctic shelf, called Antarctic Bottom Water (AABW), is transported to the north (Orsi et al., 1999).

Mathematically, the AMOC strength is defined as the maximum of the meridional overturning streamfunction ψ (Frajka-Williams et al., 2019). The overturning streamfunction is obtained by zonal and vertical integration of the meridional velocity (v):

$$\psi(z) = \int_{z}^{0} \int_{x_w}^{x_E} v(x, z')\ dx\ dz' \tag{1.9}$$

Alternatively, the AMOC can be defined in density coordinates (e.g. Zou et al., 2019), which is more appropriate at high latitudes (Frajka-Williams et al., 2019), as will be discussed later:

$$\psi(\rho) = \int_{\rho_{z=0}}^{\rho} \int_{x_w}^{x_E} v(x, \rho')\ dx\ d\rho' \tag{1.10}$$

$x_{E,W}$ denote the eastern and western boundary and ρ the density.

This mathematical definition is only directly applicable to models, where the meridional velocity is available continuously across a section. Direct observations, take a slightly different approach. The RAPID measurements at 26.5°N (Cunningham et al., 2007) for example measure different components of the circulation by applying different methods (e.g. Smeed et al., 2014). The meridional transport is defined by:

$$T(z,t) = T_{GS}(z,t) + T_{EK}(z,t) + T_{INT}(z,t) + T_{EXT}(z,t) \tag{1.11}$$

Here T_{GS} is the Gulf Stream transport (sometimes also called Florida Current at this latitude) measured by submarine cable measurements. T_{EK} is the Ekman transport based on wind stress derived from satellite measurement and T_{INT} is the interior transport derived from density profiles at the eastern and western boundary measured by tall moorings. Based on the geostrophic and hydrostatic balance (a balance between gravity and vertical pressure gradient force) it is possible to obtain the zonally integrated meridional volume transport relative to an unknown reference level (Rayner et al., 2011; McCarthy et al., 2015). To convert this relative into an absolute transport, an additional exterior transport term (T_{EXT}) is added. This transport is uniform with depth and ensures that the net flow across the section is zero (McCarthy et al., 2015; Frajka-Williams et al., 2019).

By vertically integrating the terms of equation 1.11, it is possible to obtain the volume transport streamfunction. The AMOC is then again defined as the maximum of the streamfunction as described before. The internal and external transports are often combined into a single transport, called upper mid-ocean transport (UMO). Thus the AMOC at the latitude of 26.5°N can be separated into three components that contribute to the total transport, the Gulf Stream, Ekman and upper mid-ocean transports:

$$AMOC(t) = GS(t) + EK(t) + UMO(t) \tag{1.12}$$

Five more mooring arrays provide continuous observations of the AMOC transport for different periods of time (see for example Frajka-Williams et al., 2019). These are the OSNAP (Overturning in the Subpolar North Atlantic Program; $\sim$ 56°N; Lozier et al., 2017), NOAC (North Atlantic Changes; 47°N; Rhein et al., 2019), MOVE (Meridional Overturning Variability Experiment; 16°N; Kanzow et al., 2008; Send et al., 2011), TRACOS (Tropical Atlantic Circulation and Overturning at 11°S; Herrford et al., 2021) and SAMOC (South Atlantic Meridional Overturning Circulation; 34.5°S; Meinen et al., 2013) arrays. They all rely on the aforementioned definition of the AMOC transport, but differ in the methodology to split this transport into different components and their measurement. The MOVE array for example measures the deep, rather than the shallow, limb of the overturning circulation and does not extend across the entire basin, but only to the Mid-Atlantic Ridge.

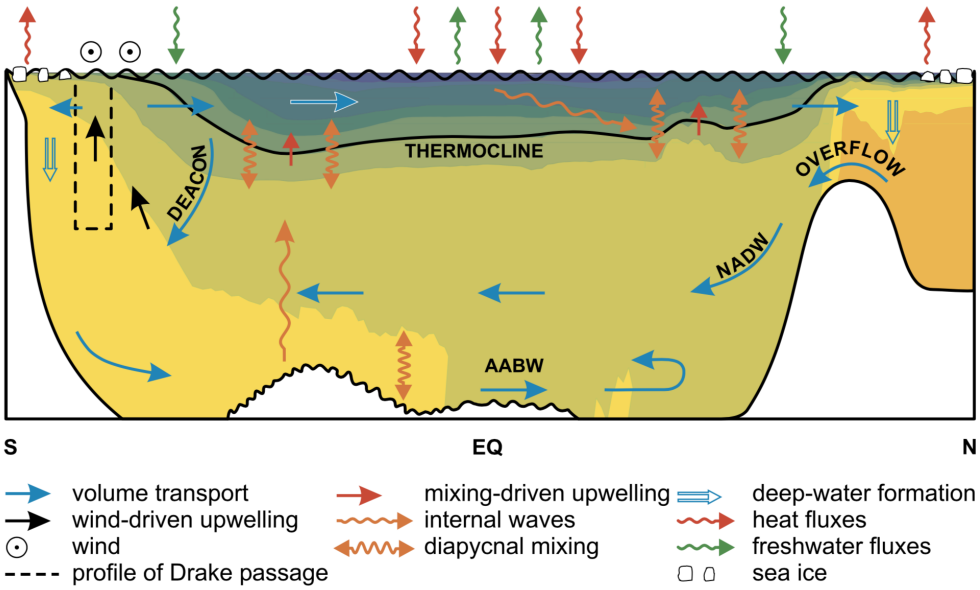

Figure 1.3: Structure and energetics of the overturning circulation, taken from Kuhlbrodt et al. (2007). Colour shading shows the zonally integrated density. The thermocline separates the light and warm upper waters from the denser and cooler deep waters. Wind-driven upwelling of deep water is indicated by black arrows and mixing-driven upwelling by two-headed orange arrows. Zonally integrated volume transports near-surface and at depth are indicated by blue arrows. Deep water formation (DWF) in the high northern / southern latitudes causes the formation of North Atlantic Deep Water (NADW) / Antarctic Bottom Water (AABW). NADW formed in the Nordic Seas has to overflow the shallow sills between Greenland, Iceland, and Scotland.

Shallow AMOC Branch

Although the AMOC itself describes the integrated flow and has no zonal dimension, this transport is not distributed uniformly across the zonal extend of the Atlantic (figure 1.4). The shallow AMOC branch is fed by water entering the South Atlantic through Drake Passage and Agulhas leakage, known as the cold and warm water routes (Rühs et al., 2019).

Water in the Indian Ocean is transported towards the southern tip of Africa in the Agulhas Current (figure 1.5). Beyond the tip of Africa, the current is no longer steered by the coastline. Without considering inertia and friction in the lateral boundary layer, the current would continue westward into the Atlantic Ocean. However, considering inertia and friction along the coast of Africa causes the current to make a sharp turn back into the Indian Ocean, known as the Agulhas retroflection (Ruijter, 1982; Beal et al., 2011). The resulting eastward current is called Agulhas Return Current.

Local instability of the flow (Weijer et al., 2013), southward propagating solitary meanders of the Agulhas Current formed in the Natal Bight (Natal Pulses; Lutjeharms & Roberts, 1988) and mesoscale eddies originating from the Mozambique Channel and East Madagascar Current (Biastoch & Krauss, 1999; Schouten et al., 2002) can cause large anti-cyclonic Agulhas rings to be shed. The Agulhas rings drift westward carrying salty and warm water of Indian Ocean origin into the South Atlantic. Water within Agulhas Rings, other mesoscale structures (filaments and cyclonic eddies) that develop in the highly variable retroflection region and water within a narrow current along the west coast of Africa (Good Hope Jet) can cross the good hope section (Lutjeharms & Cooper, 1996; Penven et al., 2001; Schubert et al., 2021; Ansorge et al., 2005), where it is then considered to have contributed to the inter-ocean exchange between the Atlantic and Indian Ocean (e.g. Biastoch et al., 2008b). The transport associated with this inter-ocean exchange is referred to as Agulhas leakage.

Figure 1.4: Pathways of the Atlantic Meridional Overturning Circulation as derived from Lagrangian studies, taken from Bower et al. (2019). Pathways in the upper limb are coloured red and in the lower limb blue. Bathymetry is shaded at 1,000-m intervals. In alphabetical order: ACC, Antarctic Circumpolar Current; ACS, Agulhas Current System; ARs, Agulhas Rings; BC, Brazil Current; BCS, Benguela Current System; DWBC, Deep Western Boundary Current; EEs, Equatorial Excursions; EUC, Equatorial Undercurrent; FC, Florida Current; GS, Gulf Stream; IP, interior pathways; IRs, Irminger Rings; LC, Loop Current; MAR, mid-Atlantic Ridge; MC, Malvinas Current; NAC, North Atlantic Current; NBC, North Brazil Current; NBCr, North Brazil Current Rings; NBUC, North Brazil Undercurrent; NEC, North Equatorial Current; NECC, North Equatorial Counter Current; NRG, Northern Recirculation Gyre; R, recirculation; SAC, South Atlantic Current; SEC, South Equatorial Current; TGBe, Tail of the Grand Bank Eddies.

Water entering the Atlantic via Drake Passage does flow northward in the Malvinas Current and then spreads east toward Cape Basin in the southern branch of the South Atlantic Subtropical Gyre (South Atlantic Current). From Cape Basin, both inflow water masses follow the northern branch of the South Atlantic Subtropical Gyre (South Equatorial Current). The majority of the northward flow into the equatorial Atlantic is concentrated along the western boundary in the North Brazil Current (Rühs et al., 2019).

Here the water is eventually entrained into the zonal equatorial current system, delaying its northward flow, or directly exported north along the western boundary. The near-surface water enters the Carribean Sea, follows the Loop Current in Gulf of Mexico to reach the southern tip of Florida and is then transported further north through the Florida Strait to continue its path in the Gulf Stream (GS; Halliwell et al., 2003; Bower et al., 2019). East of Newfoundland, the GS turns north into the North Atlantic Current (NAC) and continues east toward Europe. Especially near-surface water in the GS and NAC recirculates in the North Atlantic Subtropical Gyre (NA STG) and only little is directly exported into the Subpolar Gyre (SPG; Foukal & Lozier, 2016). Mostly water at depths below 200 m in the GS enters the SPG in the Irminger Basin, where it takes an anti-cyclonic path around the boundary of the SPG to reach the Labrador Sea, or is continuously advected eastward into the Nordic Seas (Burkholder & Lozier, 2014; Bower et al., 2019).

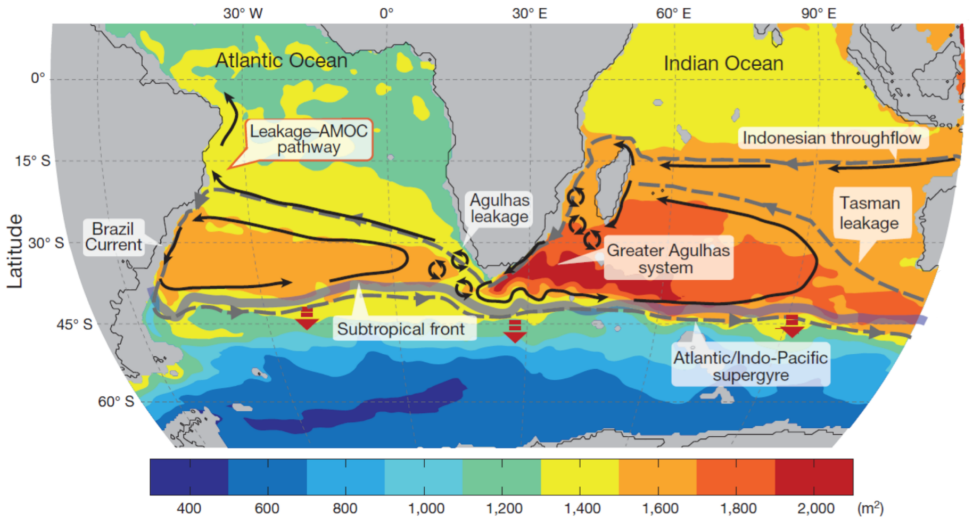

Figure 1.5: The Agulhas Current System and South Atlantic Circulation, taken from Beal et al. (2011). Colours show climatological dynamic height, indicating the mean circulation. Black arrows and labels highlight important flow features, including eddies generated in the Mozambique Channel and East Madagascar Current, the Agulhas Current and its retroflection, as well as Agulhas rings.

Sinking and Water Mass Transformation

The warm and saline surface water entering the SPG and Nordic Seas eventually returns south as NADW (e.g. Bower et al., 2019). Depending on the frame of reference, the connection between the northward and southward AMOC branches is either associated with sinking (in depth coordinates), or water mass transformation from light to dense water (in density coordinates).

Water gains density mainly by a surface exchange of heat with the atmosphere (Marshall & Plumb, 2007; Kalnay et al., 1996). The higher heat capacity of water compared to air, causes the northward ocean currents to carry its warm water far into the North Atlantic, where the large temperature difference between the air and ocean's surface causes strong turbulent heat fluxes that remove heat

from the ocean. Especially in winter, when the air-sea temperature difference is at its maximum. In addition to strong heat loss over the warm GS and NAC, the circulation itself, the distribution and shape of land masses, ice cover and other conditions can cause severe heat loss and water mass transformation to occur in specific locations of the subpolar North Atlantic and Nordic Seas (Xu et al., 2018; Marshall & Schott, 1999; Pickart et al., 2003).

Cold air outbreaks from the continent and high ice cover were shown to cause strong heat loss in the central Labrador Sea (Marshall & Schott, 1999; Våge et al., 2009). The existence of Greenland was argued to be responsible for strong wind events, called the Greenland Tip-Jet and suggested to drive strong heat loss in the Irminger Sea (Doyle & Shapiro, 1999; Pickart et al., 2003). Strong heat loss in winter and other 'preconditioning' factors cause intense vertical mixing (deep convection) that generates a large volume of weakly stratified water, locally down to more than 2000 m depth (Marshall & Schott, 1999). This water mass is the aforementioned LSW. A third region where deep mixing occurs are the Nordic Seas. Here an upward doming of isopycnals due to cyclonic flow and brine rejection from sea-ice formation were shown to create favourable conditions for deep convection (Marshall & Schott, 1999). Although the Labrador Sea was long regarded as the primary deep convection and deep water formation site, more recent publications argue that water mass transformation associated with the AMOC does occur mostly in the Irminger Sea (Lozier et al., 2019), Iceland basin (Desbruyères et al., 2019), and Nordic Seas (Chafik & Rossby, 2019). Furthermore, Zhang and Thomas (2021) even find water mass transformation in the Arctic Ocean to contribute to the mean AMOC transport.

Although dense water would sink, simply based on the hydrostatic balance, water mass transformation and sinking are not equivalent and do not always need to occur in the same place and/or at the same time. As described above, water mass transformation is often described to take place by deep mixing in the interior convection areas of the SPG or Nordic Seas, but it has been shown that the net vertical velocities in the convection regions are small. This is because downward motion in the convection regions is balanced by upwelling in the surrounding (Send & Marshall, 1995). Instead, sinking (a net downward transport of water) occurs mainly along the boundary of the subpolar North Atlantic (Katsman et al., 2018; Straneo, 2006; Spall, 2004).

Furthermore, the wind-driven horizontal circulation and AMOC are intertwined in the subpolar North Atlantic, as the isopycnals are strongly tilted. As a consequence, a barotropic transport across slanted isopycnals can be associated with an overturning in density coordinates (Yeager, 2020; Zhang & Thomas, 2021).

Deep AMOC Branch: the Deep Western Boundary Current

Dense water formed in the Nordic Seas must overflow the shallow sills separating the subpolar North Atlantic from the Nordic Seas. This primarily occurs across the Denmark Strait (maximum sill depth 630 m) and the Iceland-Scotland Ridge (maximum sill depth 840 m). As this water is more dense than water formed in the SPG it sinks down after crossing the sill, mixing with surrounding water. In the traditional view (e.g. Schott et al., 2004), the overflow water follows the boundary of the SPG, creating a continuous current along the deep boundary, which at the exit of the Labrador Sea and further south is known as the Deep Western Boundary Current (DWBC). Recent studies (e.g. Lozier et al., 2022) suggest that overflow water spreads primarily, but not exclusively, along the boundary of the SPG (see also blue arrows in figure 1.4). Deep water formed in the SPG itself, for example in the Labrador Sea, joins the flow along the boundary as well and can be seen to exit the Labrador Sea within the DWBC (Schott et al., 2004).

The dynamics of the Deep Western Boundary Current were first described by Stommel (1958) and further discussed in Stommel and Arons (1959b, 1959a). Their ideas are based on the model of Goldsbrough (1933), which describes the flow of a homogeneous ocean of constant depth on a rotating sphere. The governing equations are similar to equations 1.1 and 1.4, for a stationary flow (time derivatives are zero) and without friction (wind stress). Therefore, the governing equations

Figure 1.6: Theorised abyssal circulation, taken from Stommel (1958). Black dots indicate sources of deep water. Thick lines represent narrow boundary currents and thin lines represent the broad interior flow. Arrows show the direction of circulation.

describe a balance between Coriolis force and pressure gradient force, hence the geostrophic balance. The continuity equation is modified to include a source term and states that a surface source/sink of water must be balanced by a horizontal divergence/convergence of the flow. Note that Goldsbrough (1933) use the model to study the circulation driven by precipitation and evaporation and consider the layer to be bounded by the ocean's surface. Stommel and Arons (1959b) use the same model, but interpret the layer to be located in the deep ocean. Sources and sinks do not represent an exchange with the atmosphere, but with the overlying ocean. However, the overlying ocean has no influence on the abyssal circulation except for an exchange of water. Therefore, they still refer to a 'free surface' even though it does not represent the actual surface of the ocean.

(Stommel & Arons, 1959b) further consider an ocean basin bounded by two meridians without allowing zonal flow across the eastern boundary and a uniformly distributed sink that balances a point source of water in the north. At the western boundary deviations from the geostrophic balance are allowed. The resulting circulation pattern (figure 1.6) is an interior northward flow toward the point source that, following their argumentation, must be balanced by a southward flow along the western boundary. The northward flow arises from the fact that the distributed sink must be balanced by a convergence of the horizontal circulation. As seen in detail before (equation 1.6), a northward geostrophic flow is convergent. This interior northward flow is supplied by water from the northern point source, which is transported away from the source along the western boundary. In the southern hemisphere, their proposed circulation must be southward along the boundary and in the interior, due to the negative sign of the Coriolis parameter. Although the model and assumptions are highly simplified, the general idea that the DWBC owes its existence mainly to deep water formation in the North Atlantic is still accepted.

Direct observations from the exit of the Labrador Sea at 53°N (Schott et al., 2004), several sections in the subtropics (Swallow & Worthington, 1961; Leaman & Harris, 1990; Rhein et al., 2004) and along the coast of Brazil (Schott et al., 2005) prove that a continuous southward current along the deep western boundary exists. Furthermore, studies on the spreading of deep water produced

in the SPG, suggested that this water is transported southward in the DWBC (e.g. Talley & McCartney, 1982). However, this result has been challenged based on direct observations (Lavender et al., 2000; Biló & Johns, 2019) and models (Bower et al., 2009). These studies showed that water is not exclusively transported southward in the DWBC, but a considerable amount of water follows widespread pathways through the interior North Atlantic. Real and virtual floats were found to leave the western boundary mostly around Flemish Cap and the Tail of the Grand Banks. Furthermore, it was found that the formation rate of deep water in the Labrador Sea and its export into the subtropics are not closely tied to each other (Zou & Lozier, 2016). This is highly relevant, because it contradicts the idea that more deep water formation in the North Atlantic would directly result in a stronger transport of this newly formed water to the south, causing an increase of the AMOC.

While the deep water pathways in the North Atlantic are very complex, it was shown that the interior pathways converge toward the western boundary around 30°N. South of this latitude, the deep southward transport primarily accomplished by the DWBC (Gary et al., 2011; Biló & Johns, 2019). At 8°S, the DWBC breaks up into eddies (Dengler et al., 2004), but again forms a coherent current further south (Garzoli et al., 2015).

Upwelling of NADW: Closure of the AMOC

In order to establish a closed circulation, the deep water that is formed in the North Atlantic and transported southward must return to the surface, where it can rejoin the shallow AMOC branch. Furthermore, it was shown in tank experiments that the heat source must be located below the cooling source in order to maintain an overturning circulation, which is known as Sanströms theorem (Sanström, 1908). As the ocean is mostly heated and cooled from the surface, this implies that other sources of energy than the surface buoyancy fluxes must exist in order to maintain the AMOC (Kuhlbrodt et al., 2007).

Kuhlbrodt et al. (2007) suggest that two main processes can supply the energy needed to maintain the overturning circulation. First, the westerly winds over the Southern Ocean drive a northward Ekman transport. This transport is strongest at the latitude of the wind maximum and weaker to the south, which causes a divergence of the flow. This divergence induces an upward velocity that brings deep water toward the surface (e.g. Toggweiler & Samuels, 1995). The second process is diapycnal mixing, driven by the dissipation of internal waves and the interaction of the large-scale and mesoscale circulation with bathymetry (Munk & Wunsch, 1998). Internal waves can be generated by the wind and tides. As these waves break, they generate small scale turbulence which causes the deep water to mix with overlying warmer water. It was shown by Huang (1999) that Sanströms theorem is only applicable in the absence of turbulence and that an overturning circulation can be maintained even with heat source above the cooling source, if turbulent mixing is considered.

Kuhlbrodt et al. (2007) and Webb and Suginohara (2001) conclude that both processes, wind-driven upwelling and mixing, are important to maintain the overturning circulation. A summary of energy sources and processes maintaining the overturning circulation is shown in figure 1.3, taken from Kuhlbrodt et al. (2007).

Mesoscale Ocean Variability

In its most simplified representation, the overturning circulation was described as a continuous 'conveyor' transporting water through the oceans (Broecker, 1987). However, the upper description already shows that the AMOC is much more complex than a such coherent structure would imply. This does not only include various regional current systems and complex processes that cause water mass transformation, sinking, mixing and upwelling, but also the presence of strong mesoscale variability. The mesoscale comprises spatial scales between approximately 10 and 100 kilometres, including oceanic fronts and mesoscale eddies. Mesoscale eddies are vortices with a typical scale of about 75 km (Chelton et al., 2011).

Eddies can either develop from horizontal shear flow (barotropic instability), or vertical shear in the presence of density gradients (baroclinic instability; Eady, 1949; Gill, 1982). Baroclinic and barotropic instabilities can continuously grow (under certain conditions), by drawing energy from either available mean potential, or mean kinetic energy. The dominant scale of (baroclinic) eddies is related to the first baroclinic deformation radius. For a simplified isothermal case, the first baroclinic radius of deformation can be approximated by $L \approx \frac{N}{f}$ (Gill, 1982). f is again the latitude dependent Coriolis parameter. N is the buoyancy frequency and related to the density stratification. This equation shows that the dominant scale of eddies decreases with latitude and weaker stratification, with important implications for modelling mesoscale variability in high latitudes and on the continental shelves (Hallberg, 2013).

Eddies are highly important as they occur in vast areas of the ocean (Chelton et al., 2007, 2011) and can directly contribute to the volume transport associated with the AMOC (Müller et al., 2019; Garzoli et al., 2003; Dengler et al., 2004). Furthermore, eddies can transport water across fronts and thereby strongly contribute to lateral mixing across gradients. This was found to be of major importance in several AMOC key-regions.

Over the Southern Ocean, westerly winds drive a northward Ekman transport and Ekman pumping/suction north/south of the wind maximum, as already mentioned in the last section. This tends to steepen the isopycnals across the Antarctic Circumpolar Current (ACC). At the same time, eddies transport heat southward, flattening the isopycnals (Hogg et al., 2008; Meredith & Hogg, 2006; Gent & Danabasoglu, 2011). Because an acceleration of the winds results in more eddy activity, due to increased baroclinic instability of the circulation, eddies do not only affect the mean strength of the ACC, but also reduce its response to changes in the wind forcing ('eddy saturation'; Hogg & Blundell, 2006; Munday et al., 2013). The same mechanism causes the eddy fluxes to balance parts of the northward Ekman transport, which reduces the impact of wind changes on overturning in the Southern Ocean ('eddy compensation'; Hallberg & Gnanadesikan, 2006; Bishop et al., 2016; Gent, 2016).

Another example for the impact of eddies on an AMOC key region is the Labrador Sea. Here eddies are generated within the convection region itself, or emerge from from the boundary currents. Both types of eddies were shown to re-stratify the ocean after the convection season in winter (Rieck et al., 2019). This is especially important, because the stratification at the beginning of the winter season has a strong impact on the occurrence and depth of deep convection (Marshall & Schott, 1999). Furthermore, the regions where deep mixing occurs is set by the horizontal distribution of eddy heat fluxes (Chanut et al., 2008).

The importance of eddies is not limited to the near-surface AMOC branch, but extends to deep branch as well. As the DWBC flows around the Grand Banks, strong eddy activity causes a considerable amount of water to be deflected from the boundary into the interior ocean in models and direct observations. Thereby eddies carry water of subpolar origin toward the interior ocean and strongly impact on the export of newly formed deep water from the SPG to the NA STG (Getzlaff et al., 2006; Lavender et al., 2000).

Furthermore, Lozier (1997) proposed the existence of deep eddy-driven recirculations in the NA STG. Their existence was later confirmed by Lagrangian experiments, which revealed the existence of the aforementioned interior deep water pathways north of 30°N (Bower et al., 2009). Eddies have been shown to frequently occur along most of the DWBC pathway further south as well. Kanzow et al. (2008) mention the existence of strong mesoscale eddies close to the western boundary at depth in both models and direct observations at 16°N. Xu et al. (2012) find strong recirculations of the DWBC close to the western boundary, partly attributed to the existence of mesoscale eddies (Biló & Johns, 2020). Such recirculations were suggested to cause intense mixing between the DWBC and interior ocean (Rhein et al., 2004). In the South Atlantic, the DWBC was shown to entirely break up into eddies around 8°S (Dengler et al., 2004).

In summary, the transport within mesoscale eddies themselves, their impact on nearly all key-regions of the AMOC and their ability to drive recirculations and mixing, make mesoscale variability a key process contributing to the mean structure and variability of the AMOC. Hirschi et al. (2020) find the pathways of the AMOC (see for example figure 1.4) to be more realistically represented in eddying models. Furthermore, they find the mean AMOC to be stronger with a deeper reaching NADW cell in high-resolution models compared to coarse, non-eddying, models. Similar conclusions were drawn by most other studies investigating the impact of increasing horizontal resolution on the AMOC strength (e.g. Menary et al., 2018; Roberts et al., 2019; Storkey et al., 2018). An improved representation of mesoscale dynamics was also found to have an impact on the ocean mean temperature and salinity state, which alters the AMOC response to externally forced changes (Jackson et al., 2020).

Climate Impacts of the AMOC

The presence of deep water formation in the northern hemisphere is unique to the Atlantic and so is the interhemispheric overturning structure. The Indian Ocean is bounded by the Asian continent already at subtropical latitudes, thus water transported north is not gaining sufficient density to form deep water. Although reaching further north, the Pacific also lacks a conversion of surface to deep water and is thus characterised by two symmetric shallow overturning cells driven by wind on either side of the equator and a deeper cell converting bottom to deep water trough mixing (Ferrari et al., 2017). An explanation for the lack of deep convection in the Pacific could be related to the higher salinity of surface waters in the Atlantic (Warren, 1983). Ferreira et al. (2010) highlight the importance of Drake Passage and the asymmetry between the large Pacific and smaller Atlantic in generating these salinity differences. In an idealised set-up, they find a precipitation deficit over the smaller basin (representing the Atlantic) to result in higher salinity. As a consequence of the interhemispheric overturning structure, heat is transported northward throughout the entire Atlantic, while the heat transport is always poleward (thus southward in the southern hemisphere) in the Pacific and Indian Ocean (Trenberth & Caron, 2001). This causes the AMOC to maintain a cross-equatorial temperature gradient and contribute to a warmer surface water in the North Atlantic compared to the Pacific (Buckley & Marshall, 2016). In combination with the prevailing westerly winds at mid-latitudes, these warm sea surface temperatures contribute to the mild European climate compared the colder North American climate at the same latitude (Palter, 2015; Seager et al., 2002). Consistently, it was shown in several publications that a slow-down, or even shut-down, of the AMOC has severe consequences for the whole northern hemisphere, but especially for Europe. This includes a widespread cooling of up to 8°C and a reduction in precipitation over most of the European continent (Vellinga & Wood, 2002; Jackson et al., 2015; Orihuela-Pinto et al., 2022).

Interestingly, not every consequence of an AMOC slow-down is considered to be negative. Dietz et al. (2021) and Link and Tol (2004) both argue that a moderate slow-down of the AMOC does reduce the social cost of emitting carbon dioxide by offsetting the greenhouse warming in the northern hemisphere to some extend. By changing the local rate of warming/cooling an AMOC slow-down was also found to impact the occurrence of marine heat waves. Marine heat waves are prolonged periods of anomalously warm temperatures and were shown to have a negative impact on marine life (e.g. Pershing et al., 2015). With some local exceptions, more frequent marine heat waves are expected in the southern hemisphere, but less frequent marine heat waves in the northern hemisphere (Ren & Liu, 2021).

Impacts of AMOC variability can be more local as well. By changing the sea surface temperature in the Atlantic, the AMOC was shown to influence the frequency of major hurricanes with impacts on countries in the western subtropical North Atlantic (Yan et al., 2017). Furthermore, climate impacts of the Atlantic Multidecadal Variability (AMV) are considered as climate impacts of multi-decadal AMOC variability, since most studies point to the AMOC as the main driver of the AMV (Zhang et al., 2019). The AMV itself describes coherent changes in sea surface temperature across the whole Northern Hemisphere Atlantic on multi-decadal timescales (e.g. Drews & Greatbatch, 2017).

Many of these climate impacts are described in Zhang et al. (2019). This includes impacts on the position of the Intertropical Convergence Zone (ITCZ), related to changes in Sahel and Indian summer monsoon rainfall (e.g. Zhang & Delworth, 2006). Furthermore, changes in glacier melt and spring snowfall in the alps (Huss et al., 2010; Zampieri et al., 2013), the central U.S. drought frequency (McCabe et al., 2004), the Arctic sea-ice extend and air temperature (e.g. Chylek et al., 2009; Day et al., 2012) and many other changes that are not just limited to the Atlantic, or its surrounding countries and adjacent seas, were linked to the AMV.

In addition to the described temperature related impacts, the AMOC can impact marine ecosystems by transporting carbon dioxide rich water into the deep ocean. The formation of NADW in the Subpolar North Atlantic causes high concentrations of anthropogenic carbon dioxide (CO_2) at mid and abyssal depths (Sabine et al., 2004). This causes the water to become more acidic (lowered pH concentration). Perez et al. (2018) argue that the southward spreading of these corrosive waters within the deep AMOC limb conveys a fast acidification to the deep Atlantic, with expected negative impacts on cold water coral populations. Roberts et al. (2023) further propose that AMOC changes can have direct impacts on the status of ecosystems and the dispersal of marine organisms, by changing temperature, salinity and currents in the ocean. Changes in local currents, partly attributed to AMOC variability, were for example linked to ecosystem changes in the northeast Atlantic that occurred in the mid-1990s (Alheit et al., 2019).

The AMOC is not just a passive component responding to global climate change, but an active component as well. The residence time of CO_2 in the deep ocean is much longer than at the surface. Thus, the transports of anthropogenic carbon into the deep ocean is an important part of the global carbon cycle and impacts the overall amount of CO_2 that can be stored in the ocean (Falkowski et al., 2000). As a consequence, the AMOC can reduce the climate impact of emitting CO_2 by transferring it into the deep ocean, where it remains for a prolonged period of time.

In summary, AMOC changes have far-reaching consequences for marine ecosystems, weather patterns, and the global climate. Regardless whether these changes are expected to have a positive or negative impact, it is of major importance to understand what determines the mean strength of the AMOC and what processes cause its variability.

Variability of the AMOC and its Sources

The AMOC transport, defined as the maximum of the zonally integrated volume transport stream-function, is subject to strong variability on a range of spatial and temporal scales. The source of this variability strongly depends on the latitude and the considered timescale. All of the aforementioned processes and key regions, such as the Indian Ocean inflow via Agulhas leakage, or deep water formation in the North Atlantic, may generate variability of the AMOC. Thus, variability at a single latitude can reflect remote changes in the South and North Atlantic, as well as local changes.

Direct mooring observations of the overturning transport revealed strong variability even on short timescales from days to weeks (Rayner et al., 2011). The largest contribution on daily timescales is caused by variability of the Ekman transport and thus wind-stress variability (Cunningham et al., 2007; Moat et al., 2020). Also at the equator, wind stress was found to be the major source of strong short term variability. The standard deviation of the equatorial AMOC was found to exceed 50 Sv for 4-hourly data. However, due to the Coriolis force being zero, this variability is not caused by Ekman transport changes, but the excitation of equatorial waves (Blaker et al., 2021).

Direct observations further found the AMOC to exhibit pronounced seasonal cycles at 26°N and 42°N (Mielke et al., 2013), as well as 11°S (Herrford et al., 2021) and 34.5°S (Meinen et al., 2018). While this seasonal cycle is partly explained by the direct effect of wind stress variability via changes in the Ekman transport, seasonal variability was also found in the geostrophic interior transport (Kanzow et al., 2010). Mielke et al. (2013) find similar seasonal cycles in the AMOC

and Sverdrup transport, suggesting that the large-scale wind stress curl could contribute to the AMOC's seasonal cycle. Kanzow et al. (2010) further mention that the annual AMOC cycle at 26°N is primarily caused by local wind stress curl changes in the eastern basin. Between 30°N and 40°N, it was shown that the seasonal cycle of wind stress can drive AMOC reversals that create a minimum of the transport in boreal winter (Dewar et al., 2022).

As continuous observations of the AMOC are now long enough for statistically robust results, interannual variability of the AMOC was subject to numerous studies over the recent decade. Various observation and model based publications focus on explaining interannual variations of the AMOC. Most studies find interannual AMOC variability to be strongly linked to wind-driven processes (e.g. Biastoch et al., 2008a; Polo et al., 2014; Zhao & Johns, 2014; Elipot et al., 2016; Duchez et al., 2014; Roberts et al., 2013). This is especially wind-driven coastal upwelling that changes the density structure along the boundary and Ekman pumping driven by changes in the wind stress curl (Polo et al., 2014). Duchez et al. (2014) further argue that the upper mid-ocean geostrophic transport at 26.5°N is so closely related to the Sverdrup transport that it could be used to extend the AMOC timeseries back to years before the geostrophic moorings of the RAPID array were installed. All these studies point to a dominant contribution of wind-driven processes on AMOC variability on daily to interannual timescales. Nevertheless, there is also a considerable fraction of variability that can not be explained by any surface forcing, but emerges from internal ocean variability, for example related to the presence of mesoscale eddies. Forced and unforced variability can have the same magnitude at certain latitudes (Leroux et al., 2018; Grégorio et al., 2015).

Decadal variability is a main focus of study as well, but overall less well understood than variability on interannual timescales. Several key-regions were identified to contribute to decadal (and longer) changes of the AMOC transport. Those regions are typically the aforementioned regions responsible for water mass transformation, or regions that determine the inflow properties in the south. The results of Duchez et al. (2014) described above also hold on decadal timescales, indicating that at least one component (the geostrophic interior transport) of the mid-latitude North Atlantic AMOC reflects wind-driven changes on this timescales. At the same time, most studies argue that buoyancy forcing is the main driver of decadal AMOC variability (Biastoch et al., 2008a; Polo et al., 2014; Yeager & Danabasoglu, 2014). An increase in (winter) heat loss to the atmosphere is believed to increase the transformation from light surface water to dense water at depths, thereby increasing the AMOC transport (e.g. Megann et al., 2021). Similar to the previous discussion on the mean AMOC, also variability of the AMOC was long thought to be mainly driven by heat flux variations in the Labrador Sea (Yeager & Danabasoglu, 2014; Böning et al., 2006; Eden & Willebrand, 2001b). But especially more recent studies argue that (decadal) AMOC variability is mainly caused by changing heat fluxes in the Irminger Sea (Lozier et al., 2019; Megann et al., 2021).

Regardless whether heat fluxes in the Labrador, or Irminger Sea, are regarded more important, studies consistently link heat flux variability and associated circulation changes in the subpolar North Atlantic to the state of the North Atlantic Oscillation (NAO; Megann et al., 2021; Eden & Jung, 2001a; Robson et al., 2012; Yeager & Danabasoglu, 2014). The NAO is the leading mode of surface air pressure variability in the North Atlantic and describes a changing pressure difference between the Iceland low and Azores high pressure systems (Hurrell, 1995; Hurrell & Deser, 2010). Changes in the NAO were proposed to explain most of the decadal variability between the 1970s to 2000. After 2000 it was found that heat fluxes changed mostly in response to anomalous advection in the North Atlantic Current (Megann et al., 2021). In general, the adjustment of the ocean circulation to changes in the NAO phase are not passive, but can result in several feedbacks that may cause periodic variability. Menary et al. (2015) suggests that an increase in deep convection and the AMOC cause a speed up of the NAC and more heat transport into the SPG, which in turn reduces deep convection with a timelag. Similarly, Drews and Greatbatch (2017) suggest that an initial strengthening in the AMOC driven by heat flux variability can reverse into a state of weaker overturning by transporting more heat northward. This leads to enhanced melting of sea-ice and a reduction of deep water formation, due to a negative density anomaly caused by decreasing salinity.

Furthermore, it should be mentioned that the question about processes generating AMOC variability is not necessarily equivalent to the question which processes determine the mean AMOC strength. Accepting the conclusions of Yeager and Danabasoglu (2014) (the Labrador Sea contributed significantly to the strong AMOC in the 1990s) and Lozier et al. (2019) (the Labrador Sea has minimal contribution to the mean overturning strength) at the same time, would mean that key-regions of decadal variability must not be the regions that also determine the mean AMOC strength.

However, not only processes in the North Atlantic were shown to impact decadal AMOC variability. Biastoch et al. (2008b) attribute a larger fraction of decadal AMOC variability in the South Atlantic to variability of Agulhas leakage than to North Atlantic deep water formation. Furthermore, Yeager and Danabasoglu (2014) find the southern hemisphere wind-forcing to strongly contribute to decadal AMOC variability in the southern hemisphere, but not in the northern hemisphere. Therefore, both studies point to decadal variability being predominantly driven by changes in the same hemisphere.

AMOC changes on timescales longer than a few decades are primarily driven by external forcings. In this context, this includes greenhouse gas and aerosol concentrations (Jackson et al., 2022). A long term reduction of the AMOC by 34-45% is expected toward the end of this century, caused by increased greenhouse gas concentrations (Weijer et al., 2020). The most often proposed mechanism is a combination of melting Greenland ice sheets and increased radiative forcing. Both processes cause surface water in the SPG to become less dense, which increases stability and reduces deep convection (Mikolajewicz & Voss, 2000; Stouffer et al., 2006; Gregory et al., 2005; Swingedouw et al., 2013). Concerns were raised that this mechanism could cause a complete shut-down of deep convection and the AMOC (see Lozier (2010) for a discussion), but results obtained by Zhang and Thomas (2021) suggest that overturning may be maintained even when deep convection in the SPG is completely absent. While there is general agreement among the current state-of-the-art coupled climate models (CMIP6; Eyring et al., 2016) that the AMOC will not collapse until the end of this century (Weaver et al., 2012; Weijer et al., 2020), other studies argue that common biases favour a too stable AMOC in most climate models (Liu et al., 2017; Boers, 2021). As a consequence, they propose that the AMOC response to changing greenhouse gas concentrations may be more severe and even that the AMOC could be close to a transition from a strong into a weak overturning state (Boers, 2021). Several studies have suggested that the AMOC could be bi-stable (e.g. Stommel, 1961; Rahmstorf et al., 2005; Hawkins et al., 2011). This means that once a tipping point is reached, the AMOC could rapidly changes to a state of weaker overturning. Even if the anomaly that caused this transition is reversed, the AMOC may not recover to its previous state (Wood et al., 2003). Based on the current knowledge this does not seem to be a very likely scenario for the AMOC evolution within this century, but still highlights the need to better understand the AMOC's response to external forcing on climate (multi-decadal to centennial) timescales.

Although a collapse of the AMOC until the end of this century is unlikely, a possible bi-stability of the AMOC was used to explain rapid climate transitions on timescale of millennia. Rahmstorf (2002) describe three prevailing modes of the overturning circulation during the last 120.000 years, which is are the warm, cold and off modes. In the warm mode, NADW is produced in the Nordic Seas, while in the cold mode deep water formation only occurs in the subpolar North Atlantic. The states are named by the associated temperature in the North Atlantic. During the off mode no deep water is formed in the North Atlantic. It was found in paleo climate records, that on millennial timescales a slow warming of the Southern Ocean does coincide with a rapid cooling around Greenland (Blunier & Brook, 2001). This pattern is known as the bipolar climate sea-saw (BCS). Presumably connected to the BCS is the Bipolar Ocean Sea-Saw (BOS), which states that deep/bottom water formation increases in one hemisphere, as it decreases in the other (Swingedouw et al., 2009). It was hypothesised that a transition of the AMOC from an off, or cold state to the warm state and the associated increase in northward heat transport may explain the BOS and BCS (Rahmstorf, 2002; Crowley, 1992; Stocker, 1998). Several mechanisms were proposed that could cause the overturning circulation to switch states, most notably freshwater discharge into the North

Atlantic (e.g. Schmittner et al., 2003) and Southern Ocean (e.g. Weaver et al., 2003). Possible mechanisms involving an interaction of the South and North Atlantic to generate basin-wide AMOC changes are discussed in more detail in the next section.

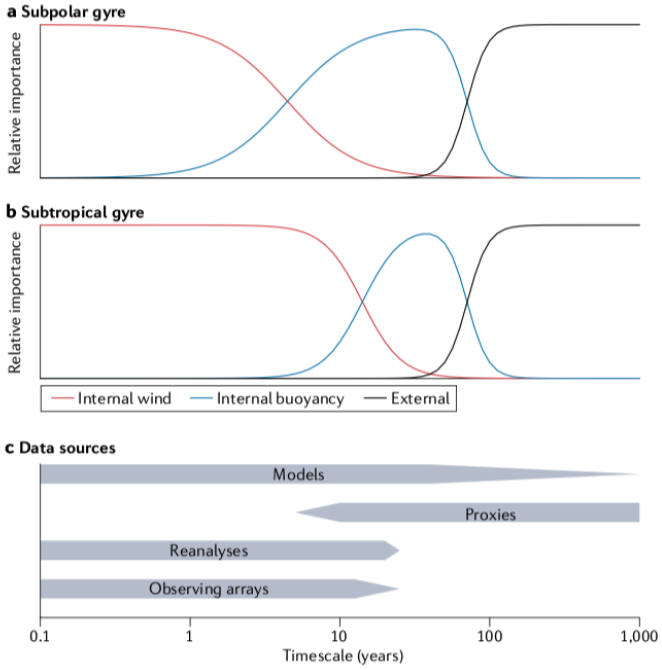

Figure 1.7: Schematic of AMOC timescales, taken from Jackson et al. (2022). a) Relative contributions of internal wind, buoyancy forcing and external forcing for Atlantic Meridional Overturning Circulation (AMOC) changes in the subpolar North Atlantic Ocean. b) As in panel a, but for the subtropical North Atlantic. c) Timescale over which different data sources are able to distinguish AMOC variability, based on their length, and assuming that the proxies used do not represent higher-frequency AMOC variability. Drivers of AMOC variability differ depending on timescales, and different data sources are appropriate for different timescales.

In general, the processes responsible for AMOC variability become less certain with increasing timescale. This is of course not surprising, because on longer timescales most results can only be inferred from models and proxies, not direct observations. A summary of the different mechanisms proposed to generate AMOC variability on different timescales and sources of data providing this information are summarised in figure 1.7, taken from Jackson et al. (2022).

1.2 The Idea and Relevance of Connectivity

Connectivity between remote ocean regions is essential to understand how the described processes that can generate AMOC variability interact. More generally, the term connectivity refers to an exchange of information, energy, or matter between two remote locations, as already introduced. Therefore, it can refer to linkages between water mass properties (such as temperature and salinity) and momentum (ocean circulation) changes, but also to the exchange of organisms between remote ecosystems. In general, connectivity can exist on all spatial and temporal scales, but in this thesis connectivity from interhemispheric (whole Atlantic) to regional scales (a few 100 to about 1000 kilometres) are in the focus.

1.2.1 Interhemispheric AMOC Connectivity

Connectivity between the hemispheres is especially important in the context of AMOC variations, since processes in both hemispheres can generate variability of the AMOC, that itself connects the hemispheres by a cross equatorial transport of water. In addition to a fundamental interest in understanding the variability of the AMOC, a special interest in interhemispheric connectivity originates from the search for predictable components of the climate system. Connectivity between remote ocean areas could allow to predict circulation changes several months, years, or even decades in advance. This idea is especially relevant with regard to the AMOC, as variability in certain key locations may generate changes in the AMOC with a considerable time lag. As an example, an increase of the Indian Ocean inflow into the Atlantic via Agulhas leakage could cause an AMOC response in the northern hemisphere a few decades later (e.g. Gordon et al., 1992; Knorr & Lohmann, 2003). Accordingly, an in-situ measurement in the South Atlantic could be used to make predictions of the North Atlantic AMOC and associated impacts on the North American and European continents. With the already described impacts of the AMOC in mind, such a prediction could be of huge benefit.

Of course, even if such connectivity exists, locally forced variability could mask changes initiated in the opposite hemisphere. It is therefore highly important to better understand the processes and key-regions that generate AMOC variability in general. As direct and continuous observations of the AMOC are sparse and only exist at few latitudes, models are a viable tool to study AMOC variability. Due to the high complexity of the AMOC, comprising various circulation systems and processes generating variability, modelling the AMOC has been a challenge for decades. Pronounced differences in the mean strength, variability and response to forced changes exist among different models and model experiments (e.g. Danabasoglu et al., 2014; Biastoch et al., 2021; Weaver et al., 2012), highlighting the need to work on improved modelling strategies to better understand the AMOC.

The two most commonly applied (realistic) set-ups to study AMOC variability are forced and coupled ocean general circulation models. Forced ocean models use prescribed atmospheric states, derived from observations using reanalysis techniques, to calculate surface heat, freshwater and momentum fluxes. In contrast, coupled models use an interactive atmosphere model, shifting the boundary condition problem from the ocean's surface to the atmosphere. Both set-ups have advantages and disadvantages.

While forced ocean models are typically able to reproduce the correct timing of (AMOC) variability on various timescales, they suppress important ocean atmosphere feedbacks, because the atmospheric state is prescribed and does not adjust to changes in the ocean model (Roberts et al., 2013; Griffies et al., 2009). This is a disadvantage in sensitivity experiments that aim to study the impact of specific changes on the AMOC, because the atmosphere may adjust to these changes as well, thereby modifying the ocean response. Furthermore, excluding ocean-atmosphere feedbacks leaves the AMOC more susceptible to freshwater changes in the North Atlantic, reducing AMOC stability (Griffies et al., 2009; Behrens et al., 2013). This is typically accounted for by restoring the sea surface salinity to climatological values, but the strength of this restoring is arbitrary and it could counteract true changes (due to changes in ocean dynamics and surface fluxes) in the salinity field by restoring it to a fixed state.

Coupling the ocean model to an interactive atmosphere model allows to omit these disadvantages by explicitly simulating ocean-atmosphere feedbacks. Nevertheless, coupled models generate internal variability that is not constraint by observations. Only toward centennial timescales, changing atmospheric boundary conditions, such as greenhouse gas concentrations, may have an impact on the ocean's evolution. Therefore, coupled models do not reproduce the correct timing of (AMOC) variability on most timescales (Cheng et al., 2013; Ding et al., 2013; Flato et al., 2013). This, however, is important to compare the model to observations and to attribute past variability to specific processes.

It is therefore an important question, whether a fully coupled model can be modified to simulate the correct timing of AMOC variability, while important ocean-atmosphere feedbacks are still simulated. Based on the large impact of wind stress variability on the horizontal circulation and the AMOC mentioned in the previous sections, such a modification could rely on the assimilation of wind stress anomalies into a coupled model. A main goal of this thesis is to study the ability of a method known as partial coupling (Ding et al., 2013; Thoma et al., 2015) to combine the advantages of forced and coupled model experiments. In partial coupling mode, reanalysed wind stress anomalies are used to force the ocean component of a coupled model, while heat and freshwater fluxes are still interactively exchanged with the atmosphere component. While the former was found to improve the timing of variability of various climate indices (Thoma et al., 2015), the latter is expected to maintain important ocean-atmosphere feedbacks. However, a detailed assessment of the Atlantic Ocean circulation and its variability in partially coupled experiments is not available. Also, partial coupling was only used in non-eddying models, but the presence of mesoscale activity could reduce the success of partial coupling by introducing unforced variability (Leroux et al., 2018; Grégorio et al., 2015). In addition to advancements in modelling, which can result in a better representation of past AMOC variability, partially coupled experiments can directly contribute to a more detailed knowledge of processes generating AMOC variability on various spatial and temporal scales. While wind stress was mostly found to impact the AMOC on interannual timescales, important open questions remain. This includes the question, whether the interannual, wind-driven variability itself can feed back on the North Atlantic buoyancy fluxes that were shown to be important on decadal and longer timescales (e.g. Jackson et al., 2022). Such a feedback could, for example, be caused by a cumulative effect of interannual variability over several years. It was suggested in other studies that heat fluxes in the SPG are affected by the ocean circulation itself (Megann et al., 2021; Menary et al., 2015) and Reintges et al. (2020) show that assimilating wind stress anomalies can impact sea surface temperatures in the North Atlantic on interannual timescales via changes in the ocean circulation. Furthermore, teleconnections to the Pacific may have an impact on the North Atlantic atmospheric circulation (e.g. King et al., 2023) and thus heat flux variability. The assimilation of observed wind stress anomalies was shown to improve the timing of variability in the Pacific even on multi-decadal timescales (Thoma et al., 2015).

Question 1:
1.1) Is it possible to improve the representation of past AMOC variability in models by assimilating observed wind stress anomalies in coupled models at eddying resolution?

1.2) On which spatial and temporal scales does wind-variability contribute to AMOC variability?

Studying the yet unknown capabilities and limitations of partial coupling provides further information how and where (wind stress) anomalies can be applied to investigate basin-wide AMOC changes and interhemispheric connectivity. In the North Atlantic, a possible feedback of wind stress changes on the buoyancy fluxes and AMOC could be exploited to force deep water and AMOC anomalies that potentially spread into the southern hemisphere. In the southern hemisphere, a possible impact of the southern hemisphere westerly winds on the AMOC could be utilised to study interhemispheric connectivity. An increase in the southern hemisphere westerlies was hypothesised to impact the AMOC directly via enhanced upwelling of deep water (Toggweiler & Samuels, 1995; Delworth & Zeng, 2008; Klinger & Cruz, 2009). Furthermore, Agulhas leakage was shown to respond to changes in the westerlies and could thereby affect the AMOC via an increased inflow of water from the Indian Ocean. Durgadoo et al. (2013) propose that an increase in the westerlies enhances northward Sverdrup transport in the South Atlantic, which must be balanced by an increase in Agulhas leakage. This is connected to an increased import of saline water into the South Atlantic and was hypothesised to affect the AMOC by increasing the density in the North Atlantic deep water formation regions (e.g. Gordon et al., 1992). Weijer et al. (2002) find freshwater/buoyancy anomalies in the Agulhas region to reach the North Atlantic and to affect the formation of NADW and the AMOC strength.

The interaction of AMOC changes forced in the southern and northern hemispheres is important for the sensitivity of the AMOC to global climate change. A warming in the North Atlantic, induced by rising greenhouse gas concentrations, increases the stability of the water column and causes the Greenland ice sheet to melt. The added freshwater close to the surface further increases stability and could therefore reduce water mass transformation in the North Atlantic and result in a weaker AMOC (e.g. Mikolajewicz & Voss, 2000; Swingedouw et al., 2013). At the same time, a significant increase in the strength of the southern hemisphere westerly winds and a southward shift have been observed over recent decades, caused by an increase in greenhouse gas concentrations and loss of stratospheric ozone (Arblaster & Meehl, 2006; Thompson & Solomon, 2002; Marshall, 2003; Swart & Fyfe, 2012; Goyal et al., 2021). This strengthening is projected to continue in the future, even as ozone concentrations recover (Ivanciu et al., 2022a; Goyal et al., 2021). In contrast to the projected changes in the North Atlantic, a strengthening of the AMOC is expected from the South Atlantic changes. Most model studies show that the North Atlantic impact dominates and project a moderate decrease in the AMOC transport until the end of this century (Weijer et al., 2020). However, the magnitude of this decline is not well constraint with models projecting a wide range of future AMOC trends. Therefore, a better understanding of AMOC changes forced in the southern and northern hemispheres, as well as their interaction, is needed.

The northward propagation of anomalies originating in the South Atlantic is of particular importance, because it could affect the AMOC's stability and the existence of tipping points on centennial and longer timescales. As mentioned before, the AMOC may have different stable states and a transition between the different states could be related to the interhemispheric advection of salt from the South Atlantic. Knorr and Lohmann (2003) for example find an increased input of salt via the warm water route (Agulhas leakage) and cold water route (Drake Passage) to re-establish deep convection and overturning following a warming of the Southern Ocean. Swingedouw et al. (2009) and Weaver et al. (2003) link deep water formation changes in the North Atlantic to freshwater anomalies in the Southern Ocean, which could explain parts of the BCS/BOS patterns. It was further proposed that a strengthening of the AMOC could increase the import of salt via its southern boundary, which would reinforce the initial strengthening by increasing the North Atlantic salinity and density. This mechanism is known as the salt-advection feedback (Weijer et al., 2019). Although this feedback acts on very long timescales and is not explicitly studied in this thesis, it provides motivation to investigate the importance of an interhemispheric advection of anomalies from the South into the North Atlantic (this is the first component of the full feedback cycle). Together with the results obtained from partially coupled experiments (see chapter 3), this causes the focus of thesis to be on anomalies that are initially forced in the South Atlantic.

Overall, an improved knowledge of connectivity between the South and North Atlantic is of major importance for the assessment of future risks. It provides potential for enhanced long-term predictability and may help to understand past changes of the Atlantic Ocean circulation. Although connectivity between the South and North Atlantic was shown to exist in several studies (e.g. Knorr & Lohmann, 2003; Weijer et al., 2002; Klinger & Cruz, 2009), many open questions remain, as currently available studies rely on model set-ups with several limitations. This includes coarse resolution, no interactive atmosphere and/or a limited length of experiments. All these aspects may modify the response of the ocean to applied changes in the southern hemisphere, or prevent a possible adjustment to be detected. Therefore, the detailed processes involved in the interhemispheric connectivity of temperature, salinity and density anomalies and the impact of such a connectivity on the AMOC are still fundamental open questions.

Question 2:
How do temperature, salinity and density anomalies forced by an increased Southern Ocean wind stress propagate into the North Atlantic in an eddying, coupled model and what is their impact on the AMOC?

1.2.2 Regional Connectivity Shaped by the Interaction of Currents with Eddies

The Impact of the DWBC and Eddies on AMOC Coherence

Although often visualised in simplified schematics with very few pathways spanning the global oceans, the AMOC is in fact a highly complex circulation and comprises various regional current systems, mesoscale and sub-mesoscale processes as outlined before (see for example Bower et al., 2019).

A fundamental question regarding the AMOC on regional scales is connected to the timescale, on which AMOC variability is coherent across a wider range of latitudes. In other words, the question, whether AMOC anomalies at remote latitudes are connected. This has direct implications for the interpretation of measurements, since the AMOC can only be measured at a limited number of latitudes. Especially continuous measurements require basin wide mooring arrays that only exist at 6 locations (with some arrays providing data only for a few years, yet). Therefore, it is important to understand, on which timescales AMOC changes measured at a single latitude are representative for basin wide circulation changes, rather than local variability and which processes are responsible for coherent variability.

Bingham et al. (2007) studied interannual AMOC coherence and found that AMOC variations are correlated within a latitude range of roughly 15° in the subtropics. In general, there are three possible mechanisms that could cause the AMOC at specific latitudes to vary in-phase, potentially with a timelag. Boundary waves were shown to propagate signals along the western boundary, causing a fast adjustment to changes in the ocean circulation over a wide range of latitudes (Getzlaff et al., 2005; Elipot et al., 2013). Second, anomalies can propagate by advection and therefore by a transport of water. Advective propagation is in general slower than a propagation by waves (e.g, Elipot et al., 2013). Furthermore, interannual AMOC variability is mostly generated by local wind forcing, as discussed above. Elipot et al. (2016) show that wind forcing itself can cause coherent variability in a larger range of latitudes in the subtropical North Atlantic.

This brings up an important question. If AMOC variability is mostly driven by wind forcing on interannual timescales (see previous sections) and if wind forcing might also explain the coherence of AMOC variability on this timescale, why is there apparently no important contribution from advection? This is especially relevant for the latitude range covered by the RAPID (26.5°N) and MOVE (16°N) arrays. It was concluded by Elipot et al. (2013) that advection in the DWBC does not play a major role for coherent variability along the Northwest Atlantic continental slope (from the Grand Banks to 39°N). A possible explanation could be the aforementioned existence of interior pathways. The southward transport is not solely in the DWBC and the large-scale eddy-driven recirculation gyre may reduce the impact of advection on coherent transport variability.

However, south of 30°N it was shown that the DWBC is the dominant pathway of the lower AMOC limb (e.g. Gary et al., 2011). Therefore, a change in the DWBC transport at 26.5°N (RAPID) may be expected to result in a similar change at 16°N (MOVE) with a timelag. This timelag would be determined by the travel time of water to the downstream section. Nevertheless, strong mesoscale activity was found to exist along the DWBC pathway in the subtropical North Atlantic (Kanzow et al., 2008; Biló & Johns, 2020). The interaction of eddies and other mesoscale features with the DWBC could add a variety of volume transport pathways between the sections, outside the main DWBC flow. Thereby, they could extend the time water needs to reach 16°N and reduce the coherence of transport variability in the DWBC. Accordingly, mesoscale variability could explain why apparently, advection is of minor importance for the coherence of AMOC variability at the MOVE and RAPID sections, although they are connected by a strong, continuous current.

Question 3:
What is the impact of mesoscale variability and advection in the DWBC on the coherence of AMOC variability in the subtropical North Atlantic?

The Impact of the DWBC and Eddies on Ecosystem Connectivity

As described above, the interaction of eddies with the DWBC could have important implications for the coherence of AMOC variability. But the potential effect of such an interaction is not limited to physical questions. The mean pathways of the AMOC (see for example figure 1.4) and their interaction with eddies can also have important implications for the connectivity of remote ecosystems. As an example, the impact of eddy-current interactions on the connectivity of ecosystems in the Northwest Atlantic, including the wreck of RMS Titanic, is studied in this thesis.

After the RMS Titanic collided with an iceberg south of Newfoundland in 1912, it sank to approximately 3800 m depth. Today the wreck provides a habitat for various deep-sea species, including the deep-sea octocoral *Chrysogorgia agassizii* (Vinogradov, 2000). Ship wrecks, such as the Titanic, could act as stepping stones, connecting natural occurring populations that otherwise would be separated by too large distances (Meyer-Kaiser & Mires, 2022). Connectivity between remote ecosystems was argued to be of major importance for the recovery of ecosystems from damage and survival under changing environmental conditions (Gary et al., 2020; Cowen & Sponaugle, 2009). Accordingly, the Titanic may contribute to the resilience of deep-sea corals and possibly other marine organisms. As the wreck is rapidly degraded by corrosion (Salazar & Little, 2017; Bright et al., 2005), it is important to understand its significance for the dispersal of deep-sea species in the North Atlantic.

The wreck's location south of the Grand Banks of Newfoundland, a highly complex oceanographic region, makes the study of larval dispersal from and to the Titanic an interesting biological, but also physical question. It was mentioned before that the region South of the Grand Banks is characterised by strong mesoscale eddy activity. This includes eddies that develop from an interaction of the DWBC with the NAC (Getzlaff et al., 2006), baroclinic instability of the DWBC around Flemish Cap (Pickart et al., 1997) and the local generation of submesoscale vortices from the DWBC flow at the Tail of the Grand Banks (Bower et al., 2013). The main DWBC core is located north of the Titanic and maximum velocities are found higher up in the water column, but eddies generated by the DWBC can reach the horizontal position of the wreck site. South of the Titanic, the GS splits into the north-eastward NAC and eastward Azores Current (Daniault et al., 2016). The GS/NAC circulation is associated with strong mesoscale activity as well. Gulf Stream rings that develop from meanders of the Gulf Stream (Brown et al., 1986) and deep cyclones generated by mixed barotropic-baroclinic instability below meander troughs (Schubert et al., 2018; Shay et al., 1995) potentially impact the circulation around the wreck site.

Depending on the vertical structure of these eddies, they could impact the flow even at 3800 m depth. Furthermore, natural occurrences of *C. agassizii* were found on the eastern slope of the Grand Banks. Larvae spawned at this location are likely transported in the DWBC toward the Titanic. Nevertheless, they can only reach the wreck, if there is a mechanisms that deflects them away from the boundary. This may be accomplished by the interaction of eddies with the DWBC. Eddies could cause a strong exchange with the interior, or trap and transport larvae towards the wreck themselves. Accordingly, the interaction of eddies with the DWBC could be highly relevant for biophysical connectivity along the Northwest Atlantic continental slope, in particular for connecting the Titanic to natural occurring ecosystems.

Question 4:
What is the role of the DWBC and mesoscale eddies in connecting deep ecosystems along the Northwest Atlantic continental slope?

1.3 Objectives and Structure of this Thesis

The main objective of this thesis is to improve our knowledge of the Atlantic Ocean circulation and how it is impacted by, or impacts, connectivity between remote ocean regions. Based on several advances in modelling, it is studied how local (wind) changes and anomalies generated in the South Atlantic affect AMOC variability. Further, it is studied how the interaction of important AMOC pathways with eddies and other mesoscale features affects physical and biophysical connectivity.

While well suited model configurations to study regional connectivity in the North Atlantic already exist, for example the VIKING20X configuration described in Biastoch et al. (2021), the study of basin-scale (especially interhemispheric) connectivity requires the development of a new configuration. This configuration should cover the whole Atlantic Ocean at eddying resolution, needs to be coupled to an interactive atmosphere model and should allow for long experiments, covering at least a few centuries, without requiring unreasonable computing time resources. A configuration satisfying these demands, FOCI-ATLAS10, is developed, as described in chapter 2.

A pre-requisite to better understand the interaction of remote key-regions on the AMOC is to study processes that can generate AMOC variability in general. In addition to direct observations, an improved representation of past AMOC variability in models is essential to improve our knowledge. Based on the importance of wind variability and the disadvantages of current model configurations, it is aimed to improve the representation of past AMOC variability in models by applying a partial coupling approach in an eddying model configuration in chapter 3. Necessary changes to the model are described in chapter 2.

Relying on the newly developed FOCI-ATLAS10 configuration and experience gained by investigating AMOC variability in partially coupled experiments, a sensitivity experiment is conducted to study interhemispheric connectivity. In a perturbation experiment with 5 ensemble members, the coupled adjustment to wind stress changes over the Southern Ocean on climate timescales is studied. Further code additions, which are described in chapter 2, were needed to perform these experiments. In chapter 4 fundamental questions on the propagation of temperature, salinity and density anomalies from the southern into the northern hemisphere and their impact on the AMOC are addressed.

Going from the basin-scale to more regional scales in chapter 5, the physical connectivity of two remote sections of long term AMOC measurements in the subtropical North Atlantic is studied. Knowing about the dominance of wind-driven AMOC variability on interannual timescales, the main objective is to assess how eddies and meanders reduces the impact of advection in the DWBC on the latitudinal coherence of AMOC variability.

A similar interaction between the DWBC, one of the most important AMOC pathways, and eddies is demonstrated to shape the connectivity of ecosystems along the Northwest Atlantic continental slope in chapter 6. Based on a set of Lagrangian experiments, it is studied how the DWBC, eddies and the bathymetry affect the dispersal of deep-sea corals.

Model development objectives (chapters 2, 3 and 4):
- Develop a nested, coupled configuration to study interhemispheric connectivity
- Joint implementation and testing of a partial coupling procedure
- Implement an online modification of the wind stress to run sensitivity experiments

Main scientific questions:
1.) Model development and sources of AMOC variability (chapter 3):
Is it possible to improve the representation of past AMOC variability in models by assimilating observed wind stress anomalies in coupled models at eddying resolution?
On which spatial and temporal scales does wind-variability contribute to AMOC variability?

2.) Interhemispheric connectivity (chapter 4):
How do temperature, salinity and density anomalies forced by an increased Southern Ocean wind stress propagate into the North Atlantic in an eddying, coupled model and what is their impact on the AMOC?

3.) Physical connectivity on regional scales (chapter 5):
What is the impact of mesoscale variability and advection in the DWBC on the coherence of AMOC variability in the subtropical North Atlantic?

4.) Biophysical connectivity on regional scales (chapter 6):
What is the role of the DWBC and mesoscale eddies in connecting deep ecosystems along the Northwest Atlantic continental slope?

CHAPTER 2

Methods: Model Development and Lagrangian Analysis

2.1 Model Configurations for Regional and Basin Scale Connectivity Studies

As outlined above, this thesis is concerned with two different spatial scales, the regional scale spanning a few 100 to 1000 kilometers and the basin scale, covering the whole Atlantic.

To study connectivity on the regional scale, it is highly important to use a model set-up with sufficient resolution to simulate the mesoscale spectrum. Questions 3 and 4 of this thesis explicitly refer to the importance of mesoscale eddies on physical and biophysical connectivity. Especially around the Grand Banks (the Titanic wreck site), a resolution of 1/10° is only marginally resolving the first baroclinic deformation radius (Hallberg, 2013) and an even higher resolution is required to simulate the full spectrum of mesoscale variability. Furthermore, the representation of the western boundary current system was shown to be significantly improved in eddying compared to coarse resolution models. Although mostly the representation of the surface western boundary currents are studied explicitly (e.g. Chassignet et al., 2020; Smith et al., 2000), the same applies to the deep western boundary current. A detailed representation of the Deep Western Boundary Current with a width of approximately 200 km (Bryden et al., 2005) and its variability therefore requires sufficiently high resolution as well.

Furthermore, the studies related to questions 3 and 4 are highly dependent on a realistic representation of the bathymetry. Small bathymetric features, such as the Island of San Salvador in the subtropical North Atlantic, were found to be highly important for DWBC circulation (Leaman & Vertes, 1996; Xu et al., 2012). The Titanic is located in a deep embayment, approximately 80 km in diameter, bounded by the Newfoundland Ridge and Brand Banks. Probably, this bathymetric setting has major implications for the dispersal of larvae spawned at the wreck site. For those reasons, both studies need to rely on a model capable to resolve such bathymetric features. It was therefore chosen, to use the existing model configuration VIKING20X for the purpose of these studies (chapters 5 and 6). For the regions of interest, VIKING20X provides the highest resolution of all model configurations currently available in the ocean dynamics working group of GEOMAR.

VIKING20X is a forced model configuration based on the ocean/sea-ice model NEMO (version 3.6 Madec, 2016). VIKING20X consists of a global 0.25° tripolar Arakawa C-grid (ORCA025; Barnier et al., 2006) and a 1/20° nest covering the Atlantic from the southern tip of Africa to the southern Nordic Seas (Biastoch et al., 2021). Both grids have 46 z-levels with increasing grid-spacing from 6 m at the surface to 250 m at depth. The surface boundary conditions are derived from either the JRA55-do (Tsujino et al., 2018), or CORE (Large & Yeager, 2009; Griffies et al., 2009) forcing datasets using bulk formulae. VIKING20X and its predecessor VIKING20 have demonstrated their ability to simulate a realistic large-scale circulation, but also details of the (deep) western boundary current system and applicability to Lagrangian dispersal studies (Biastoch et al., 2021; Rieck et al., 2019; Handmann et al., 2018; Schubert et al., 2018; Breusing et al., 2016).

However, VIKING20X has three limitations that are disadvantageous for interhemispheric connectivity studies. First, it does not include the Atlantic sector of the Southern Ocean, including Drake Passage, and the Agulhas Current retroflection in the high resolution nest domain. Second, coupling with an atmosphere model is currently not possible. Already available nested configurations in GEOMAR's earth system model FOCI (Flexible Ocean Climate Infrastructure; Matthes et al., 2020), FOCI-VIKING10 and FOCI-INALT10X only cover the South or North Atlantic separately, which is even less advantageous for interhemispheric connectivity studies than the VIKING20X nest domain. The FOCI base configuration uses a 0.5° global grid and it is currently not possible to run the ORCA025 configuration, which would be needed for a 1/20° nest, within the FOCI environment. Third, the 0.25° global and 1/20° nest grids require large computational resources, this is for both, CPU resources to execute model experiments, and storage for the output.

Questions 1 and 2 of this thesis require a model configuration that has eddying resolution, can be coupled to an atmosphere model within FOCI and requires as little computational resources as possible to allow for long time periods covered by the experiments (these needs are discussed in the introduction and chapters 3 and 4 in more detail). As such a configuration did not exist, it was newly developed for the purpose of this thesis. The need for coupling within FOCI and considerations regarding the computational demands of the configuration, led to the choice of developing a 1/10° horizontal resolution nest, although in subpolar latitudes this is not sufficient to represent all mesoscale processes realistically (Martin & Biastoch, 2022; Hallberg, 2013). A 1/20° would most likely perform better at these high latitudes, but for the purpose of studying interhemispheric connectivity, the newly developed configuration is still a major advancement over previously available configurations. In the following section, the newly developed configuration, called FOCI-ATLAS10, is described in more detail.

2.2 FOCI-ATLAS10: A Model Configuration to Study Interhemispheric Connectivity

Author contribution: The author was fully responsible for the set-up of the (FOCI-)ATLAS10 configuration and performed all described experiments.

FOCI-ATLAS10 is a 1/10° all-Atlantic nested model configuration in the coupled climate model FOCI (figure 2.1 illustrates different components of the FOCI-ATLAS10 configuration). It is designed for the purpose of studying interhemispheric connectivity and covers the most important key regions of the AMOC (at least those associated with the surface and NADW circulation) at eddying resolution in a single model. In the southern hemisphere, this includes the Agulhas Current System and Drake Passage. In the northern hemisphere, this includes the overflow sills and parts of the Nordic Seas, as well as the Labrador and Irminger Seas. Also, the complex pathways of water in-between (see chapter 1 and Bower et al., 2019) are resolved with an increased horizontal resolution, allowing for explicitly simulated mesoscale eddies and narrow boundary currents. Simulating mesoscale eddies is especially relevant in the Southern Ocean, where the impact of wind stress forcing on the circulation was found to be highly sensitive to model resolution (Gent, 2016). Furthermore, eddying resolution leads to a more realistic large-scale circulation in general (Hirschi et al., 2020; Smith et al., 2000; Chassignet et al., 2020), although 1/10° resolution is not sufficient to resolve the full mesoscale spectrum at high latitudes, as mentioned before.

2.2.1 Configuration Details

The earth system model FOCI itself provides the infrastructure to run coupled simulations. As the name implies, different ocean (and atmosphere) components can be used within the model. The base FOCI configuration described in Matthes et al. (2020) uses the non-eddying ORCA05 ocean configuration (Molines et al., 2006) with a horizontal resolution of 0.5° on a tripolar Arakawa C-Grid. The atmospheric component is provided by the ECHAM6 (Müller et al., 2018; Stevens et al., 2013) model with a spectral resolution of T63 (approximately 1.8°, or 200 km) and 95 vertical

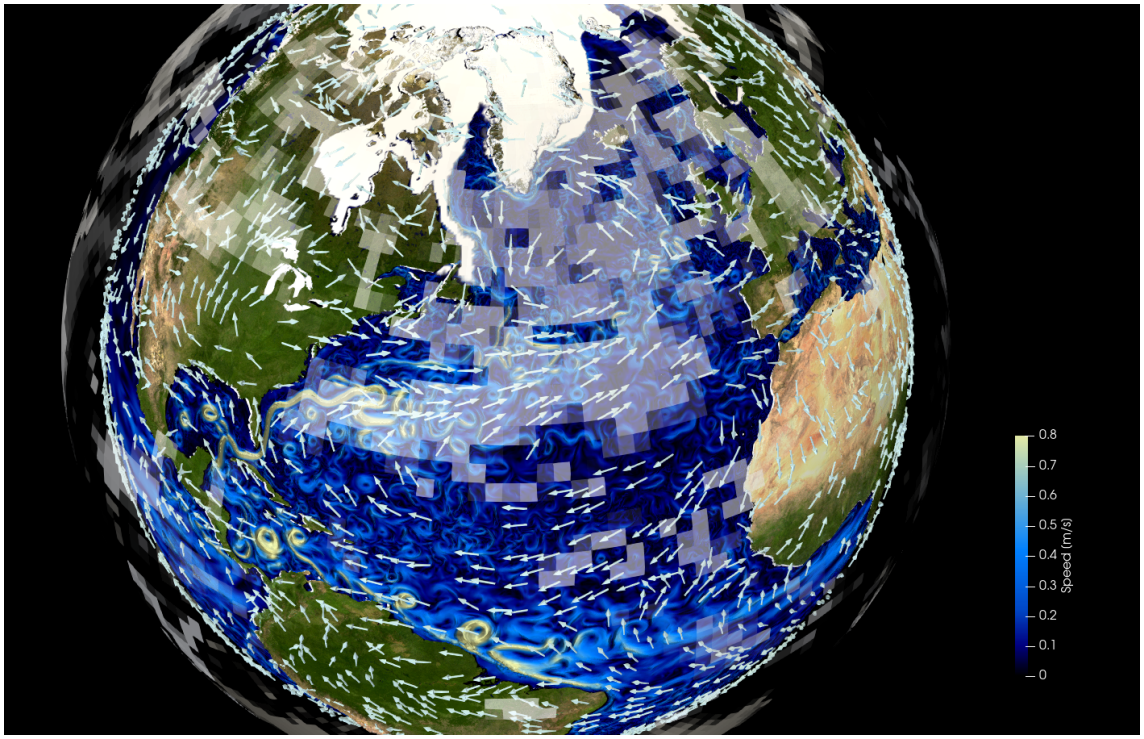

Figure 2.1: Figure illustrating the different components of the coupled configuration FOCI-ATLAS10. Shown is a surface speed snapshot (01-01-1995) on the nest and host grids (colour shading). Arrows show the surface wind field and black/white shading the total cloud cover from the atmosphere component at the same model time. Small values of total cloud cover are transparent. Ice covered areas are shown white on the ocean's surface.

hybrid sigma pressure levels with the top being at 0.01 hPa. ECHAM6 is coupled to the interactive land model JSBACH version 3 (Brovkin et al., 2009; Reick et al., 2013). JSBACH simulates land properties, such as albedo, soil moisture and vegetation distribution. Exchange between the atmosphere/land and ocean component of FOCI is accomplished by the OASIS3-MCT coupler (Valcke, 2013). The FOCI base configuration was shown to simulate an overall realistic mean state and variability of the atmosphere and ocean (Matthes et al., 2020). Especially important in the context of this thesis is a good representation of the mostly wind-driven gyre circulation and a stable AMOC with a realistic mean strength and structure, as well as a realistic magnitude of monthly to interannual variability. Nevertheless, the base configuration also shows pronounced biases, for example, a northward shift of the southern hemisphere westerly winds, a pronounced cold bias in the North Atlantic and a too strong Agulhas leakage transport. The North Atlantic bias can be significantly reduced by introducing a high resolution nest in the respective area (FOCI-VIKING10; Matthes et al., 2020; Martin & Biastoch, 2022). Also the Agulhas current system is more realistically represented with the explicit simulation of Agulhas rings in a South Atlantic nested configuration (FOCI-INALT10X). At the same time, the leakage transport is in better accordance with other high resolution (coupled) models, although underestimated compared to recent observational estimates (Ivanciu et al., 2022a).

While the land and ocean components are not changed, compared to the FOCI base configuration, a newly developed ocean configuration is introduced in FOCI-ATLAS10. This ocean configuration was specifically designed for usage within the coupled model FOCI. A forced simulation was only performed at a later stage and necessary adjustments were made that are described in a separate section. ATLAS10 (the ocean component of FOCI-ATLAS10) is a nested configuration based on

the NEMO ocean model version 3.6 (Madec, 2016), coupled to the Louvain-la-Neuve Sea Ice Model version 2 (LIM2; Fichefet & Maqueda, 1997; Vancoppenolle et al., 2009). The nest domain covers the region from 65°S to 65°N (the maximum northern extend is 72.5°N) and 99°W to 62°E (see red lines in figure 2.2c). As the global host grid, the aforementioned ORCA05 (0.5°) configuration is used. In the nest domain, the horizontal resolution is increased to 1/10° (∼5 km in subpolar latitudes and 11 km in the tropics), using the AGRIF two-way nesting procedure (Debreu et al., 2008). The resulting nest grid contains 1809 (latitude) × 1604 (longitude) grid points. Both grids have 46 z-levels with increasing grid spacing from 6 m at the surface to 250 m at depth.

Together with the grid refinement, the timestep must be reduced to ensure numerical stability. A time refinement factor of three is used in FOCI-ATLAS10. The timestep of the host model is 1800 s and accordingly the nest uses a 600 s timestep.

The host grid provides boundary conditions for the nest at every host timestep. These boundary conditions are used by the nest to calculate 3 time steps, before the host executes the next timestep. The nest feeds back information along the boundary to the host at every host timestep. After 3 time steps on the host grid, the nest solution is interpolated onto the ORCA05 grid and the host model solution is overwritten (baroclinic update).

The ocean component further provides the bottom boundary conditions for the atmosphere model via the coupler. This includes, for example, sea surface temperature, salinity and ocean currents. Using these fields and the near-surface atmospheric fields (e.g. 10 m wind, air temperature, humidity) all air-sea fluxes are calculated on the coarse atmospheric grid and then interpolated onto the ocean grid. Runoff is calculated in ECHAM6 from a horizontal discharge model (Hagemann & Gates, 2003; Matthes et al., 2020) and combined with the freshwater flux before it is provided to the ocean model. Thus, the ocean model only receives one freshwater flux that contains the net flux from runoff, evaporation and precipitation.

Surface Boundary conditions in the ocean component are calculated every 6th host timestep, which corresponds to 3 hours. New model experiments conducted in the working group after the set-up was chosen revealed that a higher coupling frequency of 1 hour reduces biases in the Southern Ocean (Sebastian Wahl, pers. communication). This was made the standard in FOCI and should be used for future experiments, also in FOCI-ATLAS10.

The described procedure to calculate the air-sea fluxes, together with the large resolution gap between the ocean (especially the nest) and atmosphere grids, prevents a direct impact of individual mesoscale features on the air-sea fluxes. Still, the more realistic representation of the ocean circulation at higher resolution, which is also represented on the host grid due to the applied 2-way nesting, feeds back on the atmospheric circulation and can change the coupled response to forced changes. As an example, a more realistic representation of the Agulhas system and associated sea surface temperature patterns can have important impacts on air-sea fluxes, as argued by Ivanciu et al. (2022b) based on Rouault et al. (2003) and Singleton and Reason (2006). Further, Martin and Biastoch (2022) find important differences in the coupled/un-coupled and nested/un-nested mean state and response to changes in Greenland runoff (using the base FOCI, FOCI-VIKING10 and forced VIKING10 configurations). This highlights the ability of the coupled, nested configuration to combine the effects of eddying resolution and coupling on longer timescales, even though the direct impact of individual mesoscale features on the atmosphere is strongly limited. Since the FOCI-ATLAS10 configuration was designed to study the basin wide (interhemispheric) circulation, these long term ocean-atmosphere feedbacks are more important than a feedback of individual mesoscale eddies on timescales of days to months.

In the following sections, the most important model parameter choices are discussed in more detail. All choices apply to the ocean component of FOCI-ATLAS10. The configuration does not require any changes in the other components of FOCI compared to the already established configurations described in Matthes et al. (2020).

Bathymetry

For the ORCA05 host grid, the bathymetry (see Molines et al., 2006) was obtained by interpolation of the ETOPO2 (2 arc-minute resolution) dataset (NOAA National Geophysical Data Center, 2006).

In contrast to most forced, nested model configurations, it was chosen to use the ORCA05 original bathymetry instead of the "updated" bathymetry generated by the nesting tools (Lemarié, 2006). In the updated bathymetry, every land grid cell on the host grid is replaced by a water grid cell, if there is at least one ocean grid cell on the nest grid in the respective area. Especially in regions with estuaries, or complicated coastlines, this leads to a large loss of land area in the host model (compare figure 2.2a,b). Although the host grid solution is regularly overwritten with the nest solution, an unrealistic large ocean area might be undesirable when the ocean model is coupled to an interactive atmosphere model. Especially in FOCI, where fluxes are calculated on the host grid only. For the grid configuration of FOCI-ATLAS10, the updated bathymetry has an additional surface ocean area of 4.5 million km^2 compared to the nest and 5.5 million km^2 compared to the original bathymetry of ORCA05. Accordingly, the updated bathymetry has a larger surface ocean area compared to the original bathymetry that is used in the base (un-nested) FOCI configuration. Furthermore, the difference between the nest and host bathymetries is smaller when the original bathymetry is used (1 million km^2 instead of 4.5 million km^2). Note that FOCI-INALT10X (see Matthes et al., 2020; Ivanciu et al., 2022a) uses the updated bathymetry, but the nest domain only covers the South Atlantic. In the South Atlantic the difference between updated and original bathymetry is much smaller compared to the North Atlantic (about 75% of the additional ocean surface area of the updated bathymetry is found north of the equator).

ECHAM6 has its own land-sea mask, which needs to be adjusted to the updated host bathymetry to avoid a mismatch between the atmosphere and ocean land-sea masks. However, updating this mask results in a calculation of fluxes based on the unrealistically large ocean surface area of the updated host bathymetry. In a forced simulation, changing surface fluxes due to a larger surface area are not a major problem, because they only affect the host grid within the nest area, which is regularly overwritten by the nest solution. But in the coupled model this can directly impact the atmospheric circulation and feed back on the circulation also on the nest grid.

Based on two experiments with the nest and the original and updated host bathymetries, it was found that the surface freshwater flux on the nest and host grids (only area of the host covered by the nest is considered) is only consistent when the original bathymetry is used. With the updated bathymetry, the annual mean freshwater flux on the host differs from the nest flux by 5%, while the difference is only 0.5% with the original bathymetry. This mismatch can be reduced to a similar value for the updated bathymetry, if the "new" ocean values are masked, showing that the mismatch is caused by the much larger ocean area itself. As it is the flux on the host grid that represents the exchange with the atmosphere, the fluxes used as bottom boundary conditions in ECHAM6 are changed by the larger ocean area. It was not tested whether this has an overall negative impact on the ocean and atmosphere circulation, but choosing the original bathymetry was concluded to lead to more realistic air-sea fluxes in the atmosphere component of FOCI.

The nest bathymetry is based on the ETOPO1 (1 arc-minute resolution) dataset (Amante & Eakins, 2009) interpolated onto the model grid (figure 2.2c). This higher resolution bathymetry was chosen, because ETOPO2 interpolated onto the nest grid with the standard smoothing applied by the nesting tools resulted in the Bosporus, and therefore the connection between the Mediterranean Sea and Black Sea, to be closed.

A special adjustment was made for the Caspian Sea, which is a closed sea. In a forced configuration, a closed sea would not have an (or a negligible) effect on the ocean outside the closed sea and can be deleted. This is different, however, in a coupled configuration. The Caspian Sea is a large body of water that can have an impact on the atmospheric circulation. As ATLAS10 is mainly designed to run within a coupled model, it was chosen to keep the Caspian Sea. Although only the host grid communicates with the atmosphere, the two-way nesting requires the Caspian Sea to be represented also on the nest grid. Here it was chosen to use the same coastline as on the coarse resolution ORCA05 grid. A higher resolved coastline in the nest would have no benefits,

but may only result in inconsistencies between the host and nest grid as described before. Note however, that this choice has basically no implications. As on the host grid, no changes in the net freshwater content of the Caspian Sea are allowed on the nest grid, but additional freshwater is distributed globally. It was found in previous, unpublished test experiments of the FOCI base configuration that the Caspian Sea would fully evaporate otherwise and this procedure was hard coded (there is no namelist parameter to switch it off, or to adjust the grid indices of the Caspian Sea) into FOCI. Therefore, it was necessary to modify the **closea.F90** routine and introduce a new configuration parameter (**jp_cfg=10**) in the NEMO namelist. In FOCI-ATLAS10 the updated **closea.F90** routine, together with **jp_cfg=10** in the nest namelist, should be used to prevent the Caspian Sea from evaporating on both, the host and nest, grids. As on the host grid, this implementation is based on the grid indices of the Caspian Sea in ATLAS10 and therefore should not be used with any other grid configuration.

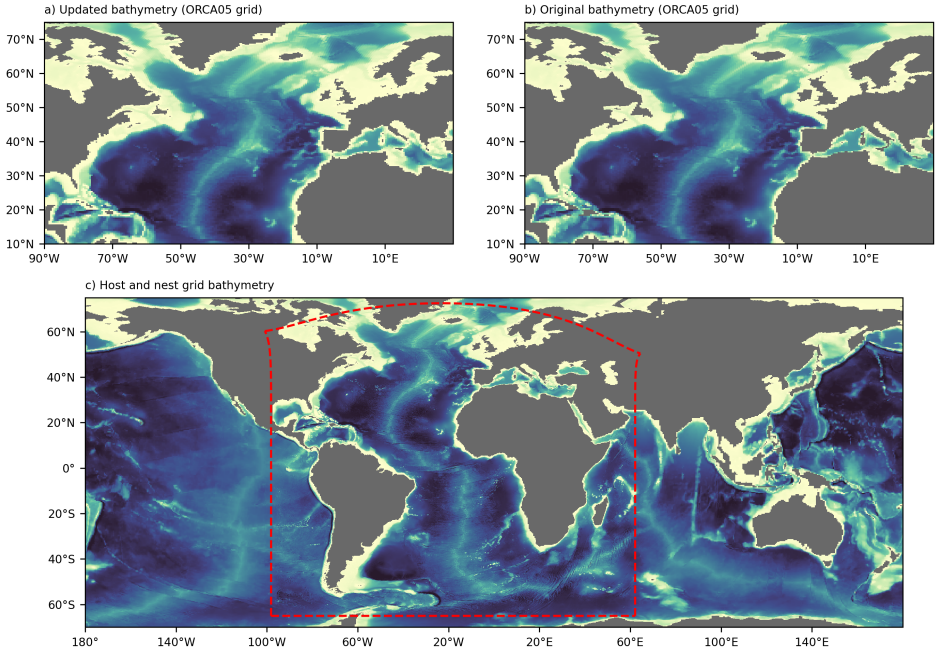

Figure 2.2: FOCI-ATLAS10 bathymetry. a) Updated bathymetry on the ORCA05 grid. b) Original ORCA05 bathymetry. c) Bathymetry on the global 0.5° host grid (ORCA05) and the 1/10° nest grid, which is bounded by the red lines.

Advection Scheme

Numerical ocean models, such as NEMO, are based on a set of 7, so called, primitive equations (Madec, 2016). These equations are derived from basic laws of physics, such as Newton's second law, mass and energy conservation. The 7 equations are the 3 Navier-Stokes equations, which describe the momentum balance in each spatial direction, the continuity equation, heat and salt conservation equations and an equation of state relating density to temperature, salinity and pressure. Different approximations and assumptions are made based on the scale of modelled processes (see Madec, 2016, for details).

For the purpose of explaining the advection scheme and its importance, only the salt conservation equation is considered here:

$$\frac{\partial S}{\partial t} = -\nabla \cdot (S\vec{u}) + D^S + F^S \tag{2.1}$$

S is salinity, $\vec{u}$ the velocity vector, D^S a parameterisation of processes on physical scales not represented by the equations (due to the applied approximations) and F^S a surface forcing term. t is time and ∇ the Nabla-operator.

A central model choice is the numerical scheme used to discretise the advective terms in the tracer conservation (first term on the right hand side of equation 2.1) and momentum equations. The different approaches discussed below are easiest to explain, if the salt conservation equation is considered in a simplified form, that is the one dimensional advection equation:

$$\frac{\partial S}{\partial t} + u\frac{\partial S}{\partial x} = 0 \tag{2.2}$$

This equation can be solved analytically and yields $S(x,t) = S(x - ut, 0)$, which states that the initial distribution of S is translated in x direction without any change in shape (see for example Farrow & Stevens, 1995, and figure 2.3). Using a finite differences (grid point) approach to solve this equation numerically, only values of S and u at specific locations (grid points) and times (time steps) are considered. Thereby, the partial derivatives are replaced by finite differences between the grid points / time steps. Knowing the values of u and S at a certain time step then allows to calculate the value of S at the next time step. Repeating this procedure provides the temporal evolution of salinity.

All numerical schemes are associated with numerical errors, which are either dispersive or dissipative. For most schemes, both errors occur. A variety of schemes with different complexity, accuracy and relative importance of dispersive and dissipative errors exist. Dependent on the type of grid, the velocity and tracer values are evaluated at the same (e.g. on an A-grid), or at different (e.g. on a C-grid) positions. The different numerical schemes implemented in NEMO to solve the tracer equations mainly differ in the procedure of interpolating tracer (for example salinity) values from T-points to the U/V-points on a C-grid (Madec, 2016). For the tracer advection, currently used schemes at GEOMAR are the Tracer Variance Dissipation (TVD; Zalesak, 1979) scheme (e.g. Schwarzkopf et al., 2019; Biastoch et al., 2021) and the upstream biased (UBS; Farrow & Stevens, 1995) scheme (Schubert et al., 2019).

Figure 2.3 illustrates the different characteristics of different schemes, when applied to the one-dimensional advection equation (equation 2.2; Farrow & Stevens, 1995). The initial distribution is a triangle and a square. The analytical solution exactly reproduces these shapes translated to right of the initial position for any time $t > t_0$. The different numerical schemes are not able to fully reproduce these shapes. A simple upwind scheme strongly smoothes the sharp gradients of the initial distribution (this is the diffusive error). In contrast, the centred scheme results in less numerical diffusion, but causes strong overshoots in negative direction and high variability on small spatial scales (this is the dispersive error). These overshoots must be balanced by an additional term in the tracer equation to damp these oscillations (D^S in equation 2.1). This can be achieved by using Laplacian ($D^S = \nu\nabla_h^2 S$), or bi-Laplacian ($D^S = -\nu_b\nabla_h^4 S$) operators. ν and ν_b are the Laplacian and bi-Laplacian viscosity and ∇_h the horizontal Nabla-Operator. These terms are called explicit diffusion terms. Both operators damp variability on small scales stronger than on large scales, but the scale dependency is stronger for the bi-Laplacian operator (Madec, 2016).

The QUICK scheme, which is almost identical to the UBS scheme (Madec, 2016), shows strongly reduced dispersive errors and slightly larger numerical dissipation, compared to the centred scheme (figure 2.3). This is the reason, why the scheme can be used in an ocean model with and without explicit diffusion terms (Farrow & Stevens, 1995; Schubert et al., 2019). The TVD scheme (the solution for this scheme is not shown in figure 2.3) on the other hand is less diffusive and explicit diffusion is needed to ensure numerical stability. Schubert et al. (2019) found that in a 1/20° model, the TVD scheme, with minimal explicit diffusion to ensure stability, is still more diffusive than the same model with UBS and no explicit diffusion. The advantages of lower diffusion are mostly a

reduced damping of small scale variability. Note that it is important to distinguish between realistic small scale features, such as fronts, narrow currents and eddies which should not be damped too strongly and the aforementioned numerical instabilities that are not desired.

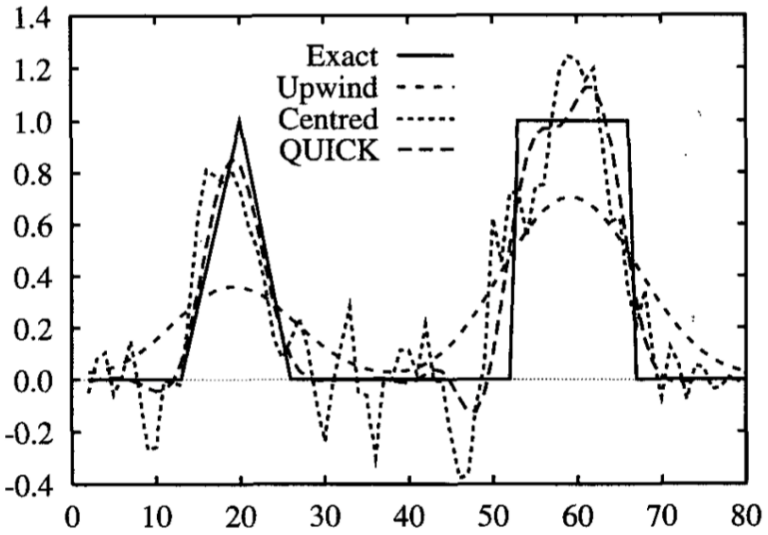

Figure 2.3: Numerical solutions of the one-dimensional advection equation for different numerical schemes, taken from Farrow and Stevens (1995). The true (analytical) solution is shown for comparison (solid line). The QUICK scheme (long dashes) is almost identical to the UBS scheme implemented in NEMO.

Only the tracer advection was discussed so far, but the basic ideas also hold for the advection of momentum in the momentum equations. The numerical discretisation of advective terms in the momentum equations, is more complicated, because the momentum equations can be represented in different forms on a curvelinear grid. This either in vector invariant, or flux form. For a detailed derivation and a discussion of the resulting implications for different schemes that can be used to solve the equation numerically, it is referred to Madec (2016). In vector invariant form, the momentum advection term is typically discretised using the energy and enstrophy conserving (EEN; Arakawa & Hsu, 1990) scheme. In flux form, the momentum advection term is split into a term representing the divergence of the momentum fluxes, which can be discretised using the UBS scheme and a second term that can be viewed as a modification of the Coriolis term and discretised using the EEN scheme (Madec, 2016).

Several test experiments of 5 years length with different advection schemes (for tracer and momentum advection), with and without explicit diffusion, and with different lateral boundary conditions showed that in key regions the circulation is slightly improved when the UBS scheme is used. The area of increased EKE in the Labrador Sea, associated with eddies emerging from the West Greenland Boundary Current System, is broader and more energetic using the UBS scheme. Also the Northwest Corner is associated with more eddy activity in the UBS experiment (figure 2.4a,b). In the southern hemisphere, variability in the Mozambique Channel that is important for the generation of Natal Pulses with an impact on the Agulhas Ring shedding (Schouten et al., 2002) is enhanced when using the UBS scheme (not shown). The ring path itself is clearly too narrow and regular in both experiments. This results from coarse atmospheric resolution, which prevents feedbacks between mesoscale current velocities and the wind field. These interactions were shown to be important for a realistic ring path (see Schwarzkopf et al., 2019). As a consequence, there was no possibility to avoid a too narrow ring path by adjusting any parameter in the ocean component of the coupled model. Nevertheless, the path is slightly broader in the experiment using the UBS

scheme (figure 2.4). It should be noted that using no explicit diffusion with the UBS scheme does not lead to grid-scale noise, even in highly variable regions as the Malvinas confluence zone.

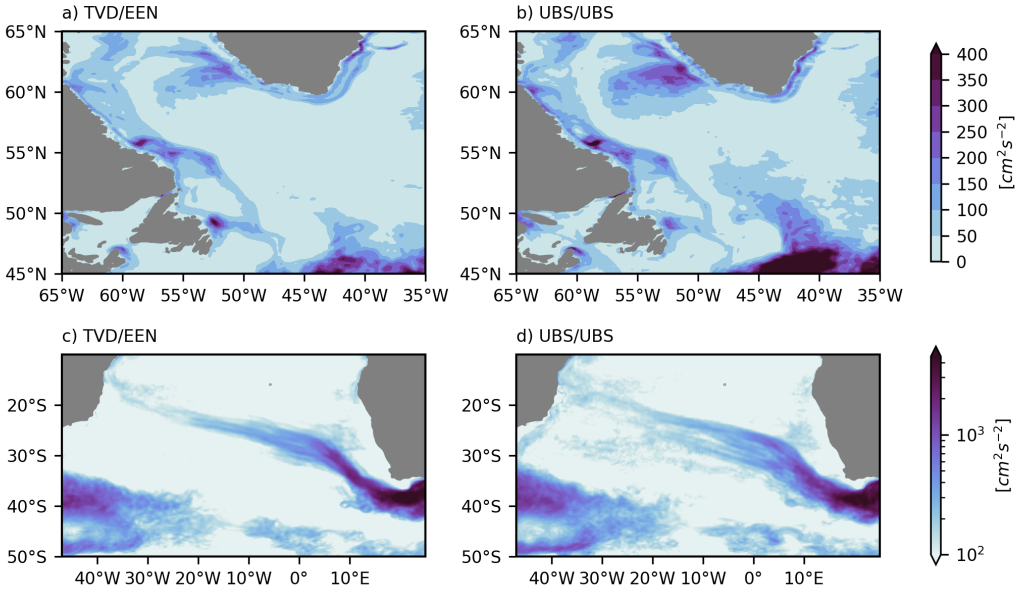

Figure 2.4: Mean surface eddy kinetic energy (1851-1855) from FOCI-ATLAS10 experiments with the TVD/EEN advection schemes and explicit diffusion and the UBS advection scheme (for tracer and momentum advection) without explicit diffusion. In both experiments, no-slip lateral boundary conditions were applied on the nest grid. Note the logarithmic colorbar for subplots c and d.

Finally, the choice was made to use the UBS scheme for discretisation of the advective terms in the momentum and tracer equations and no explicit diffusion. Further, the EEN scheme is used for the modified Coriolis term in the momentum equation in flux form. The test experiments were admittedly short and it is possible that the evolution of the AMOC and other transports could differ between the UBS and TVD/EEN experiments after a few decades (transports are very similar within the first 5 - years). Nevertheless, as described in more detail later, the chosen UBS set-up was continuously monitored and yields a stable AMOC after an initial spin-up phase (see section 2.2.2, chapter 3 and chapter 4).

Lateral Boundary Conditions

The ocean is bounded laterally by the coastline and bottom topography. There are three possible choices how to treat lateral boundaries in NEMO (Madec, 2016). First, it is possible to assume that the tangential velocity at the first land grid point is equal to the velocity of the last ocean grid point. These boundary conditions are called free-slip conditions. Second, it may be assumed that the velocity at the first land point is opposite to the tangential velocity at the last ocean grid point. Such boundary conditions are known as as no-slip boundary conditions. No-slip conditions cause linear interpolation to result in zero velocity at the coastline (in between the grid points) and are therefore more reasonable. At the same time, it was shown that no-slip boundary conditions do not perform well with an eddy permitting (0.25°) resolution (Penduff et al., 2007). The third option is a partial slip condition, which is not further discussed here.

For the resolution of 1/10° used in ATLAS10 (and higher resolution), the boundary conditions impose a difficult choice, because the northern hemisphere nests (FOCI-VIKING10 and VIKING20X)

use free-slip boundary conditions on the nest grid, except for the region around Cape Desolation, but the southern hemisphere configurations (e.g. FOCI-INALT10X) use no-slip conditions.

As expected from the different choices for VIKING and INALT, testing different combinations of lateral boundary conditions and advection schemes in several short (5 years long) experiments, revealed that the no-slip boundary conditions perform better in the southern hemisphere, but overall worse in the northern hemisphere. In the southern hemisphere, the Agulhas retroflection is slightly improved (tendency for a more realistic later retroflection of the Agulhas Current), along with a better mean current transport of the Malvinas Current, but underestimated Mozambique Channel transport (see also Schwarzkopf et al., 2019). The main disadvantage of applying no-slip boundary conditions is a too zonal North Atlantic Current, which causes a cold bias in this region. This cold bias, which is common in coupled models, is mostly eliminated by applying free-slip boundary conditions on the nest grid (compare Matthes et al., 2020; Martin & Biastoch, 2022). Note that by applying the UBS scheme, enhanced eddy activity in the Northwest Corner region is also present with no-slip boundary conditions (figure 2.4b). Other aspects of the North Atlantic circulation are better represented with no-slip conditions also in the Northern Hemisphere. For example, eddy kinetic energy is more confined to the boundary of the SPG when free-slip boundary conditions are used (especially together with the TVD/EEN advection schemes). Because the UBS advection scheme can reduce some of the disadvantages of applying the no-slip boundary conditions in the northern hemisphere, it was concluded that no-slip boundary conditions, together with the UBS advection scheme, yields the best compromise between southern and northern hemisphere performance.

While for all experiments analysed in this thesis no-slip conditions were used, both lateral boundary conditions were successfully tested and future experiments could choose free-slip conditions, depending on the region of focus.

Sponge Layer Parameter

In order to ensure a smooth transition between the partly mesoscale resolving nest and the non-eddying host at the nest boundaries, a 6 nest grid point wide sponge layer is introduced along the nest boundary. Within this sponge layer, the viscosity is increased to damp variability on scales that are not resolved by the coarse grid (Debreu et al., 2012). A too high value can lead to unrealistic conditions, as anomalies can not leave the domain and are trapped. Too low values can lead to reflections and the excitement of waves at the nest boundary. At the eastern domain boundary waves with small amplitudes were observed, triggered by the strong and highly variable Agulhas Return Current intersecting the nest boundary. The chosen sponge layer parameter of 3000 m^2 s^{-1} for FOCI-ATLAS10 is slightly higher than in FOCI-INALT10X (with a similar eastern nest boundary and same resolution) and was found to yield the best results in this area, but anomalies propagating northward along the nest boundary are still visible to a minor extend. Higher values did not lead to better results and ultimately caused the model to crash. No reflections or waves at the other domain boundaries are present with the chosen value.

2.2.2 Spin-up of the Nested Configuration

The different questions on reproducing past variability (question 1, chapter 3) and the need to isolate a specific response to forced changes in the southern hemisphere (question 2, chapter 4), required two different model spin-ups.

The former requires to incorporate historic changes in greenhouse gas concentrations and land use to conduct model experiments that reproduce the past evolution of the ocean as good as possible. For the latter, it is advantageous to exclude as many sources of long term trends as possible. Therefore, the second spin-up was run under pre-industrial conditions.

Although for a fully coupled experiment with constant pre-industrial atmospheric boundary conditions the origin of the time axis is arbitrary, it is referred to the same time axis for both experiments. Both spin-ups are initialised in 1850. Following the spin-up strategy of FOCI-

VIKING10 (Matthes et al., 2020), the model is initialised using the restart files of the 1500 year long pre-industrial control simulation of the base FOCI (0.5° without nest) configuration (FOCI-piCtl; FOCI1.3-SW038; Matthes et al., 2020). For the nest, the global restart files were interpolated onto the nest grid before initialisation. It is noted here that a spin-up from rest and climatological temperatures and salinities (World Ocean Atlas 2013; Locarnini et al., 2013; Zweng et al., 2013) was tested, but resulted in model crashes in the Mediterranean Sea, even with a strongly reduced time step. The nested model configuration was then spun-up for at least 100 years under historic (FOCI-ATLAS10-HIST), or pre-industrial (FOCI-ATLAS10-PiCTL) atmospheric boundary conditions to allow for an adjustment of the deep circulation.

These two model experiments are the basis for the different experiments used to study partial coupling and wind-driven AMOC variability in chapter 3 and sensitivity experiments to examine the impact of wind stress changes over the Southern Ocean in chapter 4. The set-up of these experiments is described in detail in the respective chapters.

As evident from figure 2.5a,b, the model shows a relatively strong secondary spin-up after initialisation. Eddies within the nest already develop within the first months after initialisation, but the AMOC is also dependent on an adjustment of the deep circulation and needs much longer to stabilise. After approximately 50-years however, the AMOC remains stable in both spin-up experiments. A similar temporal evolution can be seen for Florida Strait transport (figure 2.5d). The Drake Passage transport (figure 2.5c) shows an increase until 1900 in both spin-up experiments. Afterwards, the transport declines approximately to the initial value. The pre-industrial control run shows that pronounced multi-decadal variability is simulated for the entire length of the experiment, which suggests that these variations are not related to a spin-up, but to internal variability of the coupled model. The spin-up time of 100 years (chapter 4) and 108 years (chapter 3) is therefore regarded long enough to ensure that the following experiments are initialised after the spin-up phase. Note that both spin-ups were continued without any discontinuity to 2013 (FOCI-ATLAS10-HIST) and 2129 (FOCI-ATLAS10-PiCTL). Furthermore, it is notable that differences between the pre-industrial control and historic experiments are relatively small. In the North Atlantic (26.5°N), the AMOC and Florida Strait transports are about 1 Sv weaker after 1920 and show a drop after the 1990s in FOCI-ATLAS10-HIST. In the South Atlantic the AMOC in FOCI-ATLAS10-HIST and FOCI-ATLAS10-PiCTL show an even more similar temporal evolution and mean strength. In particular the longer pre-industrial control simulation highlights the ability of the FOCI-ATLAS10 configuration to simulate a stable AMOC over more than 200 years.

Overall, the performance of FOCI-ATLAS10 in the spin-up experiments (and their extension) matches the expectations based on the North and South Atlantic nested configurations in FOCI. Both spin-up experiments show a strongly reduced North Atlantic cold bias compared to the base FOCI configuration (Matthes et al., 2020). The cold bias is still slightly stronger than in FOCI-VIKING10 (Matthes et al., 2020; Martin & Biastoch, 2022), because of the aforementioned application of no-slip lateral boundary conditions. In the South Atlantic an Agulhas leakage transport of around 11 Sv (see chapter 4 for more details) in FOCI-ATLAS10 is in the range of estimates obtain from forced and coupled (FOCI-)INALT10X experiments (Ivanciu et al., 2022a; Schwarzkopf et al., 2019). Other key-transports, for example the Florida Strait transport (about 29 Sv after 1900) and Denmark Strait Overflow transport (about 3 Sv after 1900) are also in a realistic range compared to observations and results obtained from the (forced) VIKING20X configuration (Meinen et al., 2010; Jochumsen et al., 2017; Biastoch et al., 2021). The Southern Ocean shows a warm bias and a too weak Drake Passage transport that can also be seen in the FOCI base and FOCI-INALT10X configurations (Matthes et al., 2020; Ivanciu et al., 2022a). A more detailed assessment of the large-scale Atlantic circulation in FOCI-ATLAS10 compared to observations and other models is part of chapter 3.

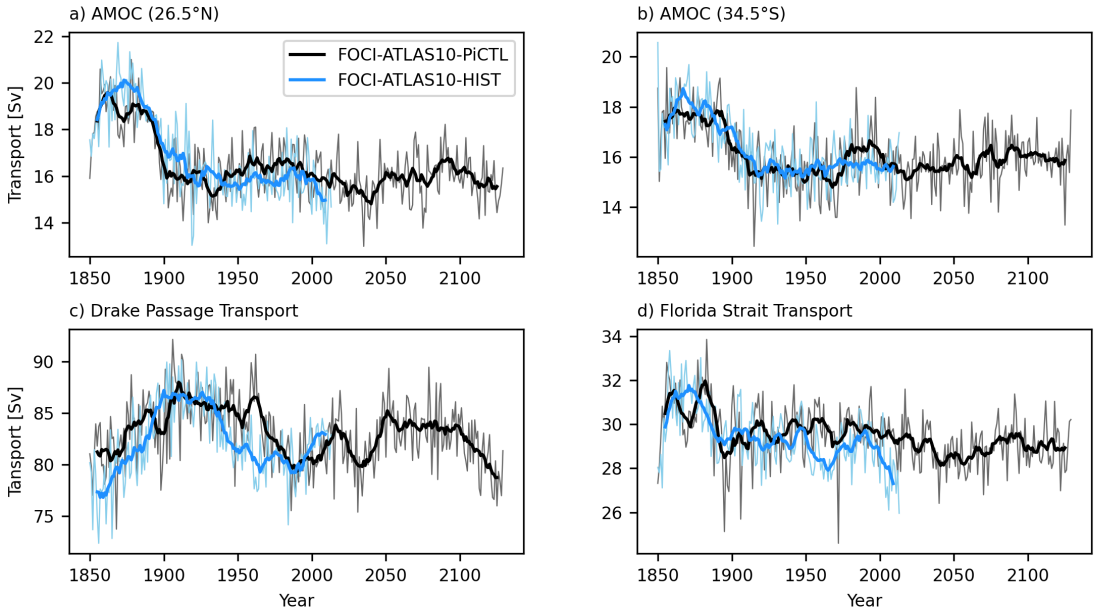

Figure 2.5: Fully coupled spin-ups of the FOCI-ATLAS10 configuration. Shown are the timeseries of selected key transports: the AMOC transports at 26.5°N (a) and 34.5°S (b), Drake Passage transport (c) and the Florida Strait transport (d). Thin lines show annual mean values and thick lines a 10-year moving average. The first 100 / 108 years are regarded as the spin-up phase, but the experiments were extended without any discontinuity.

2.2.3 ATLAS10 - Ocean-Only

For various questions it can be advantageous to run an ocean model without coupling to an interactive atmosphere model. As outlined in the introduction, a major advantage is the stronger observational constraint by deriving surface fluxes from observed (reanalysed) atmospheric fields, which results in a better timing of variability. To provide a reference experiment to judge whether partial coupling can improve the timing of (AMOC) variability compared to a fully coupled model (chapter 3), a forced experiment with the ocean component of FOCI-ATLAS10 was needed. The implementation of partial coupling was initially regarded as a necessary step to run sensitivity experiments in the beginning of the project, but it became clear that such experiments would only be possible with a more detailed understanding of circulation variability in partially coupled models itself. Accordingly, the model configuration was first developed for the use in FOCI and later adjusted to conduct a forced experiment. This can explain why certain choices were made, that had to be revisited for the forced experiment. The forced configuration is just called ATLAS10 in the following.

The surface boundary conditions of the model were calculated from the JRA55-do (version 1.5) forcing dataset (Tsujino et al., 2018). This dataset contains reanalysed atmospheric fields, such as temperature, humidity and wind, that can be used to derive the air-sea fluxes via bulk formulae.

While most of the settings remained unchanged, the very different ocean surface boundary conditions in the forced and coupled model set-ups made changes to the advection scheme and initialisation strategy necessary. Furthermore, the runoff that is provided as part of the freshwater flux in FOCI, needs to be calculated with a special procedure for the forced simulations. These three major differences between the forced and coupled versions of ATLAS10 are described in the following in more detail.

Runoff

While most input fields provided by the forcing dataset, such as air temperature, humidity, wind and others can be interpolated onto the nest and host grids during runtime to calculate air-sea fluxes, the runoff is discontinuous and must be treated differently. To ensure no loss of runoff and a correct placement of the runoff along the coastline, the remapping toolbox provided by Martin (2021) and described in Biastoch et al. (2021) was used. The procedure implemented in this toolbox redistributes runoff from the source grid to the coastline of the model grid (first ocean grid cell) within a specified radius. A distance-weighted scheme is applied, such that the largest fraction of the runoff is remapped to the nearest ocean cell along the coastline. Runoff that is further away from the coastline grid cell than the search radius is distributed across all runoff grid cells on the model grid. For ATLAS10, a search radius of 160 km was used. The river plume scheme that can be used to further redistribute large runoff values, as from the Amazon river, over more than a few grid cells was not applied here. Instead, the river mouth treatment within NEMO was activated. This river mouth treatment causes enhanced vertical mixing in grid cells with runoff and thereby acts to distribute the runoff that is provided as a surface flux.

To obtain the runoff on the nest grid, two options are available. Runoff could be remapped from the JRA55 source grid directly onto the nest grid. However, for the runoff to be more consistent on the host and nest grids and to avoid too large runoff values in individual grid cells, it was chosen to interpolate runoff from the host onto the nest grid, using the nesting tools. Runoff that is placed on land by the interpolation procedure is then redistributed to the nearest ocean grid cells.

Sensitivity to Advection Schemes and Lateral Boundary Conditions

While the AMOC in the fully coupled configuration is stable after an initial spin-up phase (figure 2.5), this is not true for the ocean-only simulation that uses the UBS advection scheme for the numerical discretisation of momentum and tracer advection. A sensitivity experiment was conducted with the TVD scheme for tracer advection and the EEN scheme for momentum advection. To match the current standard (and because the model crashes otherwise), explicit diffusion was added by laplacian (tracer equations) and bi-laplacian (momentum equations) operators, as in the VIKING20X configuration, but with the coefficients adjusted to the lower grid resolution. At the same time, different combinations of free and no-slip boundary conditions were tested. The direct comparison between ATLAS10-UBS and ATLAS10-TVD/EEN (both with no-slip) shows that the AMOC is very similar for the first 20-years. Afterwards, the AMOC with TVD/EEN slightly increases towards a weak maximum in the 1990s (this is also visible in some VIKING20X experiments shown in Biastoch et al. (2021)). With UBS, however, the AMOC shows a continued declining trend until the end of the experiment. The more stable AMOC in the fully coupled configuration with the UBS scheme suggests that the drift is related to the combination of the advection scheme and the applied surface boundary conditions. Another possible reason could be different initialisation strategies and mean states of the coupled and forced configuration. The former may be solved by re-tuning the model. Note that the restoring strength was adopted from VIKING20X that uses the TVD/EEN schemes. A stronger restoring may help to obtain a stable AMOC with the UBS scheme. Another possibility would be to add explicit diffusion, but the viscosity values should probably be smaller than used with the TVD/EEN schemes. As for the purpose of chapter 3 the most important aspect is a good representation of the AMOC, it was chosen to use the TVD/EEN schemes, instead of re-tuning the model with the UBS scheme. A more detailed analysis of the reason for these differences was not conducted, but would be an interesting future project to better understand causes of long term AMOC drifts in forced models. This analysis could go along with a more detailed analysis of the coupled sensitivity experiments described above, as it would be interesting to investigate why the coupled model behaves differently and does not show a strong drift with the UBS scheme.

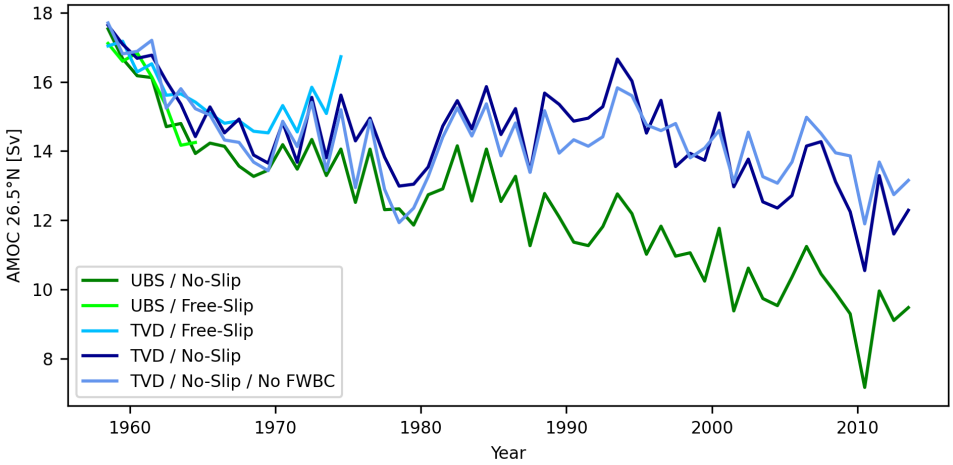

Figure 2.6: AMOC transport at 26.5°N in forced ATLAS10 experiments with different advection schemes and lateral boundary conditions. TVD always refers to the combination TVD for tracer and EEN for momentum advection. UBS is used for both tracer and momentum advection. In all experiments (except the one labelled 'No FWBC') a freshwater budget correction is applied.

A comparison of the different lateral boundary conditions shows hints that the AMOC in UBS/free-slip follows the UBS/no-slip experiment, but the experiment is too short for definite results. The same comparison for the TVD/EEN experiments shows that the AMOC tends to be slightly stronger with the free-slip boundary conditions, although the difference appears to be small.

Lastly, it was discovered that inaccuracies in the applied freshwater budget correction (FWBC), caused a strong increase in global Sea Surface Height (SSH) in 1993. The freshwater budget correction should ensure that the global surface freshwater fluxes sum-up to zero and there is no freshwater loss/gain globally during runtime. However, for nested configurations the fluxes are not available at exactly the same time on the nest and host grids, such that the correction is imperfect. This strong increase in global SSH was reproducible by restarting the experiment in the mid-80s and therefore no random error. The only possible solution to avoid this SSH increase was to switch it off. The AMOC evolution is very similar in the experiment without FWBC (TVD/No-Slip/No FWBC) and the corresponding experiment with FWBC until the mid-90s. Afterwards, the experiment without FWBC is even more stable. However, this does not necessarily mean that the FWBC destabilises the AMOC. The inaccuracies in the FWBC led to a strong input of freshwater into the ocean, which may have an impact on AMOC stability. Although the freshwater input was not locally confined, but distributed globally, the correction flux is linked to the restoring flux (see next section) and therefore had an effect on the dynamically important horizontal density gradients.

Based on these results it is recommended to use ATLAS10 (forced) either with the described TVD/EEN advection schemes, or to re-tune the model with the UBS advection scheme. Further, the freshwater budget correction, if applied, should be cautiously monitored in all nested configurations, including ATLAS10. There is no clear tendency for a better representation of the AMOC with no-slip or free-slip lateral boundary conditions and both may be used.

Initialisation and Other Adjustments

In general, there are different strategies to initialise forced simulations. The model can be started from rest and a climatological temperature and salinity field, which is similar to the strategy described by the OMIP (Ocean Model Intercomparison Project; Tsujino et al., 2020) protocol. Alternatively, the model can be restarted from a previous spin-up phase. Note however, that in contrast to the fully coupled spin-up described above, this is always connected to a discontinuity from the end of the spin-up to the beginning of the actual experiment. The forcing datasets are currently not long enough to allow for a 30-50 year (or even longer) spin-up and an experiment of similar length. After both strategies were tested, it was chosen that the OMIP style initialisation from rest and the World Ocean Atlas 2013 climatology (Locarnini et al., 2013; Zweng et al., 2013) yields a more stable AMOC than a restart from a previous spin-up phase. Another possible initialisation was tested. In this case, a restart from the fully coupled spin-up (FOCI-ATLAS10-HIST) was used. However, biases of the coupled model, especially a warm bias in the Southern Ocean, together with the prescribed atmospheric state resulted in severe deep mixing in the Southern Ocean. This caused the AABW cell to extend almost to the surface in the South Atlantic with an unrealistic transport of more than 20 Sv.

To compensate for missing ocean-atmosphere feedbacks in the forced experiment, a sea surface salinity (SSS) restoring with a piston velocity of 50 m/yr was applied. The restoring strength scales with ice-coverage and SSS is not restored in grid cells with runoff and additionally within a distance of 80 km around Greenland. This prevents an immediate damping of freshwater from rivers and melting ice-sheets (following Biastoch et al., 2021). Temperature and salinity of the Mediterranean Sea outflow below 700 m are restored using a three dimensional mask with a maximum Newtonian damping coefficient of 6.34×10^{-5}/s. These restoring settings are adapted from successful simulations of the VIKING20X model configuration (Biastoch et al., 2021). As in the forced set-up an unrealistic large ocean area on the host grid is no disadvantage, the updated bathymetry is used. Furthermore, the baroclinic update frequency is reduced to one host time step to achieve a simultaneous baroclinic update and calculation of surface boundary conditions. This was strictly necessary for all experiments using the freshwater budget correction (to ensure highest possible accuracy of the freshwater budget closure) and not strictly necessary for the last experiment without, but kept for comparability with previous experiments.

2.3 Implementation of Partial Coupling

Author contribution: The necessary implementation of new model code in FOCI was led by Jan Harlaß. The author contributed to the code development by testing and bug fixing.

In this section, a modification of the surface boundary condition calculation within the coupled model FOCI is described. In the aforementioned coupled configuration of FOCI-ATLAS10, air-sea fluxes are derived from the atmosphere component of FOCI. In the forced configuration (ATLAS10), they are calculated from reanalysed atmospheric states that are provided by the JRA55-do forcing dataset (Tsujino et al., 2018). As described in chapter 1, it may be possible to combine the advantages of both modelling strategies by applying a partial coupling.

Partial coupling refers to a procedure, in which the ocean component of a coupled model is forced with reanalysed wind stress, while heat and freshwater fluxes are interactively exchanged with an atmosphere model (Ding et al., 2013; Thoma et al., 2015). Although different methodologies are possible (e.g. Thoma et al., 2015), it was decided to use an anomaly forcing for the purpose of this thesis. The wind stress provided to the ocean model is therefore calculated completely offline (i.e. before running the partially coupled experiment) using the following equation:

$$\vec{\tau}_{an}(t) = \vec{\tau}_{re}(t) - \vec{\tau}_{re}^{clim}(t_M) + \vec{\tau}_{m}^{clim}(t_M) \tag{2.3}$$

$\vec{\tau}_{an}(t)$ is the anomaly forcing, $\vec{\tau}_{re}(t)$ is the wind stress derived from reanalysed 10 m wind at time step t. $\vec{\tau}_{re}^{clim}$ and $\vec{\tau}_{m}^{clim}$ are the monthly climatologies of the reanalysis and the coupled model in the month corresponding to time step t (t_M). Different methods exist to convert 10 m wind to wind stress and possible choices are discussed in more detail in chapter 3. This chapter focuses on the technical implementation of partial coupling in FOCI and only briefly discusses the important choices that affect the implementation. Because the wind stress is derived completely offline, the technical implementation is less complicated. However, this is not the reason for this choice. The main reason is a clean separation between climatology (purely from the coupled model) and anomaly (purely from reanalysis). This would not be given, if equation 2.3 is applied to the 10 m wind and wind stress then calculated during runtime (online). This is because the bulk formulae for wind stress contains the 10 m wind velocity squared (e.g. Large & Yeager, 2009):

$$\vec{\tau} = \rho_a C_d |\vec{u_{10}}| \vec{u_{10}} \tag{2.4}$$

with ρ_a the atmospheric density, C_d the drag coefficient and $\vec{u_{10}}$ the 10m wind velocity. Thus replacing $\vec{u}_{10}$ by $\vec{u}_{10,an} = \vec{u}_{10,re} - \vec{u}_{10,re}^{clim} + \vec{u}_{10,m}^{clim}$ (sub- and superscripts as in equation 2.3) would always lead to mixed terms. The anomaly, as well as the climatology, would depend on both, the modelled and reanalysed, winds.

For the technical implementation it follows that changes are only needed in the ocean component of the coupled model, because the fully offline calculated wind stress can be loaded from disk and directly applied to the ocean component.

A new section (**namsbc_pcpl**) was added to the nest and host namelists to provide the necessary input and to define all options provided by the implemented partial coupling procedure:

```
!-----------------------------------------------------------------------
&namsbc_pcpl   !   namsbc_pcpl partial coupling bulk formulae
!-----------------------------------------------------------------------
!     !  file name ! frequency (hours) ! variable ! time interp. !  clim  ! 'yearly'/ ! weights
! rotation ! land/sea mask !
!     !           !  (if <0  months)  !   name   !   (logical)  !  (T/F) ! 'monthly' ! filename ! pairing  ! filename
   sn_wndi  = 'FILE' ,          3          ,  'taux'  ,    .false.   ,.false. , 'yearly' , 'WHT_FILE', 'Uwnd'  ,   ''
   sn_wndj  = 'FILE' ,          3          ,  'tauy'  ,    .false.   ,.false. , 'yearly' , 'WHT_FILE', 'Vwnd'  ,   ''
   sn_mask  = 'MASK_FILE' ,     0          ,'soanomsk',    .false.   ,.true.  ,  ''      ,          ,  ''     ,   ''
! ! mask on orca grid
   cn_dir   =  'PATH_TO_STORED_FILES'   !  root directory for the location of the pcpl files
!
    ln_cfac  = .false.      !  multiplicative constant factor for wind stress fields, only with ln_mask=(F) & ln_lcomb=(F)
    rn_cfac  = 0.3          !  greater than 0, real
!
    ln_mask  = .false.      !  use mask field, all positive values allowed, ln_cfac = (F)
!
    ln_lcomb = .false.      !  linear combination of mask*pcpl + (1-mask)*model wind stress
!                           !  ln_mask = (T)   sn_mask: only 0 ... 1
!                           !  ln_cfac = (F)
```

sn_wndi and **sn_wndj** are the files (or a single file) containing the wind stress. In principle this can be wind stress from any source, including an anomaly forcing as described above. **sn_mask** is a separate file containing a two, or three dimensional (time depended) mask that can be read to apply partial coupling only regionally. Different switches were implemented to adjust the partial coupling procedure.

If all **ln_cfac**, **ln_mask** and **ln_lcomb** are *False*, the wind stress from the atmosphere model is completely overwritten in NEMO and replaced by the wind stress read from disk. This can be regarded as the standard partial coupling procedure and is used for the experiments presented in chapter 3.

It is possible to increase/decrease the wind stress read from disk by a constant factor globally, by setting **ln_cfac = .true.**. In this case, a factor defined by **rn_cfac** is multiplied with both wind stress components. The third allowed option is to apply a linear combination of the atmosphere models wind stress and the wind stress read from disk by setting **ln_mask = .true.** and **ln_lcomb = .true.**. The mask must always be provided, but can be filled with the same value at each grid point to apply a linear combination with the same weights everywhere. A mask value of zero corresponds to a wind stress purely from the atmosphere model, while a mask value of 1 corresponds to a wind stress fully read from disk. This can also be used to only apply partial coupling in certain regions to study the impact of assimilating wind stress variability in this particular region. Other combinations than the ones mentioned here, are not implemented in the standard PCPL routine and will result in an error.

To run in partial coupling mode, the **ln_pcpl** option in the main **namsbc** namelist of NEMO must be activated. This will cause NEMO to call the newly added **sbcpcpl.F90** module from the main module to calculate surface boundary conditions. As for a fully coupled configuration **ln_cpl** (in the host namelist) and **ln_echam** (in the nest namelist) must be activated. This ensures that not only the wind stress files are read, but the model still exchanges surfaces fields with the atmospheric component of FOCI to calculate heat and freshwater fluxes. **sbcpcpl.F90** contains two subroutines (one for the ocean and one for sea-ice) that calculate the model wind stress from the wind stress provided by the atmosphere component and/or the wind stress read from disk (depending on the options chosen in the **namsbc_pcpl** namelist, as described above).

After the global wind stress variables are defined, the model continues the usual time stepping algorithm.

2.4 Implementation of an Online Wind Stress Modification

Author contribution: Code modifications in FOCI were entirely implemented by the author of this thesis, but build on the partial coupling code implemented together with Jan Harlaß.

In the previous section, it was described how wind stress read from disk can be used to overwrite/modify the atmosphere models' wind stress in the ocean component of FOCI. A similar procedure to manipulate the wind stress from the atmosphere component when provided to the ocean component is applied in chapter 4. Building on the code implemented for partial coupling, the option to read a two dimensional mask and to provide a constant parameter c (**rn_cfac**) to enhance/reduce the wind stress globally were used to modify the coupled models' own wind stress after it is provided to the ocean component. A new option was defined, with **ln_cfac** and **ln_mask** activated, while **ln_lcomb** is deactivated in the **namsbc_pcpl** namelist. With this combination of namelist parameters, the coupled models' own wind stress is multiplied with a constant parameter c and a two, or three dimensional (time dependent) mask, to only modify the wind stress in specific regions. No additional data (e.g. from reanalysis) needs be read. The surface (or 10 m) wind in the atmosphere component of FOCI is not affected by this procedure.

The wind stress provided to the ocean model $\vec{\tau}$ is then calculated as follows:

$$\tau_x(i,j) = \tau_{x,E}(i,j)(1 + w(i,j)c) \tag{2.5}$$

$$\tau_y(i,j) = \tau_{y,E}(i,j)(1 + w(i,j)c) \tag{2.6}$$

τ_E is the wind stress provided by the atmospheric component of FOCI at grid point (i,j). The subscripts x and y denote the zonal and meridional component. w is a two dimensional mask on the ocean grid (for nested configurations the mask must be available on the host and nest grids). Although the mask can technically contain any values, values between 0 and 1 are used for the purpose of this thesis. A mask value of 1 corresponds to the full increase in wind stress defined by c. Here $c = 0.3$ which corresponds to a 30% increase of the atmosphere models' wind stress. A mask value of 0 corresponds to the atmosphere models' wind stress without any modification. The routine was modified analogously for the wind stress over ice that is provided separately to NEMO by ECHAM6. All code modifications apply to the **sbcpcpl.F90** module.

2.5 Lagrangian Connectivity - Numerical Versus Analytical Schemes

One of the main tools to study physical and biophysical connectivity is the calculation of Lagrangian trajectories. These trajectories can be interpreted as pathways of water volumes, or individual particles (van Sebille et al., 2018). Lagrangian trajectories can only represent connectivity via advective processes and potentially diffusion. As mentioned in chapter 1, other physical process, such as waves and atmospheric bridges, can cause connectivity as well. Calculating Lagrangian trajectories from the Eulerian velocity field of the model requires to solve the following equation:

$$\frac{\partial \vec{r}(a,t)}{\partial t} = \vec{u}(\vec{r}(a,t),t) \tag{2.7}$$

$\vec{r}(a,t)$ is the position of volume element (particle) a at time t and $\vec{u}(\vec{r}(a,t),t)$ is the Eulerian velocity at this position. To represent the effects of diffusion and unresolved physics, the equation must be modified, as described in more detail by van Sebille et al. (2018). However, for the purpose of this thesis no diffusion terms were added to the equation.

Different approaches to solve equation 2.7 exist. The equation can be solved numerically with an explicit or implicit (not further discussed here) time stepping scheme, or analytically. The methods themselves, together with their implementation in different software packages, come with several advantages and disadvantages. Therefore, both methods are used in this thesis for different questions.

While the ARIANE package developed at the Laboratoire de Physique des Océans (LPO) in Brest (Blanke & Raynaud, 1997) provides an implementation of an analytical scheme, the Parcels (v2.2.1) algorithm developed at Utrecht University provides a numerical solution (Delandmeter & van Sebille, 2019).

The Parcels algorithm was shown to reproduce the ARIANE results for the volume transport between the Agulhas Current at 32°S and the Good Hope section, which represents Agulhas leakage (Schmidt et al., 2021). Nevertheless, the conservation of volume transport along the trajectory, this is the volume multiplied by the velocity, is essentially based on the analytical scheme and not ensured for a numerical scheme. Note that even with the analytical scheme, the transport is only conserved for a steady flow. In time varying flows, this is achieved by assuming piecewise steady flow between two consecutive time steps of the model's velocity field (van Sebille et al., 2018). While the volume transport is conserved, this is not true for water mass properties. Diffusive mixing can cause water mass properties to change along the trajectory. As a consequence, tracer and volume transport pathways are not necessarily the same (van Sebille et al., 2018). Furthermore, errors associated with numerical schemes lead to a mismatch between forward and backward in time trajectories. The analytical scheme is at least theoretically able to exactly reproduce a forward

trajectory in backward direction. In reality there can be a slight mismatch, probably introduced by round off errors, but still the agreement is much better compared to numerical schemes.

Because the transport into and out of any grid cell must be zero based on the analytical scheme, the vertically integrated transport is free of divergence. This is another advantage, because it allows to define the Lagrangian Streamfunction (Blanke et al., 1999). The Lagrangian Streamfunction ψ_L provides a useful 2 dimensional representation of the volume transport pathways from the 3 dimensional trajectory data and is obtained by vertically integrating the transport across all grid cell boundaries:

$$\begin{aligned} \partial_i \psi_L &= \sum_k M_y \\ \partial_j \psi_L &= -\sum_k M_x \end{aligned} \tag{2.8}$$

i, j, k are the indices of a grid cell. M_x, M_y is the sum of the transports associated with all trajectories intersecting the grid cell boundaries in zonal (x), or meridional (y) direction. $\partial_{i,j}$ denotes differences between the grid cell boundaries in the respective directions.

However, numerical schemes and their implementation in Parcels have their own advantages. Parcels provides much more flexibility in defining release positions and allows to add active motion to the particles. As mentioned before, numerical schemes do not generally perform worse than analytical schemes. Especially for studies that are meant to simulate living organisms that may swim, as larvae, Parcels is the superior choice.

To study volume transport pathways in chapter 4 and 5, the analytical scheme implemented in ARIANE is used. Especially for chapter 5, it is important that backward and forward in time trajectories yield equivalent results, as experiments are conducted in both directions and directly compared. This is only ensured (with minor errors) for the analytical scheme. Idealised experiments in chapter 5 make use of the much more flexible implementation in Python provided by Parcels, but are not meant to represent realistic volume transport pathways. For the analysis conducted in chapter 4, matching forward and backward trajectories are less important. Still, my personal choice was to use the analytical scheme that mathematically justifies the interpretation of trajectories as volume transport pathways. Nevertheless, the results obtained by Schmidt et al. (2021) indicate that numerical schemes (Parcels) and analytical schemes (ARIANE) yield similar results for volume transport estimates. Choosing a numerical scheme is therefore not expected to strongly impact the results presented here and would have been appropriate as well. In chapter 6, the dispersal of living marine organisms is studied and all experiments are in the same time direction (forward in time). To achieve more flexibility in the release strategy and to add active movement, the numerical scheme implemented in Parcels was chosen. Throughout this thesis, trajectories from ARIANE (analytical scheme) are interpreted as volume transport pathways and those from Parcels (numerical scheme) as particle pathways. It shall be clearly noted, however, that this is not an unambiguously true definition beyond this thesis and the interpretation may change based on the context of other studies.

Note that by now, the Parcels package also provides the analytical scheme implemented in ARIANE and may be used as an equivalent replacement, but the discussed advantages and disadvantages of numerical versus analytical schemes still apply.

CHAPTER 3

Partial Coupling: A Method to Improve Ocean Circulation Variability in Models?

Model development and sources of AMOC variability:

The described forced and fully coupled configurations of (FOCI-)ATLAS10 are well suited for the purpose of studying past ocean circulation variability. But as all other forced and coupled configurations they are associated with disadvantages that come with the different methods to calculate ocean surface boundary conditions. It is therefore evaluated in this chapter, whether a coupled model can be modified to simulate the correct timing of variability, while keeping important ocean-atmosphere feedbacks. Partially coupled experiments with the eddying FOCI-ATLAS10 model configuration are conducted to analyse the basin wide impact of wind stress variability on the circulation, in particular on the AMOC, with the ultimate goal to improve the representation of past ocean circulation variability in models. Partial coupling refers to an assimilation of observed (reanalysed) wind stress anomalies into the ocean component of a coupled model, while heat and freshwater fluxes are still interactively exchanged with the atmosphere component. It is shown that partially coupled experiments are able to maintain the stability of the fully coupled configuration, while the timing of AMOC variability on sub-decadal timescales is significantly improved. On longer timescales, a limited feedback of wind stress variability on the North Atlantic buoyancy fluxes is found to limit the success of partial coupling to reproduce the timing of variability. At the same time, the newly developed FOCI-ATLAS10 configuration is compared to observations and other models, demonstrating its ability to simulate important aspects of the Atlantic Ocean circulation realistically.

Related publication:

Schulzki, T., Harlaß, J., Schwarzkopf, F. U. and Biastoch, A. (2022). Toward ocean hindcasts in earth system models: AMOC variability in a partially coupled model at eddying resolution. Journal of Advances in Modeling Earth Systems, 14, e2022MS003200, https://doi.org/10.1029/2022MS003200

Author contribution: The author was fully responsible for the set-up of the nested configuration, for designing and running the experiments and for all analysis/figures. He wrote the initial and final manuscript. The author did contribute to the technical implementation of partial coupling in FOCI (see section 2), but it was led by Jan Harlaß.

JAMES | Journal of Advances in Modeling Earth Systems

RESEARCH ARTICLE
10.1029/2022MS003200

Toward Ocean Hindcasts in Earth System Models: AMOC Variability in a Partially Coupled Model at Eddying Resolution

Tobias Schulzki[1], Jan Harlaß[1], Franziska U. Schwarzkopf[1], and Arne Biastoch[1,2]

[1]GEOMAR Helmholtz Centre for Ocean Research Kiel, Kiel, Germany, [2]Christian-Albrechts Universität zu Kiel, Kiel, Germany

Key Points:

- Partially coupled (PCPL) models are able to simulate ocean-atmosphere feedbacks necessary to maintain a stable Atlantic Meridional Overturning Circulation (AMOC)
- AMOC variability in PCPL experiments is significantly correlated to forced ocean models on timescales below 5 years and at all latitudes
- Wind stress curl contributions to decadal AMOC variability can be reproduced in PCPL, while the buoyancy contribution cannot

Supporting Information:

Supporting Information may be found in the online version of this article.

Correspondence to:

T. Schulzki,
tschulzki@geomar.de

Citation:

Schulzki, T., Harlaß, J., Schwarzkopf, F. U., & Biastoch, A. (2022). Toward ocean hindcasts in earth system models: AMOC variability in a partially coupled model at eddying resolution. *Journal of Advances in Modeling Earth Systems*, *14*, e2022MS003200. https://doi.org/10.1029/2022MS003200

Received 19 MAY 2022
Accepted 1 DEC 2022

Author Contributions:

Conceptualization: Tobias Schulzki, Arne Biastoch
Formal analysis: Tobias Schulzki
Funding acquisition: Arne Biastoch
Methodology: Tobias Schulzki, Jan Harlaß, Franziska U. Schwarzkopf
Project Administration: Arne Biastoch
Software: Tobias Schulzki, Jan Harlaß, Franziska U. Schwarzkopf
Supervision: Arne Biastoch

Abstract While forced ocean hindcast simulations are useful for a wide range of applications, a key limitation is their inability to simulate ocean-atmosphere feedbacks. As a consequence, they need to rely on artificial choices such as sea surface salinity restoring and other corrections affecting the surface freshwater fluxes. Fully coupled models overcome these limitations, but lack the correct timing of variability due to weaker observational constraints. This leads to a mismatch between forced and coupled models on interannual to decadal timescales. A possibility to combine the advantages of both modeling strategies is to apply a partial coupling (PCPL), that is, replacing the surface winds stress in the ocean component by wind stress derived from reanalysis. To identify the capabilities, limitations and possible use cases of partial coupling, we perform a fully coupled, two partially coupled and an ocean-only experiment using an all-Atlantic nested ocean configuration at eddying resolution in a global climate model. We show that the correct timing of Atlantic Meridional Overturning Circulation (AMOC) variability in PCPL experiments is robust on timescales below 5 years. Mid-latitude wind stress curl changes contribute to decadal AMOC variability, but North Atlantic buoyancy fluxes are not significantly altered by incorporating reanalyzed wind stress anomalies, limiting the success of PCPL on this timescale. Long term trends of the AMOC in PCPL mode are consistent with fully coupled model experiments under historic atmospheric boundary conditions, suggesting that a partially coupled model is still able to simulate the important ocean-atmosphere feedbacks necessary to maintain a stable AMOC.

Plain Language Summary The Atlantic Meridional Overturning Circulation (AMOC) is one of the most important quantities characterizing the circulation in the Atlantic Ocean and influences the climate in its surrounding countries. It is traditionally simulated with forced ocean-only or coupled ocean-atmosphere models. In this study we force the ocean component of a coupled climate model with observed wind stress anomalies, aiming to combine the advantages of these two most often applied modeling strategies, while omitting their respective key limitations. This can ultimately lead to an improved representation of the AMOC in models, a prerequisite to understand past and future changes of this complex circulation system. Furthermore, our set of model experiments directly isolates the role of wind variability on various timescales and different latitudes, improving our knowledge of processes generating changes in the AMOC.

1. Introduction

Owing to its major importance for the ocean heat transport and thus climate variability, the Atlantic Meridional Overturning Circulation (AMOC) has been a focus of study for several decades (Lozier, 2012). Still today, the complex AMOC is not fully understood in terms of strength, meridional coherence, drivers of long term changes and many other aspects. The existence of strong variability on interannual and decadal timescales makes the detection and attribution of potential recent AMOC changes challenging (Jackson et al., 2022). Direct observations for at least several decades would be needed to infer long term trends and their drivers. A detailed knowledge of mechanisms determining the past AMOC evolution is particularly important to assess future risks in the light of climate change, with models projecting a weakening of the AMOC until the end of this century (Weijer et al., 2020).

In addition to direct (yet sparse) observations by mooring arrays in the North and South Atlantic, numerical models largely contribute to our understanding of past AMOC variability. One of the most frequently used model set-ups are ocean general circulation models (OGCMs) forced with momentum, heat and freshwater fluxes derived from a prescribed atmospheric state based on reanalysis products, using bulk formulae, and thus incorporating observa-

Visualization: Tobias Schulzki
Writing – original draft: Tobias Schulzki
Writing – review & editing: Tobias Schulzki, Jan Harlaß, Franziska U. Schwarzkopf, Arne Biastoch

tions (Griffies et al., 2009; Tsujino et al., 2018). As a result, they are typically able to capture the observed timing of AMOC variability on various timescales (Roberts et al., 2013). A major disadvantage of forced (ocean-only) model simulations, however, is that prescribing the atmospheric state leaves very limited ability of the oceanic evolution to feed back to the atmospheric forcing (only through the bulk formulae's dependency on the ocean state). As a consequence, they typically act overly sensitive to freshwater forcing and require the application of sea-surface salinity (SSS) restoring terms (Griffies et al., 2009; Rahmstorf & Willebrand, 1995). This restoring term has an arbitrary strength and is not based on physical laws, nor empirical equations. Additionally, the global freshwater budget is not closed in such a model set-up (Griffies et al., 2009). Even if budget corrections are applied, they involve a redistribution of freshwater with horizontal patterns that are not expected to be realistic. Especially multidecadal trends and decadal variability of the AMOC were shown to be highly sensitive to restoring and budget correction choices (Behrens et al., 2013; Biastoch et al., 2021).

However, models are not limited to the ocean and OGCMs can be embedded in earth system models (ESMs) that simulate the interaction of several components of the climate system. These coupled models allow to explicitly simulate ocean-atmosphere feedbacks, therefore SSS restoring is not necessary. Also, energy and freshwater budgets are (nearly) closed without the need for artificial corrections. In contrast to forced OGCMs, ESMs only incorporate observations via atmospheric boundary conditions such as trace gas concentrations and land use changes. Variability of climate indices like ENSO, but also variability of the ocean circulation (e.g., AMOC), are generated internally in the coupled model. While the magnitude and/or period of this variability can be in agreement with observations, the timing of variability (e.g., years of maximum/minimum AMOC transport) is not (Cheng et al., 2013; Ding et al., 2013; Flato et al., 2013). Especially for sensitivity experiments with changes to one model parameter, or variable (e.g., increased CO_2 concentration), internally generated variability with unknown timing makes the attribution of changes more difficult. As a consequence, many scientific questions can only be addressed statistically in ensemble experiments.

An attempt to combine the advantages of the two modeling strategies is to apply a partial coupling (PCPL; Ding et al., 2013). Here, surface heat and freshwater fluxes are exchanged between the ocean and atmosphere model, as done in a fully coupled ESM. The wind stress (or momentum flux) on the other hand is calculated from reanalyzed wind, replacing the wind stress that would otherwise be provided from the atmospheric to the oceanic component of the model. Thoma et al. (2015) showed that PCPL can improve the timing of historical climate fluctuations, especially in the Pacific. Even multidecadal variability, namely the Pacific Decadal Oscillation (PDO), is simulated with improved timing. Additionally, their partially coupled model is also able to reproduce interannual variations of the AMOC as observed at 26.5°N. This result is in line with various studies showing that interannual AMOC variations at this latitude are mostly attributable to wind forcing (Biastoch et al., 2008; Zhao & Johns, 2014). Still, it is not clear whether partial coupling is similarly successful at other latitudes, since AMOC variability at different latitudes can have strongly different characteristics (e.g., Blaker et al., 2021; Jackson et al., 2022). Furthermore, AMOC variability in the South Atlantic was shown to have a significant contribution from intrinsic (un-forced) variability and is thus less tied to the applied (wind stress) forcing (Grégorio et al., 2015; Leroux et al., 2018). Thoma et al. (2015) only studied AMOC variability on interannual timescales and the question remains, whether PCPL experiments and observations (or ocean-only models) are also correlated on shorter and longer (decadal) timescales.

Partial coupling has the potential to improve the representation of the AMOC in hindcast simulations by combining the advantages of coupled and ocean-only simulations. Following Danabasoglu et al. (2014) the term 'hindcast' is used here to describe forced OGCM simulations with the goal to reproduce the past climate and should not be confused with initialized forecasts of the past (also called hindcast, e.g., Reintges et al. (2020)). Even if partial coupling may not be an alternative to coupled and forced simulations, it could provide a valuable set-up for sensitivity experiments with more specific questions. Although Thoma et al. (2015) provide a comprehensive analysis of variability in partially coupled experiments, several important characteristics of such simulations are currently unknown. In particular, this includes possible spatial and temporal limitations to reproduce past AMOC variability. Therefore, it is not yet possible to decide for which scientific questions partial coupling can be an advantageous alternative to forced or fully coupled model experiments and to envision possible improvements of the procedure.

Here, our aim is to provide a detailed description of the technical implementation of partial coupling in a high-resolution coupled model and to study its capability to reproduce the past ocean circulation (variability).

Although our focus is on the AMOC transport, the AMOC is an integrative measure and thus incorporates various circulation systems. We also study the impact of partial coupling on the basin-scale horizontal gyres, which dominate the large-scale circulation in the horizontal plane and may be even more directly influenced by the applied wind stress forcing. The motivation for this study and our main goals can be summarized by the following questions:

- Does a partially coupled ESM reproduce the observed large-scale ocean circulation, including its timing of variability? Specifically:
  – Do PCPL experiments simulate a realistic mean large-scale circulation and multi-decadal trends?
  – Is the correct timing of (AMOC) variability in PCPL experiments limited to certain latitudes, or timescales?

Our analysis is based on the comparison of fully coupled, partially coupled and forced (ocean-only) model experiments. All experiments were performed with a global nested configuration covering the whole Atlantic Ocean at an eddying resolution of 1/10°. This resolution includes an important range of variability, since the presence of eddies throughout large areas of the Atlantic Ocean and their importance was shown in many studies (e.g., Chelton et al., 2011; Hallberg & Gnanadesikan, 2006; Rieck et al., 2019). Several aspects of the large-scale circulation and its variability were shown to improve with a higher horizontal resolution, including the gyre circulation and AMOC (Hirschi et al., 2020). A better representation of the mesoscale is thus expected to cause a more realistic response to the applied surface forcing, but also introduce more variability into individual current components (Biastoch et al., 2021).

First, we provide a detailed description of the model configuration, implementation of partial coupling and the applied surface momentum and buoyancy forcing in Section 2. We then show how partial coupling affects the mean large-scale circulation, as well as its variability and long term evolution in Section 3. Section 4 contains an in-depth analysis of the timing of variability in partially coupled simulations with a strong focus on the AMOC.

2. Model and Methods

In this study, we employ the flexible ocean and climate infrastructure (FOCI), a coupled ocean-atmosphere-land model (Matthes et al., 2020), capable of including high-resolution ocean nests, to perform a series of model experiments. We here utilize a coupled (FOCI-ATLAS10) and an un-coupled (ATLAS10) configuration with an eddying Atlantic Ocean. In the following we describe the coupled configuration and the implementation of partial coupling. Afterward we describe the un-coupled (ocean-only) configuration and analyze the wind stress, heat and freshwater fluxes driving the ocean component in the different experiments.

2.1. Coupled Configuration: FOCI-ATLAS10

The ocean component of the coupled model is based on the Nucleus for European Modeling of the Ocean (NEMO) version 3.6, ocean sea-ice model (Madec, 2016). The Louvain-la-Neuve Sea Ice Model version 2 (LIM2; Fichefet & Maqueda, 1997; Vancoppenolle et al., 2009) is used as the sea-ice component.

ATLAS10 consists of a global grid (hereafter referred to as host) with a therein embedded, so called, nest with increased grid resolution. The host has a horizontal resolution of 0.5° on a tripolar Arakawa C-grid and 46 z-levels with increasing grid spacing from 6 m at the surface to 250 m at depth with application of partial cells at the seafloor (ORCA05 configuration; Barnier et al., 2006; Biastoch et al., 2008).

The nested area covers the Atlantic Ocean from 99°W to 62°E and from 65°S to approximately 65°N (Figure 1). Within the nest, the horizontal resolution is increased to 1/10°. This corresponds to a grid spacing of ∼5 km at high latitudes and 11 km in the tropics. Along with the higher horizontal resolution, the time step on the nest grid is reduced by a factor of 3 to ensure the CFL criterion is fulfilled. The vertical axis is unchanged compared to the host. The nest bathymetry is obtained by interpolating the ETOPO1 data set (Amante & Eakins, 2009) onto the model grid using the nesting tools (Lemarié, 2006). Thereby, also an updated bathymetry for the host is generated, where coastlines are adjusted, assuring grid cells on the host grid communicating to ocean cells on the nest grid, are also represented as ocean cells. However, in our coupled simulations, due to the coupling procedure itself (see below), the standard ORCA05 coastline is used in the host to avoid inconsistencies between the ocean's and the atmosphere's land-sea masks.

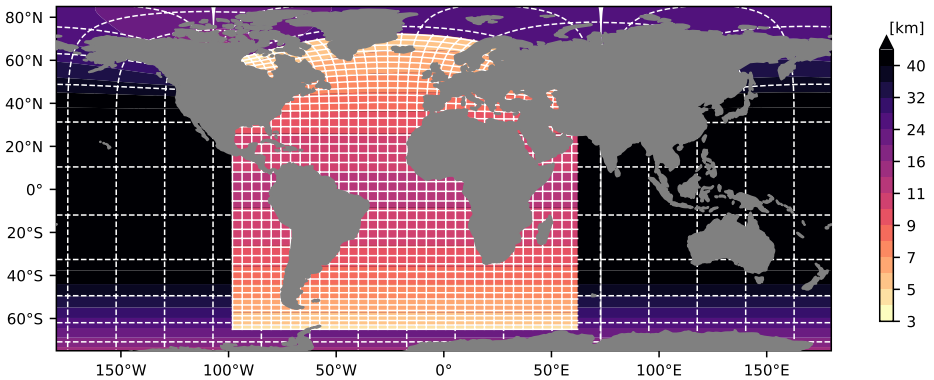

Figure 1. Visualization of the oceanic grid in the ATLAS10 nested configuration. Color shading shows the zonal distance between grid points. Every 45th grid line of the nest and host is shown.

Exchange between the nest and host is accomplished by 2-way Adaptive Grid Refinement in Fortran (Debreu et al., 2008). The global host not only provides lateral boundary conditions for the nest, but information is also fed back to the host at every time step along the nest boundary. After a given number of such cycles, the host is updated with the nest solution inside the full 3-dimensional domain covered by the nest (baroclinic update). This also holds for the sea-ice component which is integrated on both, the nest and the host grid. The lateral boundary of the nest involves a 6 nest grid point wide sponge layer to damp outgoing flow features that are smaller than resolved by the coarse host grid. We use a sponge layer coefficient of 3,000 $m^2\ s^{-1}$. While free-slip lateral momentum boundary conditions are used on the host grid, no-slip is used in the nest, mostly due to slightly more realistic/enhanced mesoscale variability in key regions as the Labrador Sea or Mozambique Channel (see also Quartly et al., 2013; Rieck et al., 2019; Schwarzkopf et al., 2019). However, it should be mentioned that overall no-slip boundary conditions perform less well in the northern than in the southern hemisphere. Especially the North Atlantic Current (NAC) path is less realistic (compare Penduff et al. (2007)).

On both model grids the vertical eddy viscosity and diffusivity coefficients are derived from a turbulent kinetic energy model (TKE; Blanke & Delecluse, 1993; Bougeault & Lacarrere, 1989).

In the non-eddying host we use the Total Variance Dissipation (TVD; Zalesak, 1979) scheme for tracer advection with a Laplacian diffusion operator acting along iso-neutral surfaces with an eddy diffusivity of 600 $m^2\ s^{-1}$. Further, we apply a Gent and McWilliams (GM) eddy parameterization (Gent & Mcwilliams, 1990) with an eddy induced velocity coefficient of 1,000 $m^2\ s^{-1}$. Lateral advection of momentum is represented in vector invariant form, where the vorticity term is solved using the energy and enstrophy conserving (EEN; Arakawa & Hsu, 1990) scheme. Lateral diffusion of momentum is accomplished by a bi-Laplacian operator acting along geopotential surfaces with a maximum eddy viscosity of $6 \times 10^{11}\ m^4\ s^{-1}$.

In the eddying nest, the tracer and momentum advection equations are solved using the self-diffusive upstream-biased scheme (UBS; Farrow & Stevens, 1995; Madec, 2016). No additional explicit diffusion terms were used in the advection equations. The UBS scheme was chosen, as it was found to perform similar to the TVD/EEN advection schemes (used on the host grid) in the coupled configuration, but with a slightly better representation of eddy activity (higher, more realistic, SSH variance and EKE) in many regions.

Surface boundary conditions for FOCI-ATLAS10's ocean component are derived from interactive atmosphere and land models. The atmospheric component of FOCI is provided by ECHAM6 (Müller et al., 2018; Stevens et al., 2013) with 96 vertical levels and a spectral resolution of T63 (~200 km) in the horizontal plane. Albedo, soil moisture, snow cover, leaf area and vegetation distribution are interactively simulated by the JSBACH land model (Brovkin et al., 2009; Reick et al., 2013).

Surface boundary conditions are calculated in ECHAM6 and provided to the host grid via the OASIS3-MCT coupler (Valcke, 2013). These include solar and non-solar heat fluxes, freshwater fluxes and wind stress. The wind stress calculation includes ocean current feedbacks ("relative wind"). A direct exchange between the ocean nest and atmosphere is currently not implemented, consequently, only the host grid is directly coupled to

ECHAM6 (every 3 hr), while the nest grid receives the same atmospheric state as boundary conditions every 30 min (constant for 3 hr) interpolated onto its oceanic grid. The nest itself feeds back its baroclinic solution onto the host grid every third host grid time step (90 min), thereby indirectly also affecting the atmosphere. The exchange with the sea-ice model takes place every 3 hr on the host and every 30 min on the nest grid.

A fully coupled historical experiment is initialized with atmospheric boundary conditions of the year 1850. The ocean and atmosphere initial states are taken from the end of a 1,500 years long FOCI (un-nested standard configuration) control simulation described in Matthes et al. (2020). To initialize the nest, all restart variables are interpolated from the ORCA05 grid to the ATLAS10 grid. The model is then integrated for 163 years until 2013 under historic atmospheric boundary conditions that follow the CMIP protocol as described in Meinshausen et al. (2017). This experiment will be referred to as FOCI-ATLAS10-CPL (short: CPL) in the following. The first 108 years, regarded as the spin-up, are not analyzed here.

2.2. Partial Coupling

As described above, the ocean component receives surface boundary conditions from the interactive atmosphere in the fully coupled configuration. When using partial coupling the wind stress is no longer calculated by ECHAM6, but derived from reanalyzed 10 m wind fields. The heat and freshwater fluxes still depend on the wind simulated by ECHAM6. In this study we employ the 10 m wind fields provided by the JRA55-do version 1.5 data set (Tsujino et al., 2018) to force the ocean component of FOCI. The 10 m wind is converted to wind stress using bulk formulae (Large & Yeager, 2009). We neglect ocean current feedbacks and derive the wind stress formulated as "absolute winds." We use a constant atmospheric density of 1.22 kg m^{-3} and a drag coefficient that depends on the wind speed according to Large and Yeager (2009). We do not account for atmospheric stability, that is, we use 10 m wind rather than 10 m neutral wind, as the necessary input fields to keep a clean separation between wind stress climatology (purely from the model) and wind stress anomaly (purely from reanalysis) were not available.

Following Thoma et al. (2015), we calculate an anomaly forcing in which the wind stress anomalies are taken from the 3-hourly resolved reanalyzed wind stress interpolated onto the ECHAM6 T63 grid, while the climatology is replaced. To derive the applied wind stress climatology, we employ two different strategies: In a first experiment (FOCI-ATLAS10-PCPL-LOW; short PCPL-L) the monthly climatology of the reanalysis is replaced by the monthly climatology of an un-nested FOCI 3-member ensemble, under a historical forcing based on the years 1850–2013. We use the same procedure to calculate the wind stress climatology in the FOCI ensemble, as for the reanalysis (based on the 10-m wind). As discussed later this results in a lower mean wind stress compared to CPL, but a similar mean wind stress compared to the ocean-only simulation described below. Choosing the 3-member ensemble climatology was based on initial experiments run without the 1/10° ocean nest and then kept for PCPL-L. Differences between the FOCI-ATLAS10-CPL climatology and FOCI (un-nested) ensemble climatologies are overall small, except for a slightly stronger mean wind stress in the North Atlantic in CPL. Because the main purpose of PCPL-L is to investigate, whether the mean wind stress impacts the ability of PCPL to reproduce the timing of AMOC variability, the 3-member ensemble climatology is still suited here. With the second experiment (FOCI-ATLAS10-PCPL-HIGH; short PCPL-H) we are aiming at generating a wind stress forcing as comparable as possible to CPL. Therefore, we replace the reanalysis wind stress climatology by the 1958–2013 climatology derived from CPL. Here we directly use the wind stress calculated and stored by ECHAM6 and do not apply the offline bulk formulae to the 10 m wind.

The wind stress anomaly forcing is provided on the ECHAM6 T63 grid and then interpolated onto the host and nest grids. The wind stress forcing is not interpolated in time, but constant at all model time steps within 3 hr for both, host and nest. A summary of the partial coupling procedure applied here is visualized in Figure 2.

The partially coupled experiments are initialized from the FOCI-ATLAS10-CPL simulation from the last time step on 31 December 1957. Subsequently the model is integrated forward over the length of the atmospheric boundary condition data set (until 2013), resulting in 56 years long model simulations. Apart from the different surface boundary conditions in the ocean component of FOCI, all settings described above are identical for FOCI-ATLAS10-CPL and the two FOCI-ATLAS10-PCPL experiments.

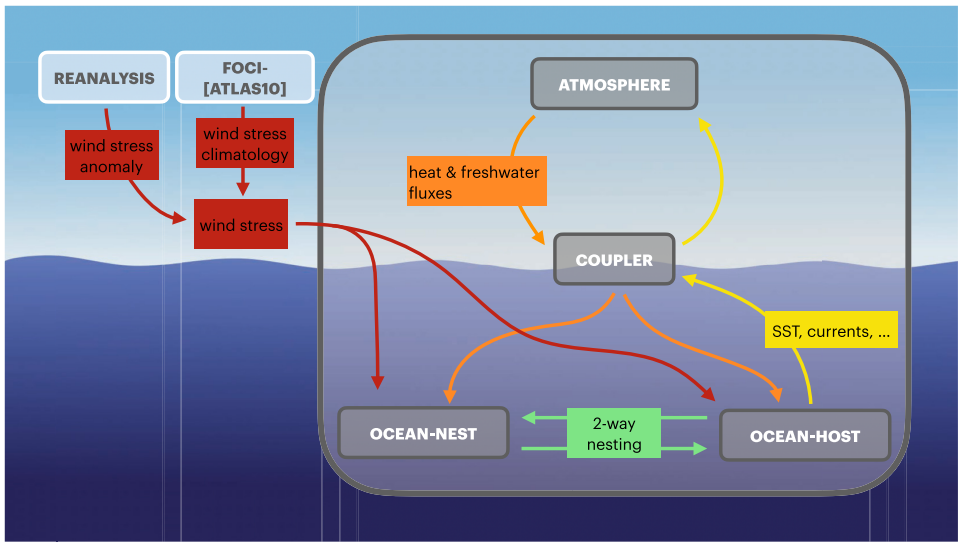

Figure 2. Schematic diagram showing the implementation of partial coupling in the FOCI-ATLAS10 configuration. Components that are part of FOCI and interact during runtime are enclosed in the large gray box. Wind stress is calculated offline and read from disk.

2.3. Ocean-Only Configuration: ATLAS10

Additional to the coupled configuration, we run a forced (ocean-only) experiment using the ocean component of FOCI-ATLAS10. All surface fluxes are derived from the JRA55-do version 1.5 forcing data set. This experiment is referred to as ATLAS10-OCO (short: OCO). During runtime, all variables, except runoff, are interpolated onto the nest and host grids. Surface fluxes are then derived from the forcing data set using bulk formulae (Large & Yeager, 2009). The runoff was first remapped onto the host grid using the procedure of Martin (2021) described in Biastoch et al. (2021) with a search radius of 160 km, but without application of the described river plume scheme. Afterward, the runoff was interpolated onto the nest grid assuring no loss of runoff on land by redistribution to the nearest ocean grid points. Within NEMO, river mouth treatment is activated, increasing vertical mixing within the top 10 m of the water column at every runoff grid point.

As many namelist parameters as possible remain unchanged compared to the (partially) coupled set-ups described above. The main purpose of this experiment is to provide a best estimate of the AMOC variability's timing, in a set-up comparable to our fully and partially coupled experiments. We adopt restoring settings from a successful model simulation of the North Atlantic in the higher resolved VIKING20X model, described in Biastoch et al. (2021): SSS restoring is applied with a piston velocity of 50.0 m yr^{-1} everywhere, excluding ice-covered regions, in grid cells with runoff and additionally within a distance of 80 km around Greenland. Therefore, the freshwater input from rivers and ice-sheet melting is not immediately damped. Also the Mediterranean Sea outflow (below 700 m) is restored to climatological temperature and salinity values using a three dimensional mask with a maximum Newtonian damping coefficient of 6.34×10^{-5} s^{-1}. In an ocean-only experiment the atmospheric forcing is prescribed and the larger ocean area of the updated host bathymetry can be used. Together with the surface boundary conditions, which are calculated simultaneously on the host and the nest grid at every exchange time step (30 min), the full exchange (including baroclinic update) between the two components takes place. A main difference between the ocean-only and FOCI-ATLAS10 configurations is the use of the TVD and EEN advection schemes, not only on the host, but also on the nest grid instead of the UBS scheme. As on the host grid, a Laplacian diffusion operator is added to the tracer advection equation and a bi-Laplacian operator to the momentum advection equation. Eddy diffusivities are adjusted to the higher grid resolution (120 m^2 s^{-1} and 2.4×10^{10} m^4 s^{-1}). The reason for this switch is to achieve a more realistic multi-decadal AMOC trend. The UBS scheme, together with the model settings tuned for the TVD/EEN schemes, did cause the AMOC to considerably decrease over time. Note that this is not the case for the coupled configuration, where UBS does not cause a long term AMOC decline.

Table 1
Overview of Experiments

Experiment	CPL	PCPL-L	PCPL-H	OCO
Mode	CPL	PCPL	PCPL	OCO
Heat/freshwater	ECHAM6	ECHAM6	ECHAM6	JRA55-do
Wind stress anomalies	ECHAM6	JRA55-do	JRA55-do	JRA55-do
Wind stress climatology	ECHAM6	FOCI-Ensemble	CPL	JRA55-do
Forcing resolution	T63 (≈1.9°)	T63 (≈1.9°)	T63 (≈1.9°)	TL319 (0.5625°)
Current feedback	Yes	No	No	Yes
Initialization	FOCI-piCtrl	CPL	CPL	WOA13/at rest
Years	1850–2013	1958–2013	1958–2013	1958–2013

Note. Modes: CPL = fully coupled, PCPL = partially coupled, OCO = ocean-only. The (spatial) forcing resolution indicates on which grid the momentum and freshwater fluxes are provided. Current feedback denotes whether the ocean current is considered for calculating the wind stress from 10 m wind.

ATLAS10-OCO was initialized in 1958 from rest, using temperature and salinity from the World Ocean Atlas 2013 (WOA13; Locarnini et al., 2013; Zweng et al., 2013) climatology and run for 56 years until 2013. A summary of all model experiments can be found in Table 1 and the years covered by the respective experiments are visualized in Figure 3a.

2.4. PCPL—Wind Stress and Buoyancy Forcing

Before studying the performance of partial coupling, we compare the wind stress and buoyancy forcing that is applied in the different model experiments.

The most important characteristics of the different wind stress forcings are visualized by timeseries of the zonal mean zonal wind stress at 47°N (Figure 3a). CPL and PCPL-H simulate a higher mean wind stress than OCO and PCPL-L. The magnitude and timing of variability is nearly the same in OCO, PCPL-L, and PCPL-H, but differs in CPL. In the following we analyze the wind stress in more detail focusing on the zonal mean zonal wind stress, due to its importance for the large-scale circulation (e.g., by setting the latitudinal position of basin scale oceanic gyres and impacting their strength based on Sverdrup theory).

The zonal mean zonal wind stress (Figure 3b) has nearly the same meridional structure in CPL and the two partially coupled experiments (PCPL-L and PCPL-H) when referring to the position of maxima and minima only. The PCPL-H and CPL climatologies are the same by construction. Note that small differences between PCPL-H and CPL are still possible, because they are only identical when averaged over the full forcing period (1958–2013), but here we solely consider the period used for further analysis in the following sections (1970–2013). The meridional structure in PCPL-L matches the (un-nested) FOCI-ensemble and is thus not tied to CPL's climatology. In CPL, due to the 2-way nesting, the higher resolution in the nest also affects the host, which in turn can change the atmospheric circulation compared to the FOCI-ensemble. However, this does not seem to notably alter the meridional structure of the zonal wind stress, as apparent in the very similar position of maxima and minima in PCPL-H/CPL and PCPL-L. It should be pointed out that neither monthly and annual anomalies, nor long-term trends in PCPL mode are affected by the replacement of the climatology, but are fully based on the reanalyzed wind stress.

In contrast, the mean strength differs between CPL/PCPL-H and PCPL-L, with the former having the strongest mean zonal wind stress at most latitudes. As a result, the wind stress curl in the center of the basin scale oceanic gyres is also stronger in CPL/PCPL-H (Figure 3c). While in PCPL-H a climatology based on the wind stress calculated by ECHAM6 during runtime is used, we employ the CORE bulk formula (Large & Yeager, 2009), that is also used in OCO, to derive the wind stress climatology from 10 m wind offline in PCPL-L. The online application of the ECHAM6 bulk formula (based on Louis (1979)) and the offline application of the CORE bulk formula results in a considerably different wind stress for the same 10 m wind. The result of these different strategies is one experiment being more comparable to CPL (PCPL-H) and the second being closer to OCO (PCPL-L). Both strategies have advantages and disadvantages. While the higher mean wind stress in PCPL-H is expected to

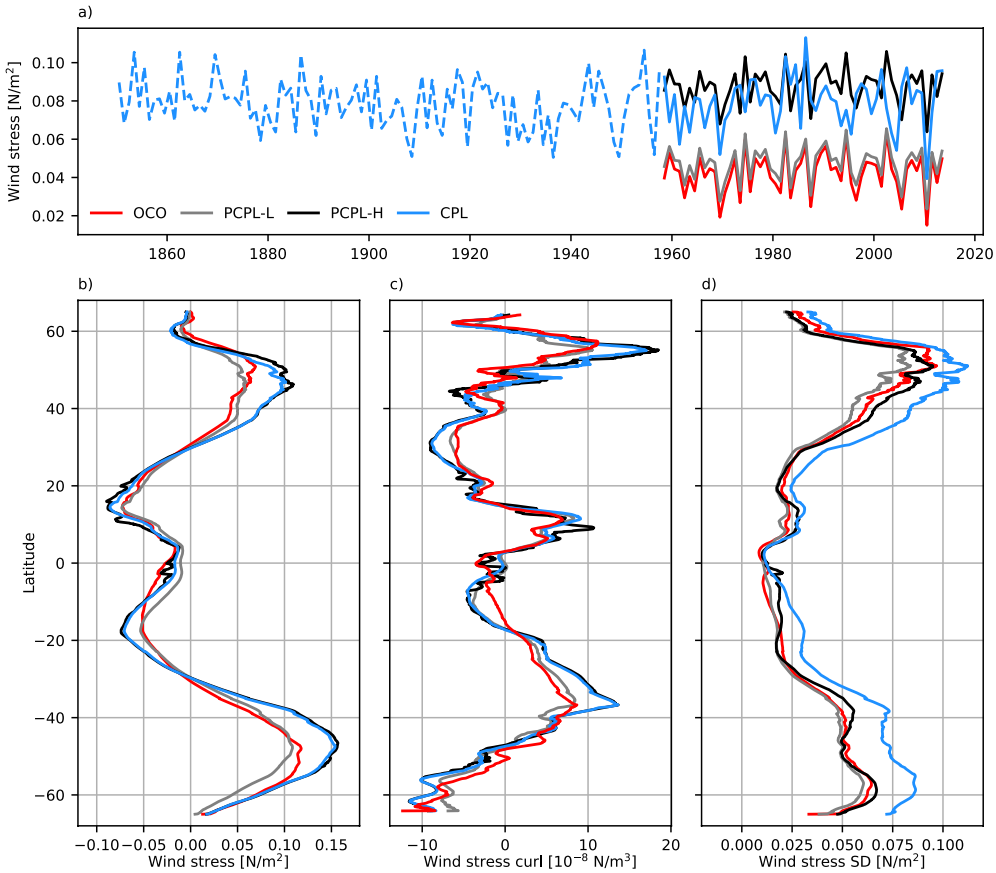

Figure 3. Timeseries of the annual mean zonal mean zonal wind stress at 47°N (a). The spin-up period of the fully coupled simulation is indicated by a dashed line. 1970–2013 zonal mean zonal wind stress (b), zonal mean wind stress curl (c) and standard deviation of the zonal mean zonal wind stress (d) in the Atlantic (including the Atlantic sector of the Southern Ocean).

minimize a secondary spin-up and subsequent model drift after switching to PCPL mode, the lower wind stress in PCPL-L allows for a better comparison to OCO. This is the comparison we are most interested in. By retaining the mean meridional structure of FOCI in PCPL-L, this spin-up may be less strong. In particular the position of the southern hemisphere westerlies differs considerably in FOCI and the reanalysis products.

Except for the equatorial region, CPL also shows the strongest zonal mean zonal wind stress variability (Figure 3d). This is likely caused by a combination of differences in the bulk formulae and the explicit simulation of feedbacks. Note that PCPL does exclude feedbacks that directly involve a surface momentum transfer. Further, the wind stress variability is very similar in PCPL-H and PCPL-L, since both are derived from reanalyzed 10 m wind using the offline CORE bulk formula. Neglecting ocean currents and atmospheric stability to create the PCPL forcing does not seem to have a large impact on the variability. In OCO wind stress is calculated during runtime incorporating the ocean and atmosphere's (provided by the forcing data set) states, but variability is comparable to the PCPL experiments (that use the same 10 m wind anomalies) at most latitudes. In particular there is not a bias toward lower, or higher, variability in both PCPL experiments. The meridional structure of wind stress variability is overall similar in the PCPL experiments and also compares well with OCO.

As visible in Figure 3a, wind stress variability at 47°N is highly correlated between PCPL-H, PCPL-L, and OCO by construction. This is true for all other latitudes as well. The fully coupled simulation is not correlated to OCO, nor the PCPL experiments.

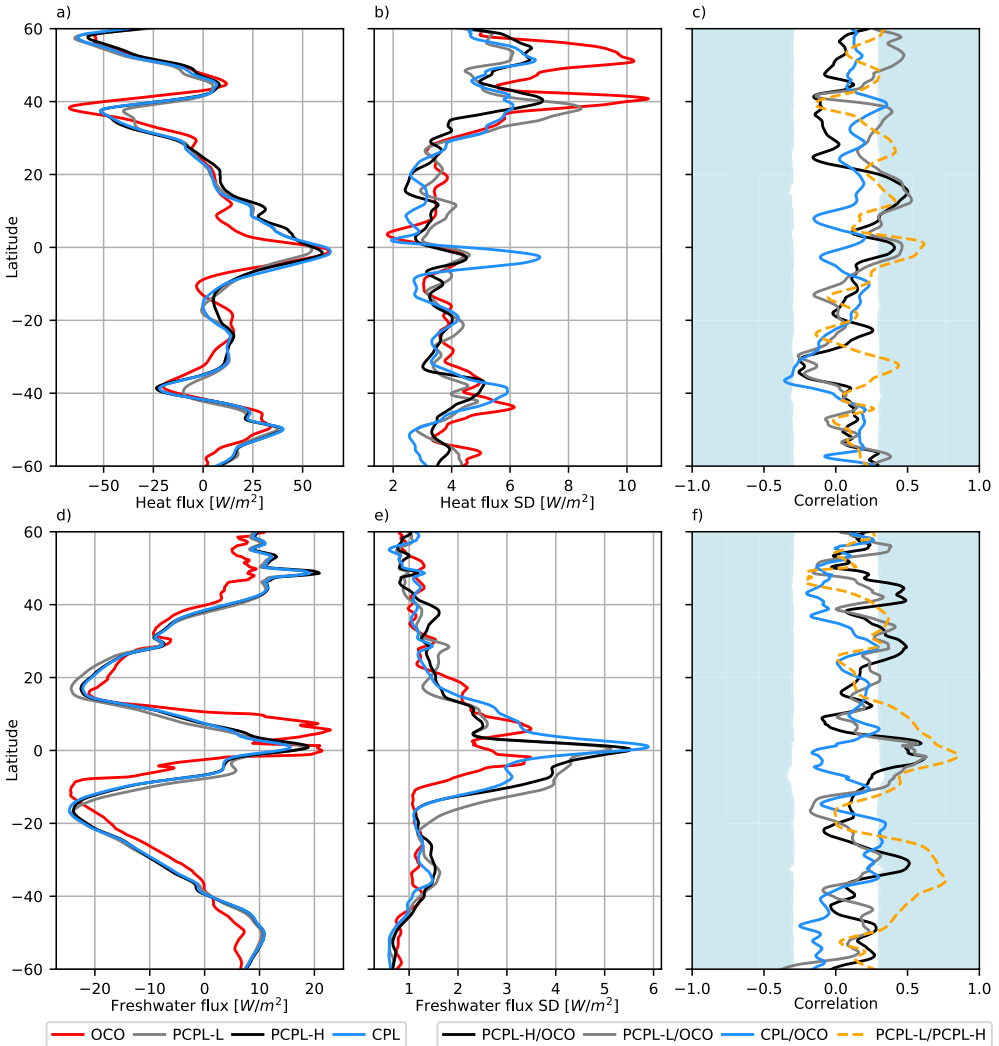

Figure 4. 1970–2013 zonal mean heat flux (a) and standard deviation (b) based on detrended annual means in the Atlantic (including the Atlantic sector of the Southern Ocean). Correlations of annual and zonal mean (detrended) heat fluxes are shown in (c). (d–f) analogously show the heat equivalent freshwater flux. Both fluxes are defined positive downward (ocean heat and freshwater gain). The fluxes were smoothed with a 31 grid point (3°) boxcar filter before calculating correlations.

As expected from the analysis by Thoma et al. (2015), partial coupling does not considerably change the mean heat and freshwater fluxes and their magnitude of variability (Figure 4). The freshwater flux is provided as a heat-equivalent freshwater flux here (e.g., Cerovečki et al., 2011). Both buoyancy flux components are very similar in PCPL-L/H and CPL. Differences to OCO are more pronounced, because of the very different approaches of calculating the surface boundary conditions in the coupled and un-coupled set-ups. Especially the stronger heat flux variability in the northern Atlantic and the increased tropical rainfall in OCO stand out. Overall, the assimilation of wind stress variability does not affect the timing of heat and freshwater flux variability in the Atlantic. The correlation is not significant, except for spikes at individual latitudes. Significance levels are calculated based on a two-sided student *t*-test, considering serial correlation by calculating effective degrees of freedom following Emery and Thomson (2001). Note that with a confidence interval of 95% there is still a 5% chance of falsely rejecting the null hypothesis (zero correlation). Such spikes likely have no physical meaning as long as they don't cover a larger latitude range, or are consistent across different experiments. The only region with a correlation that is significant for all experiments, except CPL/OCO, is the tropical Atlantic. It is possible that this

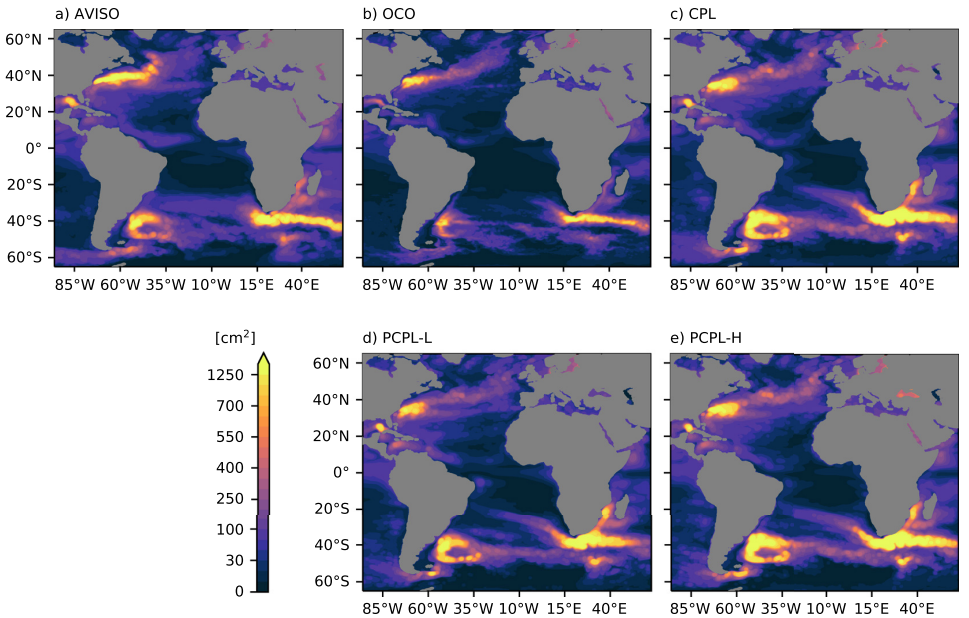

Figure 5. SSH variance (1993–2013) based on detrended 5-day means from AVISO (a), OCO (b), CPL (c) PCPL-L (d) and PCPL-H (e). All model fields show SSH variance on the nest grid.

correlation is caused by an atmospheric bridge to the equatorial Pacific and therefore mediated by the atmosphere models response to ENSO. Our PCPL experiments are very successful in reproducing the observed ENSO state, consistent with Thoma et al. (2015). As a result, also the timing of heat flux variability in the equatorial Pacific is significantly improved (Figure S1 in Supporting Information S1). The correlation of monthly Niño3.4 SST anomalies to observations (Rayner et al., 2003) is above 0.8 for both PCPL experiments and therefore even higher than reported by Thoma et al. (2015).

3. Mean State, Variability and Multidecadal Trends

In the following, we address our first question on the ability of the FOCI-ATLAS10 configuration and partial coupling to realistically reproduce the past large-scale circulation. We therefore analyze patterns of mesoscale activity and the vertically integrated (gyre) and zonally integrated (overturning) volume transports, the magnitude of their interannual variability and long term trends.

3.1. SSH Variance

A main benefit of a model at 1/10° resolution is the explicit simulation of mesoscale eddies in vast areas of the ocean. The surface circulation of the Atlantic is often dominated by mesoscale eddies, rather than coherent currents (e.g., Chelton et al., 2011). Their importance is also highlighted in studies showing a more realistic representation of the AMOC in high-resolution models (Hirschi et al., 2020). It is thus important to study, whether FOCI-ATLAS10 is able to adequately represent mesoscale activity and whether it changes in partial coupling mode.

At 1/10° resolution, ATLAS10 is able to simulate vigorous mesoscale activity throughout most of the Atlantic Ocean (Figure 5). Overall, the spatial patterns of SSH variability in CPL, OCO, PCPL-H, and PCPL-L are very similar and mostly agree with the SSH variance derived from satellite altimetry (AVISO). Especially in the Malvinas Confluence Zone and the Agulhas region. Also the western boundary north of the equator, including the Gulf of Mexico, and the NAC are characterized by strong eddy activity. It should be noted that the model simulates very few West Greenland Current eddies, compared to higher resolved models (Rieck et al., 2019). Also the north-west corner is not pronounced in ATLAS10 and high values of SSH variance along the NAC

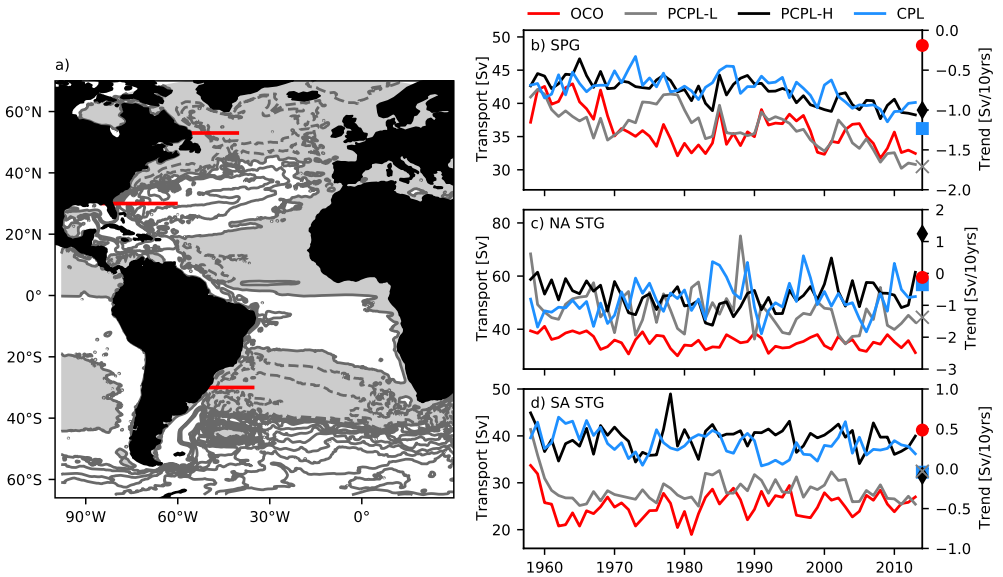

Figure 6. Horizontal gyre circulation: Mean (1970–2013) barotropic stream function in Sv from CPL (a). Annual mean transports of the Subpolar Gyre (b), North Atlantic Subtropical Gyre (c) and South Atlantic Subtropical Gyre (d). Linear trends (1970–2013) are marked on the right *y*-axis. The sections used to derive the gyre transports are shown in panel (a).

pathway are more confined to the North American coast, most likely as a consequence of the no-slip lateral boundary condition (Section 2.1). Another notable difference is seen in the pathway of Agulhas Rings. AVISO shows increased SSH variance between 40°S and 20°S extending across the full width of the Atlantic. SSH variance in OCO is clearly lower in this region, suggesting that Agulhas Rings are less intense, less frequent, or decay faster. In contrast, CPL shows a very strong and narrow pathway of Agulhas Rings that nearly reaches the western boundary. The partially coupled experiments show a very similar pathway. Based on sensitivity experiments with absolute and relative wind by Schwarzkopf et al. (2019), the interaction between the wind forcing and mesoscale Agulhas Rings is important for a realistic representation of the ring path. Even when using relative wind in FOCI-ATLAS10 (as in CPL), the wind stress calculation is performed on the coarser ECHAM6 grid and therefore the wind stress does not change across the eddy, excluding a feedback between the mesoscale current direction and the large scale wind. Also note the comparably high variance in the Caspian Sea in OCO. In contrast to all FOCI experiments (see Section 2), non-zero net freshwater fluxes in the Caspian Sea are allowed in OCO. Because of the prescribed atmosphere in OCO, unrealistic fluxes in the closed basin do not affect remote ocean areas.

Although the SSH variance is very heterogeneous, OCO shows the overall lowest variance, while PCPL-H and CPL simulate SSH variance that can be twice as large in certain regions (e.g., the Agulhas Retroflection). PCPL-L simulates variability with a magnitude in-between. This is true for SSH variance in the individual regions discussed above and also the full nest domain. The comparison between PCPL-H and PCPL-L suggests that the mean wind stress plays an important role for the magnitude of SSH variance.

3.2. Horizontal Gyre Circulation

General features of the long term mean gyre circulation (exemplarily shown for the fully coupled experiment (CPL) in Figure 6a) agree among all our simulations and are also in agreement with other models of comparable (or higher) resolution (e.g., Hirschi et al., 2020; Schwarzkopf et al., 2019). In the south Atlantic, the Drake Passage inflow turns northward into the highly variable region of the Malvinas confluence. Further north, the South Atlantic Subtropical Gyre (SA STG) covers the latitudes between 40°S and 20°S. In the North Atlantic positive stream function values, indicating the anticyclonic flow of the North Atlantic Subtropical Gyre (NA

STG), are seen between 18°N and 40°N. The Gulf Stream separates from the US coast just north of 34°N (Cape Hatteras). At higher latitudes CPL simulates a vigorous cyclonic flow associated with the Subpolar Gyre (SPG).

We define the gyre strength by evaluating the maximum (minimum) of the barotropic stream function for the NA STG (SPG and SA STG). We choose the latitudes of 53°N (SPG), 30°N (NA STG) and 30°S (SA STG). These sections are shown in Figure 6a.

The mean gyre circulation at all latitudes is similar in CPL and PCPL-H, both simulating a stronger transport compared to OCO and PCPL-L. This is consistent with the stronger mean wind stress curl and thus mainly caused by the different methodologies used to calculate the wind stress. For the SPG, where estimates from coupled models with comparable resolution are available, ATLAS10 simulates a similar mean gyre transport. The SPG transport ranges from 36 to 42 Sv in our set of model experiments, while Meccia et al. (2021) derive a range of 35–55 Sv. Their estimate for the NA STG transport (at 34°N) is 55–95 Sv; all experiments presented here, except OCO, simulate a mean transport within this range (58–76 Sv). OCO, the only ocean-only experiment, simulates a slightly weaker transport of 46 Sv. For further analysis we chose to not follow Meccia et al. (2021), because the estimated transport at 34°N is clearly affected by mesoscale recirculations and eddies. It is questionable, whether the barotropic stream function maximum at this latitude is a good estimate of the large-scale gyre strength. The effect can be reduced, but not eliminated, by instead calculating the gyre transport at 30°N, avoiding the highly eddying NAC. The NA STG transport is lower by 10–24 Sv when derived at 30°N. The mean transport of the SA STG ranges from 25 Sv in OCO and 29 Sv in PCPL-L to 38 Sv in CPL and 40 Sv in PCPL-H.

Interannual variability (standard deviation of detrended annual means) is comparable in all experiments, except for a lower variability of the NA STG in OCO. Note that models with the strongest mean transport not necessarily simulate the highest variability.

In all experiments, except OCO, the SPG transport shows a significant negative trend. Note that we calculate trends after 1970, to eliminate the initial spin-up phase of OCO and secondary spin-up after switching to PCPL mode in PCPL-L. The magnitude of the SPG trend is strongest in PCPL-L (−1.7 Sv/10 yrs) and lower, but still highly significant (p-value <0.01; the p-value denotes the probability of accepting the null-hypothesis, i.e., the trend is equal to 0) in PCPL-H (−1 Sv/10 yrs) and CPL (−1.2 Sv/10 yrs). Especially PCPL-H and CPL simulate a stable gyre transport until the late 1980s, before the transport starts to decline. Although slightly masked by a secondary spin-up, PCPL-L seems to simulate the onset of a long term negative trend in the same time period. The similar timing and magnitude of trends in PCPL-H and CPL suggest that they are related to the historic atmospheric boundary conditions that are applied in both experiments. The stronger trend in PCPL-L likely reflects a transient adjustment to the lower mean wind stress (curl) in the subpolar North Atlantic (SPNA) that adds to the weakening under rising CO_2 concentrations. Despite using the latitude of 30°N, the NA STG trends are clearly affected by the strong mesoscale activity and sensitive to the time period chosen. CPL and OCO do not simulate a significant trend. PCPL-L simulates a weakening, which is only significant for the time period 1958–2013 and again is most likely an adjustment to the lower mean wind stress (curl). PCPL-H shows a significant strengthening of 1.2 Sv/10 years for the time period 1970–2013 (p-value = 0.03). The multidecadal SA STG trends are not significantly different from zero in any experiment.

None of the mentioned (significant) trends are directly related to local changes in the wind field that are small in the North Atlantic. The wind stress curl trends at 53°N and 30°N are smaller than 0.22×10^{-8} N m^{-3}/10 years in CPL and smaller than 0.05×10^{-8} N m^{-3}/10 years in PCPL-L/H and OCO. All these trends are insignificant (p-value >0.58). It is more likely that they are related to the response of the oceanic circulation to the atmospheric boundary conditions in CPL and PCPL-H. PCPL-L shows a model drift toward a lower mean gyre strength over the full experiment. But this drift can be (mostly) eliminated by retaining the stronger mean wind stress of the fully coupled configuration. Therefore, we can state that PCPL in general is able to simulate a stable gyre circulation that is still free to adjust to changes in for example, the radiative forcing, as long as the coupled model's inherent wind stress climatology is used. This is an important result and may be useful to distinguish between artificial trends in ocean-only simulations and real trends that are forced by the surface boundary conditions. Note that the salinity restoring in an ocean-only experiments can locally counteract changes in the surface freshwater forcing, or ocean circulation, by restoring toward a climatological field.

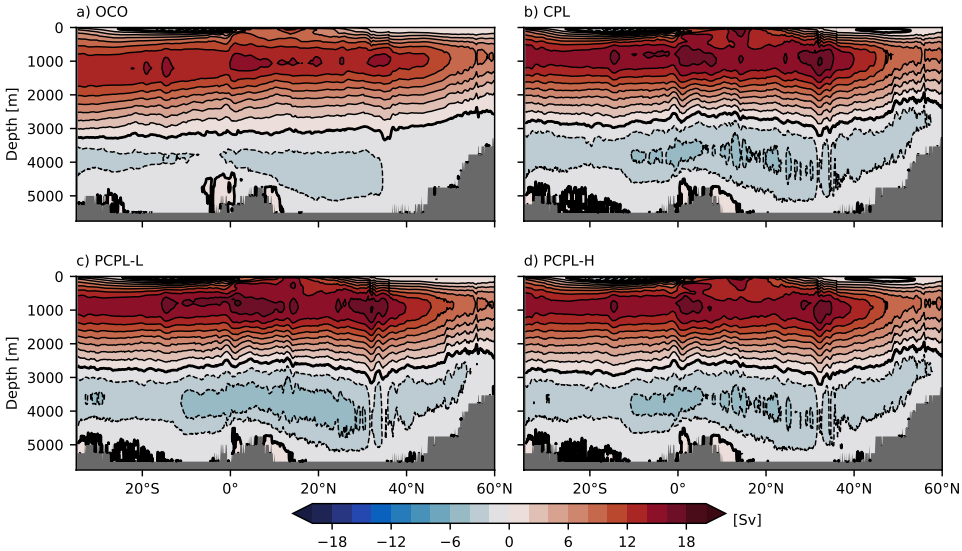

Figure 7. Mean 1970–2013 Meridional Overturning Stream function in OCO (a), CPL (b), PCPL-L (c) and PCPL-H (d). Contours are drawn with an interval of 2 Sv (the zero contour is drawn bold).

3.3. AMOC

The mean AMOC structure is similar in all model experiments, with a northward flow of surface water and a southward return flow of North Atlantic Deep Water (NADW) at mid-depth connected by sinking north of about 40°N (Figure 7). At abyssal depths the flow of Antarctic Bottom Water (AABW), formed in the Southern Ocean, is directed northward. Compared to OCO, the AABW and NADW cells, are clearly stronger in the (partially) coupled experiments, but the latter still covers a larger depth range in OCO. Especially south of 20°N, the zero-crossing of the Meridional Overturning Stream function is located approximately 500 m deeper in OCO. Since it continuously deepens toward the south in OCO, but slightly rises south of 20°S in PCPL and CPL, this difference can be as large as 700 m south of 20°S. This suggests that the shallower NADW cell in CPL, PCPL-L, and PCPL-H is not caused by reduced water mass transformation in the North Atlantic (NA), but a stronger formation of AABW. Although the mean wind stress in PCPL-H and PCPL-L considerably differs, the mean AMOC structure is still similar. PCPL-L simulates a slightly stronger NADW cell in the Subtropical Atlantic, and the AABW cell covers an even larger vertical range in the South Atlantic (SA) compared to CPL and PCPL-H. The NADW and AABW cells are nearly unchanged when PCPL-H is compared to CPL. The mean AMOC structure in density coordinates supports this result (Figure S2 in Supporting Information S1). Especially PCPL-H and CPL show little difference. In PCPL-L only the North Atlantic Shallow Tropical Cell is weaker, due to the lower mean wind stress. OCO simulates the weakest NADW cell in our set of experiments. The AMOC in density space (Figure S2 in Supporting Information S1) reveals that this is likely connected to reduced water mass transformation in the North Atlantic. Different mechanisms could be responsible for this result. In addition to different surface boundary conditions (including precipitation, runoff and heat fluxes), model choices such as SSS restoring and the advection scheme could be responsible. Also the initialization strategy differs. CPL (and therefore all FOCI-ATLAS10 experiments) is based on a 1,500-year long pre-industrial control simulation and therefore has a much longer spin-up time. OCO is initialized from climatological hydrography and an ocean at rest in 1958.

Figure 8 shows the temporal evolution of the AMOC strength at different latitudes of long-term measurements. The AMOC strength is defined as the maximum overturning stream function in depth or density space. In the SPNA the Overturning in the Subpolar North Atlantic Program (OSNAP) array measures the AMOC since 2014 and estimates a mean transport of 16.6 Sv (Lozier et al., 2019). Although the model experiments do not cover this time period, the AMOC transports in CPL (18.4 Sv), PCPL-H (17.6 Sv) and PCPL-L (17.3 Sv) are all slightly above the OSNAP estimate, while OCO simulates a weaker AMOC of 14.8 Sv. Overturning across the OSNAP section is calculated resembling observations and thus in density coordinates (here we use potential density

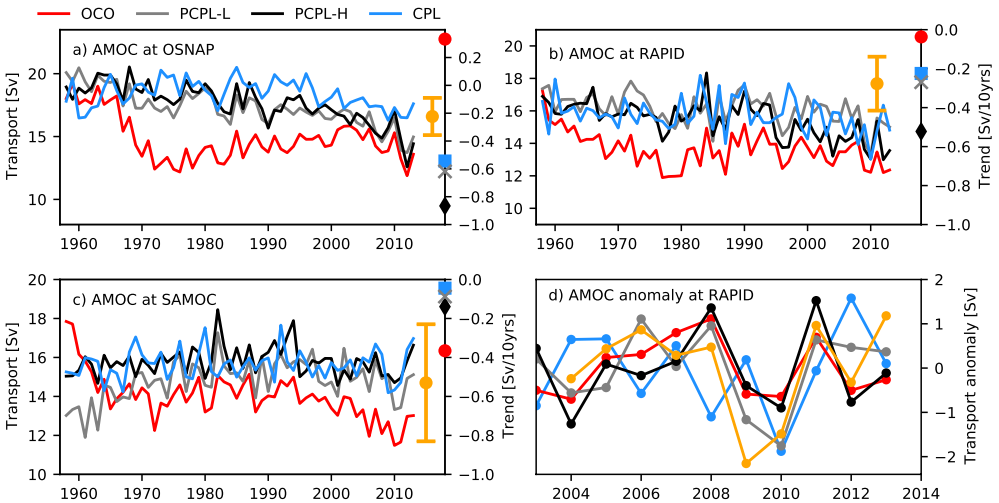

Figure 8. Annual mean Atlantic Meridional Overturning Circulation (AMOC) transports at the OSNAP (a), RAPID (26.5°N; b) and SAMOC (34.5°S; c) sections. Linear trends (1970–2013) are marked on the right *y*-axis. Observational mean and standard deviation from annual means are indicated by error bars in the center of the respective observational time period. Note that the observations do not cover the same time period shown for the model. Panel (d) shows the detrended AMOC anomaly at the RAPID section, including the observed timeseries (orange).

referenced to the surface). A similar result is obtained for the RAPID section at 26.5°N, where observations show a mean transport of 17.7 Sv (2004–2014; McCarthy et al., 2015). The model transports range from 15.8 to 16.1 Sv in the three FOCI-ATLAS10 experiments and 13.7 Sv in OCO. During the RAPID period (2004–2013), transports in the model are lower compared to the full timeseries and range between 13 Sv in OCO and 15.3 Sv in PCPL-L. In the South Atlantic (South Atlantic Meridional Overturning Circulation (SAMOC) section at 34.5°S) the difference between FOCI-ATLAS10 and the ocean-only configuration is less pronounced. Still OCO simulates the weakest AMOC strength (14.1 Sv). PCPL-L (14.8 Sv), PCPL-H (15.8 Sv) and CPL (15.6 Sv) all simulate a stronger overturning. All these estimates are close to the observed value (14.7 Sv; 2009–2018; Meinen et al., 2018). Both, RAPID and SAMOC, transports are calculated in depth space, for a better comparison to the observations, as the maximum of the overturning stream function below 500 m. As noted before, the mean AMOC is not highly sensitive to the mean wind stress forcing. PCPL-H and PCPL-L differ by less than 1 Sv despite the very different mean gyre transports.

In summary, the strength of the AMOC in the fully coupled and the two partially coupled simulations is similar, while it is slightly weaker in the ocean-only experiment. OCO shows a spin-up behavior until approximately 1970. While the AMOC strength is comparable to the PCPL experiments right after initialization at OSNAP and RAPID, it strongly decreases over the first years, before it stabilizes. As for the gyre transports, trends are calculated from 1970 to 2013 to exclude this initial spin-up phase. Still, there is a significant negative trend (p-value <0.01) at the OSNAP section in all experiments, except OCO. It is strongest in PCPL-H (−0.9 Sv/10 yrs) and weaker in PCPL-L (−0.6 Sv/10 yrs) and CPL (−0.5 Sv/10 yrs). OCO shows an increase of 0.4 Sv/10 years (p-value = 0.01).

AMOC trends at the RAPID section have the same sign as the OSNAP trends, but are weaker in PCPL-L, PCPL-H and CPL. The negative trend is again stronger in PCPL-H than in PCPL-L (−0.3 Sv/10 years, p-value = 0.02) and CPL (−0.2 Sv/10 years, not significant) and could reflect a downstream propagation of the signal seen at the OSNAP section. In this case it may be expected that the stronger trend in PCPL-H at OSNAP leads to a stronger trend at RAPID. Consistently, a weak positive OSNAP trend in OCO coincides with no trend at the RAPID section. It is somewhat surprising that, in contrast to the gyre transports, the trend is slightly stronger in PCPL-H than in PCPL-L. This suggest that the lower mean wind stress does not significantly reduce the NA overturning within 50 years. In general the magnitude of the NA AMOC change in the (partially) coupled experiments is comparable to estimates of the coupled CMIP6 ensemble (Weijer et al., 2020). The AMOC differences between the decades 2004–2013 and 1975–1984 at 26.5°N are −1.8 Sv (PCPL-H), −0.9 Sv (CPL) and −0.5 (PCPL-L).

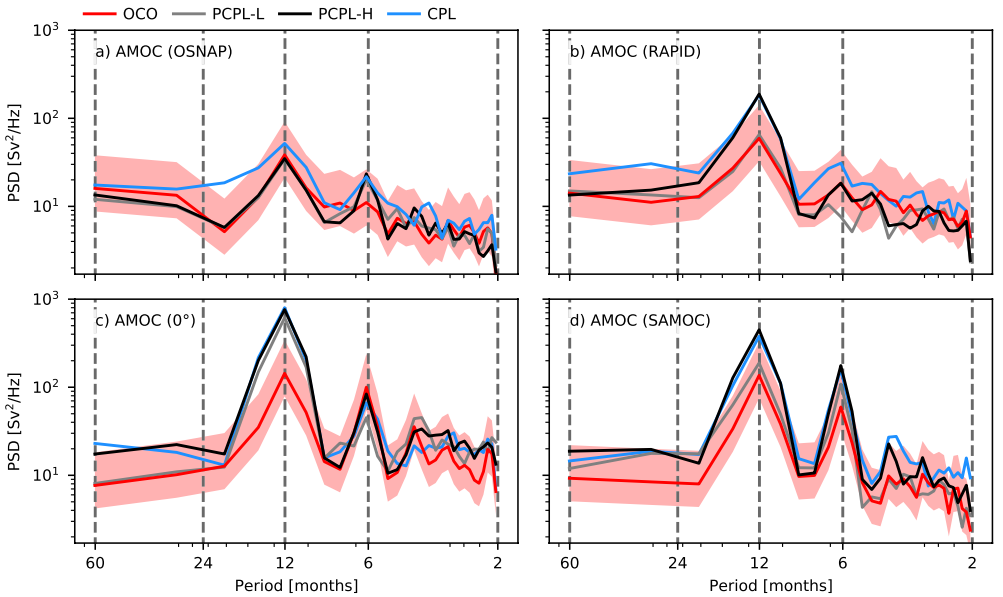

Figure 9. Power spectral density (PSD) of the Atlantic Meridional Overturning Circulation timeseries at OSNAP (a), RAPID (26.5°N; b), 0° (c) and SAMOC (34.5°S; d). Red shading shows the 95% confidence interval of the PSD estimate for OCO.

The CMIP6 ensemble shows a change between 0 and −4 Sv, with an ensemble mean of −1.2 Sv. This suggests that the trends in the (P)CPL experiments are a response to the atmospheric boundary conditions. To fully rule out that a model drift introduced by the partial coupling procedure exists, an additional set of experiments would be needed (e.g., a partially coupled experiment under pre-industrial atmospheric boundary conditions). However, based on the reasonable magnitude of the trends compared to the fully coupled experiment and other coupled models, we are confident that the AMOC in PCPL mode is not subject to significant model drift for the time period analyzed here. The different trends in OCO can be explained by various differences in the surface forcing compared to the (partially) coupled experiments, including the choices for the non-physical restoring term and the freshwater input provided by the forcing data set. Biastoch et al. (2021) showed that especially the AMOC trend is highly sensitive to small changes in the North Atlantic freshwater budget. They argue that a moderate negative AMOC trend after the 1990s is currently the best estimate, which would make the (P)CPL trends more realistic than the OCO trend.

At 34.5°S trends are close to zero and non-significant in PCPL-H/L and CPL. Only OCO still simulates a strongly negative trend with −0.4 Sv/10 years.

We investigate the variability of the AMOC in more detail by showing spectra of timeseries at 4 different latitudes (Figure 9). Additional to the already mentioned sections, we show the equatorial AMOC since it was shown to have distinct variability (Blaker et al., 2021). All following analysis is based on the period from 1970 to 2013 and the AMOC in z-coordinates, except for the overturning at OSNAP where density coordinates are used.

It is visible that the AMOC in CPL is most variable at all latitudes and on nearly all timescales. Still, on most timescales the difference between the experiments is not significant. In the North Atlantic, CPL simulates higher variability, especially at timescales longer than a year. At the equator both, CPL and PCPL-H simulate higher variability than OCO and PCPL-L, suggesting that the high variability could result from the higher mean wind stress. At the SAMOC section, only variability in CPL does not strongly decrease toward shorter timescales, causing the variability to be significantly higher than in all other experiments. The seasonal cycle at all latitudes is stronger in CPL than in OCO. Only at OSNAP it is also stronger than in PCPL-H, suggesting that it is not just determined by the magnitude of the wind stress' seasonal cycle (which is the same by construction due to the replaced climatology) in the SPNA. At the equator, the seasonal cycle is similarly strong in PCPL-H, PCPL-L and CPL. Here FOCI seems to exaggerate the seasonal cycle compared to the JRA55 reanalysis, independent of the

wind stress' seasonal cycle that is expected to be weaker in PCPL-L. At 34.5°S a pronounced semi-annual cycle exists in all simulations and also in observations (Meinen et al., 2018). A similar semi-annual cycle is present in all experiments at the equator. The strength of the semi-annual cycles is not systematically stronger/weaker in any of the configurations. While at SAMOC it is slightly more pronounced in (P)CPL than in OCO, the opposite is true at the equator. At OSNAP (P)CPL hints on a weak semi-annual cycle, but a similar peak is missing in OCO.

The overall higher variability of CPL compared to OCO could have different reasons. One is the stronger wind stress variability (likely dominant on short timescales) in CPL due to different strategies and formulae used to convert wind to wind stress. However, the difference on these timescale is very small except for mentioned difference at the SAMOC section. On timescales longer than a year the explicit simulation of feedbacks involving the wind forcing in CPL could cause higher variability. This seems to be important in the NA. PCPL excludes feedbacks that involve changes of the surface momentum transfer by prescribing the surface wind and shows lower variability with a magnitude comparable to OCO. In the SA this mechanisms seems to be less important, as variability in at least one PCPL experiment is similar to CPL.

Another interesting feature of the equatorial AMOC is a very strong increase of spectral power on timescales shorter than 1 month in agreement with Blaker et al. (2021). All experiments, including the partially coupled simulations, are able to simulate this high variability (not shown). This strong variability is also the reason to use the monthly mean AMOC here, since defining the AMOC strength based on 5-day means at the equator considerably changes the spectrum even on interannual timescales. A definition based on the monthly mean overturning stream function is more robust and representative for the strength of the NADW cell.

In conclusion, PCPL is able to retain the overall stable AMOC of the fully coupled simulation. Trends in the North Atlantic are similar in these experiments and possibly directly related to the applied historic atmospheric boundary conditions. This highlights the ability of PCPL to retain a stable AMOC, that is, maintain the important ocean-atmosphere feedbacks that were shown to be missing in forced experiments (e.g., Behrens et al., 2013), without the need to introduce an artificial modification of the surface water mass properties, or fluxes. Whether variability in PCPL mode is more similar to OCO or CPL depends on the latitude, timescale and mean wind stress of the PCPL forcing. In all cases differences are mostly non-significant. Thus, the magnitude of AMOC variability in PCPL mode is comparable to fully coupled and ocean-only experiments. In the next section we study, if PCPL is also able to reproduce the correct timing of this variability.

4. Timing of Variability

As exemplarily shown for FOCI-ATLAS10, coupled climate models are often able to simulate a realistic AMOC strength and magnitude of its variability. In order to study past AMOC changes, compare the model to observations and attribute extreme events to specific conditions, an ocean hindcast with the correct timing of variability is needed. This is generally not given in a coupled climate model and thus one of the main motivations to implement a partial coupling. Therefore, this section contains a detailed study of the timing of variability in the PCPL experiments.

First, we show the correlation between all experiments for the annual mean timeseries discussed before (time period 1970–2013). In order to study interannual variations, we remove low frequency variability from the timeseries by applying a 5-year highpass filter. This seems more reasonable than linear detrending, because linear detrending does not remove all low frequency variability.

Partial coupling does show skill to reproduce the timing of interannual variations of the SPG (Figure 10). The correlation between the SPG timeseries within the PCPL experiments (PCPL-L/PCPL-H) and between them and OCO is above 0.6 and significant based on a confidence level of 95%. Correlations for the NA STG are mostly insignificant, except for an anti-correlation between PCPL-L and OCO. The lack of correlation is probably a result of intrinsic, that is, unforced variability. The western branch of the NA STG gyre is characterized by strong mesoscale activity. Even different ocean-only simulations with the same forcing are not highly correlated in this region (not shown). The anti-correlation, although significant at 95%, is not expected to have a physical explanation. In contrast to the positive SPG correlations, it only occurs for one pair of experiments. For the SA STG we find a significant correlation of 0.4 between PCPL-H and OCO that could arise from the similar wind forcing. However, there is no correlation between PCPL-L and OCO, or PCPL-L and PCPL-H. The wind stress anomalies are derived from the same data set in all these experiments. This suggests that either the correlation

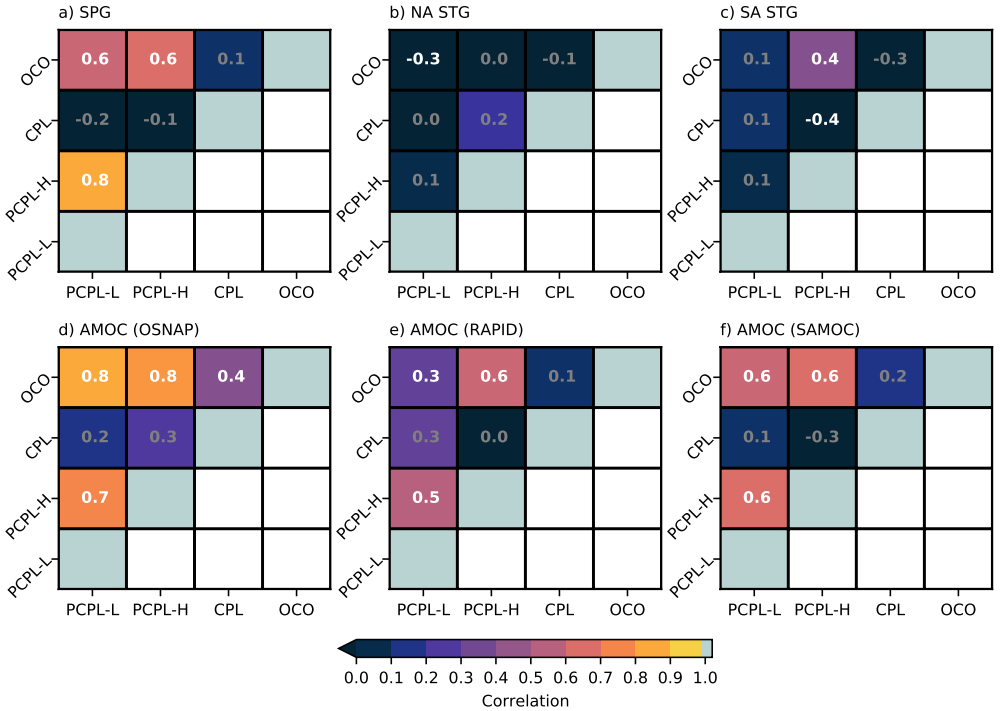

Figure 10. Correlation matrices for 5-year highpass filtered annual mean transport timeseries (1970–2013). (a) Subpolar Gyre, (b) North Atlantic Subtropical Gyre, (c) South Atlantic Subtropical Gyre, (d) Atlantic Meridional Overturning Circulation (AMOC) (OSNAP), (e) AMOC (RAPID; 26.5°N), (f) AMOC (SAMOC; 34.5°S). Correlations that are significant (not significant) based on a confidence level of 95% are displayed white (gray).

is significant by chance, or that the effect of wind variability is masked in PCPL-L. Note that mesoscale variability (SSH variance) is reduced in PCPL-L compared to PCPL-H, however, and probably not the cause here. A possible explanation is that the adjustment to the lower mean wind stress in PCPL-L has a non-linear impact on interannual variability (low frequency variability itself was removed by the filter before calculating the correlation). As expected, none of the gyre transports are significantly correlated between CPL and OCO. The high SPG correlation for both, PCPL-L and PCPL-H, but lack of robust STG correlation could be an expression of a stronger link between the gyre circulation and AMOC (discussed below). This is in line with Yeager (2020) reporting on a strong coupling of the density space AMOC and SPG transport variability.

For the AMOC, results are more robust across the different sections. Correlations between PCPL and OCO are significant and exceed 0.8 at OSNAP, 0.3 at RAPID and 0.6 at SAMOC. The correlations between PCPL-L and PCPL-H are similar to the correlations between PCPL (PCPL-H/PCPL-L) and OCO at the respective latitude. This gives confidence that the correlations are not just by chance, but indeed show an improved timing of variability in the PCPL experiments. Again CPL and OCO are uncorrelated, except for a positive correlation of 0.4 at the OSNAP section. CPL is not correlated to either PCPL experiment making it likely that this correlation is by chance.

An example for the ability of PCPL to simulate interannual variability of the AMOC is provided in Figure 8d. The strong minimum of the AMOC at 26.5°N in 2010 (McCarthy et al., 2012) is well reproduced in PCPL-L. The AMOC is rather stable until 2008, then drops by about 3 Sv and recovers to its previous strength by 2011 in PCPL-L and the RAPID observations. This result is in agreement with Thoma et al. (2015). PCPL-H and OCO simulate a similar temporal evolution, but underestimate the minimum. As a result, a secondary minimum in 2012 (which is also visible in observations) has nearly the same magnitude. The fully coupled (CPL) experiment does show a very different temporal evolution. Although the year 2010 shows a comparably weak AMOC transport, it does not stand out as clearly as in all other experiments and is most likely just co-incident.

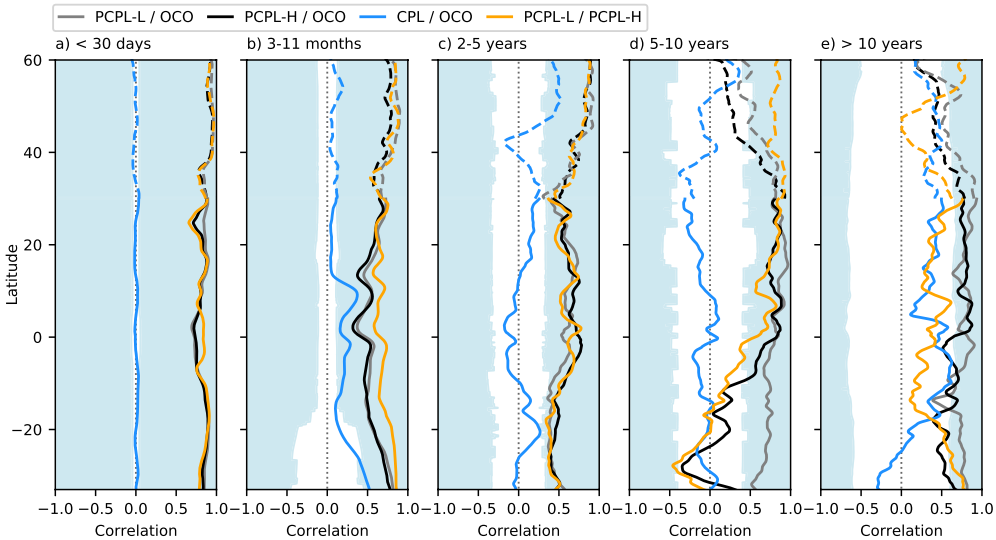

Figure 11. Correlation of the Atlantic Meridional Overturning Circulation (AMOC) transport in CPL / PCPL-L / PCPL-H, and OCO between 34°S and 60°N on different timescales. (a) high-frequency (30 days highpass filtered), (b) subannual (3–11 months bandpass filtered), (c) interannual (2–5 years bandpass filtered), (d) interannual—decadal (5–10 years bandpass filtered) and (e) decadal (10 years lowpass filtered and detrended) variability. Blue shading indicates correlation coefficients, that are statistically significant based on a confidence level of 95%. The meridional overturning stream function was smoothed with a 31 grid point (3°) boxcar filter before calculating the AMOC strength. South of 30°N the AMOC is calculated in depth space (solid), density coordinates are used further north (dashed). All timeseries start in 1970 and end half the filter time period prior to 2014.

So far we have only considered annual means, but the question remains whether PCPL is similarly successful in reproducing the timing of AMOC variability on shorter and longer timescales. Furthermore, the AMOC at specific latitudes may not be representative for the entire Atlantic and we expand our analysis to all latitudes between 34.5°S and 60°N. Here, the AMOC south of 30°N is defined as the maximum overturning stream function in depth space below 500 m. Since the subpolar North Atlantic overturning is more adequately represented in density coordinates (e.g., Lozier et al., 2019), we define the AMOC as the maximum overturning stream function in density space (potential density anomaly referenced to the surface) between 26.65 and 28 kg m^{-3} north of 30°N. All timeseries used for calculating correlations start in 1970 and end half the filtering time period prior to 2014.

It is clearly visible in Figure 11a that PCPL is capable of reproducing the correct timing of variability on short timescales (shorter than 1 month). The correlation between PCPL and OCO is around 0.8 at most latitudes. This very high correlation is likely a direct result of the wind-driven Ekman transport, shown to cause strong AMOC variability on short timescales (Cunningham et al., 2007). CPL, as expected, shows no significant correlation (95% confidence level). As mentioned before, significance levels are calculated based on a two-sided student *t*-test considering serial correlation by calculating effective degrees of freedom following Emery and Thomson (2001).

Note that we only define the AMOC strength using the 5-day mean overturning stream function to study the high frequency variability. For the following longer timescales we use monthly means, since they allow for a more robust estimate of the overturning strength close to the equator (see Section 3.3). Overall, the meridional structure of the correlation is similar for the subannual timescale (3–11 months; Figure 11b). The correlation between CPL and OCO is slightly higher, but mostly below 0.3. A considerable difference is an increase of the CPL/OCO correlation south of 20°S. As shown in Figure 9d, the AMOC shows a semi-annual cycle that is also visible in CPL. Therefore, not only the presence of this semi-annual cycle, but also its timing is reproduced in the fully coupled simulation to a certain extend. This suggests that the semi-annual cycle is a response to the atmospheric boundary conditions (e.g., solar radiation). Furthermore, a decrease in correlation to OCO between 30°N and 20°S with a minimum just north of the equator is visible for both, PCPL-L and PCPL-H. As the correlation between the two PCPL runs does not show this decrease, we suggest that differences in the representation of the equatorial circulation between the (partially-) coupled and un-coupled configurations could be the reason. The

corresponding currents span approximately the latitude range, where the correlation between PCPL and OCO differs most from the correlation between the two PCPL experiments.

On interannual timescales (2–5 years; Figure 11c), the correlation to OCO is significantly higher than zero at all latitudes in PCPL-L and PCPL-H. Thus, also on timescales longer than a year the assimilation of only wind stress anomalies can improve the timing of AMOC variability throughout the entire Atlantic. This result is in line with studies showing that the locally wind-driven Ekman transport also contributes to interannual variability (Blaker et al., 2015; McCarthy et al., 2012). Further, wind induced Ekman pumping and the resulting Sverdrup transport has an important impact on interannual AMOC variability (Duchez et al., 2014). The correlation decreases from values around 0.9 in the SPNA to 0.4 in the South Atlantic. This agrees with an increasing fraction of intrinsic interannual variability shown by Grégorio et al. (2015) and Leroux et al. (2018). In addition to this decrease toward the south, the correlation varies at individual sections. Just north of the southern tip of Africa there is local maximum in correlation that can explain the higher correlation at SAMOC than at RAPID seen before, especially for PCPL-L.

Even on interannual to decadal timescales (5–10 years; Figure 11d) the PCPL experiments show an improved timing of variability compared to CPL in the tropical and subtropical North Atlantic. PCPL-H and PCPL-L are both significantly correlated to OCO between the equator and 40°N. At subpolar latitudes the correlation between PCPL-H and OCO decreases to insignificant values north of 40°N. The PCPL-L/OCO correlation also decreases, but remains just at the margin of being significant, while the PCPL-L/PCPL-H correlation does not show a decrease. A possible explanation is an emerging impact of the upper ocean density, that was shown to be important for (multi-) decadal AMOC variability (Zhang et al., 2022). Although buoyancy fluxes are unconstrained in PCPL water mass properties are more similar between PCPL-H and PCPL-L than between the two experiments and OCO. This could lead to a similar AMOC response to the applied wind forcing in the two PCPL experiments. Differences between the experiments become visible south of the equator. While the PCPL-H/OCO correlation remains high to about 15°S and drops to insignificant values further south, the PCPL-L/OCO correlation remains high for the whole South Atlantic. At the same time the correlation between the two PCPL experiments strongly decreases and becomes negative south of 20°S. A possible explanation for the lower correlation at the southern boundary of the Atlantic is connected to the source of AMOC variability in the different experiments. While AMOC anomalies in the South Atlantic in PCPL-H seem to mostly enter the Atlantic from the south and spread toward the equator, such northward spreading anomalies are only visible in PCPL-L and OCO to about 25°S (not shown). North of this latitude anomalies spread predominantly southward in these experiments. The stronger and more northward penetrating anomalies generated in the Southern Ocean in PCPL-H, are likely connected to the strongly enhanced wind stress compared to OCO and PCPL-L. The stronger wind stress in PCPL-H drives more variable and deeper mixing in the Southern Ocean and could therefore enhance the production of bottom water that spreads northward into the Atlantic. Nevertheless, also PCPL-L shows enhanced Southern Ocean mixing compared to OCO, consistent with a slightly decreasing correlation south of 25°S.

On longer timescales (>10 years; Figure 11e), the two PCPL experiments are not correlated throughout most of the Atlantic. Still, both experiments are significantly correlated to OCO south of 40°N. Especially because the filtering period is long compared to the length of our timeseries and the magnitude of decadal variability is small in all experiments, the correlations between PCPL-H/L and OCO should be interpreted with caution here. Most studies identify the subpolar North Atlantic as the main source of decadal AMOC variability (e.g., Biastoch et al., 2008; Jackson et al., 2022; Megann et al., 2021; Robson et al., 2012). Although the buoyancy fluxes in PCPL mode are not constraint by observations, atmospheric teleconnections to the Pacific (where heat flux variability is fairly well reproduced in the equatorial region), or an accumulated effect of the improved timing of AMOC variability on interannual timescales, could also influence the North Atlantic buoyancy forcing. However, none of our analysis supports such a hypothesis. We have already shown in Section 2.4 that the timing of the annual mean buoyancy forcing in the Atlantic is not significantly changed by partial coupling. Acknowledging that fluxes in different seasons may have a different impact on AMOC variability, we repeat our analysis for the northern hemisphere winter (DJF) heat flux, but do not find major differences. The variability in winter is higher in CPL than in all other experiments, but the correlation is still insignificant between PCPL-L/H and OCO, not only on interannual, but also on decadal timescales (Figure S3 in Supporting Information S1). Furthermore, the zonal mean heat flux could not be representative for the heat flux in specific AMOC key regions. We also calculated correlations for the Labrador, Irminger and southern Nordic Seas heat fluxes. Especially buoyancy (mainly heat) fluxes in the first two regions were identified by Megann et al. (2021) to impact decadal AMOC variability.

Again, a significant correlation is not found between any of our experiments (except for PCPL-L and PCPL-H in the Nordic Seas on decadal timescales). Furthermore, the correlations only being significant south of 40°N makes the North Atlantic an even more unlikely source of the AMOC correlation between the PCPL experiments and OCO. Thus, assuming the correlations reflect a physical mechanism, the only possible explanation is an impact of low frequency variability of the wind stress itself via changes in the Ekman or Sverdrup transports. We do find decadal variability of the Sverdrup transport, derived from the JRA55-do forcing data set to match the AMOC evolution in PCPL-L/H and OCO at the RAPID and SAMOC sections (Figure S4 in Supporting Information S1). Note that decadal wind stress variability in all these experiment is the same by construction. There is a striking similarity between the Sverdrup and AMOC transports in PCPL-L and OCO (correlations exceed 0.7 at both sections). The correlation is similarly high in PCPL-H at the SAMOC section, but slightly lower and not significant at the RAPID section (0.5). Still there is a high agreement (and correlation) before the late 1990s. Note that a positive (negative) anomaly of the Sverdrup transport is associated with a stronger Sverdrup gyre in the northern (southern) hemisphere. Thus a spin-up of the gyre is associated with a spin-down of the AMOC in the northern hemisphere, which matches observations and other models (McCarthy et al., 2012; Yeager, 2015). In the southern hemisphere, however, the AMOC transport increases together with the Sverdrup gyre transport. We do find hints on anti-correlations (correlations) of the decadal gyre (estimated as described in Section 3.2) and AMOC transports in the northern (southern) hemisphere, but most of them are insignificant. It is likely that the aforementioned impact of mesoscale variability on our gyre estimate also masks the wind stress curl driven signals on longer timescale. The timeseries in Figure S4 in Supporting Information S1 further reveal, why in the mid-latitude North Atlantic the AMOC in PCPL-H and PCPL-L are significantly correlated to OCO, but not to each other. PCPL-L resembles the variability in OCO better than PCPL-H before the 2000s, while PCPL-H is more successful after 2000. Decadal Ekman transport anomalies are also significantly correlated with the AMOC transport, but their magnitude is negligible compared to the Sverdrup transport. Based on these results, we hypothesize that low frequency variability in mid-latitudes winds can force low frequency AMOC variability. In experiments with stronger buoyancy driven decadal variability in the SPNA, however, this is likely masked. It is interesting to note that a similar high correlation between the AMOC and Sverdrup transport can not be seen in CPL (not shown). It is beyond the scope of this study to make a conclusive statement on the impact of low frequency wind forcing on the AMOC, since a large set of longer sensitivity experiments would be required.

We conclude that a correct timing of AMOC variability in PCPL mode is robust on interannual and shorter timescales. On interannual-decadal timescales the correlation depends on the latitude and seems to be sensitive to the mean Southern Ocean wind stress in the SA and water mass properties in the NA. A model with smaller biases than FOCI[-ATLAS10] in those regions could be more successful in reproducing the timing of interannual-decadal variability. It is unlikely that partial coupling is able to reliably reproduce the timing of decadal AMOC variability. The timing of the buoyancy (heat and freshwater) flux variability is not in agreement with the ocean-only simulation. There could be an additional impact of low frequency wind driven variability on the AMOC that is reproduced in PCPL mode, but only apparent in the absence of strong buoyancy driven AMOC variability in the North Atlantic.

5. Summary and Conclusion

With this study we aim at improving ocean hindcast simulations by applying a technique known as partial coupling in an eddying coupled climate model, showing its capabilities and limitations and help to identify possible use cases. Furthermore, our study reveals important aspects of the impact of wind forcing on AMOC variability on different timescales. We motivated our research by asking the following questions:

Do PCPL experiments simulate a realistic mean large-scale circulation and multi-decadal trends?

The nested ATLAS10 configuration is able to simulate a realistic mean gyre circulation in the ocean-only, fully coupled and partially coupled set-ups. The mean gyre transports are mostly determined by the mean wind stress curl and thus depend on the exact procedure used to convert 10 m wind from reanalysis and the model to wind stress. Here we compare two partially coupled experiments, with different mean wind stress. While PCPL-L uses a mean wind stress similar to the ocean-only experiment, PCPL-H is designed to match the fully coupled configuration as close as possible. The disadvantage of the former is a short secondary spin-up phase when switching to PCPL mode and possible long term model drift. This is clearly visible in the gyre transports (especially the SPG transport), but the AMOC is less affected within 56 years after initialization. The higher mean wind stress

of PCPL-H minimizes an initialization shock, but is no longer comparable to the mean wind stress applied in the ocean-only reference experiment.

The magnitude of interannual transport variability is not systematically affected by partial coupling. Mesoscale activity, as an important part of the horizontal circulation, is also reasonably well represented at 1/10° resolution in many regions. CPL and both PCPL experiments simulate a too narrow Agulhas Ring path, which is a result of the coarse atmospheric resolution and additionally, the application of absolute wind in PCPL mode (compare Schwarzkopf et al., 2019).

The mean structure and strength of the AMOC is very similar in the CPL and PCPL experiments, but slightly weaker in the ocean-only configuration. Still, the NADW cell reaches deeper in OCO, probably caused by less formation of Antarctic Bottom Water. It is likely that substantial differences in the surface boundary conditions between forced and coupled set-ups have an important contribution to the weaker transport in OCO. It was shown that mean heat, freshwater and momentum fluxes differ compared to the (partially-) coupled FOCI-ATLAS10 experiments. Also differences outside the nest area, for example, in the Arctic Ocean, are likely to contribute (Biastoch et al., 2021). The mean AMOC strength is found to be weakly sensitive to the mean wind stress forcing and resulting mean gyre transports. The mean AMOC strength in PCPL-H and PCPL-L differs by less than 0.5 Sv in the SPNA and is also similar to the transport in CPL, despite SPG transports differing by several Sverdrups. In the subtropical Atlantic, between approximately 30°S and 30°N, the AMOC is stronger in PCPL-L, with differences below 1 Sv at most latitudes. At least in the northern hemisphere, this is consistent with the dynamic coupling of the NA STG and the AMOC. As described by Yeager (2015) and supported by Section 4, the NA STG and AMOC response to wind stress curl changes are of opposite sign. In PCPL-L the initial reduction in wind stress (curl) drives a decreasing NA STG transport and possibly results in a stronger mean AMOC compared to PCPL-H and CPL. At the SAMOC section the AMOC is about 1 Sv weaker in PCPL-L than in PCPL-H, possibly a direct response to the weaker southern hemisphere westerlies.

AMOC variability at the latitudes considered here is largest in CPL on most timescales, due to a higher wind stress (variability) and the explicit simulation of feedbacks that involve surface momentum fluxes. The latter seems to be more important in the North Atlantic. Dependent on latitude and timescale, PCPL-H is closer to OCO than to CPL, or vice versa. PCPL-L is more comparable to OCO on all timescales, except for the equatorial seasonal cycle. Because PCPL-H, PCPL-L and CPL all show nearly the same power at annual periods, the strong seasonal cycle is rather related to differences in the heat and freshwater flux variability in FOCI than to wind stress.

PCPL shows promising results to simulate reasonable long term trends, meaning trends are related to the applied surface forcing rather than model drift. Unrealistic large downward trends in the gyre transports, especially in the SPNA, are visible in PCPL-L, but can be eliminated by keeping the mean wind stress of the fully coupled configuration (depicted by PCPL-H). AMOC trends at OSNAP and RAPID are slightly stronger in PCPL-H than PCPL-L, but the RAPID trends in both experiments are comparable to trends in CPL and the CMIP6 ensemble (Weijer et al., 2020), suggesting that the historic atmospheric boundary conditions (e.g., rising greenhouse gas concentrations) are responsible for a weakened AMOC after the 1970s. As already argued above, the gyre and AMOC response to a reduction in wind stress curl is of opposite sign in the subtropics according to Yeager (2015). At least for the RAPID section, their results are consistent with a weaker declining trend in PCPL-L. Therefore, various local and remote processes contribute to the magnitude of the trend at the considered latitudes and we can not fully prove that partial coupling does not introduce a long term model drift. Still, our results strongly suggest that important ocean-atmosphere feedbacks are still maintained in PCPL mode. This is a success, since it shows that partial coupling allows to omit the SSS restoring necessary to obtain a stable AMOC in the ocean-only set-up.

Is the correct timing of (AMOC) variability in PCPL experiments limited to certain latitudes, or timescales?

In addition to a realistic mean circulation and long term evolution, an ocean hindcast should be characterized by the correct timing of variability on the timescale of interest. Thoma et al. (2015) already showed the success of partial coupling for interannual AMOC variability at 26.5°N. We were able to confirm this result in an eddying model configuration and to systematically study the limitations of partial coupling on various timescales and throughout the whole Atlantic Ocean, not only for the sake of model development, but also to gain insight into

the impact of wind forcing on AMOC variability. Our results are based on a comparison between the partially coupled and ocean-only experiments.

Overall, partial coupling is able to simulate the correct timing of AMOC variability on timescales from submonthly to interannual (periods shorter than approximately 5 years) independent of the procedure used to generate the anomaly forcing. The correlation between the PCPL experiments and OCO are mostly higher than 0.6 and significantly different from 0 at all latitudes. This result matches and confirms the current knowledge of processes contributing to AMOC variability on these timescales. Variability on short timescales was shown to be dominated by the wind-driven Ekman transport (Cunningham et al., 2007). Also on interannual timescales wind-forcing was shown to be the major driver for AMOC variability (Biastoch et al., 2008; Zhao & Johns, 2014). The latitudinal dependence, with higher correlations in the North Atlantic, is consistent with an increasing fraction of intrinsic variability (i.e., variability not related to the applied surface forcing) in the South Atlantic. Grégorio et al. (2015) derive a ratio of intrinsic to total interannual AMOC variance close to zero north of 45°N and up to 45% at 30°S. A similar dependency of intrinsic AMOC variability on the latitude was obtained by Leroux et al. (2018).

The strong impact of wind forcing does extend to interannual—decadal variability, but our results suggest that the upper ocean density becomes increasingly important in the subpolar North Atlantic. This hypothesis is based on results of Zhang et al. (2022) and the higher correlation between PCPL-H and PCPL-L compared to the correlation to OCO. As water mass properties in PCPL-H and PCPL-L are much more similar, the NA AMOC response to the same wind stress anomalies could be more similar as well. In the Southern Ocean the stronger mean wind stress in PCPL-H generates stronger AMOC anomalies, possibly connected to deep mixing events north of the ice edge. These anomalies penetrate further north into the SA than anomalies of Southern Ocean origin in PCPL-L and OCO at periods between 5 and 10 years. This causes the PCPL-H/OCO and PCPL-H/PCPL-L correlations to drop in the southern hemisphere on this timescale.

On timescales longer than 10 years the correlation between PCPL and OCO depends on the latitude. PCPL-L/H and OCO are significantly correlated south of 40°N. Most studies find buoyancy driven processes to dominate AMOC variability on decadal timescales (e.g., Biastoch et al., 2008; Jackson et al., 2022; Megann et al., 2021; Robson et al., 2012). Buoyancy fluxes are unconstrained in PCPL mode and there is no correlation between the PCPL and ocean-only experiments on interannual, or decadal, timescales. Therefore, it is unlikely that the mentioned AMOC correlation is caused by a feedback of interannual ocean variability driven by the wind stress on the low frequency buoyancy forcing. Instead, the correlation is more likely explained by an AMOC response to low frequency wind variability via changes in the Sverdrup transport. This is not necessarily in contradiction to the aforementioned studies highlighting the impact of buoyancy driven variability. All experiments, including OCO, simulate little decadal variability, suggesting that the impact of the SPNA heat flux variability is underestimated. In experiments with strong decadal variability of the SPNA overturning, we expect these processes to mask the wind contribution.

Our timeseries are not long enough to study variability on interdecadal timescales. Based on the results of Eden and Jung (2001), showing that the NA interdecadal (periods around 30 years) circulation variability is caused by the oceans response to NAO heat flux forcing, it is unlikely that PCPL is able to simulate the correct timing. Still, the AMV was shown to have an improved timing in PCPL simulations and an improved timing of multidecadal variability in the Pacific (PDO) may impact the Atlantic via teleconnections on longer timescales (Thoma et al., 2015).

Apart from the integrative quantity of the AMOC, other circulation metrics are less strongly correlated in PCPL and OCO. For the gyre estimates intrinsic (i.e., unforced) mesoscale variability of the eddying model seems to have a large impact. The same is true for individual currents, such as the Florida Strait transport, although we did not include the analysis here. Only the SPG is significantly correlated, which hints on a strong connection to the AMOC in agreement with Yeager (2020). Due to the computational cost of the eddying resolution, our experiments are limited to a single model run. Although our main conclusions are not expected to change, the spread of a partially coupled ensemble on different timescales could reveal more information about the robustness of the timing of AMOC variability in PCPL mode. At the same time, an ensemble at eddying resolution is often not feasible and thus the ability of a single run to reproduce the timing of variability studied here is highly relevant.

In summary, a main motivation to study partial coupling is the reduction of arbitrary choices in the surface boundary condition calculation of an ocean-only experiment. At the same time, the correct timing of ocean

circulation variability in such forced simulations should be retained as good as possible, which is not given in fully coupled experiments. Our results show that PCPL can achieve the first goal. Both PCPL experiments simulate a stable AMOC with trends comparable to the fully coupled experiment. Further, the magnitude and timing of AMOC variability on timescales shorter than 5 years is well reproduced. Although we find an AMOC correlation between PCPL and OCO outside subpolar latitudes caused by low frequency wind variability, we do not find any hints that partial coupling does impact the timing of buoyancy flux variability in the North Atlantic. As a result, a single PCPL experiment can not be expected to reproduce the timing of decadal AMOC variability, limiting its applicability for the use case of hindcast simulations. However, the correct timing of AMOC variability on short and interannual timescales, together with a stable AMOC over multiple decades, can be useful for all studies focusing on sub-decadal processes. Note that the (partially) coupled configuration is only marginally more computational expensive than the ocean-only configuration, if run with a coarse atmospheric resolution. For a new configuration that is to be used to study interannual AMOC variability, it can be advantageous to use a partially coupled model. It avoids several arbitrary choices, not only restoring and budget corrections, but also details of the runoff interpolation that is typically not provided on the model grid.

There are many more use cases in sensitivity experiments that focus on specific processes, rather than reproducing past ocean variability in general. As presented here, PCPL is useful to assess the impact of wind forcing on the AMOC. In addition, PCPL allows to infer the ocean's dynamical role in driving atmospheric variability. As an example, the 2009/2010 minimum of the AMOC is expected to have changed the ocean heat transport (McCarthy et al., 2012) and could have fed back to the atmosphere. PCPL allows to study, whether the AMOC downturn did change the atmospheric circulation and contributed to the strongly negative winter NAO phase in the winters of 2009/2010 and 2010/2011 (Buchan et al., 2014). This would not be possible in a fully coupled configuration, since it is not expected to reproduce the same AMOC minimum. Neither it could be studied in an ocean-only set-up, because the atmospheric state is prescribed. An application of PCPL in ocean modeling could focus on linkages between the AMOC and SPG transports, since the timing of both is very well reproduced in PCPL. By prescribing different wind patterns in a coupled model it is possible to investigate the nature of this linkage, without altering the response by also prescribing heat and freshwater fluxes. Furthermore, the good performance of PCPL in the tropical Pacific and hints on an improved timing of buoyancy flux variability in the tropical Atlantic could be interesting for studies on teleconnections between the two ocean basins in tropical latitudes.

The capabilities identified here make partial coupling an interesting addition to ocean-only and coupled models as discussed above. At the same time, it was not possible to make conclusive statements about the timing of decadal variability in partially coupled models that would be needed for the application in hindcast simulations. This may provide further motivation to expand our analysis and investigate modifications to the partial coupling procedure in order to perform successful ocean hindcasts in earth system models.

Data Availability Statement

All data shown in the figures, scripts, model name lists and essential model input is publicly available (Schulzki et al., 2022) at: https://hdl.handle.net/20.500.12085/57ea9d04-2bd4-4a27-8994-3e19982731bd. The Ssalto/Duacs altimeter products (Taburet & Pujol, 2022) were produced and distributed by the Copernicus Marine and Environment Monitoring Service (CMEMS), https://marine.copernicus.eu/. OSNAP data (Li et al., 2021) were collected and made freely available by the OSNAP (Overturning in the Subpolar North Atlantic Program) project and all the national programs that contribute to it (www.o-snap.org). Data from the RAPID AMOC monitoring project (Frajka-Williams et al., 2021) is funded by the Natural Environment Research Council and are freely available from www.rapid.ac.uk/rapidmoc.

Acknowledgments
The authors gratefully acknowledge the Earth System Modelling Project (ESM) for funding this work by providing computing time on the ESM partition of the supercomputer JUWELS (Jülich Supercomputing Centre, 2019) at the Jülich Supercomputing Centre (JSC). The study was supported by the European Union's Horizon 2020 research and innovation programme under grant agreement No. 818123 (iAtlantic). We thank 3 anonymous reviewers for their many constructive comments and helpful suggestions during the review process which helped to improve our manuscript.

References

Amante, C., & Eakins, B. (2009). ETOPO1 1 arc-minute global relief model: Procedures. *NOAA Technical Memorandum NESDIS. NGDC-24*. https://doi.org/10.7289/V5C8276M

Arakawa, A., & Hsu, Y.-J. G. (1990). Energy conserving and potential-enstrophy dissipating schemes for the shallow water equations. *Monthly Weather Review*, *118*(10), 1960–1969. https://doi.org/10.1175/1520-0493(1990)118⟨1960:ECAPED⟩2.0.CO;2

Barnier, B., Madec, G., Penduff, T., Molines, J.-M., Treguier, A.-M., Le Sommer, J., et al. (2006). Impact of partial steps and momentum advection schemes in a global ocean circulation model at eddy-permitting resolution. *Ocean Dynamics*, *56*(5), 543–567. https://doi.org/10.1007/s10236-006-0082-1

Behrens, E., Biastoch, A., & Böning, C. W. (2013). Spurious AMOC trends in global ocean sea-ice models related to subarctic freshwater forcing. *Ocean Modelling*, *69*, 39–49. https://doi.org/10.1016/j.ocemod.2013.05.004

Biastoch, A., Böning, C. W., Getzlaff, J., Molines, J.-M., & Madec, G. (2008). Causes of interannual–decadal variability in the meridional overturning circulation of the midlatitude North Atlantic Ocean. *Journal of Climate*, *21*(24), 6599–6615. https://doi.org/10.1175/2008JCLI2404.1

Biastoch, A., Schwarzkopf, F. U., Getzlaff, K., Rühs, S., Martin, T., Scheinert, M., et al. (2021). Regional imprints of changes in the Atlantic Meridional Overturning Circulation in the eddy-rich ocean model VIKING20X. *Ocean Science*, *17*(5), 1177–1211. https://doi.org/10.5194/os-17-1177-2021

Blaker, A. T., Hirschi, J. J.-M., Bell, M. J., & Bokota, A. (2021). Wind-driven oscillations in the meridional overturning circulation near the equator. Part I: Numerical models. *Journal of Physical Oceanography*, *51*(3), 645–661. https://doi.org/10.1175/JPO-D-19-0296.1

Blaker, A. T., Hirschi, J. J.-M., McCarthy, G., Sinha, B., Taws, S., Marsh, R., et al. (2015). Historical analogues of the recent extreme minima observed in the Atlantic Meridional Overturning Circulation at 26°N. *Climate Dynamics*, *44*(1), 457–473. https://doi.org/10.1007/s00382-014-2274-6

Blanke, B., & Delecluse, P. (1993). Variability of the tropical Atlantic Ocean simulated by a general circulation model with two different mixed-layer physics. *Journal of Physical Oceanography*, *23*(7), 1363–1388. https://doi.org/10.1175/1520-0485(1993)023⟨1363:VOTTAO⟩2.0.CO;2

Bougeault, P., & Lacarrere, P. (1989). Parameterization of Orography-induced turbulence in a Mesobeta–scale model. *Monthly Weather Review*, *117*(8), 1872–1890. https://doi.org/10.1175/1520-0493(1989)117⟨1872:POOITI⟩2.0.CO;2

Brovkin, V., Raddatz, T., Reick, C. H., Claussen, M., & Gayler, V. (2009). Global biogeophysical interactions between forest and climate. *Geophysical Research Letters*, *36*(7). https://doi.org/10.1029/2009GL037543

Buchan, J., Hirschi, J. J.-M., Blaker, A. T., & Sinha, B. (2014). North Atlantic SST anomalies and the Cold North European weather events of winter 2009/10 and December 2010. *Monthly Weather Review*, *142*(2), 922–932. https://doi.org/10.1175/MWR-D-13-00104.1

Cerovečki, I., Talley, L. D., & Mazloff, M. R. (2011). A comparison of Southern Ocean air–sea buoyancy flux from an ocean state estimate with five other products. *Journal of Climate*, *24*(24), 6283–6306. https://doi.org/10.1175/2011JCLI3858.1

Chelton, D. B., Schlax, M. G., & Samelson, R. M. (2011). Global observations of nonlinear mesoscale eddies. *Progress in Oceanography*, *91*(2), 167–216. https://doi.org/10.1016/j.pocean.2011.01.002

Cheng, W., Chiang, J. C. H., & Zhang, D. (2013). Atlantic Meridional Overturning Circulation (AMOC) in CMIP5 models: RCP and historical simulations. *Journal of Climate*, *26*(18), 7187–7197. https://doi.org/10.1175/JCLI-D-12-00496.1

Cunningham, S. A., Kanzow, T., Rayner, D., Baringer, M. O., Johns, W. E., Marotzke, J., et al. (2007). Temporal variability of the Atlantic Meridional Overturning Circulation at 26.5°N. *Science*, *317*(5840), 935–938. https://doi.org/10.1126/science.1141304

Danabasoglu, G., Yeager, S. G., Bailey, D., Behrens, E., Bentsen, M., Bi, D., et al. (2014). North Atlantic simulations in coordinated ocean-ice reference experiments phase II (CORE-II). Part I: Mean states. *Ocean Modelling*, *73*, 76–107. https://doi.org/10.1016/j.ocemod.2013.10.005

Debreu, L., Vouland, C., & Blayo, E. (2008). AGRIF: Adaptive grid refinement in Fortran. *Computers & Geosciences*, *34*(1), 8–13. https://doi.org/10.1016/j.cageo.2007.01.009

Ding, H., Greatbatch, R. J., Latif, M., Park, W., & Gerdes, R. (2013). Hindcast of the 1976/77 and 1998/99 climate shifts in the Pacific. *Journal of Climate*, *26*(19), 7650–7661. https://doi.org/10.1175/JCLI-D-12-00626.1

Duchez, A., Hirschi, J. J.-M., Cunningham, S. A., Blaker, A. T., Bryden, H. L., de Cuevas, B., et al. (2014). A new index for the Atlantic Meridional Overturning Circulation at 26°N. *Journal of Climate*, *27*(17), 6439–6455. https://doi.org/10.1175/JCLI-D-13-00052.1

Eden, C., & Jung, T. (2001). North Atlantic interdecadal variability: Oceanic response to the North Atlantic Oscillation (1865–1997). *Journal of Climate*, *14*(5), 676–691. https://doi.org/10.1175/1520-0442(2001)014⟨0676:NAIVOR⟩2.0.CO;2

Emery, W. J., & Thomson, R. E. (2001). Chapter 5—Time-series analysis methods. In W. J. Emery & R. E. Thomson (Eds.), *Data analysis methods in physical oceanography* (pp. 371–567). Elsevier Science. https://doi.org/10.1016/B978-044450756-3/50006-X

Farrow, D. E., & Stevens, D. P. (1995). A new tracer advection scheme for bryan and Cox type ocean general circulation models. *Journal of Physical Oceanography*, *25*(7), 1731–1741. https://doi.org/10.1175/1520-0485(1995)025⟨1731:ANTASF⟩2.0.CO;2

Fichefet, T., & Maqueda, M. A. M. (1997). Sensitivity of a global sea ice model to the treatment of ice thermodynamics and dynamics. *Journal of Geophysical Research*, *102*(C6), 12609–12646. https://doi.org/10.1029/97JC00480

Flato, G., Marotzke, J., Abiodun, B., Braconnot, P., Chou, S. C., Collins, W., et al. (Eds.). Climate change 2013: The physical science basis. Contribution of working group I to the fifth assessment report of the intergovernmental panel on climate change (pp. 741–882). Cambridge University Press. https://doi.org/10.1017/CBO9781107415324.020

Frajka-Williams, E., Moat, B., Smeed, D., Rayner, D., Johns, W., Baringer, M., et al. (2021). Atlantic Meridional Overturning Circulation observed by the RAPID-MOCHA-WBTS (RAPID-Meridional overturning circulation and heatflux array-western boundary time series) array at 26N from 2004 to 2020 (v2020.1) [Dataset]. NERC EDS British Oceanographic Data Centre NOC. https://doi.org/10.5285/cc1e34b3-3385-662b-e053-6c86abc03444

Gent, P. R., & Mcwilliams, J. C. (1990). Isopycnal mixing in ocean circulation models. *Journal of Physical Oceanography*, *20*(1), 150–155. https://doi.org/10.1175/1520-0485(1990)020⟨0150:IMIOCM⟩2.0.CO;2

Grégorio, S., Penduff, T., Sérazin, G., Molines, J.-M., Barnier, B., & Hirschi, J. (2015). Intrinsic variability of the Atlantic Meridional Overturning Circulation at interannual-to-multidecadal time scales. *Journal of Physical Oceanography*, *45*(7), 1929–1946. https://doi.org/10.1175/JPO-D-14-0163.1

Griffies, S. M., Biastoch, A., Böning, C., Bryan, F., Danabasoglu, G., Chassignet, E. P., et al. (2009). Coordinated Ocean-Ice reference experiments (COREs). *Ocean Modelling*, *26*(1), 1–46. https://doi.org/10.1016/j.ocemod.2008.08.007

Hallberg, R., & Gnanadesikan, A. (2006). The role of eddies in determining the structure and response of the wind-driven southern hemisphere overturning: Results from the modeling eddies in the Southern Ocean (MESO) project. *Journal of Physical Oceanography*, *36*(12), 2232–2252. https://doi.org/10.1175/JPO2980.1

Hirschi, J. J.-M., Barnier, B., Böning, C., Biastoch, A., Blaker, A. T., Coward, A., et al. (2020). The Atlantic Meridional Overturning Circulation in high-resolution models. *Journal of Geophysical Research: Oceans*, *125*(4), e2019JC015522. https://doi.org/10.1029/2019JC015522

Jackson, L. C., Biastoch, A., Buckley, M. W., Desbruyères, D. G., Frajka-Williams, E., Moat, B., & Robson, J. (2022). The evolution of the North Atlantic Meridional Overturning Circulation since 1980. *Nature Reviews Earth & Environment*, *3*(4), 241–254. https://doi.org/10.1038/s43017-022-00263-2

Jülich Supercomputing Centre. (2019). JUWELS: Modular tier-0/1 supercomputer at the Jülich supercomputing centre. *Journal of Large-Scale Research Facilities*, *5*(A135). https://doi.org/10.17815/jlsrf-5-171

Large, W. G., & Yeager, S. G. (2009). The global climatology of an interannually varying air–sea flux data set. *Climate Dynamics*, *33*(2), 341–364. https://doi.org/10.1007/s00382-008-0441-3

Lemarié, F. (2006). NEMO/AGRIF nesting tools, User's Guide (30 January 2006). Retrieved from https://forge.ipsl.jussieu.fr/nemo/wiki/Users/SetupNewConfiguration/AGRIF-nesting-tool

Leroux, S., Penduff, T., Bessières, L., Molines, J.-M., Brankart, J.-M., Sérazin, G., et al. (2018). Intrinsic and atmospherically forced variability of the AMOC: Insights from a large-ensemble ocean hindcast. *Journal of Climate*, *31*(3), 1183–1203. https://doi.org/10.1175/JCLI-D-17-0168.1

Li, F., Lozier, M. S., Bacon, S., Bower, A., Cunningham, S., de Jong, M., et al. (2021). Meridional overturning circulation observed by the OSNAP (overturning in the Subpolar North Atlantic program) array from August 2014 to May 2018 [Dataset]. Georgia Institute of Technology. https://doi.org/10.35090/gatech/65537

Locarnini, R. A., Mishonov, A. V., Antonov, J. I., Boyer, T. P., Garcia, H. E., Baranova, O. K., et al. (2013). World Ocean Atlas 2013, volume 1: Temperature (Technical Report No. NOAA Atlas NESDIS 73).

Louis, J.-F. (1979). A parametric model of vertical eddy fluxes in the atmosphere. *Boundary-Layer Meteorology*, *17*(2), 187–202. https://doi.org/10.1007/BF00117978

Lozier, M. S. (2012). Overturning in the North Atlantic. *Annual Review of Marine Science*, *4*(1), 291–315. https://doi.org/10.1146/annurev-marine-120710-100740

Lozier, M. S., Li, F., Bacon, S., Bahr, F., Bower, A. S., Cunningham, S. A., et al. (2019). A sea change in our view of overturning in the subpolar North Atlantic. *Science*, *363*(6426), 516–521. https://doi.org/10.1126/science.aau6592

Madec, G. (2016). *NEMO ocean engine*. Note du Pole de modelisation, Institut Pierre-Simon Laplace (IPSL), France. No 27, ISSN No 1288-1619.

Martin, T. (2021). Runoff remapping for ocean model forcing. https://doi.org/10.3289/SW_2_2021

Matthes, K., Biastoch, A., Wahl, S., Harlaß, J., Martin, T., Brücher, T., et al. (2020). The flexible ocean and climate infrastructure version 1 (FOCI1): Mean state and variability. *Geoscientific Model Development Discussions*, *2020*, 1–53. https://doi.org/10.5194/gmd-2019-306

McCarthy, G., Frajka-Williams, E., Johns, W. E., Baringer, M. O., Meinen, C. S., Bryden, H. L., et al. (2012). Observed interannual variability of the Atlantic Meridional Overturning Circulation at 26.5°N. *Geophysical Research Letters*, *39*(19). https://doi.org/10.1029/2012GL052933

McCarthy, G., Smeed, D., Johns, W., Frajka-Williams, E., Moat, B., Rayner, D., et al. (2015). Measuring the Atlantic Meridional Overturning Circulation at 26°N. *Progress in Oceanography*, *130*, 91–111. https://doi.org/10.1016/j.pocean.2014.10.006

Meccia, V. L., Iovino, D., & Bellucci, A. (2021). North Atlantic gyre circulation in PRIMAVERA models. *Climate Dynamics*, *56*(11), 4075–4090. https://doi.org/10.1007/s00382-021-05686-z

Megann, A., Blaker, A., Josey, S., New, A., & Sinha, B. (2021). Mechanisms for late 20th and early 21st century decadal AMOC variability. *Journal of Geophysical Research: Oceans*, *126*(12), e2021JC017865. https://doi.org/10.1029/2021JC017865

Meinen, C. S., Speich, S., Piola, A. R., Ansorge, I., Campos, E., Kersalé, M., et al. (2018). Meridional overturning circulation transport variability at 34.5°S during 2009–2017: Baroclinic and barotropic flows and the dueling influence of the boundaries. *Geophysical Research Letters*, *45*(9), 4180–4188. https://doi.org/10.1029/2018GL077408

Meinshausen, M., Vogel, E., Nauels, A., Lorbacher, K., Meinshausen, N., Etheridge, D. M., et al. (2017). Historical greenhouse gas concentrations for climate modelling (CMIP6). *Geoscientific Model Development*, *10*(5), 2057–2116. https://doi.org/10.5194/gmd-10-2057-2017

Müller, W. A., Jungclaus, J. H., Mauritsen, T., Baehr, J., Bittner, M., Budich, R., et al. (2018). A higher-resolution version of the Max Planck institute Earth System model (MPI-ESM1.2-HR). *Journal of Advances in Modeling Earth Systems*, *10*(7), 1383–1413. https://doi.org/10.1029/2017MS001217

Penduff, T., Le Sommer, J., Barnier, B., Treguier, A.-M., Molines, J.-M., & Madec, G. (2007). Influence of numerical schemes on current-topography interactions in 1/4° global ocean simulations. *Ocean Science*, *3*(4), 509–524. https://doi.org/10.5194/os-3-509-2007

Quartly, G., de Cuevas, B., & Coward, A. (2013). Mozambique channel eddies in GCMs: A question of resolution and slippage. *Ocean Modelling*, *63*, 56–67. https://doi.org/10.1016/j.ocemod.2012.12.011

Rahmstorf, S., & Willebrand, J. (1995). The role of temperature feedback in stabilizing the thermohaline circulation. *Journal of Physical Oceanography*, *25*(5), 787–805. https://doi.org/10.1175/1520-0485(1995)025⟨0787:TROTFI⟩2.0.CO;2

Rayner, N. A., Parker, D. E., Horton, E. B., Folland, C. K., Alexander, L. V., Rowell, D. P., et al. (2003). Global analyses of sea surface temperature, sea ice, and night marine air temperature since the late nineteenth century. *Journal of Geophysical Research*, *108*(D14). https://doi.org/10.1029/2002JD002670

Reick, C. H., Raddatz, T., Brovkin, V., & Gayler, V. (2013). Representation of natural and anthropogenic land cover change in MPI-ESM. *Journal of Advances in Modeling Earth Systems*, *5*(3), 459–482. https://doi.org/10.1002/jame.20022

Reintges, A., Latif, M., Bordbar, M. H., & Park, W. (2020). Wind stress-induced multiyear predictability of annual extratropical North Atlantic sea surface temperature anomalies. *Geophysical Research Letters*, *47*(14), e2020GL087031. https://doi.org/10.1029/2020GL087031

Rieck, J. K., Böning, C. W., & Getzlaff, K. (2019). The nature of eddy kinetic energy in the Labrador Sea: Different types of mesoscale eddies, their temporal variability, and impact on deep convection. *Journal of Physical Oceanography*, *49*(8), 2075–2094. https://doi.org/10.1175/JPO-D-18-0243.1

Roberts, C. D., Waters, J., Peterson, K. A., Palmer, M. D., McCarthy, G. D., Frajka-Williams, E., et al. (2013). Atmosphere drives recent interannual variability of the Atlantic meridional overturning circulation at 26.5°N. *Geophysical Research Letters*, *40*(19), 5164–5170. https://doi.org/10.1002/grl.50930

Robson, J., Sutton, R., Lohmann, K., Smith, D., & Palmer, M. D. (2012). Causes of the rapid warming of the North Atlantic Ocean in the mid-1990s. *Journal of Climate*, *25*(12), 4116–4134. https://doi.org/10.1175/JCLI-D-11-00443.1

Schulzki, T., Harlaß, J., Schwarzkopf, F. U., & Biastoch, A. (2022). Toward ocean hindcasts in earth system models: AMOC variability in a partially coupled model at eddying resolution [Dataset]. GEOMAR Helmholtz Centre for Ocean Research Kiel. https://hdl.handle.net/20.500.12085/57ea9d04-2bd4-4a27-8994-3e19982731bd

Schwarzkopf, F. U., Biastoch, A., Böning, C. W., Chanut, J., Durgadoo, J. V., Getzlaff, K., et al. (2019). The INALT family—A set of high-resolution nests for the Agulhas current system within global NEMO ocean/sea-ice configurations. *Geoscientific Model Development*, *12*(7), 3329–3355. https://doi.org/10.5194/gmd-12-3329-2019

Stevens, B., Giorgetta, M., Esch, M., Mauritsen, T., Crueger, T., Rast, S., et al. (2013). Atmospheric component of the MPI-M Earth System model: ECHAM6. *Journal of Advances in Modeling Earth Systems*, *5*(2), 146–172. https://doi.org/10.1002/jame.20015

Taburet, G., & Pujol, M.-I. (2022). Global Ocean gridded L 4 sea surface heights and derived variables reprocessed copernicus climate Service [Dataset]. Chang. https://doi.org/10.48670/moi-00145

Thoma, M., Gerdes, R., Greatbatch, R. J., & Ding, H. (2015). Partially coupled spin-up of the MPI-ESM: Implementation and first results. *Geoscientific Model Development*, *8*(1), 51–68. https://doi.org/10.5194/gmd-8-51-2015

Tsujino, H., Urakawa, S., Nakano, H., Small, R. J., Kim, W. M., Yeager, S. G., et al. (2018). JRA-55 based surface dataset for driving ocean–sea-ice models (JRA55-do). *Ocean Modelling*, *130*, 79–139. https://doi.org/10.1016/j.ocemod.2018.07.002

Valcke, S. (2013). The OASIS3 coupler: A European climate modelling community software. *Geoscientific Model Development*, *6*(2), 373–388. https://doi.org/10.5194/gmd-6-373-2013

Vancoppenolle, M., Fichefet, T., Goosse, H., Bouillon, S., Madec, G., & Maqueda, M. A. M. (2009). Simulating the mass balance and salinity of Arctic and Antarctic sea ice. 1. Model description and validation. *Ocean Modelling*, *27*(1), 33–53. https://doi.org/10.1016/j.ocemod.2008.10.005

Weijer, W., Cheng, W., Garuba, O. A., Hu, A., & Nadiga, B. T. (2020). CMIP6 models predict significant 21st century decline of the Atlantic Meridional Overturning Circulation. *Geophysical Research Letters*, *47*(12), e2019GL086075. https://doi.org/10.1029/2019GL086075

Yeager, S. (2015). Topographic coupling of the Atlantic overturning and gyre circulations. *Journal of Physical Oceanography*, *45*(5), 1258–1284. https://doi.org/10.1175/JPO-D-14-0100.1

Yeager, S. (2020). The abyssal origins of North Atlantic decadal predictability. *Climate Dynamics*, *55*(7), 2253–2271. https://doi.org/10.1007/s00382-020-05382-4

Zalesak, S. T. (1979). Fully multidimensional flux-corrected transport algorithms for fluids. *Journal of Computational Physics*, *31*(3), 335–362. https://doi.org/10.1016/0021-9991(79)90051-2

Zhang, Q., Chang, P., Yeager, S. G., Danabasoglu, G., & Zhang, S. (2022). Role of sea-surface salinity in simulating historical decadal variations of Atlantic Meridional Overturning Circulation in a coupled climate model. *Geophysical Research Letters*, *49*(4), e2021GL096922. https://doi.org/10.1029/2021GL096922

Zhao, J., & Johns, W. (2014). Wind-forced interannual variability of the Atlantic Meridional Overturning Circulation at 26.5°N. *Journal of Geophysical Research: Oceans*, *119*(4), 2403–2419. https://doi.org/10.1002/2013JC009407

Zweng, M. M., Reagan, J. R., Antonov, J. I., Locarnini, R. A., Mishonov, A. V., Boyer, T. P., et al. (2013). World Ocean Atlas 2013, volume 2: Salinity (NOAA Atlas NESDIS 74).

Journal of Advances in Modeling Earth Systems

Supporting Information for

Toward Ocean Hindcasts in Earth System Models: AMOC Variability in a Partially Coupled Model at Eddying Resolution.

Tobias Schulzki[1], Jan Harlaß[1], Franziska U. Schwarzkopf[1], Arne Biastoch[1,2]

[1]GEOMAR Helmholtz Centre for Ocean Research Kiel, Kiel, Germany

[2]Christian-Albrechts Universität zu Kiel, Kiel, Germany

Contents of this file

Introduction

This file contains additional figures supporting the analysis presented in the main text: The ability of partial coupling to reproduce the correct timing of ENSO and equatorial Pacific heat fluxes is demonstrated in Figure S1.
In addition to the AMOC in depth coordinates, we provide the mean AMOC in density coordinates from all model experiments in Figure S2.
Complementing our analysis of the annual mean Atlantic heat flux variability, we include a Figure (S3) of winter (DJF) heat flux variability. It is especially the winter heat flux that is expected to have an impact on the AMOC.
To provide further information on the correlation between the partially coupled and un-coupled experiments on decadal timescales, we provide timeseries of the AMOC and Sverdrup transports at the RAPID and SAMOC sections in Figure S4.

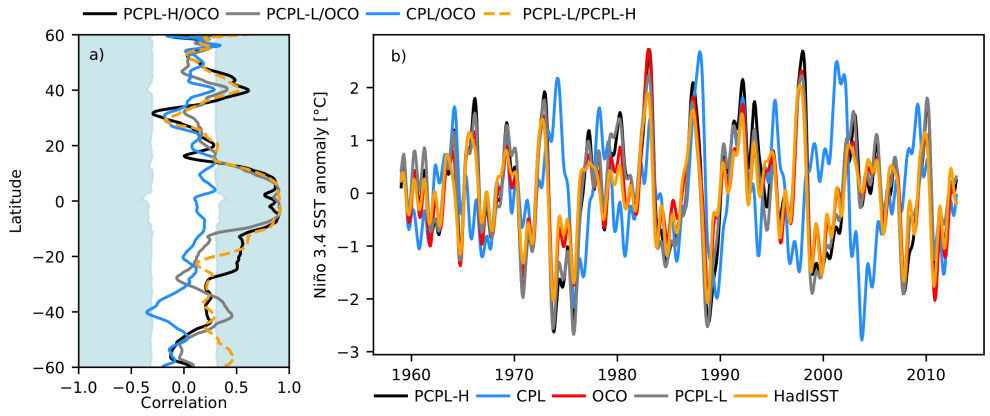

Figure S1. a) Correlation of detrended annual and zonal mean heat fluxes in the Pacific (derived from the coarse resolution host model). The fluxes were smoothed with a 7-grid point (3°) boxcar filter before calculating correlations. b) ENSO timeseries. Here the Niño3.4 Sea Surface Temperature anomaly is used as the ENSO index.

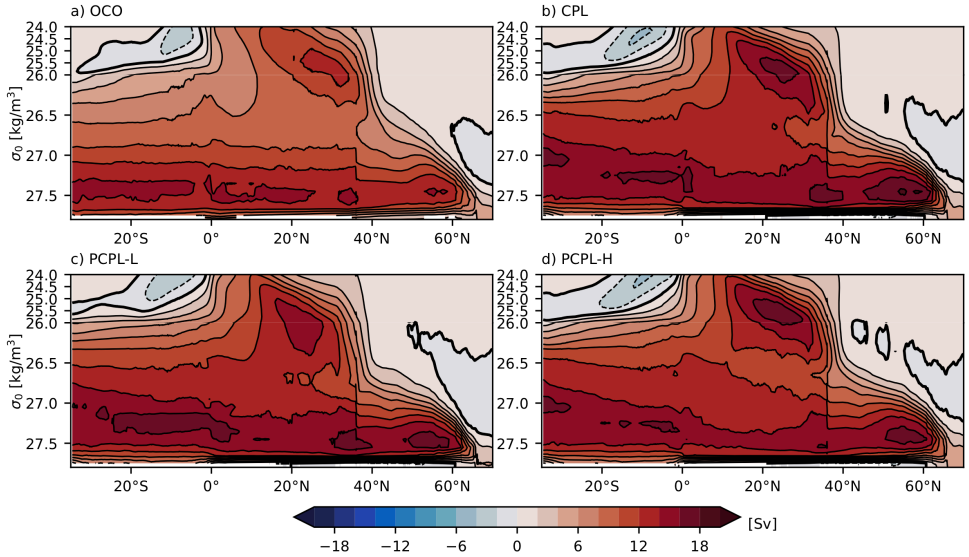

Figure S2. Mean 1970-2013 Meridional Overturning Streamfunction in σ_0 coordinates in OCO (a), CPL (b), PCPL-L (c) and PCPL-H (d). Contours are drawn with an interval of 2 Sv (the zero contour is drawn bold).

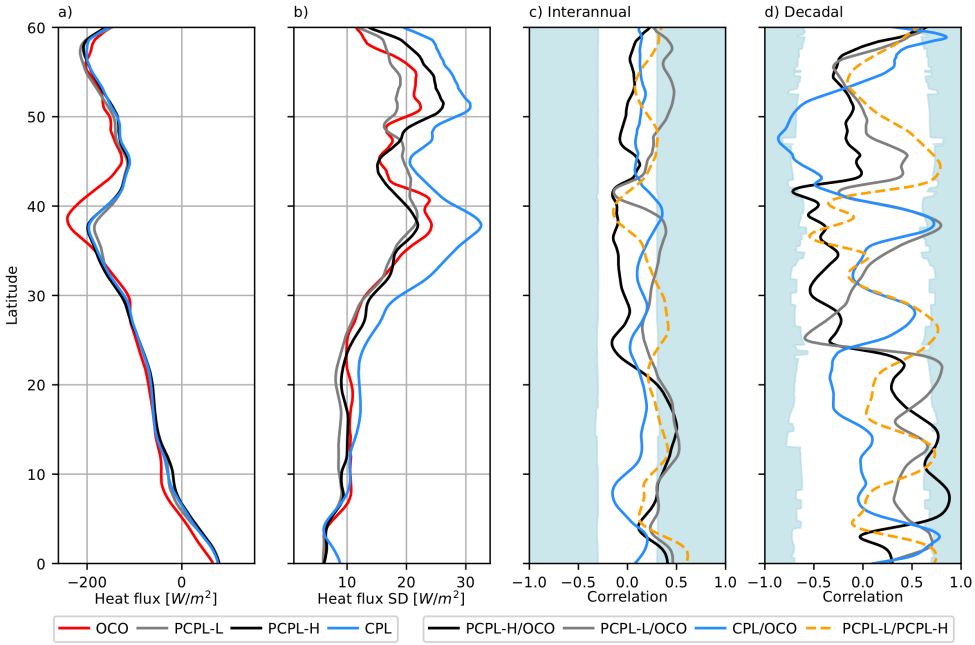

Figure S3. 1970-2013 northern hemisphere zonal mean heat flux in winter (DJF; a) and its standard deviation (b) in the Atlantic (including the Atlantic sector of the Southern Ocean). c) Correlations of the zonal mean heat flux based on winter means and d) based on 10-year lowpass filtered winter means. The fluxes were smoothed with a 31-grid point (3°) boxcar filter before calculating correlations. All timeseries were detrended before calculating the standard deviation, or correlation.

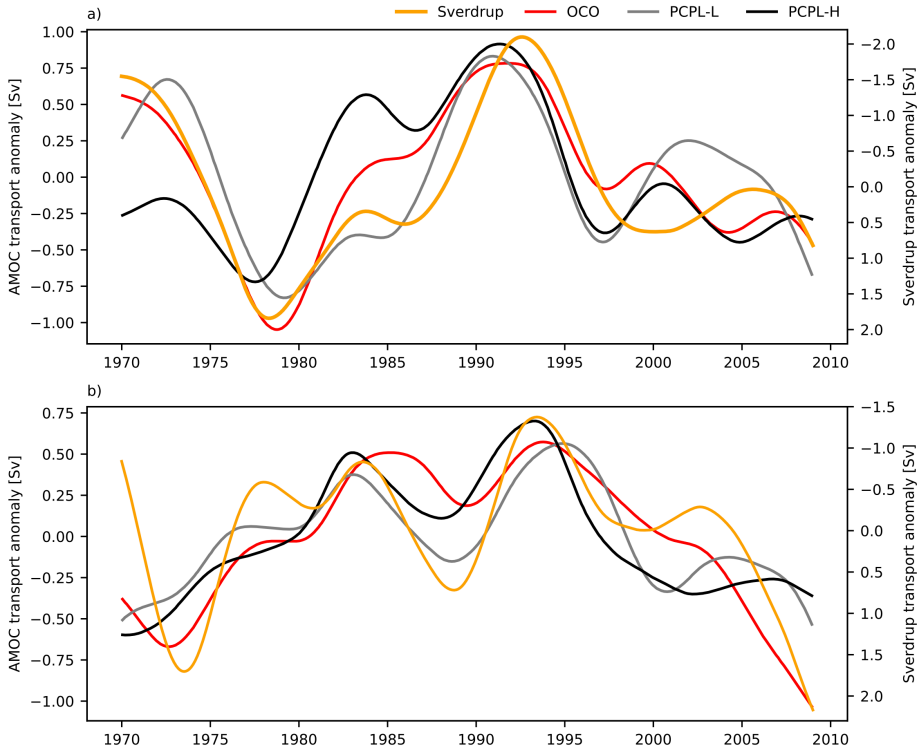

Figure S4. Decadal (10-year lowpass filtered) anomalies of the Sverdrup and AMOC transports at 26.5°N (a) and 34.5°S (b). The Sverdrup transport was calculated from wind stress derived from the JRA55-do wind using offline bulk formulae.

CHAPTER 4

Interhemispheric Propagation of Temperature, Salinity and Density Anomalies and Their Impact on the AMOC

Interhemispheric connectivity:

As demonstrated in the previous chapter, the FOCI-ATLAS10 configuration is able to simulate a realistic Atlantic Ocean circulation, including an AMOC that is comparable to observations in terms of mean strength and structure. Further, it was analysed how wind stress changes impact the AMOC on sub-monthly to decadal timescales.
In this chapter, FOCI-ATLAS10 is deployed to study the importance of interhemispheric connectivity for the AMOC adjustment to wind stress changes over the Southern Ocean on climate (multi-decadal to centennial) timescales. For a long time it has been an open question, how the southern hemisphere, in particular the southern hemisphere westerly winds and Agulhas leakage, contribute to AMOC variability. Previous studies are limited by coarse ocean resolution, a short length of experiments, no interactive atmosphere, or a combination of those. Therefore, the newly developed FOCI-ATLAS10 configuration provides a unique set-up, specifically designed for the purpose of studying interhemispheric connectivity in an eddying, coupled model configuration. In this chapter, it is shown that increasing the Southern Ocean wind stress by 30% in a 5 member ensemble perturbation experiment leads to an increase of the warm and saline Indian Ocean inflow via Agulhas leakage by 3.8 Sv (35%). Based on a combination of Lagrangian and Eulerian analysis, it is shown that the northward propagation of anomalies generated by an increased inflow of Indian Ocean water into the South Atlantic is a complex interplay of advection, mixing and local atmospheric responses. As a consequence, anomalies do not simply follow the advective pathways of the leakage water. The AMOC responds to the Southern Ocean wind stress increase with a strengthening of 1.2 Sv (7%) after approximately 80 years. Anomalous water mass transformation associated with the increased AMOC mainly occurs at the entry into the Nordic Seas, while enhanced sinking is found to occur after the Nordic Seas overflow has crossed the sills. Therefore, AMOC changes in depth and density coordinates are linked through an increase in overflow density.

This chapter has not been published, or submitted for publication. The references can be found in the main reference list of this thesis.

Author contribution: The author was fully responsible for implementing necessary code changes, the design of the perturbation experiment and its execution, all Lagrangian experiments, all analysis/figures and wrote the text of this chapter.

1. Introduction

The Atlantic Meridional Overturning Circulation (AMOC) describes the zonally integrated flow of water and is characterised by a northward flow of warm water in the upper ocean and southward return flow at mid-depths (Lozier, 2012). Due to its large impact on the climate of countries surrounding the Atlantic Ocean (e.g. Zhang et al., 2019), strong efforts were made to better understand the complex circulation associated with the AMOC (Lozier, 2012; Buckley & Marshall, 2016; Jackson et al., 2022). The meridional AMOC transport was shown to substantially vary on all timescales from days to millennia (Rayner et al., 2011; Blaker et al., 2021; Schmittner et al., 2003), but several open questions remain on the sources of this variability. This includes the role of the Southern Hemisphere (SH) and of the SH westerly winds (SWW) in particular. The SWW experienced strong changes over the last decades and are expected to continue to strengthen until the end of this century, due to rising greenhouse gas concentrations (Arblaster & Meehl, 2006; Swart & Fyfe, 2012; Goyal et al., 2021; Ivanciu et al., 2022a). A potential impact of this strengthening on the Atlantic Ocean circulation could reduce an AMOC slow-down expected from increased radiative forcing due to anthropogenic CO_2 emissions (Weijer et al., 2020). It is therefore of major importance to better understand the interhemispheric connectivity of the AMOC and sources of AMOC variability in general.

Several mechanisms were hypothesised, how the SH could drive changes in the AMOC. In 1995, Toggweiler and Samuels (1995) introduced the 'Drake Passage Effect'. They note that an increase of the Southern Ocean (SO) wind stress does increase northward Ekman transport into the South Atlantic (SA) and upwelling of deep water in the SO, which must be balanced by an increase of the deep southward flow and formation of North Atlantic Deep Water (NADW) in the subpolar/polar North Atlantic. Note that SO wind stress and SWW are used to describe the same winds, with the only difference that a change in SWW can also have an direct impact on turbulent heat/freshwater fluxes, while SO wind stress only refers the associated momentum transfer. It was indeed shown in modelling studies that a shift and strengthening can result in a strong response of the AMOC (e.g. Delworth & Zeng, 2008; Klinger & Cruz, 2009). However, studies comparing coarse to eddying models indicate that the AMOC response to changes of the SO wind stress strongly depends on the resolution of the model. While coarse resolution models show a very strong overturning response, this is not found in eddying models that simulate at least parts of the mesoscale spectrum in the SO, or use an eddy parameterisation that is allowed to increase in response to an increased wind stress (Gent, 2016). The reason for this result is that a fraction of the Ekman transport divergence is balanced by eddy fluxes, not upwelling of deep water. Enhanced Ekman pumping north of the wind maximum and suction south of the wind maximum is associated with an increased meridional density gradient, steeper isopycnals and increased baroclinic instability. The latter leads to enhanced eddy activity in the Southern Ocean (Hogg & Blundell, 2006; Meredith & Hogg, 2006; Hallberg & Gnanadesikan, 2006, see also chapter 1 for a detailed discussion of Ekman transport and pumping). These eddies transport heat southward and tend to flatten the isopycnals (Hogg et al., 2008; Gent & Danabasoglu, 2011). As a result, the eddy field reduces the impact of wind stress changes on the Antarctic Circumpolar Current (ACC; 'eddy saturation'), whose strength is linked to the isopycnal slope, and on the overturning circulation ('eddy compensation'; Hallberg & Gnanadesikan, 2006; Munday et al., 2013; Gent, 2016; Bishop et al., 2016). As a consequence of eddy saturation, the cold water inflow route of the AMOC via the ACC transport through Drake Passage (e.g. Rühs et al., 2019) is not expected to significantly increase with enhanced SO wind stress. Furthermore, it was argued that coupling to an responsive atmosphere reduces the 'Drake Passage Effect' (Rahmstorf & England, 1997).

Therefore, the main response to a SWW increase may not be related to its direct effect on Ekman transport, but potentially to an increase of the warm and saline inflow from the Indian Ocean via Agulhas leakage. Agulhas leakage was shown to increase in response to strengthened SWW at least temporarily (Durgadoo et al., 2013). Furthermore, Rühs et al. (2019) find an increase in Agulhas leakage to result in a decreasing contribution of the cold water route to the upper AMOC limb,

which would further reduce the importance of the Drake Passage inflow in response to strengthened SWW. It was hypothesised that the fast atmospheric damping of temperature anomalies, caused by an increased inflow via Agulhas leakage, generates a positive density anomaly that is advected into the North Atlantic, where it triggers enhanced deep water formation and an increase in the AMOC strength (Gordon et al., 1987; Knorr & Lohmann, 2003; Gordon et al., 1992). Weijer et al. (2002) showed that different mechanisms may be responsible for the propagation of density anomalies from the Indian Ocean inflow to the subpolar North Atlantic. After introducing anomalies in the Agulhas region, they are carried toward the western boundary by Rossby waves (Biastoch et al., 2008b), where continental shelf waves along the boundary and equatorial Kelvin waves propagate density anomalies further into the North Atlantic within the first decade (Weijer et al., 2002). A similar mechanisms was found by Webb et al. (2021), but triggered by changes in the wind stress itself. Although this mechanism induced an AMOC response in both studies, a much larger AMOC anomaly occurred when the first salinity anomalies reached the Subpolar Gyre (SPG) after 30 years in Weijer et al. (2002). This advective timescale is consistent with model and observation based studies, suggesting water from Agulhas leakage to reach the subtropical North Atlantic within 20 years and the subpolar North Atlantic within 30-40 years (van Sebille et al., 2011; Rühs et al., 2013). Experiments used by Webb et al. (2021) only cover 15 years and likely do not capture any response mediated by advection. Also, a similar experiment with the same model by Hogg et al. (2017) covers 50 years and showed a fast adjustment to increased SO wind stress, but no secondary strengthening after 30 years. Wei et al. (2012) find the development of strong AMOC anomalies to be considerably delayed and only pronounced approximately 100 years after an increase of the SO wind stress. This suggests that the Lagrangian advection of water volumes may not fully reflect the propagation of temperature and salinity anomalies that could lead to an increase in overturning. Furthermore, the relative importance of deep convection in different regions of the subpolar North Atlantic and Nordic Seas is still debated (e.g. Lozier et al., 2019; Chafik & Rossby, 2019). As a consequence, it is not clear how temperature, salinity and density anomalies that potentially develop in the North Atlantic cause a change in the AMOC transport.

In summary, several studies have tried to decipher the role of the Southern Hemisphere, and the Southern Ocean wind stress in particular, on the AMOC. However, most of the available model experiments suffer from different limitations, namely coarse resolution (e.g. Weijer et al., 2002; Wei et al., 2012; Knorr & Lohmann, 2003), no interactive atmosphere (e.g Webb et al., 2021; Hogg et al., 2017), a limited length of the experiments (e.g. Farneti & Delworth, 2010; Bishop et al., 2016; Webb et al., 2021), or a combination of those. Coarse (non-eddying) resolution models may not be able to simulate key-processes along the pathway of anomalies, in the formation sites of NADW, or the inflow into the Atlantic Ocean via Agulhas leakage realistically. Furthermore, coarse resolution models were shown to exaggerate the overturning response to stronger SO Ekman divergence (Gent, 2016). At the same time global models at eddying resolution are more computational expensive and were run only for a few decades, for example 40 years in Farneti and Delworth (2010), or 15 years in Webb et al. (2021). As indicated above, some models show a longer adjustment timescale and 40 years may not be sufficient to capture the onset of the AMOC response generated by the advection of anomalies, even though the advective timescale of leakage water is shorter. Furthermore, atmospheric adjustments to an increase in Agulhas leakage (Haarsma et al., 2011) could result in a different response of a coupled model compared to forced ocean models, in addition to a strong local dependency of the Southern Ocean response to wind perturbations on the surface buoyancy flux (Abernathey et al., 2011). Furthermore, prescribing the atmospheric state changes the North Atlantic's response to freshwater anomalies introduced by modifications of the Greenland runoff (Martin & Biastoch, 2022). Although a different source of anomalies is studied in this chapter, this result is most likely still valid and highlights the need for coupling. As a consequence, there seems to be a role of the SWW in generating AMOC variability, but many details of this connection remain unexplained. There is still a lack of understanding with regard to the importance of advective processes and possible atmospheric adjustments.

The aim of this chapter is to provide new insight into the Atlantic Ocean circulation by using a coupled, nested configuration that covers the entire Atlantic and Atlantic sector of the Southern Ocean at 1/10° horizontal resolution. The nested configuration requires significantly less computational resources than a comparable global configuration and allows for an ensemble perturbation experiment with 5 members of 120 years length each. Based on this perturbation experiment with a 30% increase of the SO wind stress maximum, two main questions are addressed:
1.) What are the pathways and timescales of southern hemisphere temperature, salinity and density anomalies propagating into the North Atlantic?
2.) How does the AMOC respond to (wind stress) changes in the Southern Hemisphere?

Although this study is motivated by projections of increasing Southern Hemisphere winds under climate change (e.g. Ivanciu et al., 2022a; Goyal et al., 2021), it is not the goal to project future changes caused by this increase. The focus is on fundamental mechanisms that determine the propagation of signals and how they affect overturning in the North Atlantic. After introducing the model and experimental design, the initial South Atlantic response to enhanced wind stress over the Southern Ocean, the northward propagation of temperature, salinity and density anomalies and their impact on the AMOC are analysed.

2. Methodology

2.1 Model Configuration & Experiments

A perturbation experiment in the earth system model FOCI (Matthes et al., 2020) is conducted. The atmospheric component of FOCI is provided by ECHAM6 (Müller et al., 2018; Stevens et al., 2013) with a horizontal resolution of T63 and 96 vertical levels. The JSBACH model (Brovkin et al., 2009; Reick et al., 2013) is used as an interactive land component. The ocean component of FOCI is provided by the NEMO version 3.6 (Madec, 2016) based, nested ATLAS10 configuration described in chapter 2 and 3 (Schulzki et al., 2022) of this thesis. ATLAS10 consist of a 1/10° nest grid, embedded into a 0.5° global grid, called host. Both grids have 46 vertical levels with increasing vertical spacing from the surface to abyssal depths. A two-way exchange between both grids is handled using the AGRIF library (Debreu et al., 2008). While on the host grid free-slip lateral boundary conditions are used, no-slip boundary conditions are applied in the nest. Further, on the host grid the momentum advection equation is discretised using the energy and enstrophy conserving (EEN; Arakawa & Hsu, 1990) scheme and the advection of tracers by using the Tracer Variance Dissipation (TVD; Zalesak, 1979) scheme. Tracer diffusion is accomplished by a Laplacian operator acting along iso-neutral surfaces with an eddy diffusivity of 600 m^2/s and lateral diffusion of momentum by a bi-Laplacian operator acting along geopotential surfaces with a maximum eddy viscosity of 6×10^{11} m^3/s. In contrast, self-diffusive upstream-biased scheme (UBS; Farrow & Stevens, 1995; Madec, 2016) was used on the nest grid, without additional explicit diffusion terms. Only on the host grid, a Gent and McWilliams (GM) eddy parameterisation (Gent & McWilliams, 1990) with a spatially and temporally varying eddy induced velocity coefficient is used (Treguier et al., 1997). The maximum coefficient is set to 1000 m^2/s. Surface fluxes are calculated every 3 hours by the atmosphere model and subsequently interpolated onto the host and nest grids.

For reference, a 180 years long fully coupled FOCI-ATLAS10 experiment with pre-industrial atmospheric boundary conditions is used. This experiment is initialised using a 100-year long spin-up of the nested configuration. The spin-up itself is initialised from the last timestep of a 1500-year long pre-industrial control simulation of the un-nested FOCI configuration described in Matthes et al. (2020).

A 5-member ensemble perturbation experiment is performed to study the Atlantic wide impact of strengthened southern hemisphere westerly winds and the northward spreading of temperature, salinity and density anomalies. Therefore, both wind stress components over the Southern Ocean are increased by a maximum of 30%. Note that only adding an anomaly to the zonal component

does change the direction of the wind stress, deforming high/low pressure systems on shorter timescales and causing the long time mean to be mostly zonal even in regions that otherwise have a non-negligible meridional component.

The pattern of the applied wind stress anomaly shown in figure 4.1c,d has an idealised hanning type window shape with it's maximum aligned with the maximum zonal mean zonal wind stress of the control experiment. Thus, the experiment focuses on a strengthening of the wind and does not include a long term shift in position. The anomaly pattern was chosen to ensure a smooth transition into the region without an added wind stress anomaly. Similar to studies of Delworth and Zeng (2008); Bishop et al. (2016) and others, changing heat and freshwater fluxes directly caused by a speed-up of the SWW are not considered. Changes are only applied in the momentum flux calculation of the ocean component. The atmospheric component of the coupled model is not directly affected by this procedure and can only respond to possible changes in the ocean component.

The anomaly pattern, together with a maximum increase of 30%, causes the mean meridional wind stress between 45°S and 60°S to be 17% higher in the perturbation experiment compared to the control experiment. This value is close to the wind stress increase in FOCI under the high emission SSP 5-8.5 scenario until 2100, without interactive ozone (Ivanciu et al., 2022a). Although the purpose of this study is not to project the AMOC change under climate change, it is still desired to use a reasonable increase. If the response is non-linear, down-scaling from an excessively large anomaly may not be possible. Still, for the purpose of detecting the signal propagation, an anomaly that is at the upper limit of realistic values is needed to be able to distinguish the signal forced in the southern hemisphere from intrinsic variability within the coupled model. To avoid an initialisation shock, the wind stress anomaly is linearly increased to reach the full magnitude after one year and is then constant for the remainder of the experiment. The individual ensemble members are initialised 15-years apart to capture different states (e.g. Atlantic Multidecadal Variability states) of the ocean (figure 4.1a).

2.2 Eulerian Analysis

The Eulerian analysis is based on identifying significant changes in the perturbation experiment compared to the control experiment. To analyse the spatial pattern of anomalies, an ensemble mean of temporally averaged fields from all ensemble members is calculated. The same years, relative to the initialisation, are used. The control field consists of the same five time periods taken from the control experiment. Due to the initialisation of the ensemble members 15 years apart, also the control fields are 15 years apart. As an example, year 20 in first ensemble member corresponds to year 20 of the control experiment, but year 20 in the second ensemble member corresponds to year 35 in the control experiment. Using this method, it is possible to estimate the significance of differences between the control mean field (based on the five different time periods) and the perturbation experiment's mean field (based on the five ensemble members), using a two-tailed t-test. Changes in the perturbation experiment are regarded significant, based on confidence level of 95%.

A similar approach is used for timeseries. Here the five timeseries of the perturbation ensemble members are averaged. For the control, the corresponding years in the control experiment are used as described before, resulting in five 120 year long timeseries that are shifted by 15 years. Again, based on two-tailed t-test and a confidence level of 95%, a confidence interval for the mean of the five control values at each time step is calculated. Except stated differently in the figure caption, timeseries are smoothed using a 10-year boxcar window, as this study is focused on (multi-)decadal changes in the AMOC, not interannual variability. A 5-year boxcar window is applied, if changes occur already in the beginning of the timeseries.

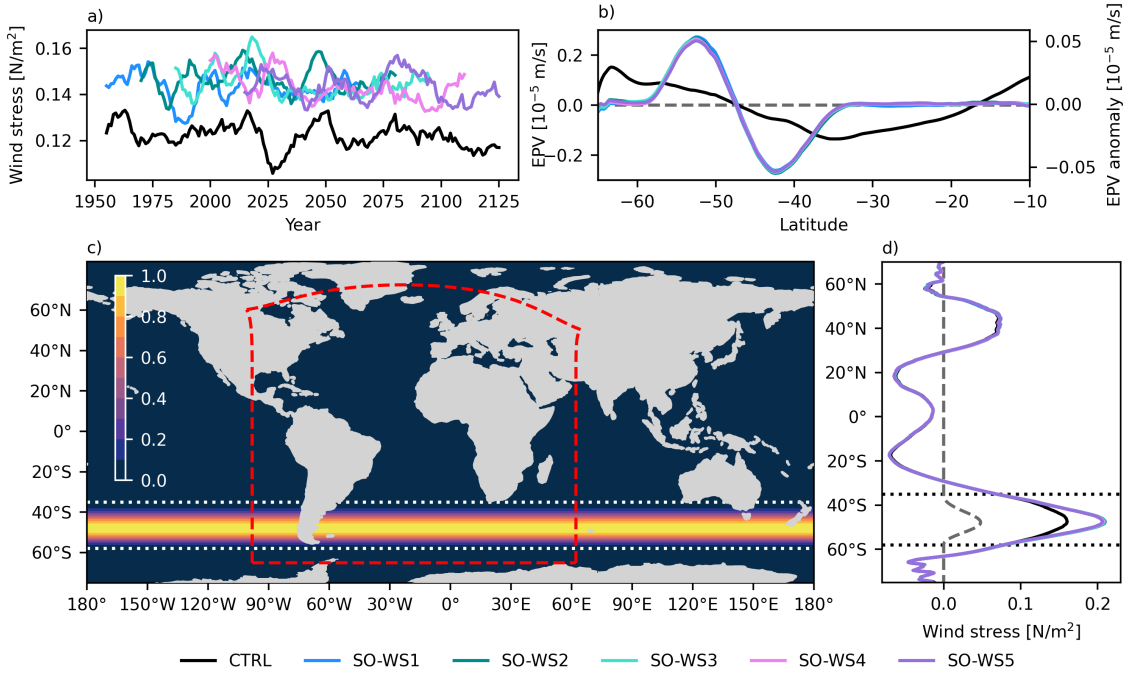

Figure 4.1: Experimental set-up and wind stress changes. a) Zonal mean zonal wind stress between 60°S and 45°S. b) Zonal mean Ekman pumping velocity (EPV) in the control experiment (black) and difference between the ensemble members and the control (see legend for color coding). c) Anomaly pattern. Colour shading indicates the mask values. One corresponds to the full 30% increase, while 0 indicates no modification of the wind stress. Red lines indicate the nest boundary of the ATLAS10 ocean component. d) Zonal mean zonal wind stress in all experiments calculated on the global host grid and anomaly pattern (dashed).

2.3 Lagrangian Experiments

To complement the Eulerian analysis of temperature, salinity and density anomalies, Lagrangian experiments to analyse advective pathways and timescales are performed. All experiments are based on the ARIANE algorithm, which solves the advection equation using an analytical scheme (Blanke & Raynaud, 1997). The full 4-dimensional model output with a temporal resolution of 5-days is used as input fields here.

A first experiment follows Biastoch et al. (2015) and aims to estimate the Indian Ocean inflow into the Atlantic via Agulhas leakage. Water volumes are released every 5 days for the entire length of all experiments in the Agulhas Current at 32°S (see for example Schmidt et al., 2021) and integrated forward for 5-years. The release section is marked green in figure 4.2a. The water volumes are counted as leakage water, if they cross the Good Hope section (see figure 4.2a). ARIANE seeds particles automatically along the release section according to the transport across the section. Each water volume represents a fraction of the total transport, at maximum 0.1 Sv. Due to the analytical scheme, this transport is conserved along the trajectory.

Similar to the method applied by Rühs et al. (2013), output from the first experiment is used in a second experiment to extend only the trajectories that cross the Good Hope section ('leakage volumes') to 100 years. Due to the strongly increased computational cost of running such long experiments and storing individual trajectories with a temporal resolution of 5 days, experiments are only conducted in the control experiment and for 10 years (years 5-15 in the control). This experiment is used to derive the advective timescale from Agulhas leakage into the tropics and North Atlantic.

Because lateral and diapycnal mixing can lead to differences in the advective spreading of water volumes and the actual development of anomalies, a second experiment is performed by releasing water in the North Brazil Current at 11°S at densities between 26.6 and 27.3 kg/m^3. It was found that anomalies in this density range are less well captured by the first experiment, which shows most leakage volumes to cross 11°S at lower density. Instead, this density range is mostly occupied by water that has entered the Atlantic via Drake Passage and subsequently joined a northwest-ward flow after circulating through the Cape Basin (Rühs et al., 2019). Since it was shown that the shallow AMOC branch converges in the North Brazil Current (NBC; e.g. Rühs et al., 2019), the combination of both experiments captures the pathways of the whole upper AMOC branch and in particular those of the anomalies seen in the perturbation experiment.

As before, the initial water volumes are seeded automatically to represent a fraction of the total transport (maximum 0.1 Sv) across the section and integrated for 100 years. Water volumes are released every five days for 10 years (years 5-15 of the control experiment). Output is stored with a temporal resolution of 5 days.

3. South Atlantic Response

After the wind stress is increased, different processes in the Southern Ocean and South Atlantic respond on very short timescales.

The wind stress increases the ACC strength on average by 2.4 Sv. Thus, the 30% increase in wind stress maximum only relates to 3% increase of the ACC transport trough Drake Passage and for most of the timeseries differences between the control and perturbation experiments are not significant (figure 4.2e). It is assumed, that this is caused by eddy saturation in agreement with Munday et al. (2013) and Bishop et al. (2016). Further, the anomalous Ekman divergence south of the wind stress maximum drives more upwelling of salty deep water and causes strong increases in salinity near the surface (figures 4.1b and 4.2a). Nevertheless, these anomalies through anomalous Ekman suction occur mostly in the top 50 m of the Southern Ocean and changes below are weak (figure 4.2b,d). Especially the slope of isopycnals below this depth is not affected (not shown), which is consistent with the minor ACC response. The position of the subtropical front, here defined as the 11°C isotherm at 100 m depth (Orsi et al., 1995), is not affected either (figure 4.2b).

The wind increase does, however, increase the warm, saline inflow from the Indian Ocean via Agulhas leakage. The leakage transport estimated from Lagrangian experiments, does significantly increase. The ensemble mean Agulhas leakage transport is about 3.8 Sv (35%) higher than in the control experiment (figure 4.2f). The Agulhas leakage response is very fast and occurs within the first 5 years. Afterwards, Agulhas leakage remains at a higher level for the entire length of the experiment.

This increased inflow of warm and saline water from the Indian Ocean causes strong temperature and salinity anomalies in the Cape Basin. Anomalies along the Good Hope section (figure 4.2g) show strong salinity anomalies near the surface and down to 1500 m (26-27.2 kg/m^3). Below this depth, water becomes slightly fresher. Here the ensemble mean salinity difference multiplied by the haline contraction coefficient derived from the control experiment is shown, which is positive throughout the entire water column. Thus negative/positive values are associated with a decrease/increase in salinity. Similarly, figure 4.2h shows the effect of changing temperatures on the density with positive/negative values being associated with a temperature decrease/increase. The temperature also increases at the surface, but anomalies are most pronounced between 400 and 700 m (26.5-27.2 kg/m^3). Following the argumentation of other studies, the main reason for the reduced temperature anomalies near-surface is fast atmospheric damping (Weijer et al., 2002; Ivanciu et al., 2022a; Haarsma et al., 2011). While the salinity increase outweighs the temperature increase to create a positive density anomaly at the surface , the opposite is true below 400 m, where the effect of increasing temperatures causes the density to be lower (figure 4.2g,h). The total density anomaly is indicated by white contours.

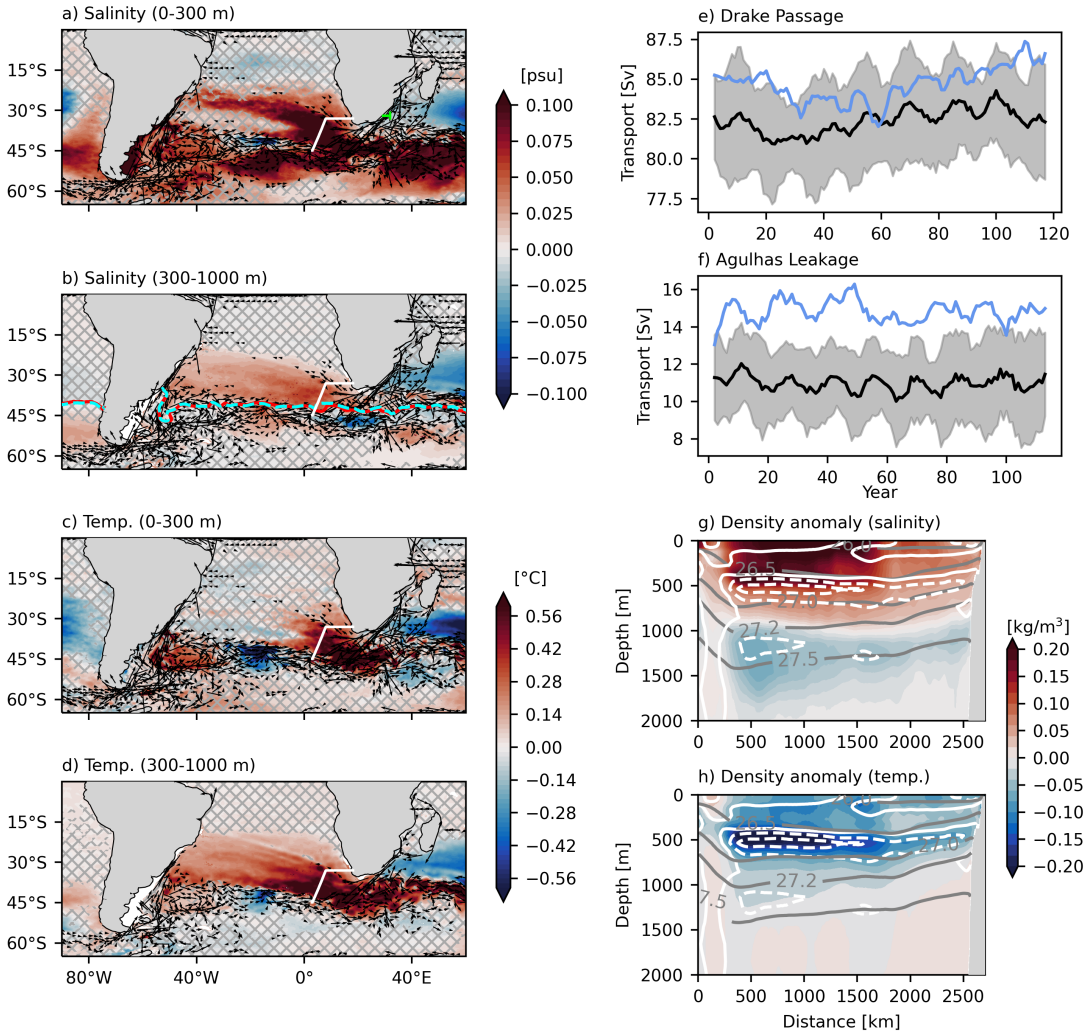

Figure 4.2: South Atlantic response. a-d) Ensemble mean salinity and temperature anomalies (years 5-15) in different depth layers. Arrows show the mean velocity in the same depth layer from the control experiment (speeds lower than 5 cm s^{-1} are masked). Hatching in a-d indicates non-significant values. The white lines show the Good Hope section and the green line in a) the release section for the ARIANE experiments. In b) the Subtropical Front from the control (cyan) and from the perturbation ensemble mean (red) are shown. e,f) Ensemble mean Drake Passage and Agulhas leakage transports, smoothed using a 5-year boxcar window. For the control experiment grey shading indicates the 95% confidence interval. g,h) Ensemble mean density anomaly due to temperature and salinity changes at the Good Hope section (years 5-15). Grey contours indicate the mean density in the control experiment. White contours show the ensemble mean difference in density (0.05 kg/m^{-3} intervals)

Lagrangian experiments show that water released in the Agulhas Current, may cross the Good Hope section as deep as 2000 m (figure 4.3a). Therefore, the depth range covered by the anomalies is consistent with the depth range of the warm and saline inflow. The same statement, although not shown here, can be made for density ranges. It is therefore proposed that the reason for the strong temperature and salinity anomalies extending throughout the whole water column from the surface down to 1500 m is an increased inflow of Indian Ocean water into Cape Basin. The water mixes in the Basin and spreads north-eastward along the main ring path and eastward in a secondary pathway at 35°S. In agreement with the anomalies, leakage volumes cross the Good Hope section along the entire section except for the south-western most part, which is located in the South Atlantic Current (SAC). Note that the anomaly pattern is not expected to fully match the probability distribution of Lagrangian particles crossing the Good Hope section, because water volumes tracked by the Lagrangian experiment do not maintain their properties. Lateral mixing can lead to strong anomalies occurring in areas that are only crossed by few leakage water volumes (e.g. Rühs et al., 2019). Furthermore, the design of the wind stress anomaly causes enhanced Ekman pumping between the wind stress maximum (figure 4.1b) and 35°S. In general, the associated increase in intermediate water formation is expected to result in a subsurface freshening and cooling and is thus not consistent with the salinity and temperature increase. Note that the formation region of intermediate water in FOCI-ATLAS10 is shifted north due to a position bias of the mean westerly winds in FOCI(-ATLAS10) (see Matthes et al., 2020; Schulzki et al., 2022, chapter 3). Nevertheless, in the Cape Basin the increased inflow via Agulhas leakage and increased Ekman pumping could lead to the injection of more salty and warm surface water into the layer below 300 m. This may contribute to the anomalies being most pronounced between approximately 500 and 1000 km and not at the position where most leakage volume cross the Good Hope section.

An alternative hypothesis could be that anomalies enter the Atlantic via Drake Passage and spread eastward in the SAC. But horizontal maps clearly suggest that the mid-depth temperature (and salinity) increase is of Indian Ocean origin (figure 4.2b,d). Below the near-surface layers, temperature and salinity anomalies can be significant within the first 15 years near Drake Passage, but are much stronger in the Cape Basin. Especially, they are mostly confined to the latitudes of mean westward flow and clearly not carried by the eastward flow within the SAC.

In summary, the Agulhas leakage inflow covers the full depth range of the anomalies, anomalies peak in the Cape Basin and extend from Cape Basin towards the west in a latitude range characterised by mean westward flow in the model. Furthermore, the anomaly pattern matches anomalies seen in Haarsma et al. (2011) driven by a direct modification of Agulhas leakage, not involving a wind stress perturbation, and in Ivanciu et al. (2022a) based on composites of years with strong Agulhas leakage. It is therefore concluded that the anomalies north of the subtropical front are predominantly generated by an increased inflow of warm and saline water from the Indian Ocean via Agulhas leakage.

4. Northward Propagation of Anomalies

The SA response to the increased southern hemisphere wind stress is dominated by an increase in salinity and temperature between the surface and approximately 1500 m depth, driven by an increase in Agulhas leakage. This water is part of the upper AMOC limb and therefore expected to spread further north. In the following sections it is investigated, how the described anomalies propagate north via a range of processes, including advection.

4.1 Propagation into the Equatorial Atlantic

The water entering the South Atlantic via Agulhas leakage creates strong anomalies in the South Atlantic Subtropical Gyre (SA STG). A zonal section at 11°S indicates that the anomalously salty and warm water is transported northward along the western boundary and reaches the entry into the tropical Atlantic (figure 4.4).

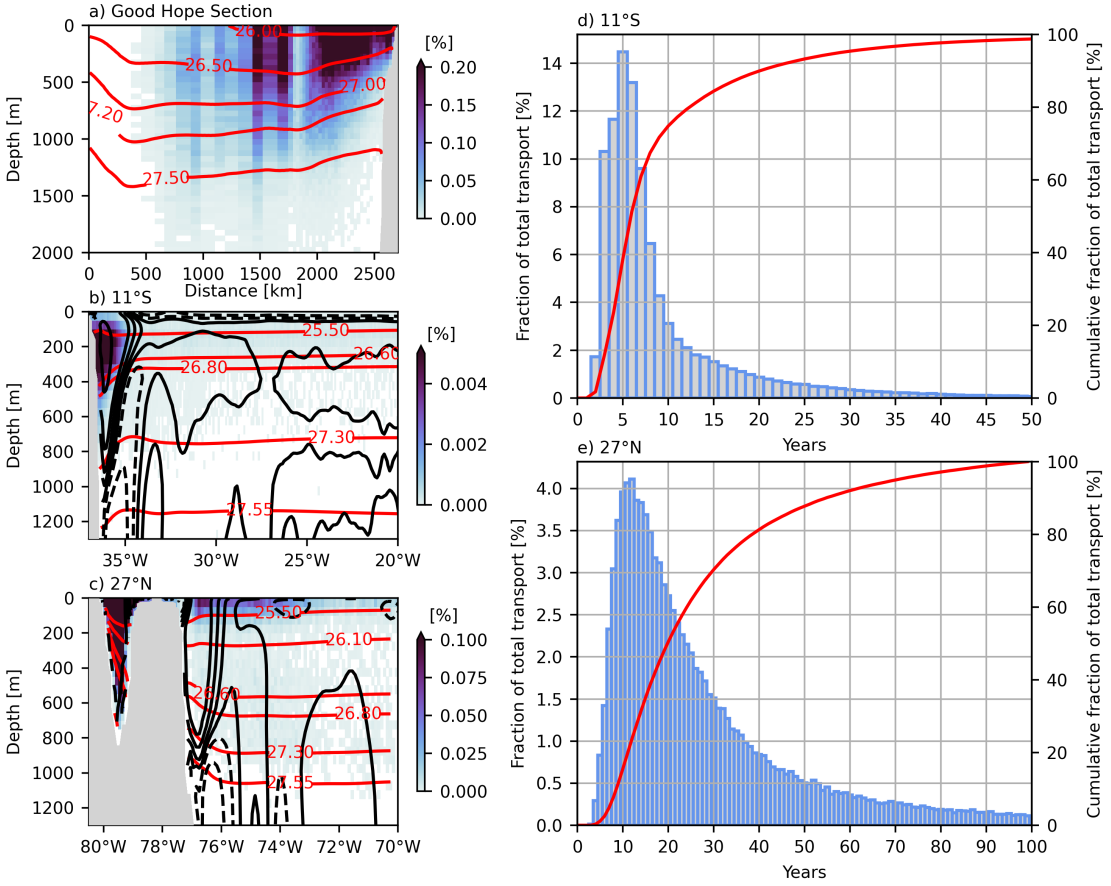

Figure 4.3: Advection of leakage volumes. a) Probability of leakage volumes to cross the Good Hope section within bins of 0.3° longitude × 50 m size (the longitude bins are mapped onto a distance axis). b,c) Same, but for 11°S and 27°N (bin sizes 0.1° longitude × 50 m). For all probability sections, only the first crossing is considered. Red/black contours show mean density/meridional velocity from the control experiment. Transit time distribution to 11°S (d) and 27°N (e). The left y-axis and bars indicate the fraction of the total transport that arrives within 1-year bins. The right y-axis and red lines show the cumulative fraction of the total transport that has arrived. It is assumed that all volumes have arrived after 50/100 years at 11°S/27°N.

The Lagrangian experiments reveal that 8.1 Sv of the 12.5 Sv 'leakage water' released per timestep reach the 11°S section. Thus, on average 65% of the leakage transport is exported into the tropics. Water entering the Atlantic via Agulhas leakage mainly occupies the depth range between 100 and 500 m in the NBC (figure 4.3b), which agrees well with Rühs et al. (2019). In FOCI-ATLAS10, this corresponds to the density range between 25.5 and 26.6 kg/m^3 (figure 4.3b). It is notable that a significant salinity increase is only visible in the lower part of this depth range after 20 years in the NBC. The upper 250 m show a significant cooling and a non-significant freshening. Both freshening and cooling are spread across the entire section shown here and peak outside the NBC (figure 4.4a,b).

The depth range below (500-900 m; 26.6-27.3 kg/m^3), where only few leakage particles cross the section (figure 4.3b), shows a strong warming and salinity increase (figure 4.4a,b). Water in this density (depth) range is mostly supplied by the inflow via Drake Passage (Rühs et al., 2019). Based on the aforementioned results, these water volumes acquire a temperature and salinity anomaly in the Cape Basin, rather than carrying anomalies into the Atlantic via the SAC (figure 4.2b,d). Their gain in temperature and salinity is caused by mixing with the Indian Ocean inflow at depth and

possibly by the injection of more warm and saline near-surface water due to local Ekman pumping in the Cape Basin.

In general, the structure of anomalies agrees between the 11°S and the Good Hope sections, but the density layers occupied by the anomalies change along the way across the South Atlantic. The upper anomalies, dominated by salinity changes, extend to lighter water masses, while the deeper anomalies, dominated by temperature changes, slightly gain density. Presumably due to mixing with surrounding water.

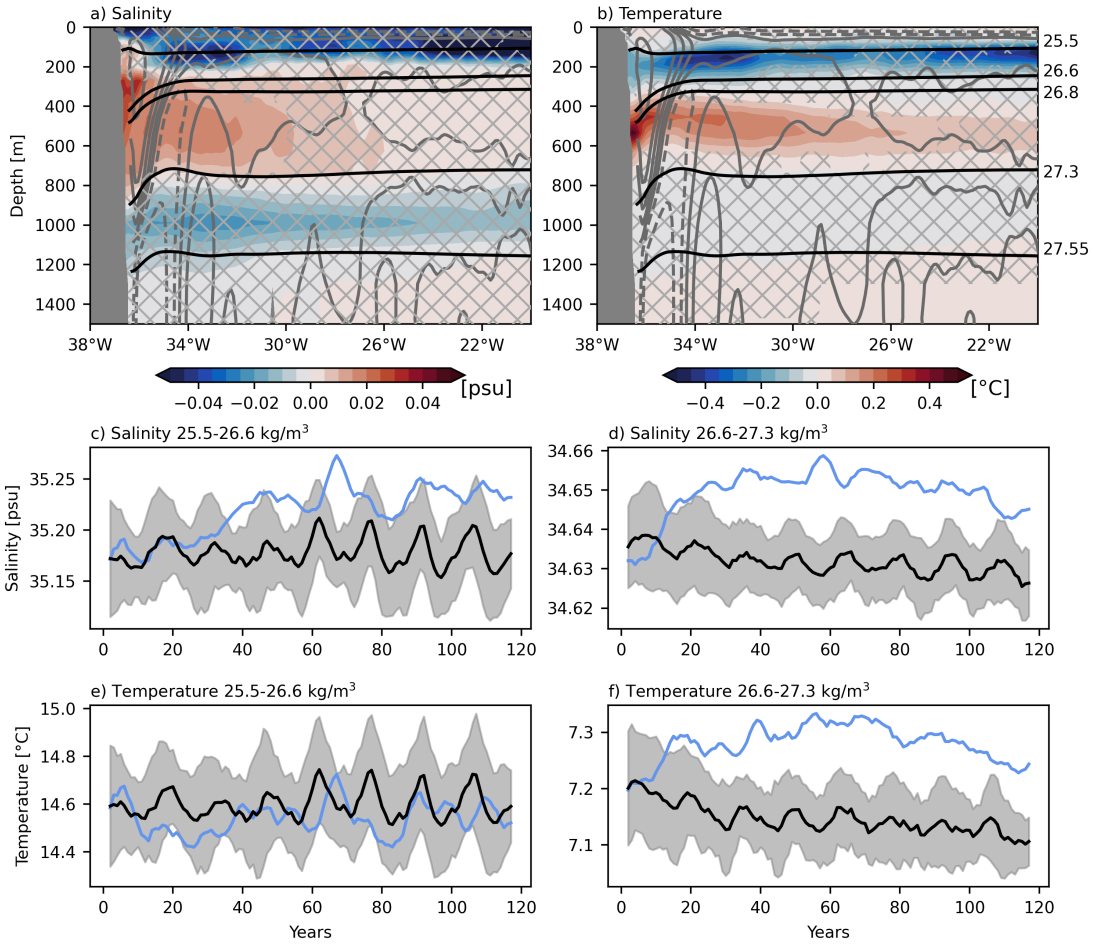

Figure 4.4: Temperature and salinity changes along the western boundary at 11°S. a,b) Ensemble mean temperature and salinity anomalies (years 20-30). Hatching indicates non-significant values. Grey/black contours show the mean velocity/density from the control experiment. Density contours are labelled on the right y-axis of b) in kg/m^3. Ensemble mean (blue) and control (black) salinity (c-d) and temperature (e-f) averaged in density ranges and within the North Brazil Current (western boundary to 35°W). Timeseries are smoothed using a 5-year boxcar window. Grey shading indicates the 95% confidence interval of the control time series.

As the density lines better represent the transition between the anomalies in figure 4.4a,b compared to depth levels, timeseries are calculate for the density ranges 25.5-26.6 kg/m^3 and 26.6-27.3 kg/m^3. Note that the density ranges are calculated for each ensemble member individually to capture the effect of the temperature and salinity anomalies on the isopycnals themselves. However, the vertical displacement of isopycnals is small compared to the defined density ranges and isopycnals from the control are a good representation of the considered density range for all experiments.

The timeseries show that the upper density range experiences an initial cooling (figure 4.4e). This cooling is only at the margin of being significant, because it peaks outside the NBC (here only the NBC west of 35°N is considered). An increase in salinity was visible in the lower part of this density range, but is partly compensated by a freshening of the upper part (figure 4.4a). Only after 30 years, the salinity increase outweighs the freshening and a strong increase in salinity sets in. The temperature remains insignificantly different from the control experiment. This is again in agreement with the assumption that the near-surface temperature anomaly is mostly eroded by atmospheric damping. In contrast, the mid-depth layer (26.6-27.3 kg/m^3) shows a sharp increase in temperature and salinity already after 10 years.

The transit time distribution of leakage water volumes shows that a salinity increase in the 25.5-26.6 kg/m^3 density layer may be expected within a decade, purely based on the advective timescale of the volume transport. Already 10 years after release in the Agulhas Current, almost 70% of the water volumes have reached 11°S, with the modal value of the distribution being 6 years (figure 4.3d). In agreement, anomalies are seen to appear within 20 years in the deeper part of this density range. Above 250 m, however, mixing of the warmer, more saline water from the south with the colder, fresher water that occupies this depth range at 11°S delays the development of positive salinity anomalies. When averaged over the full density range predominantly occupied by leakage volumes, significant changes only occur after year 30 (figure 4.4c).

Although the deeper density range (26.6-27.3 kg/m^3) is mostly supplied by water that is not directly originating from the Agulhas Current (leakage water volumes), the development of anomalies after 10 years is consistent with the expected transit time distribution.

Since the near-surface freshening and cooling is not consistent with advection from the south, another mechanism must be responsible. This is enhanced upwelling in the equatorial region and the Guinea Dome. Haarsma et al. (2011) find a similar coupled response (with opposite sign) to a shut-down of Agulhas leakage. Following their argumentation, a warming of the subtropics, due to an increase in Agulhas leakage, results in a southward shift of the Intertropical Convergence Zone (ITCZ). Connected to this southward shift, there is a significant increase in rainfall (causing a negative upward freshwater flux anomaly) south of the equator, a strengthening of the northern hemisphere trade winds and a weakening of the southern hemisphere trade winds (figure 4.5b,d). The near-surface cooling (figure 4.5a) is caused by increased equatorial upwelling, as the northern hemisphere wind stress increase overcompensates the southern hemisphere decrease. Another strong response can be seen in the Guinea Dome region. Haarsma et al. (2011) also found the Guinea Dome to strongly respond to changes in Agulhas leakage due to advection of the equatorial anomaly into this region. Furthermore, the South Atlantic salinity decrease is consistent with an increase in precipitation caused by the southward shifting ITCZ. In contrast, the local heat flux changes are small and, if significant, tend to damp the near-surface temperature anomalies (figure 4.5c).

The anomalously fresh and cold water, generated by enhanced equatorial upwelling, spreads across the tropical Atlantic and mixes with the anomalously saline water arriving from the SA STG, as described before. Thereby it prevents the development of strong salinity (and temperature) anomalies in the western boundary current above 250 m depth. In addition to the shift in the ITCZ position, increased evaporation over the Cape Basin may supply more moisture to the atmosphere, which is transported to the equator by the southern hemisphere trade winds. This can cause an additional increase in rainfall. The deeper layers, where anomalies in the NBC appear first, are not affected by these near-surface anomalies.

Once the warm and saline water masses from the South Atlantic enter the tropical Atlantic, the predominantly zonal currents spread them toward the eastern boundary. This is for example evident from a basin wide temperature and salinity increase in the depth range 300-1000 m (for example figure 4.7g, but similar anomalies along the equator can already be seen after 10-20 years).

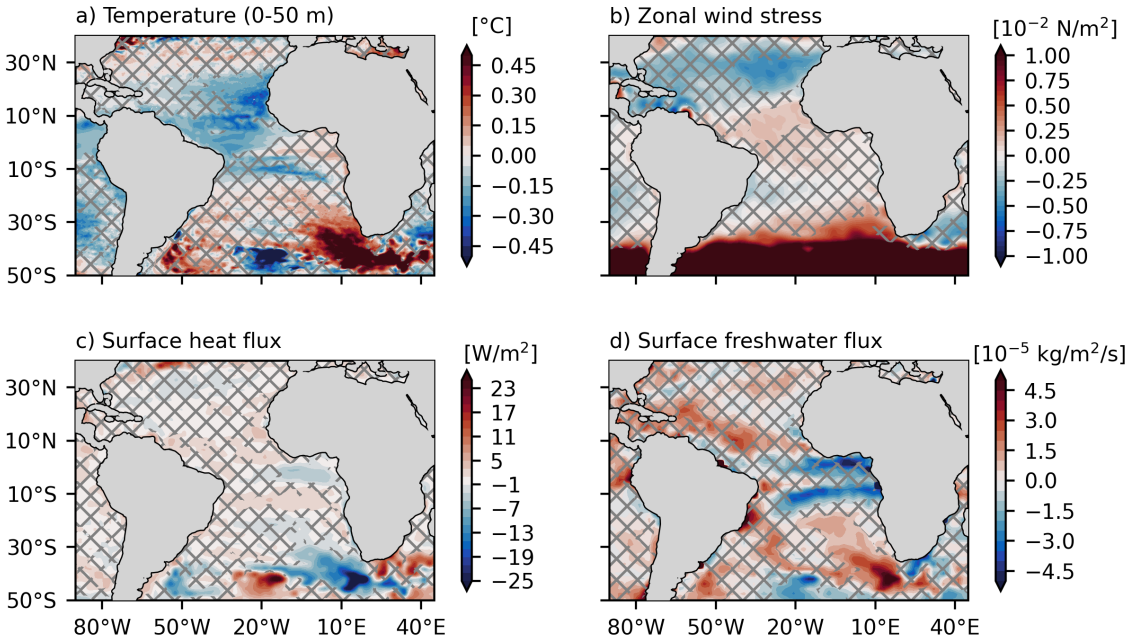

Figure 4.5: Changes in the surface tropical Atlantic. All panels show the ensemble mean anomaly (years 10-20). Non-significant values are hatched grey. a) Temperature averaged over the top 50 m, b) zonal mean zonal wind stress, c) downward surface heat flux and c) upward surface freshwater flux.

4.2 Propagation into the Subtropical North Atlantic

Further north, anomalies can be seen to develop in the subtropical North Atlantic in the perturbation experiment. Above 500 m the whole water column is more salty and between 200 and 500 m slightly warmer in the perturbation experiment (years 50 to 70). Strong temperature and weaker salinity anomalies can also be seen centred between 500 and 1100 m depth after 50 years, spread across the entire Atlantic (figure 4.6c,d).

Propagation of Mid-Depth Anomalies (500-1000 m)

In contrast to the described density layers occupied by the mid-depth anomalies at 11°S (26.6-27.3 kg/m^3), the anomalies are found in the 26.8-27.55 kg/m^3 layer at 27°N. Therefore, the anomalously warm and salty water mass gains density along the pathway by mixing with surrounding water. The zonal mean temperature anomaly clearly suggests that water spreads northward, forming a continuous tongue of warm water that gains density and sinks toward the subtropical North Atlantic (figure 4.6a,b). The anomalies in this depth (density) are not confined to the western boundary and can not be seen in the Gulf Stream (GS) at all, although at least the upper part of the density range is also found in the GS. Instead, the horizontal distribution (figure 4.6c,d) suggests that the anomalously warm and saline water mass is transported northward via interior pathways (this is discussed in more detail below). The time period shown was chosen to capture the stage when anomalies are still growing. As a result, anomalies are not yet significant for the whole section (compare figure 4.6i,j). As already described for changes in the Cape Basin, this layer carries a negative density anomaly, due to a dominance of thermal expansion over haline contraction (see for example figure 4.8h).

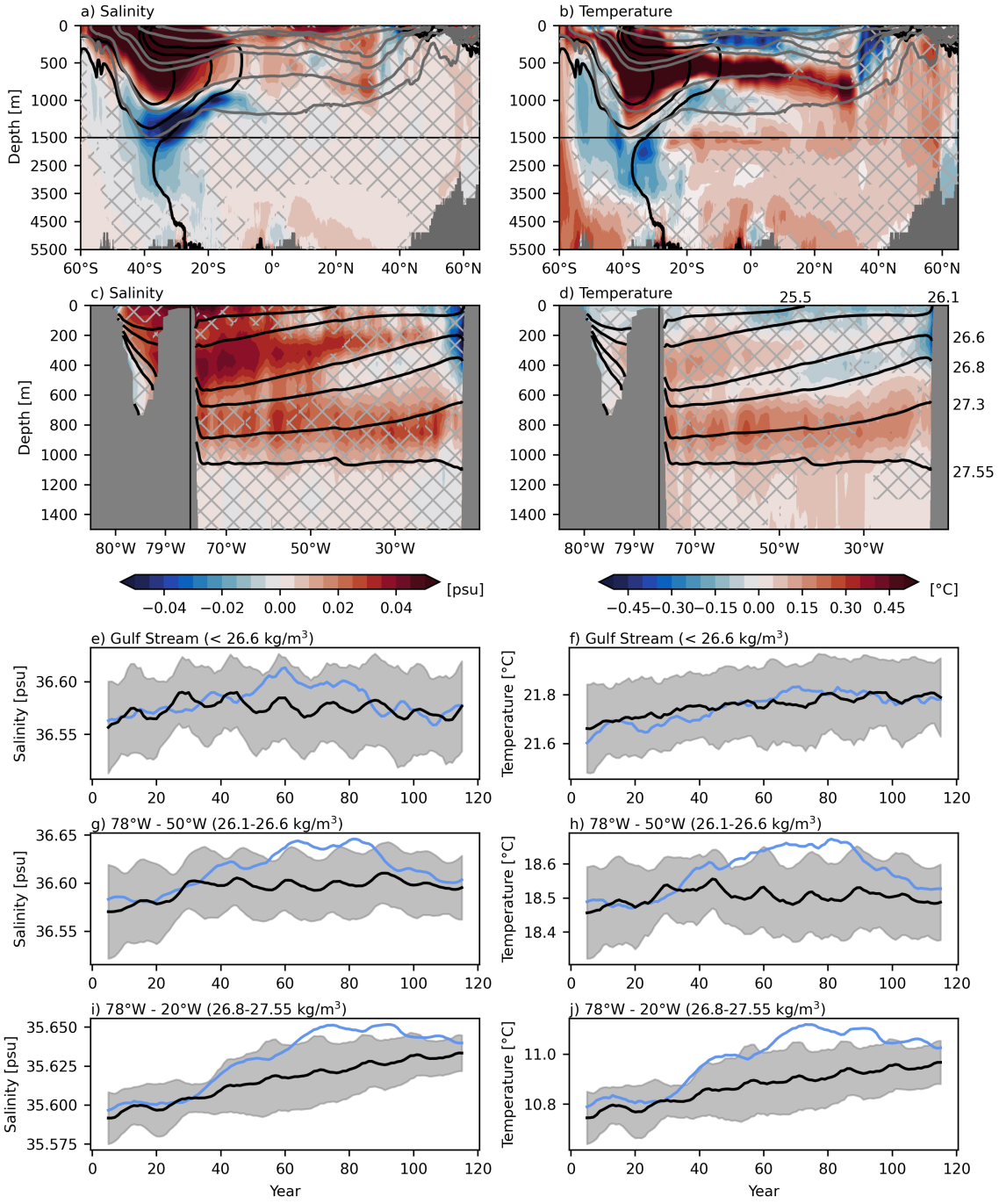

Figure 4.6: Water mass changes in the subtropical North Atlantic. a,b) Ensemble mean zonal mean salinity and temperature anomaly (years 50-70). Black/grey contours show mean salinity/density from the control experiment. c,d) Zonal section of the ensemble mean temperature and salinity anomaly (years 50-70) at 27°N. Hatching indicates non-significant differences. Black contours show mean density from the control experiment. Subplots a-d show the same isopycnals, which are labelled in d). e-j) Ensemble mean (blue) and control (black) temperature and salinity in density layers in the Gulf Stream (e,f), along the western boundary east of the Florida Strait (g,h) and the whole zonal extend of the Atlantic (i,j). Grey shading indicates the 95% confidence intervals for the control experiment.

Lagrangian experiments releasing water volumes in the 26.6-27.3 kg/m^3 density layer in the NBC at 11°N support the hypothesis that these anomalies spread via interior pathways. Water volumes tend to sink during several zonal excursion into the interior ocean (figure 4.7a). A large number of these water volumes spread eastward around 20°N. From there, they spill into the central North Atlantic Subtropical Gyre (NA STG; figure 4.7a,c), consistent with the development of anomalies spread across the basin (figure 4.6c,d). Note that figure 4.7c shows the first crossing of 27°N. Therefore, it can be ruled out that this water has recirculated in the NA STG. Although FOCI-ATLAS10 is not able to fully represent the complex equatorial circulation with a large number of zonal jets (e.g Ménesguen et al., 2019), it simulates a series of latitudinally alternating zonal currents below the thermocline. These currents can explain the strong zonal excursions up to 20°N. The density layer in which these water volumes cross 27°N in the eastern Atlantic is even higher than the core of the temperature anomaly (although this was already higher than the release density). This is not necessarily a mismatch. As the water volumes gain density, they mix with surrounding water of the same density, presumably around 20°N. Therefore, it is likely that all density classes between the release and arrival density can develop anomalies by mixing with these water volumes. Again, a perfect match is not expected due to mixing, but the Lagrangian probability shown in figure 4.7a and the ensemble mean temperature anomaly between years 50 and 70 in figure 4.7g show high agreement. Furthermore, the development of anomalies after 30-40 years (figure 4.6i,j) is consistent with the advective timescale of water following this interior pathway. The 100 years long experiments are clearly not able to capture the full connectivity, but the transit time distribution shows that within 30 years a significant amount of water volumes have reached 27°N and the gradual build up of the anomaly is consistent with the rather broad distribution (figure 4.7f).

Propagation of Near-Surface Anomalies

The larger fraction of water volumes released in the 26.6-27.3 kg/m^3 density layer across the NBC tend to rise along the pathway to cross 27°N above 500 m depth (figure 4.7c). Of the total transport released in the NBC per timestep (12.7 Sv), 43% (5.4 Sv) reach the 27°N section within 100 years. 22% (1.2 Sv) of this transport cross 27°N below 500 m and 78% (4.2 Sv) above 500 m. As mentioned before, 100 years are not sufficient to capture the full transit time distribution of the deep pathway, so the fraction and total transport is expected to increase for Lagrangian experiments that cover more than 100 years. Figure 4.7d,e show that the water volumes crossing 27°N above 500 m are predominantly, but not exclusively, released in the more shallow part of the seeding density range. Different pathways are taken by these volumes. Either they are entrained into the Equatorial Undercurrent and rise along its eastward pathway to eventually return west in the South or North Equatorial Currents (see exemplary trajectory in figure 4.7b), or they follow several recirculations closer to the western boundary in which they rise (an exemplary trajectory for this pathway is not shown). Both pathways transport the water volumes into the Gulf of Mexico, where they join the Florida Current. Furthermore, it is visible that these water volumes can leave the GS and recirculate in the western NA STG. A very similar distribution can be seen for the leakage volumes that cross the NBC at lighter densities. An average transport of 6.2 Sv (50% of the released leakage volumes) reaches 27°N within 100 years, predominantly in the GS (4.3c).

Although the near-surface shows strong salinity anomalies along the western boundary, advection of the salinity (and temperature) anomaly does not seem to be the main source of anomalies above 500 m. In the GS at densities lower than 26.6 kg/m^3, the salinity starts to increase after 40 years, peaking after 60 years (figure 4.6e). These changes are confined to the Gulf Stream, Antilles Current and its first recirculation (figure 4.6c,d). In general, this is consistent with the advective timescale. It was shown that in the density layer occupied by the majority of leakage volumes at 11°S, the salinity increase is only dominant after 30 years (figure 4.4c). The advective timescale from 11°S to 27°N is about 10 years (figure 4.3d,e). Thus, fast advection along the western boundary would be consistent with the timing and pattern of these anomalies. Further, no temperature anomaly develops within the GS, consistent with insignificant temperature changes in

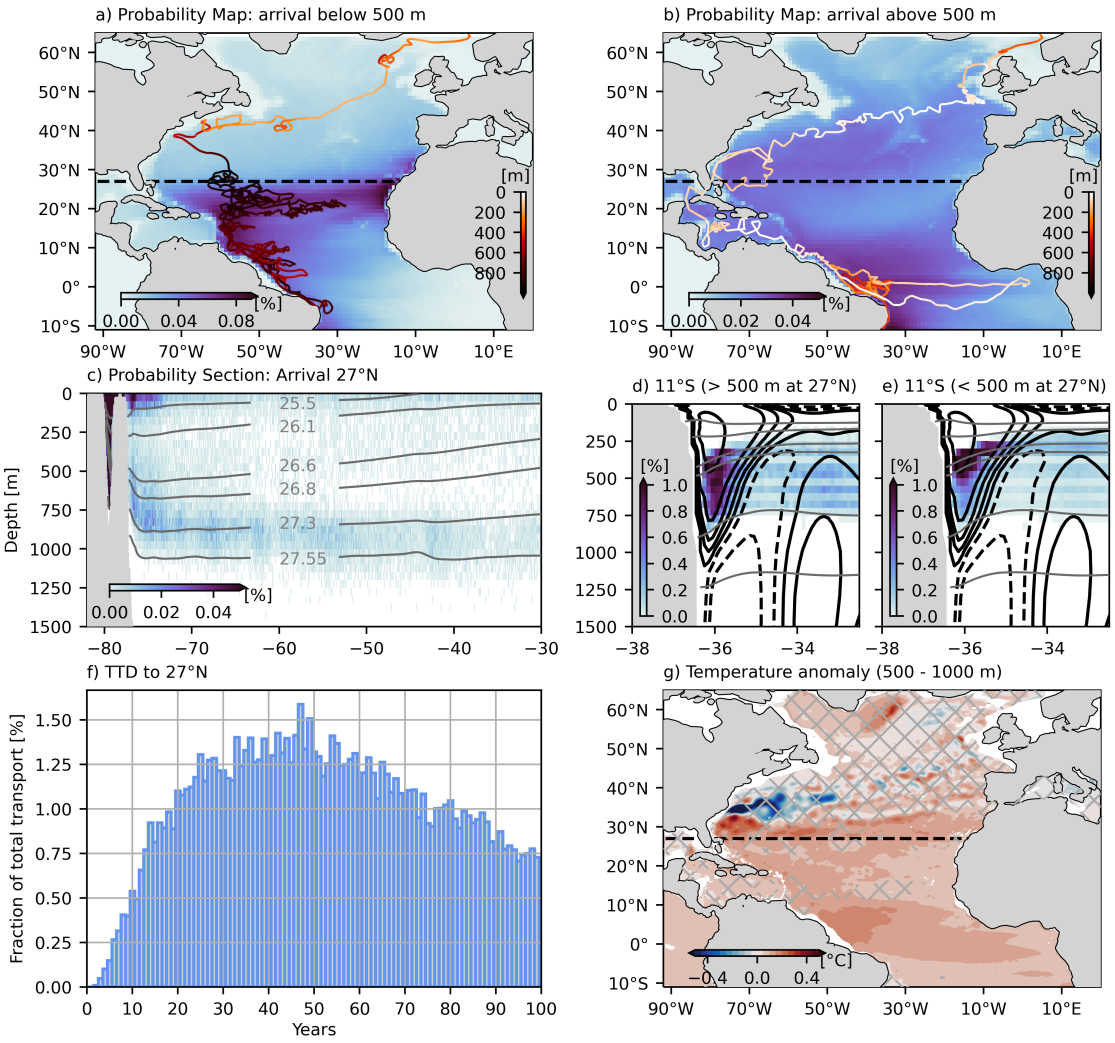

Figure 4.7: Lagrangian spreading of North Brazil Current water in the 26.8-27.3 kg/m^3 density range. Probability of water volumes that cross 27°N above (a) and below (b) 500 m to appear in 1° longitude × 1° latitude bins. Exemplary trajectories are colored by their depth. c) Probability to cross 27°N within 0.1° longitude × 50 m depth bins (only the first crossing of the latitude is considered). Initial distribution of all particles at 11°S, which cross 27°N below 500 m (d) and above 500 m (e) later on. Grey contours show the mean density from the control experiment and are labelled in c). f) Transit time distribution of all water volumes that cross 27°N below 500 m. g) Ensemble mean temperature anomaly (years 50-70) averaged over the 500-1000 m depth range. The dashed lines indicates 27°N and grey hatching indicates non-significant differences.

the near-surface NBC at 11°S. Although this hints on a potential pathway of salinity anomalies along the western boundary, these anomalies appear to be attenuated by other processes in the coupled model. Salinity anomalies are not significant when averaged over all densities lighter than 26.6 kg/m^3. They are marginally significant when averaged over the 26.1-26.6 kg/m^3 (not shown, but compare figure 4.6c), but the reason for changes in this density layer is likely not advection as discussed below. Furthermore, the anomalies only persist for a short period of time. After 80 years, anomalies in the Gulf Stream are no longer visible (figure 4.6e). It is hypothesised that the anomalies spreading from 11°S to 27°N along the western boundary are damped by mixing with fresher water in the near-surface tropical Atlantic. After 30 years the salinity increase in the NBC was found to overcome the freshening and consistently the GS salinity rises after 40 years. However, after 60 years a near-surface freshening of the NA STG caused by changes of northern hemisphere westerly winds (see also figure 4.8a,c) reduces anomalies in the GS again. The reason for this change is discussed below. The time when near-surface anomalies disappear is consistent with the time when freshwater anomalies recirculate in the NA STG.

Anomalies at Intermediate Depth (200-500 m)

Anomalies in the 26.1-26.6 kg/m^3 layer show a salinity and temperature increase after 30-40 years (figure 4.6g,h). These anomalies clearly reach a maximum outside the GS and extend further across the Atlantic than at densities lower than 26.1 kg/m^3 (figure 4.6c,d). These anomalies are more complicate to attribute to a specific source, because they can result from different processes. The initial warming and salinity increase after 30 years suggests that anomalies arrive together with the deeper anomaly, or are generated by vertical mixing with deeper anomalies. Note that water released in the mid-depth temperature and salinity anomaly in the NBC can also cross 27°N in the 26.1-26.6 kg/m^3 density range, especially along the western boundary (figure 4.7c). A recirculation of anomalies brought to 27°N in the GS is not consistent with a warming and also the salinity increase in the GS was shown to be small. The strongest contribution to anomalies in this density range is probably a local wind change that is described in more detail below (see also figure 4.8a). Consistent with this assumption, the strongest and significant anomalies can be seen after 40 years when the wind anomaly starts to develop. This change in wind stress causes stronger Ekman pumping around 27°N and leads to temperature and salinity anomalies between 200 and 500 m depth by displacing the thermo- and haloclines downward.

In summary, anomalously warm (and salty) water at mid-depths spreads into the North Atlantic via interior pathways and fills the NA STG between 500 and 1000 m depth. Salinity anomalies in the GS, consistent with advection from the South Atlantic, only appear for a short period of time, because other adjustments of the coupled model (most likely a wind shift) compensate the advection of anomalously salty water. In addition, anomalies outside the GS, but above 500 m develop by enhanced Ekman pumping. Overall, the main pathway for anomalies from the South Atlantic into the NA STG does not seem to be the Gulf Stream, but advection along interior pathways below 500 m in the here presented experiment. However, this is only because atmospheric adjustments of the coupled model cause mixing with anomalously fresh water along the shallower pathways in the western boundary current system. In an ocean-only set-up, the near-surface western boundary may appear to be the dominant pathway, as atmospheric adjustments are not simulated. Because there are hints on (salinity) anomalies being advected in the GS, it is also possible that larger anomalies could overcome the counteracting adjustments of the coupled model.

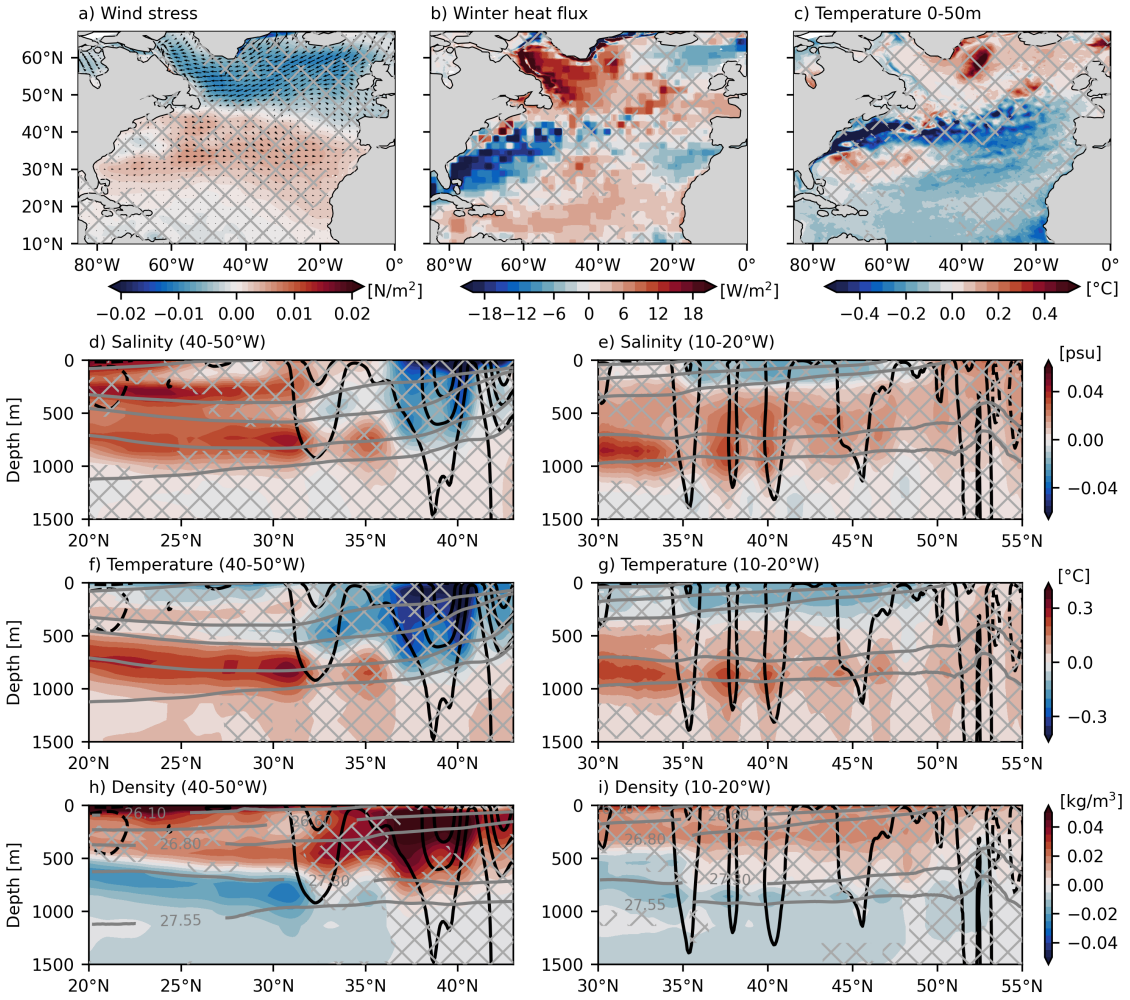

Figure 4.8: Changes across the Subpolar-Subtropical Gyre boundary. Ensemble mean wind stress (a, shading: zonal wind stress), winter mean (JFM) downward heat flux (b) and top 50 m temperature (c) anomalies. d,f,h) Ensemble mean salinity, temperature and density anomaly between 40°W and 50°W. e,g,i) same, but averaged between 10°W and 20°W. Black/grey contours shown the mean zonal velocity/density from the control experiment. In all subplots anomalies for years 60 to 80 are shown and grey hatching indicates non-significant differences.

4.3 Propagation into the Subpolar North Atlantic and Nordic Seas

It was shown that mid-depth anomalies propagate into the NA STG via advection. However, the zonal mean anomalies (figure 4.6a,b) show that the northward propagation of anomalies becomes even more complex in latitudes covered by the mostly zonal GS and North Atlantic Current (NAC). While especially the temperature anomaly shows a continuous tongue of warm water south of 35°N, it disappears in the zonal mean further north. Still, it can be seen that the SPG becomes warmer and more saline (see for example figure 4.10).

Advection in the GS and NAC

During no time period, it is possible to continuously track the anomalies in the GS, after its separation from the coast, or in the western NAC. Lagrangian experiments reveal that the water volumes that cross into the SPG (here 53°N) do not simply follow the near-surface flow, even when crossing 27°N in the top 500 m (figure 4.9e). Instead, they follow several recirculations around the western or entire NA STG and sink along the pathway. The exemplary trajectory in figure 4.9e crosses 27°N around 200 m, but after several recirculations it reaches the SPG below 500 m depth. This is in good agreement with Burkholder and Lozier (2014) and Berglund et al. (2017). The mode of the transit time distribution for water volumes following these pathways is around 35 years. When crossing the 53°N water volumes cover a depth range between 0 and 700 m (figure 4.9g).

Maps, as well as the zonal mean anomalies between 40°W and 50°W, show that south of the GS/NAC strong anomalies develop, but within the GS/NAC anomalies are not significant and even more important of opposite sign (figure 4.8d,f,h and 4.9a-d). The entire GS/NAC west of approximately 20°W and down to 1000 m tends to be colder and fresher in the perturbation experiment. Further, the negative anomalies are centred in the GS/NAC position of the perturbation experiment, indicated by the ensemble mean 10 cm/s speed contour (figure 4.9a-d). Thus, these changes do not just reflect a southward shift of the currents compared to the control experiment. The Lagrangian pathways, together with the anomaly pattern, suggest that the near-surface anomalies, which are already insignificant at 27°N in the GS (for most density layers), are eroded by mixing in the GS extension and western NAC and not able to cross into the SPG. Even though the sinking particles may cross the mid-depth NA STG, warm due to the mid-depth anomaly and then rejoin the NAC at greater depth, this does not seem to provide a pathway into the SPG, because the GS and western NAC show a cooling down to 1000 m.

The reason for this cooling and freshening in the GS extension could be related to a dynamical response. The arrival of the mid-depth temperature and salinity anomalies after 40 years is associated with a negative density anomaly as discussed before (see also 4.8h). The negative density anomaly is larger at the western boundary than at the eastern boundary, although the anomaly spreads across the entire Atlantic (density is not shown, but compare figure 4.3g). This is also consistent with more Lagrangian water volumes crossing 27°N first along the western boundary (figure 4.3c). A stronger decrease in density at the western boundary results in more southward geostrophic transport. This southward transport is partly balanced by a speed up of the Gulf Stream and Antilles Current (this is discussed later, see figure 4.17). A speed up of the GS and the associated speed up of the Northern Recirculation Gyre (NRG) causes upper ocean divergence and leads to a subsurface cooling and freshening (Zhang, 2008). Although, the GS extension and NAC are colder in the perturbation experiment they could still contribute to anomalies further north. However, not through the mean advection of anomalous temperature and salinity, but the anomalous advection of mean temperature and salinity.

Atmospheric Response

Furthermore, an atmospheric response that starts to develop after 40 years could generate strong anomalies in the SPG. It is characterised by negative wind stress anomalies (easterly winds) in the SPG region and positive anomalies in NA STG. This pattern is associated with a southward shift of the northern hemisphere westerlies (figure 4.8a). Dewar et al. (2022) describe a similar wind anomaly and speculate that it could be caused by enhanced winter heat loss to the atmosphere over the NA STG. Indeed winter heat loss is strongly enhanced in the western NA STG (figure 4.8b, similar anomalies in the NA STG can be also seen for years 40-60). Note however, that the near-surface temperature anomaly during years 60-80 is negative (figure 4.8c). It is hypothesised that after 40 years the strengthened GS transport causes initially warmer sea surface temperatures by anomalous northward advection of the mean temperature (this is not shown, but can be seen in the experiment). The stronger heat loss causes a southward shift of the winds. Between years

60-80 the stronger heat loss is maintained in the presence of negative SST anomalies, by increased wind speeds over the NA STG.

The southward shifting winds are further associated with anomalous northward Ekman transport into the SPG and anomalous southward Ekman transport into the NA STG. This leads to a warmer, more saline SPG and a cooler, fresher NA STG. Although temperature changes are not significant in the SPG, the pattern of near-surface temperature anomalies supports this hypothesis (figure 4.8c). Furthermore, the southward shifting winds are also linked to a southward shift of the boundary between Ekman suction (north of the wind stress maximum) and Ekman pumping (south of the wind stress maximum), which could contribute to a near-surface warming and salinity increase north of the westerlies. The more southern position of Ekman suction causes upwelling of warmer and more saline water, especially because it could cause enhanced upwelling of anomalous warm and salty water that has arrived from the south. Additionally, the wind shift is consistent with the pattern of heat flux changes (figure 4.8b) in the central and western SPG. The negative wind stress anomaly results in smaller turbulent heat fluxes and less cold air outbreaks from the continent that are important for strong heat loss events in the Labrador Sea (Marshall & Schott, 1999). A southward shift of the westerlies is also associated with increased rainfall south and decreased rainfall north of the intergyre boundary, consistent with the changes in salinity (figure 4.8e). Lastly, the changes in wind enhance the negative wind stress curl over the central NA STG and could reinforce the initial spin-up of the gyre that was described above.

Deep Pathways into the SPG

The deeper anomalies seen at 27°N, represented by water volumes released in the NBC at 11°S and subsequently crossing 27°N below 500 m, can also take a different pathway avoiding strong mixing in the western NAC. Of the 12.7 Sv released in the NBC about 1.9 Sv (15%) reach 53°N within 100 years per release timestep. 1.4 Sv take the aforementioned shallow pathway (GS/NAC and recirculation in the NA STG) and cross 27°N above 500 m, while 0.5 Sv take the deep pathway after crossing 27°N below 500 m. Most of the water volumes that reach the SPG from the deeper depth range follow the eastern boundary northward at depths between 500 and 1500 m (figure 4.9f). They directly cross into the SPG without being transported in the NAC and predominantly in the 200-1000 m depth range (figure 4.9h).

In agreement with the deep volume transport pathway, the zonal mean anomalies between 10°W and 20°W, show more continuity across the NAC down to 1000 m (figure 4.8e,g,i). Water in this longitude range becomes warmer and saltier, approximately bounded by the 27.55 kg/m^3 density contour at depth, but extending to the surface. This suggests that intense vertical mixing within the western extension of the NAC causes the anomaly to spread across the entire water column. The ensemble mean temperature and salinity anomaly maps (years 60-80) also hint on a propagation of anomalies into the SPG along the eastern boundary (figure 4.9 a-d). Especially the anomalies between 500-1000 m depth show a continuous warming and salinity increase across the NAC. The appearance of anomalies after 50-60 years is consistent with the advective spreading of the mid-depth anomalies along the eastern boundary. Although the 100 years long experiments are again clearly too short to capture the full transit time distribution, it is visible that a significant number of water volumes can reach 53°N within 50-60 years after being released in the NBC (figure 4.9i,j). However, it should be noted that neither the maps, nor the sections show significant changes north of 40°N. This could be caused by the mentioned vertical mixing that spreads the anomaly over a larger volume of water, reducing its magnitude, and lateral mixing with the cooler, fresher water found in the GS and western NAC.

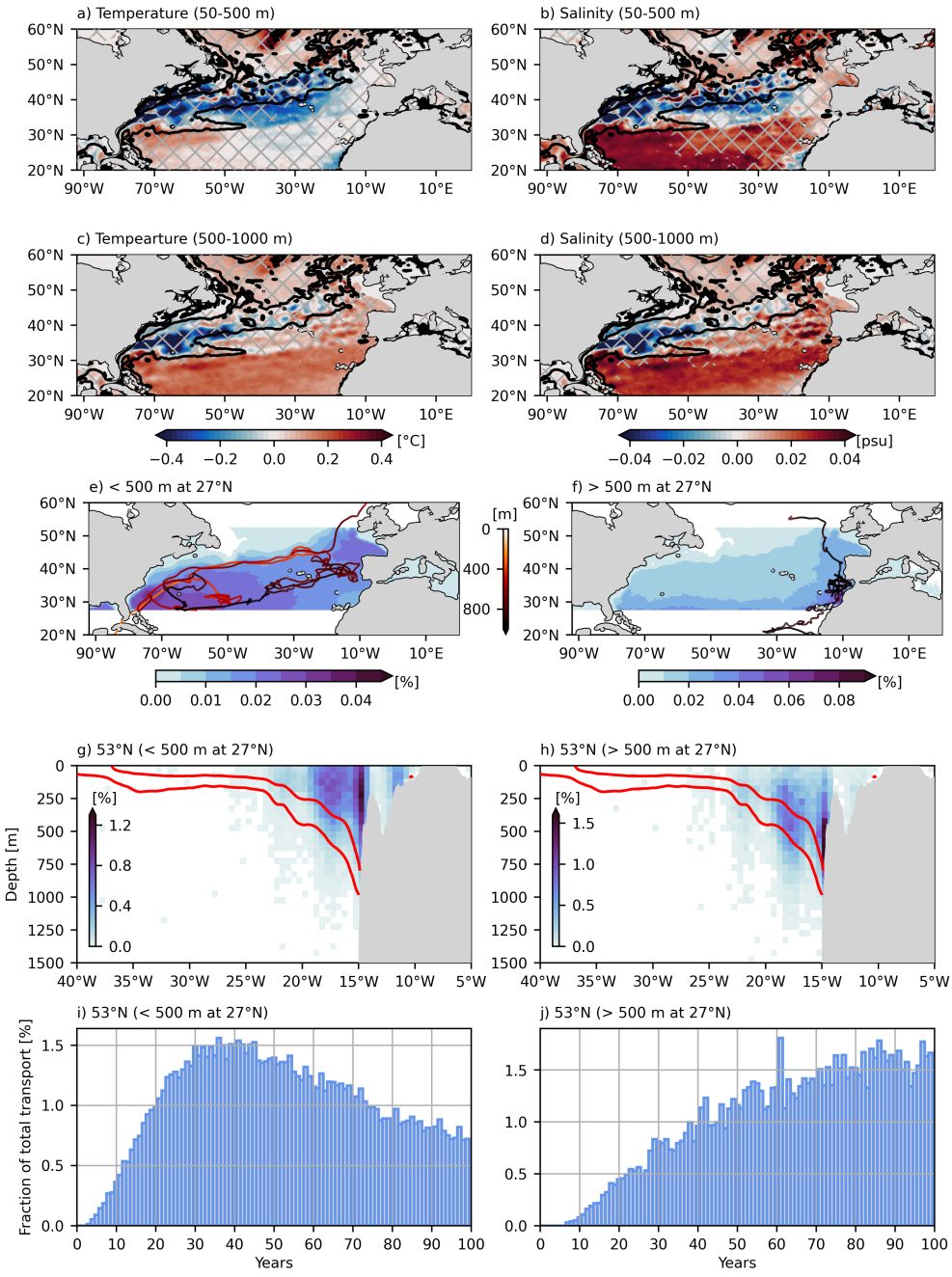

Figure 4.9: Propagation of anomalies across the Subpolar-Subtropical Gyre boundary. a-d) Ensemble mean temperature and salinity anomalies (years 60-80) averaged over different depth ranges. Grey hatching indicates non-significant differences. Black lines show the 10 cm/s contour of surface speed from the perturbation ensemble mean, indicating the position of the Gulf Stream and North Atlantic Current. Probability maps of Lagrangian water volumes to cross 0.5° longitude x 0.5° latitude bins after crossing 27°N above (e), or below (f) 500 m. Exemplary trajectories are coloured by their depth. Probability to cross 53°N in 0.5° longitude x 50 m depth bins after crossing 27°N above (g), or below (h) 500 m (only the first crossing of 53°N is considered). Red contours show the 27.3 and 27.55 kg/m^3 isopycnals from the control experiment. Transit time distribution from 11°S to 53°N for water volumes crossing 27°N below (i) and above (j) 500 m depth.

In summary, the SPG becomes warmer and more saline in the perturbation experiment after approximately 50-60 years. The processes responsible for the development of anomalies in the SPG are highly complex. Mechanisms that could explain the development of anomalies are an enhanced Gulf Stream transport, a southward shift of the westerlies and the arrival of anomalies along the eastern boundary. Probably all of these mechanisms have a contribution to the anomalies seen in the perturbation experiment, but it is beyond the scope of this chapter to evaluate their relative importance. Furthermore, the NA STG-SPG transition can generate temperature and salinity variations via a myriad of additional mechanisms. One of them is a northward shift of the gyre's southern boundary, which allows a more northward penetration of the warm and saline NA STG water (Burkholder & Lozier, 2011; Martin et al., 2015). However, a strong shift in the SPG boundary is not present in the experiments, even though the zero wind stress curl line shifts slightly south with the winds. Another mechanism that can generate anomalies in the SPG is a change in the AMOC, which is discussed later. While the described wind response is found to be consistent with reduced heat loss in the central and western SPG, heat loss in the eastern SPG (Iceland Basin and Rockall Trough region) increases (figure 4.8b). Most likely this is caused by the emergence of temperature (and salinity) anomalies. Rising temperatures increase the air-sea temperature difference, especially in winter, and generate stronger turbulent heat fluxes.

Anomalies at the OSNAP Section

Associated with the aforementioned anomalies, the whole SPG, here represented by changes along the OSNAP section (Lozier et al., 2019), becomes warmer and more saline after 60 years (figure 4.10a,b). Except for the Rockall Trough region and the boundary currents, which tend to become more dense, most of the SPG develops a negative density anomaly (figure 4.10c). Therefore, the warming overcompensates the salinity increase. The Rockall Through region does not show a negative density anomaly, because it lacks a near-surface warming. This is consistent with the increased winter heat loss in this region discussed before (figure 4.8b). As hypothesised, the warm and saline water enters the Rockall Through region along the eastern boundary and/or is generated by an anomalously strong GS/NAC, or northward Ekman transport. The temperature anomaly is then damped by the atmosphere, creating a positive density anomaly.

The increased density in the near-surface boundary currents along the east and west of Greenland is likely related to the changes in wind stress as well. The ice-cover east of Greenland decreases (not shown), exposing more open water to the cold atmosphere, which leads to a stronger heat loss (figure 4.8b). It is possible that the anomalous southward wind stress drives onshore Ekman transport, which forces more exchange between the cold, fresh East Greenland Current and the warm, saline Irminger Current. This can cause the sea-ice to retreat and salinity to increase. The stronger heat flux damping due to less sea-ice then reduces the temperature anomaly, leaving a positive density anomaly close to the surface. The negative density anomalies in the Irminger and Labrador Sea is presumably driven by the aforementioned combination of anomalous northward Ekman transport of warm water, in combination with reduced winter heat loss in the western and central SPG, due the southward shifting westerly winds. The anomalies in the Labrador and Irminger Basin reach down beyond 2000 m, which is in agreement with very deep winter mixed layers in both areas in FOCI-ATLAS10.

Between years 80 and 100 the salinity and temperature anomalies have grown and are now significant almost everywhere (figure 4.10d,e). The Labrador Sea, initially less dense, becomes more dense in the perturbation experiment, but both changes are mostly not significant (figure 4.10f). The most notable difference to the previous period (years 60-80) is a strong increase in density along Greenland reaching down to 3000 m. This anomaly occurs at depths beyond the NA STG inflow that are supplied by the dense overflow from the Nordic Seas.

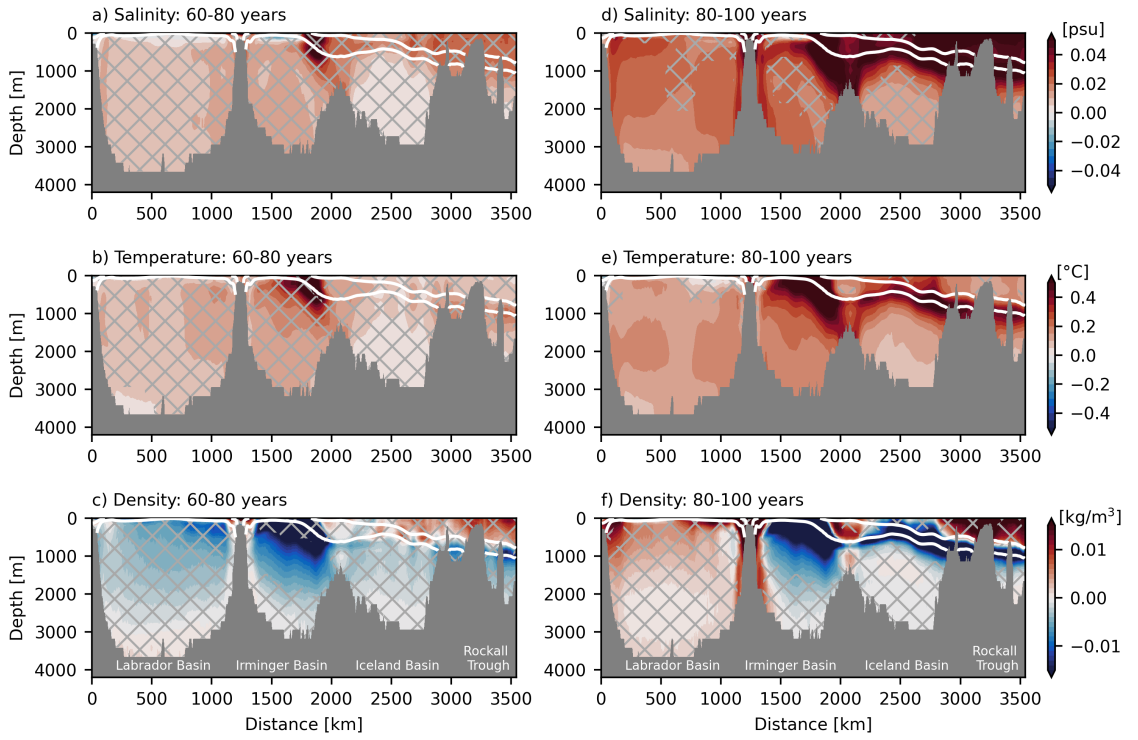

Figure 4.10: Changes along the OSNAP section. a-c) Ensemble mean salinity, temperature and density anomalies (years 60-80). d-f) same but for years 80 to 100. Grey hatching indicates non-significant differences. White contours show the 27.3 and 27.55 kg/m^3 isopycnals from the control experiment. Names of the different basins in the subpolar North Atlantic are shown in the bottom panels.

Anomalies in the Nordic Seas and Overflows

Therefore, it is now examined how this strong density anomaly in the deep SPG is generated. Water in the Rockall Through region and Iceland basin at densities higher than 27.3 kg/m^3 is less dense, but this water is too deep to cross into the Nordic Seas. Water in the top 400 m, which is the main depth range of the inflow into the Nordic Seas (Orvik et al., 2001), is dominated by positive salinity and density anomalies. As described before, the reason is an anomalous ocean heat loss that damps the arriving temperature, but not salinity, anomalies. Maps of temperature, salinity and density anomalies clearly show that in the top 400 m significant temperature anomalies only exist south of the sills (figure 4.11a,c,e). At the same time, salinity anomalies do extend across the entire Nordic Seas and lead to a significant increase in density. This more dense water flows cyclonically around the Nordic Seas. Although the inflow is mostly confined to the upper ocean, the salinity and temperature anomalies can be seen down to 1000 m depth, consistent with deep mixing in the Nordic Seas. The anomalies follow the cyclonic circulation around the Nordic Seas to again reach the sills and re-enter the SPG as Denmark Strait and Iceland-Scotland overflow.

The section across the Denmark Strait (figure 4.12a-c) clearly shows that the overflow water becomes saltier, but not warmer, resulting in a positive density anomaly that enters the SPG. The overflow, defined as water with density higher than 27.8 kg/m^3 (e.g Våge et al., 2013), shows significant changes in salinity after approximately 80 years. Density rises already after 60 years, but the increase between years 60 and 80 is caused by a non-significant cooling. Afterwards the temperature of the overflow stabilises, not showing a positive anomaly, and the salinity increase causes the overflow density to rise even further (figure 4.12d,f,h). A similar description is valid for

the Iceland-Scotland Overflow water (Figure 4.12e,g,i). The main difference is that an increase in salinity and density sets in earlier (after 60 years) and the temperature tends to increase as well, although not significant. Both results are reasonable, because the Iceland-Scotland overflow is in close proximity to the main inflow pathway and mixing may occur.

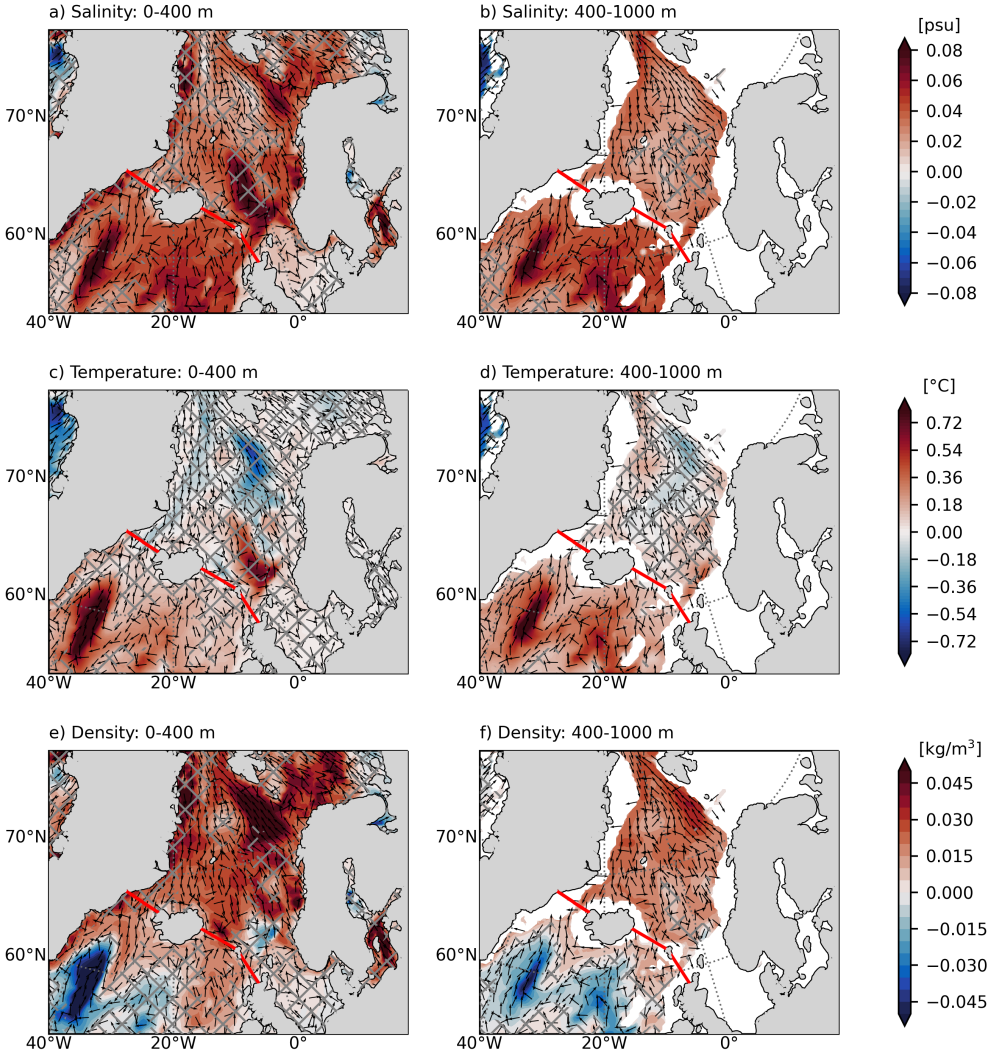

Figure 4.11: Changes in the Nordic Seas. a,c,e) Ensemble mean salinity, temperature and density anomalies averaged over the top 400 m. b,c,f) same, but averaged between 400 and 1000 m. Red lines indicate the section used to derive the overflow properties. Vectors show the mean velocity from the control experiment in the respective depth layers. Grey hatching in all subplots indicates non-significant differences and anomalies are calculated for years 80 to 100.

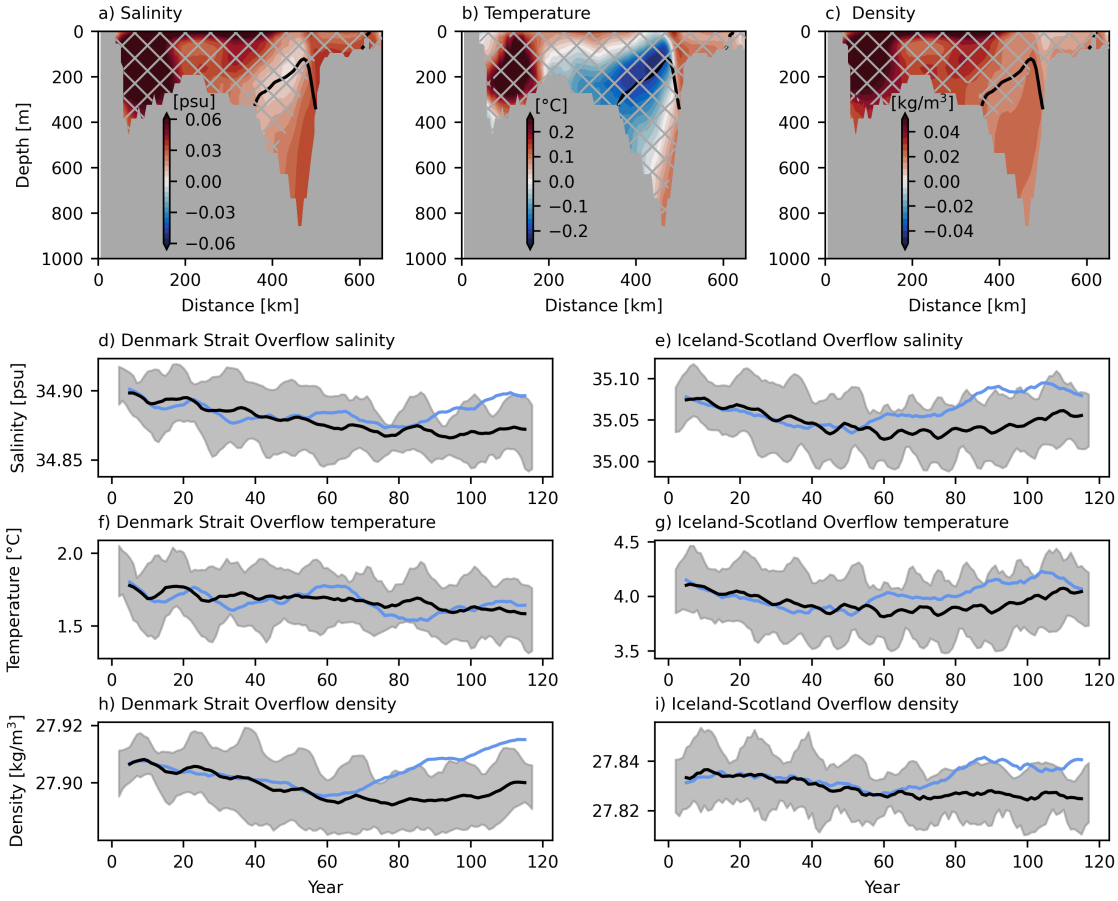

Figure 4.12: Changes in the Nordic Seas overflow properties. a-c) Ensemble mean salinity, temperature and density anomalies (years 80-100) across the Denmark Strait. Grey hatching indicates non-significant differences. The black contour shows the position of the 27.8 kg/m^3 isopycnal in the control experiment. d,f,h) Ensemble mean (blue) and control (black) Denmark Strait overflow temperature, salinity and density (defined as the mean at densities exceeding 27.8 kg/m^3). e,g,i) same, but for the Iceland-Scotland overflow. Grey shading represents the 95% confidence interval for the control experiment.

Deep Water Anomalies in the SPG and NA STG

It is further possible to track the increase in density from the overflow sills along the SPG boundary. A map of the density anomaly between 1500 and 3000 m (years 80-100) shows no significant changes, except for a narrow band along the boundary of the SPG, where density is significantly higher than in the control experiment (figure 4.13a). This suggests that the density anomaly spreads around the SPG within less than 20 years. The anomaly can be clearly seen in the Deep Western Boundary Current (DWBC) at the exit of the Labrador Sea (53°N) after 90 years (figure 4.13c-e). It is interesting to note that a temperature and salinity increase sets in already after 50-60 years, consistent with the first anomalies appearing in the SPG, as described before. However, these changes are mostly density compensating. Only after 90 years, when the salinity strongly rises, while the temperature anomaly remains constant, a strong increase in density occurs.

From the exit of the Labrador Sea the anomalies are exported into the subtropics. The salinity anomaly averaged over 2000-3000 m (the layer occupied by the DWBC, but not by water recirculating in the NA STG) suggests that the anomaly is quickly transported south in the DWBC and

interior southward pathways. South of approximately 30°N, the anomalies are mostly confined to the DWBC. Between years 110-120 a positive salinity anomaly can be seen extending southward to the equator (figure 4.13b).

In summary, the more saline and dense water enters the Nordic Seas and spreads in the eastern basin to the north. The shallow sill depth and atmospheric damping prevent strong temperature anomalies to occur in the Nordic Seas. The density anomaly then follows the cyclonic circulation into the western Nordic Seas to generate an overflow density anomaly that propagates along the boundary of the SPG. Density compensating salinity and temperature anomalies that start to develop in the SPG deep convection regions before anomalies in the overflow water reach the Irminger and Labrador Basins, spread in the DWBC and interior pathways to reach the subtropical North Atlantic at depth below 1500 m.

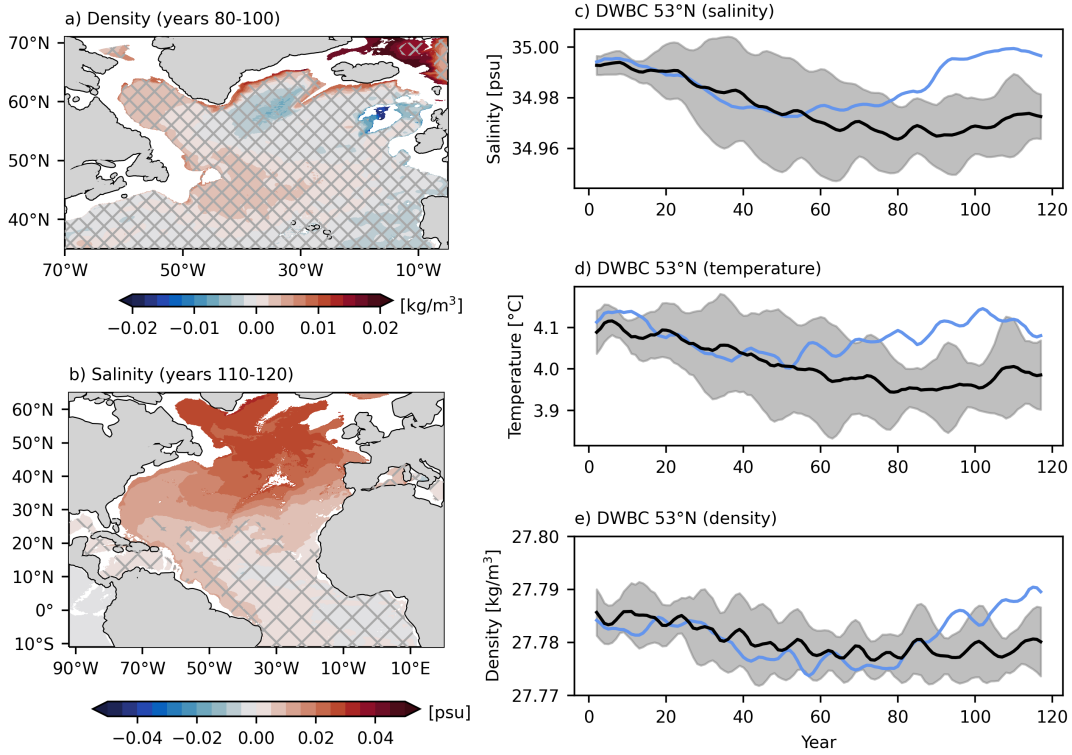

Figure 4.13: Changes in the deep Subpolar Gyre and Deep Western Boundary Current. a) Ensemble mean density anomaly (years 80-100) averaged between 1000 and 3000 m. b) Ensemble mean salinity anomaly (years 110-120) averaged between 2000 and 3000 m. Grey hatching indicates non-significant differences. c-e) Ensemble mean (blue) and control (black) salinity, temperature and density in the Deep Western Boundary Current at 53°N (below 400 m). Grey shading indicates the 95% confidence interval for the control experiment.

5. AMOC Response

The initial South Atlantic overturning response to the increase in wind stress is only small. Significant changes in the Overturning Streamfunction do not occur within the first years, except for a minor strengthening and extension of the shallow tropical cell (similar to figure 4.14d 25.5-26.5 kg/m^3, but already visible after 10 years). This is consistent with the aforementioned increase in equatorial upwelling. However, the changes have no major impact on the net northward/southward transports above/below the overturning maximum, as evident from figure 4.14a,b.

Nevertheless, it was shown that sub-surface salinity and temperature anomalies can propagate from the South Atlantic into the North Atlantic. The arrival of temperature and salinity anomalies in the eastern SPG were suggested to generate a positive density anomaly. Coinciding with the first development of density anomalies in the overflow after 60 years, the AMOC transport starts to increase (figure 4.14a,b). After 80 years, the AMOC transport is significantly stronger in the perturbation experiments (1.2 Sv in the ensemble mean). Although differences are visible in the latitude of the maximum AMOC anomaly, the AMOC in density and depth coordinates show a similar temporal evolution. Once AMOC anomalies start to develop in the North Atlantic, they are quickly propagated south within a few years.

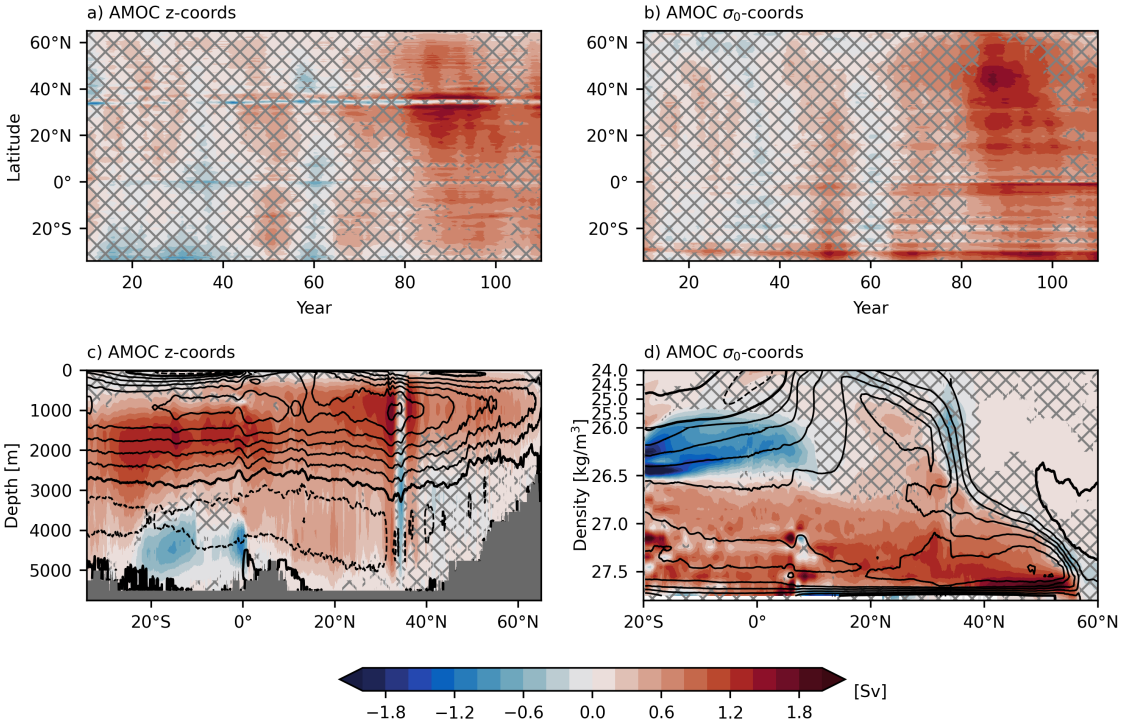

Figure 4.14: Changes in the Atlantic Meridional Overturning Circulation. Hovmöller diagram of the ensemble mean AMOC transport anomaly in depth (a) and density (b) coordinates. The AMOC timeseries was smoothed by applying a 10-year boxcar filter. Ensemble mean anomaly of the meridional overturning streamfunction (years 80-100) in depth (c) and density (d) coordinates. Grey shading indicates non-significant differences. Black contours (3 Sv intervals) show the mean streamfunction of the control experiment.

The mean overturning streamfunction anomaly between years 80 and 100 shows a basin wide spin-up of the NADW cell, with enhanced sinking between 45°N and 60°N. The pattern is broken by a locally anomalous counter-clockwise circulation across the GS/NAC (approximately 35°N).

This is in good agreement with Dewar et al. (2022). They show that a wind anomaly, very similar to the one shown in 4.8a, can drive an anomalous counter-clockwise circulation cell via Ekman transport changes. However, this local cell does not seem to break the latitudinal coherence of AMOC changes and it is not visible in density coordinates. The AMOC streamfunction in density coordinates reveals a spin-up of the NADW cell (density higher than 26.5 kg/m^3) mostly driven by enhanced water mass transformation between 40°N and 60°N and the subsequent increase in overflow density.

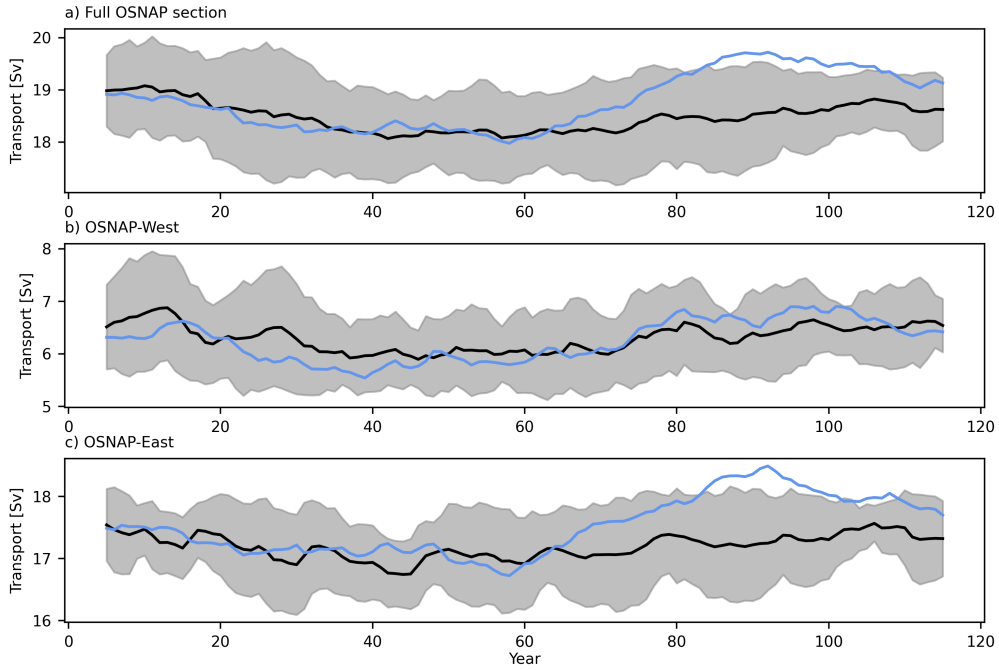

Figure 4.15: Overturning across the OSNAP section. a) Ensemble mean (blue) and control (black) overturning transport (defined in density coordinates) across the full OSNAP section, OSNAP-West (b, west of Greenland) and OSNAP-East (c, east of Greenland). Grey shading indicates the 95% confidence interval for the control experiment.

The clear AMOC anomaly in the experiment allows to further evaluate how the temperature, salinity and density anomalies generated in the SPG cause the AMOC to increase. In density coordinates, a speed up of the AMOC is associated with enhanced water mass transformation from light to dense water. The streamfunction anomaly suggests that this mainly occurs in the SPG and southern Nordic Seas. Calculating the overturning across the OSNAP section in density coordinates further reveals that the full response is caused by enhanced overturning north of OSNAP-East and thus in the Rockall Through region and Iceland Basin (figure 4.15). The Labrador Sea does not contribute to the overturning response in the here presented model experiments. Overturning changes across OSNAP-West are not visible. Although the Irminger Sea is located north of OSNAP-East, density in the central Irminger Sea is found to be lower in the perturbation experiment and thus there is no increase in light to dense water mass transformation in this basin (figure 4.10c,f). This is consistent with the previous result that a positive density anomaly in the North Atlantic develops from atmospheric damping of temperature anomalies around the shallow sills separating the Nordic Seas and North Atlantic. The timing is consistent, as well. The perturbation ensemble starts to deviate from the control experiment after 60 years, which was the time first temperature and salinity anomalies appear in SPG.

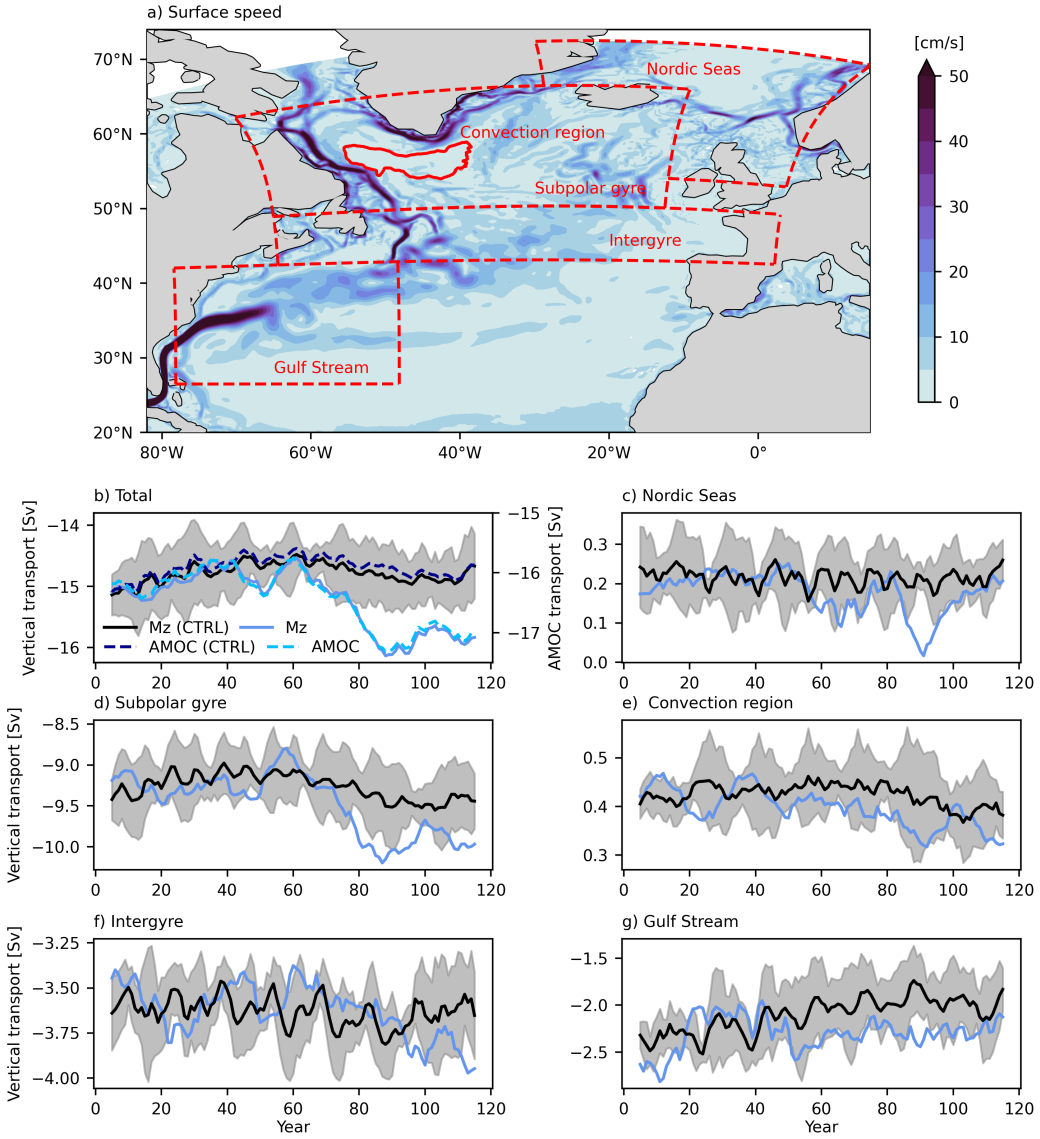

Figure 4.16: Changes in the vertical transport across the overturning maximum (1060 m depth). a) Mean surface speed from the control (CTRL) experiment and definition of the regions used in subpanels b-g. The solid red line shows the 1000 m March mixed layer depth contour from the control experiment. b) Ensemble mean (blue) and control (black) net vertical transport (Mz) across 1060 m depth and AMOC transport at 26.5°N. The sign of the AMOC transport is reversed to match the sign of vertical velocities associated with an increased AMOC transport. c-g) Ensemble mean (blue) and control (black) net vertical transport in the different regions defined in a). Grey shading shows the 95% confidence interval for the control experiment.

This more dense water then returns to the SPG within the overflow and was found to spread along the deep boundary of the SPG. Katsman et al. (2018) show that an increase in density along the boundary generates enhanced downward vertical transport. This is supported by the perturbation experiment. The total vertical transport across the depth of the overturning maximum (1060 m) in the different sub-regions shown in figure 4.16a closely matches the AMOC transport at 26.5°N (figure 4.16b). Splitting this transport into the contribution from different sub-regions reveals that the largest contribution to the anomalous vertical transport, associated with the AMOC

increase, comes from the SPG, outside the deep convection regions (figure 4.16c-g). The deep convection region is here defined by the extend of the 1000 m March mixed layer depth contour. Significant anomalies can occur in other regions as well, but their magnitude is still small (of order 0.1 Sv), while the SPG contribution is of order 1 Sv. Note that this vertical transport just provides information about the AMOC in depth coordinates and not about a possible contribution to overturning in density coordinates via a diapycnal transports.

Lastly, it is investigated how the AMOC response manifests within the circulation across the 26.5°N section (position of the RAPID mooring array). Therefore, the upper AMOC branch is decomposed into Ekman, Upper Mid-Ocean (UMO) and Gulf Stream (Florida Strait) transport (e.g. Rayner et al., 2011). The Antilles Current is often regarded as part of the UMO, but investigated individually here. The decomposition shows that the UMO changes after 40 years, consistent with the decrease in western boundary density and increase in wind stress curl (via the Sverdrup relation, see chapter 1) mentioned before (figure 4.17a). This transport is mostly compensated by an increase of the Antilles Current and Gulf Stream and does not cause a strong AMOC change. A net AMOC increase can be seen, after the Gulf Stream transport strongly increases after 60 years, while the UMO remains at an average value. Note that indicating significant changes was omitted, because several different timeseries are compared in the same panel. The AMOC transport (thick black lines) is significantly different from the control experiment after 80 years, as mentioned before.

In the deep AMOC branch, the southward transport within the DWBC strongly increases by up to 3.5 Sv in the ensemble mean after 60 years (figure 4.17b). However, also the interior northward transport (offshore the western boundary) does increase, leaving a residual that matches the AMOC increase. Thus, the AMOC transport increase results from the residual between changes in the DWBC transport and the interior recirculation.

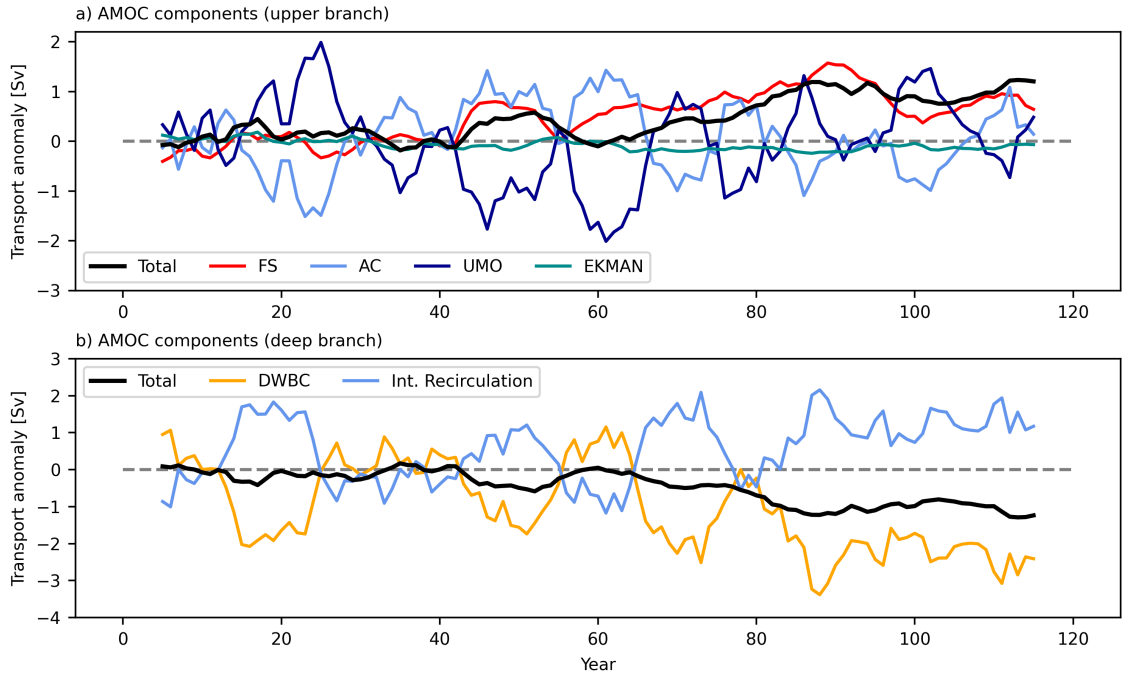

Figure 4.17: Components of the AMOC at 26.5°N. For the upper branch, the total AMOC transport difference between the ensemble perturbation experiment and the control (black) is split into the contribution from the Florida Strait (FS, or Gulf Stream), Antilles Current (AC), upper mid-ocean (UMO) and Ekman transports. The deep branch is split into the Deep Western Boundary Current (DWBC) and interior recirculations (transport east of the zero mean meridional velocity contour offshore the western boundary).

6. Summary and Discussion

Based on a 5-member ensemble experiment with enhanced wind stress over the Southern Ocean, the propagation of temperature, salinity and density anomalies from the South Atlantic into the North Atlantic and their impact on the Atlantic Meridional Overturning Circulation are studied. Probably for the first time, such an analysis is conducted in a coupled model at eddying resolution with several ensemble members of more than 100 years length each.

Northward Propagation of Temperature and Salinity Anomalies

The main impact of a Southern Ocean wind stress increase on the South Atlantic is via a sustained increase of Agulhas leakage by 3.8 Sv (35%) in the ensemble mean. The increase in Agulhas leakage causes strong temperature, salinity and density anomalies in the Cape Basin down to 1500 m. While atmospheric damping reduces the near-surface temperature anomaly to generate a positive density anomaly, at depth below 400 m thermal expansion dominates haline contraction to generate a negative density anomaly. An advection of anomalies from the Drake Passage within the SAC does not contribute to water mass anomalies below approximately 100 m. Mixing with leakage water still generates anomalies at depths that are mostly occupied by water that has entered the South Atlantic via Drake Passage (compare Rühs et al., 2019). Local Ekman pumping in the Cape Basin might contribute to the mid-depth anomalies as well. Both processes only affect water volumes that enter the South Atlantic via Drake Passage when they arrive in the Cape Basin. This is consistent with Rühs et al. (2019), who note that the Drake Passage inflow water acquires its characteristics mostly in the South Atlantic, not in the Pacific.

Based on a combination of Lagrangian and Eulerian analysis, it was possible to show that the mid-depth anomaly spreads across the South Atlantic to join the North Brazil Current. Within the tropical Atlantic, alternating zonal currents (Ménesguen et al., 2019) cause the anomaly to spread zonally and eventually to spill into the central NA STG along the full zonal extend of the Atlantic below 500 m depth. There are hints on salinity anomalies reaching 27°N in the Gulf Stream and recirculating in the western NA STG, but mixing with anomalously fresh water that results from different atmospheric adjustments strongly reduces the magnitude of anomalies in the near-surface layer. There are no temperature anomalies propagating from the South into the North Atlantic along the western boundary. Anomalies that are still visible at 27°N near-surface can not be detected in the GS extension/NAC. After separating from the US coast, the GS shows non-significant anomalies of opposite sign (colder and fresher) west of 20°W for most time periods after year 50. The discontinuity of the anomalies in this region is likely caused by intense mixing within the highly variable Gulf Stream extension, as well as atmospheric and dynamic ocean adjustments. Still, the GS/NAC may contribute to positive salinity and temperature anomalies further north by the anomalous advection of mean temperature and salinity.

Another possible pathway for anomalies is found outside the western boundary current system, despite those currents being the main pathway for water volumes tracked by Lagrangian experiments. This is possible because the Lagrangian water volumes do not conserve their temperature and salinity. Instead, anomalies seem to cross into the SPG along the eastern boundary. Diapycnal mixing and rising isopycnals across the NAC then cause anomalies in the eastern SPG to emerge at the surface. Although it is not possible to proof the existence of this pathway with high certainty, because anomalies are not continuously significant across the NA STG-SPG boundary, it is hypothesised that mean advection of anomalous temperature and salinity can contribute to an increase in temperature and salinity in the SPG.

Furthermore, a southward shift of the northern hemisphere westerlies is triggered, presumably by enhanced heat loss over the Gulf Stream. This change in wind stress generates strong temperature and salinity anomalies in the SPG via changes in Ekman transport, Ekman pumping, heat fluxes and potentially precipitation. The AMOC itself can contribute to water mass changes in the SPG as well. After an initial strengthening, the enhanced AMOC transport would import more warm and

saline subtropical water into the SPG. In this context, it should be noted that a cooling in the Gulf Stream region and warming in the central to eastern SPG, that is somewhat similar to the changes seen here, was described as the AMOC fingerprint by Zhang (2008). This highlights that once anomalies of the AMOC are present, this will generate anomalies of its own. It is therefore possible that a fourth mechanism (in addition to three mentioned above) leads to the SPG temperature and salinity changes in the perturbation ensemble. However, the AMOC only shows significant changes after 80 years, while the wind shift and anomalies in the SPG were already seen after 50-60 years. Thus, the currently best explanation is that the AMOC is not the initial trigger for the anomalies, but potentially reinforces them later.

Across most of the SPG, these changes result in a decrease in density. This especially includes the SPG deep convection regions. In contrast, the eastern SPG (Rockall Through and parts of the Iceland basin) shows a positive density anomaly, caused by anomalous heat flux damping. This reduces the temperature anomaly in the eastern SPG, while leaving the salinity anomaly mostly unaltered.

The positive density anomaly is advected into the Nordic Seas across the shallow sills and returns as more dense overflow. This overflow then follows the DWBC around the SPG boundary and appears at the exit of the Labrador Sea after 90 years.

At the end of the experiments, the salinity anomaly has spread along the deep western boundary (2000-3000 m) as far south as the equator. North of 30°N anomalies spread across a wide zonal band, but they are more confined to the western boundary further south. This is consistent with the presence of interior pathways north of this latitude and the assumption that most of the deep southward transport further south is concentrated in the DWBC (Bower et al., 2009; Gary et al., 2011, and chapter 5 of this thesis).

AMOC Response to Increases in the SWW and Agulhas Leakage

In response to increasing salinity in the SPG and Nordic Seas, the AMOC increases by 1.2 Sv (7%) after approximately 80 years. First AMOC anomalies can be seen to emerge across the OSNAP section after about 60 years, consistent with the development of temperature and salinity anomalies in the SPG and overflows.

Therefore, the AMOC increase coincides with enhanced water mass transformation in the Rockall Trough and Iceland Basin region, as described before. This is in agreement with Desbruyères et al. (2019), who argue that heat loss in this region has a dominant contribution to water mass transformation associated with the AMOC.

The more dense water returns to the SPG across the overflow sills and feeds the deep flow along the SPG boundary. In agreement with an increase in overflow density after 60 years and results obtained by Katsman et al. (2018), a strong increase in the net vertical transport across the overturning maximum (1060 m) can be seen in the SPG outside the deep convection region.

These results suggest that water mass transformation (thus the AMOC in density coordinates) and sinking (thus the AMOC in depth coordinates) are linked through the generation of anomalous dense water that flows into the Nordic Seas and returns to the SPG as more dense overflow. Deep convection in the SPG has no contribution to the development of AMOC anomalies in the here presented experiments. This must not necessarily mean that local heat fluxes in these regions can not generate AMOC variability, but only that they don't play a major role for the AMOC response to anomalies generated in the South Atlantic in FOCI-ATLAS10. Note for example that the southward shift of the northern hemisphere westerlies is closer to the NAO- pattern than the NAO+ pattern and the former is typically associated with decreasing AMOC transports. Southward shifting westerlies reduce heat loss over the western and central SPG, decreasing deep convection (Marshall & Schott, 1999; Dickson et al., 1996) and water mass transformation with direct impacts on the AMOC transport (e.g. Yeager et al., 2021; Menary et al., 2020; Megann et al., 2021). This is consistent with the decreasing density in the Labrador and Irminger Seas in response to such a wind shift, as described above. Still, overturning

increases in the perturbation experiment because of positive density anomalies that develop in the eastern SPG and Nordic Seas. In the absence of anomalies arriving from the south in the eastern SPG, the same wind pattern may cause the AMOC to weaken. Therefore, the response to southern hemisphere wind stress changes found here is distinct from NAO related AMOC anomalies and also from the proposed mechanism that generates AMOC anomalies linked to the Atlantic Multidecadal Variability (AMV). Drews and Greatbatch (2017) for example suggest a phase transition in the AMV to be initiated by anomalous convection in the Labrador Sea. This points to the fact that different mechanisms and regions can be responsible for changes in the AMOC.

Once AMOC anomalies develop in the southern subpolar North Atlantic, the anomaly is propagated south within a few years. The only mechanism fast enough to explain such a propagation speed are boundary waves, which is consistent with the proposed propagation of AMOC anomalies by Getzlaff et al. (2005).

AMOC changes in the upper branch at the RAPID section (26.5°N) manifest mostly in a speed-up of the Gulf Stream. In the deep AMOC branch, the transport increase results from a residual between the increased southward DWBC transport and the northward interior recirculations.

It is notable that before year 80, there are no significant changes in the ensemble mean AMOC. Thus, the northward propagation of Agulhas leakage anomalies via wave processes (Biastoch et al., 2008b; Weijer et al., 2002; Webb et al., 2021) does not play a major role in the perturbation experiment conducted here. For a comparison with Weijer et al. (2002), the reason could be related to the small magnitude of overturning anomalies resulting from fast wave adjustments after introducing density anomalies in the Agulhas region. The slower advective response was found to be much stronger in their experiments. Especially because a coupled model is used here, internal variability could mask such a small AMOC response. A similar case can be made for a comparison with Biastoch et al. (2008b), who evaluated differences between a coarse model without Agulhas rings and an experiment with explicitly simulated rings. Here it is not clear, whether the increase in Agulhas leakage is actually caused by stronger and/or more Agulhas rings, or maybe leakage outside of rings (e.g. Schubert et al., 2021). Webb et al. (2021) apply a wind anomaly that is similar to the anomaly applied here and there are two possible explanations why they still find a stronger AMOC response within the first 20 years after applying the anomaly. First, Webb et al. (2021) argue that planetary waves that cause an AMOC response are triggered by Ekman pumping and related changes in isopycnal depth. Ekman pumping could be mostly compensated by eddy fluxes, in the eddying FOCI-ATLAS10 configuration. It is found that indeed Ekman pumping changes only have very limited impact on the density stratification across the ACC below 100 m. As a consequence, the response could be too strong in the 1/4° model used in the study of Webb et al. (2021). The more likely explanation, however, is that the wave response in FOCI-ATLAS10 is underestimated, because of a northward position bias of the southern hemisphere westerlies. Webb et al. (2021) show that the wave mediated response is much stronger, if the winds do not only increase, but also shift south. Therefore, the impact of wave processes could be sensitive to the position of the westerlies and their northward bias in FOCI(-ATLAS10) may reduce the magnitude of this response. As a consequence, it may not be detectable in the perturbation experiment conducted here.

It is therefore likely that the wave mediated response to density changes in the Agulhas region is too small to be detected here and that a wave mediated response to changes in Ekman pumping is underestimated because of the position bias of the SWW in FOCI-ATLAS10.

Furthermore, the ocean has clearly not fully adjusted to the wind perturbation at the end of the experiment. The deep density anomaly reaches the exit of the Labrador Sea only after 90 years and is still rising after 120 years. This suggests that the full anomaly may not be reached at this point and the AMOC anomaly may continue to grow. At the same time, the complex processes in the North Atlantic could also trigger stabilising negative feedbacks (e.g. Menary et al., 2015; Drews & Greatbatch, 2017) that reduce the AMOC strength again. Only the initial, transient AMOC response is studied here.

Concluding Remarks

The results of this chapter suggest that a 30% increase of the wind stress maximum over the Southern Ocean, which is roughly comparable to the expected increase under rising greenhouse gas concentrations in the high emission SSP 5-8.5 scenario (Ivanciu et al., 2022a), results in a sustained increase of Agulhas leakage by 3.8 Sv (35%) and strengthening of the AMOC by about 1.2 Sv (7%) after 80 years.

Although an Agulhas leakage response is in general consistent with Durgadoo et al. (2013), they find an adjustment of the circulation to reduce Agulhas leakage to its previous value within two decades after the wind stress was increased. A similar adjustment is not found here. This could have different reasons. First, Durgadoo et al. (2013) use a forced ocean-only model that does not allow for an atmospheric adjustment to the increase in Agulhas leakage. Therefore, it is possible that the prescribed atmospheric state causes a different adjustment of the large-scale circulation to the changing wind stress and leakage compared to a coupled model. Furthermore, they mention that an interaction with a strengthened ACC could result in the return of Agulhas leakage to previous values. A significant change in the ACC is absent in the here described experiment. The reason for this difference is likely that the nested configuration used in Durgadoo et al. (2013) does not cover Drake Passage at eddying resolution and they do not apply an eddy parameterisation on the coarse host grid. As a consequence, their model configuration is not able to simulate an eddy saturated ACC. Another possible explanation is that the coupled model does exhibit a position bias of the southern hemisphere westerly winds, such that the wind stress increase is less well aligned with the ACC in FOCI-ATLAS10.

The impact of Agulhas leakage on temperature and salinity anomalies in the South Atlantic is consistent with Ivanciu et al. (2022a), who analyse composites of years with high and low Agulhas leakage in a South Atlantic nested configuration in FOCI. They find temperature and salinity anomalies reaching down to 1000 m depth across the Good Hope section in years of strong Agulhas leakage. The anomaly pattern is very similar to the anomaly pattern seen in FOCI-ATLAS10 in response to increased SO wind stress. Further, they find the salinity and temperature anomalies to spread across the South Atlantic, with the pattern yet again matching the here obtained results. They only show anomalies averaged over the top 1000 m and thus only find a limited westward extend of the temperature anomaly, which is strongly damped near surface. Isolating the depth range below 300 m may have resulted in a more westward extension of significant temperature anomalies. For salinity, the westward extend of anomalies is less depth dependent and therefore even more similar to the anomalies seen here. Ivanciu et al. (2022a) further find an exceptionally strong warming that extends across the South Atlantic in response to increasing greenhouse gas concentrations. They directly link this pattern to an increase in Agulhas leakage caused by strengthened westerly winds, as done here.

Overall, the results are in agreement with previous studies that propose an impact of increasing SWW on overturning in the North Atlantic (e.g. Delworth & Zeng, 2008; Wei et al., 2012). Because the South Atlantic response is dominated by an increase of Agulhas leakage, this chapter also provides direct evidence for an impact of Agulhas leakage on the overturning circulation. Such a connection is a long existing hypothesis (e.g. Gordon et al., 1992; Weijer et al., 1999), but evidence only comes from simplified and/or coarse resolution models (e.g. Knorr & Lohmann, 2003; Weijer et al., 2002).

The mechanisms how changes in the Southern Ocean and South Atlantic could affect the production of NADW seem to be more complex in an eddying, coupled model. This chapter provides a much more detailed description of the anomaly pathways and the coupled adjustment. The study of Weijer et al. (2002) suggests the GS and NAC to be the dominant pathway for anomalies, while there are no hints for an important contribution from mean advection of anomalous temperature and salinity in the GS/NAC to the development of anomalies in the SPG in the model experiment analysed in this chapter. It is possible that their coarse resolution model underestimates mixing in the GS/NAC and can not fully capture the dynamic response of a strengthened circulation. Furthermore, their model is driven by climatological wind stress, preventing any adjustment of

the wind. This was found to be an important source of near-surface anomalies throughout the perturbation experiment and highlights the importance to conduct such experiments in a coupled set-up, as done here. A possible contribution from the mean advection of anomalies was found below the thermocline and away from the western boundary. Anomalies below the thermocline were already shown to cross the tropical Atlantic by Haarsma et al. (2011).

The results of this chapter are consistent with Biastoch et al. (2015), who find the North Atlantic heat content to rise after Agulhas leakage was increased. Although the heat content was not examined directly, temperature anomalies from Agulhas leakage were shown to reach the North Atlantic sub-surface. However, the perturbation experiment does not show a fast AMOC response to changes in Agulhas leakage within 2 decades that was for example described by Biastoch et al. (2015), or Rühs et al. (2022). A response of the AMOC sets in after 60 years (significant changes appear after 80 years). This is much longer than expected from the advective timescale of leakage water into the North Atlantic mainly via the Gulf Stream (Rühs et al., 2013; van Sebille et al., 2011), which was verified to be similar in FOCI-ATLAS10. The advective timescale of the hypothesised pathway at greater depth, away from the western boundary, however, is consistent with a response time of roughly 60 years. This is independent of the question which of the aforementioned mechanisms is ultimately most important for the development of anomalies in the SPG, because all are probably linked to the advection of water below 500 m. An AMOC change within 20 years would be more consistent with a response mediated by waves and as argued before, such a response could be underestimated in FOCI-ATLAS10. A missing wave response was already discussed, but for the two studies of Biastoch et al. (2015) and Rühs et al. (2022) mentioned above, it is not clear whether the wave mediated response is triggered by a change in winds that also affect Agulhas leakage (following Webb et al., 2021), or by an increase in Agulhas leakage itself (following Biastoch et al., 2008b). As argued above, the absence of a strong wave mediated AMOC response to increasing wind stress is most likely explained by the position bias of the southern hemisphere westerlies in FOCI-ATLAS10. A wave mediated response to changes caused by Agulhas leakage itself may be to small to be detected here. Thus, the currently best explanation is that the same change in the westerly winds cause a fast adjustment via waves, which is seen in Biastoch et al. (2015), Rühs et al. (2022) and Webb et al. (2021), but missing (underestimated) in FOCI-ATLAS10, and a slower response via advection, mixing and related atmospheric adjustments seen here. If the fast response seen in Biastoch et al. (2015) and Rühs et al. (2022) is actually not triggered by the wind but Agulhas leakage itself, there is currently no convincing hypothesis why such a response would be below the detection threshold in FOCI-ATLAS10.

Further, Weijer and van Sebille (2014) find no coherent variability of Agulhas leakage and overturning in a coupled model. Nevertheless, this may not necessarily be in contradiction to the results of this chapter, because the mechanism described here is rather complex and there are different coupled responses (especially in the equatorial Atlantic) that counteract the propagation of anomalies from the south. Thus, the here described mechanism is presumably only relevant in case of a strong and sustained leakage increase, rather than decadal, or even interannual, variability. Smaller and shorter changes of Agulhas leakage may be damped too strongly before reaching the subpolar North Atlantic via advection.

Lastly, it is important to state that not all individual ensemble members exactly resemble the ensemble mean. Different influences could cause individual members to show a different behaviour. As an example, the state of the AMOC during initialisation could lead to faster/slower advective propagation and other anomalies generated by internal variability could change the response time as well. As a consequence, it is not always possible to clearly decipher the chain of events from ensemble mean changes. Nevertheless, the hypothesis explaining the ensemble mean changes is dynamical consistent, increasing the confidence that it correctly describes the underlying physical processes of the coupled models response to the applied SO wind stress perturbation and related increase in Agulhas leakage.

The experimental design was motivated by a past and possible future increase of the southern hemisphere westerlies. Based on the results of this chapter, changes in the SWW (here only the wind stress related changes were studied) could have a non-negligible impact on the AMOC by modulating Agulhas leakage. Thereby, the purely wind stress (momentum flux) driven response could counteract an AMOC slowdown caused by a local warming of the North Atlantic and increased freshwater input from melting glaciers to a certain extend. This chapter presents a dynamical consistent explanation for the interhemispheric propagation of anomalies and how they affect the AMOC. Since FOCI-ATLAS10 shows a position bias of the southern hemisphere winds, a weak ACC and an anomalously warm Southern Ocean (all of these biases could be connected), it is possible that the true ocean response to changes in the SO wind stress is not exactly the same. Nevertheless, the experiment can also be interpreted as a sensitivity experiment regarding Agulhas leakage and is thus relevant, regardless of the process generating this increase. Several studies suggest that Agulhas leakage might have increased over the last decades and will continue to increase in the future (e.g. Rühs et al., 2022; Ivanciu et al., 2022a). Its impact on the AMOC is therefore of major interest.

In summary, this chapter provides a consistent theory how temperature and salinity anomalies of southern hemisphere origin propagate north and how they force an overturning anomaly in the North Atlantic. Extending the experiments could answer several more open questions. It is not clear whether the AMOC strengthening is sustained or just a transient response. Additionally, it can be studied, if the AMOC increase can feed back onto the import of saline water into the South Atlantic, hence whether the positive salt-advection feedback (e.g. Weijer et al., 2019) can further amplify the AMOC response. Furthermore, open questions remain on the impact of deep water anomalies generated in the North Atlantic re-appearing at the surface via diapycnal mixing and wind-driven upwelling in the South Atlantic.

CHAPTER 5

Mesoscale Variability in the Deep Subtropical North Atlantic and its Impact on the DWBC and AMOC Coherence

Physical connectivity on regional scales:

In accordance with existing literature, it was seen in the last chapter that anomalies in the deep AMOC limb follow interior pathways north of 30°N, while they are more confined to the deep western boundary further south. This bears a potential impact of advection in the DWBC on the coherence of AMOC variability. But at least on interannual timescales, local wind-driven variability seems to dominate AMOC variability, rather than the advective propagation of transport anomalies. Based on a combination of Eulerian analysis and a set of Lagrangian experiments, this chapter demonstrates why advection in the DWBC is unlikely a source of coherent interannual (AMOC) variability at 26.5°N and 16°N, two latitudes of long-term AMOC measurements. Although the DWBC is responsible for a considerable volume transport of 20 Sv connecting the two latitudes, mesoscale variability along the DWBC pathway strongly influences the coherence of transport variations. Eddies and meanders are generated along the DWBC pathway with an important contribution from barotropic energy transfer. They introduce a variety of different pathways for water volumes between the sections and cause transport anomalies to be strongly altered when reaching the downstream latitude. This reduces the (lag-) correlation of the DWBC transport timeseries at 26.5°N and 16°N. Consistent with this result, the AMOC shows a significant correlation only instantaneously, likely driven by large-scale wind patterns, but not at timelags that would be in agreement with the advective timescale of the DWBC (approximately one year).

Related publication:

Schulzki, T., Getzlaff, K., & Biastoch, A. (2021). On the variability of the DWBC transport between 26.5°N and 16°N in an eddy-rich ocean model. *Journal of Geophysical Research: Oceans*, 126, e2021JC017372, https://doi.org/10.1029/2021JC017372

Author contribution: The author was fully responsible for the Lagrangian experiments, the analysis/figures and wrote the initial and final manuscript. Note that the general idea for this publication is rooted in the master thesis (Schulzki, 2019), but was extensively modified and expanded. No text, nor figures of this chapter were taken from the master thesis. All Lagrangian experiments were completely new, redesigned or significantly extended. Most importantly, several scientific results are significantly different and beyond the master thesis. In particular, this includes completely new analyses and ideas that were realised with regard to the main question in the context of this thesis (see chapter 1).

JGR Oceans

RESEARCH ARTICLE
10.1029/2021JC017372

Key Points:

- Eddies and meanders cause strong temporal variability of the Deep Western Boundary Current (DWBC) flow
- Temporal variability extends the DWBC's advective timescale
- Mesoscale recirculations lead to a decorrelation of the DWBC transport at 26.5°N and 16°N

Supporting Information:

Supporting Information may be found in the online version of this article.

Correspondence to:

T. Schulzki,
tschulzki@geomar.de

Citation:

Schulzki, T., Getzlaff, K., & Biastoch, A. (2021). On the variability of the DWBC transport between 26.5°N and 16°N in an eddy-rich ocean model. *Journal of Geophysical Research: Oceans*, *126*, e2021JC017372. https://doi.org/10.1029/2021JC017372

Received 19 MAR 2021
Accepted 5 MAY 2021

On the Variability of the DWBC Transport Between 26.5°N and 16°N in an Eddy-Rich Ocean Model

Tobias Schulzki[1], Klaus Getzlaff[1], and Arne Biastoch[1,2]

[1]GEOMAR Helmholtz Centre for Ocean Research, Kiel, Germany, [2]Kiel University, Kiel, Germany

Abstract The southward flow of North Atlantic Deep Water makes up the major component of the deepwater limb of the Atlantic Meridional Overturning Circulation (AMOC). In the subtropical North Atlantic, it's flow is concentrated along the continental slope, forming a coherent Deep Western Boundary Current (DWBC). Both, observations and models show a high variability of the flow in this region. Here we use an eddy-rich ocean model to show that this variability is mainly caused by eddies and meanders. Their formation process involves an important contribution from energy transfer by barotropic instability. They occur along the entire DWBC pathway and introduce several recirculation gyres that result in a decorrelation of the DWBC transport at 26.5°N and 16°N, despite the fact that a considerable mean transport of 20 Sv connects the two latitudes. Water in the DWBC at 26.5°N is partly returned northward. Because the amount of water returned depends on the DWBC transport itself, a stronger DWBC does not necessarily lead to an increased amount of water that reaches 16°N. Along the pathway to 16°N, the transport signal is altered by a broad and temporally variable transit time distribution. Thus, advection in the DWBC cannot account for coherent AMOC changes on interannual timescales seen in the model.

Plain Language Summary The Atlantic Meridional Overturning Circulation describes a northward flow of warm water close to the surface, while cold water of North Atlantic origin is transported to the south at depth. The resulting transport of heat to the north has a pronounced impact on the northern hemisphere climate and is therefore of major interest. An improved understanding of the deep flow can help to interpret past and future changes of the overturning circulation. In the subtropical North Atlantic this deep southward flow is believed to be less complex than in other regions and more confined to the western boundary. However, our results show that eddies with radii of several tens of kilometers and offshore shifts of the current impact the spreading of water. These circulation features introduce a large variety of pathways from 26.5°N to 16°N, two latitudes of long term measurements. Additionally, they cause parts of the southward transport toward 16°N to return northwards. As a result, transport changes are not propagated southward, although a strong mean flow connects the latitudes. Therefore, advection along the western boundary can not explain the modeled similarity of overturning transport changes at both latitudes.

1. Introduction

The Atlantic Meridional Overturning Circulation (AMOC) transports warm surface water northwards. It is responsible for the northward ocean heat transport with a pronounced impact on the large scale climate, especially in Europe (Srokosz & Bryden, 2015). At depth the AMOC exports cold water of North Atlantic origin (North Atlantic Deep Water; NADW) to the south, which carries anthropogenic carbon dioxide (CO_2) and other trace gases (Pickart et al., 1989; Sabine et al., 2004) away from the uptake regions in the north. A main component of the AMOC's deep limb is the Deep Western Boundary Current (DWBC; Rhein et al., 2015). While north of ~26°N interior pathways away from the western boundary were shown to exist, the flow of NADW seems to be concentrated in a coherent DWBC further south (Bower et al., 2009; Gary et al., 2011). This potentially leads to a faster spreading of tracers and trace gases in the subtropical North Atlantic (STNA). However, tracer-based velocity estimates are about one order of magnitude lower than current-meter measurements of the DWBC speed (Lee et al., 1996; Rhein et al., 2015). Observations (Kanzow et al., 2008; Lee et al., 1996) and models (Lüschow et al., 2019) suggest that the deep flow is subject to strong temporal variability associated with meanders of the DWBC and eddies. Leaman and Vertes (1996) find eddies triggered by the marked topography of San Salvador (~24°N) to reduce the mean southward

velocity of RAFOS floats compared with their speed within the DWBC itself. Mesoscale activity seems to have a strong impact on the DWBC's advective timescale, which is directly related to the southward spreading speed of temperature and salinity anomalies and the residence time of climate relevant trace gases in the deep ocean.

In addition to its importance for the transport of water masses and its properties, advection is one of three mechanisms that can cause coherent AMOC transport variability at remote sections. In modeling studies AMOC changes on interannual to decadal timescales are often found to be in phase across the STNA (e.g., Biastoch et al., 2008). In contrast to these studies, long-term AMOC measurements at the RAPID (26.5°N) and MOVE (16°N) arrays show opposing trends (Frajka-Williams et al., 2018) and interannual variations do not seem to be in phase. This raises the question on which timescale coherent changes at MOVE and RAPID may be expected and what physical drivers can cause them. Several studies suggest that boundary waves are an important driver for the propagation of AMOC signals (e.g., Getzlaff et al., 2005; Zhang, 2010). Another important process is the wind forcing, with large scale wind patterns leading to meridionally coherent AMOC changes over several degrees of latitude (Elipot et al., 2016). Although advection within the DWBC was found to be of minor importance for the coherence of variations at latitudes north of 38°N (Elipot et al., 2013), it may be different in the latitude range between 16°N and 26.5°N due to the absence of interior pathways. We do not call into question that AMOC anomalies primarily spread via wave processes in the STNA (Zhang, 2010) and that coherent variations can be caused by common wind forcing (Elipot et al., 2016). Here we want to study the missing impact of advection, which is not a trivial attempt. In a highly simplified ocean, where all water in the DWBC at 26.5°N reaches 16°N with a single transit time and constitutes all of the DWBC transport at 16°N, the correlation of the two transport timeseries would be one at the timelag corresponding to this transit time. Accordingly, under the right conditions advection can lead to highly correlated transport anomalies at remote sections. Although the real ocean is more complex, the presence of a single deepwater pathway allows to assume that deviations from these conditions are not as strong as north of 38°N.

Here we systematically assess how DWBC transport variability affects the spreading of deepwater and the coherence of transport changes at remote sections in the STNA. Our analysis is guided by the following main questions of this study:

1. How does temporal variability affect the southward spreading of deepwater in the STNA?
2. Can advection in the DWBC cause coherent AMOC changes in the STNA?

In order to address these questions, we use an an eddy-rich (1/20°) ocean model that is described and compared to observations in Section 2. Using a Lagrangian approach that is introduced in Section 3, we study volume transport pathways in the STNA and the DWBC's advective timescale (Section 4.2). Further we show how temporal variability reduces the correlation of the DWBC transport across 26.5°N and 16°N (Section 4.3) based on a purely advective view. Finally, we study physical mechanisms that drive mesoscale variability along the DWBC pathway in Section 4.4.

2. Ocean General Circulation Model

2.1. VIKING20X Configuration

In this study we use 5-day mean fields from a hindcast simulation performed with the eddy-rich ocean general circulation model configuration VIKING20X (Biastoch et al., 2021; Rieck et al., 2019). VIKING20X is a nested configuration based on the Nucleus for European Modeling of the Ocean (NEMO) version 3.6 coupled ocean/sea-ice model (Madec, 2016). The model is an expanded and improved version of VIKING20 (Böning et al., 2016). The global base model has a horizontal resolution of 0.25° on a tripolar C-grid and 46 z-levels with increasing grid spacing from 6 m at surface to 250 m at depth (ORCA025; Barnier et al., 2006). Via AGRIF two-way nesting (Debreu et al., 2008), the horizontal resolution is increased to an eddy-resolving 0.05° in the Atlantic Ocean between 70°N and 34°S. The model is forced with interannually varying air-sea fluxes derived from the CORE (version 2) data set using Bulk formulae (Large & Yeager, 2009). The model was spun-up for 30 years and then run for another 52 years covering the time period from 1958 to 2009.

2.2. Representation of the AMOC and DWBC

VIKING20X simulates a realistic overturning circulation, with a clockwise NADW cell and counter-clockwise bottom water cell (Figure S1). Consistent with observations, the maximum overturning transport is reached around 1,100 m depth (Smeed et al., 2014). The maximum AMOC transport at 26.5°N is 19.5 ± 0.6 Sv (2004–2008) compared to 18.6 ± 1 Sv derived from the RAPID array (Smeed et al., 2014). Thus, the transport falls inside the observational uncertainty expressed in terms of the standard deviation of annual means. At 16°N the modeled AMOC transport of 19.4 ± 0.8 Sv (2000–2009) exceeds the observed transport at MOVE (16.3 ± 2.6 Sv) by 3.1 Sv (Send et al., 2011).

The position, vertical structure and transport of the DWBC at 26.5°N are in good agreement with observations and other high resolution models (Bryden et al., 2005; Xu et al., 2012). The zonally averaged velocity profile within 100 km from the western boundary (Figure 1d) is comparable to estimates from Johns et al. (2005) covering a similar distance from the western boundary. In both, VIKING20X and observations, the DWBC velocity reaches its maximum at 2,000 m depth. The 1990 to 1999 mean vertically integrated southward transport of 35.7 Sv is close to mooring based estimates of 34.6 ± 3.7 Sv (Bryden et al., 2005). Also its variability is in line with previous studies. The standard deviation of the model transport is 9.7 Sv. Johns et al. (2005) report a standard deviation between 11.7 Sv (from current meters) to 14 Sv (from dynamic height moorings). Both are calculated from 40-hour low-pass filtered timeseries. Slightly higher values than our estimate based on 5-day means are therefore expected. At 16°N the DWBC transport of 29.5 Sv is also in a realistic range (25.6–28.9 Sv; Rhein et al., 2004), although long-term estimates are not published to our knowledge.

Nevertheless, there are some important differences between the modeled and observed DWBC at 26.5°N. The 10-year mean velocity exceeds 30 cm s^{-1} at individual grid points (Figure 1b). This seems high compared to mooring observations at 26.5°N indicating multi-year mean speeds of 16 cm s^{-1} (Bryden et al., 2005). Together with the realistic transport and velocity profile this suggests that the modeled DWBC is too narrow. Xu et al. (2012) and Bryden et al. (2005) find a horizontal extend of 130–160 km rather than 100 km in VIKING20X. The DWBC at 26.5°N stands out with an increased temporal variability of the flow at depth below 1,000 m (Figure 1c). In general, this agrees with the observation of strong temporal fluctuations of the DWBC strength (Kanzow et al., 2006; Lee et al., 1990, 1996), but Eddy Kinetic Energy (EKE) values are in the range of 30 cm^2 s^{-2} and therefore lower than maximum values of around 100 cm^2 s^{-2} presented by Biló and Johns (2020). Likely the mentioned discrepancies are related, as offshore meanders will increase variability, extend the mean DWBC width and reduce the mean velocity close to the western boundary. The long term mean EKE in the DWBC around 26.5°N shows a high spatial variability. Values slightly north of 26.5°N can reach up to 90 cm^2 s^{-2}. Still, such high values are too strongly confined in the vertical and to the western boundary (Figure S2). This spatial heterogeneity hints on an impact of small scale bathymetric features on the EKE within the DWBC itself. Their representation in the model could contribute to the underestimated variability at 26.5°N. Offshore variability was shown to be associated with northward propagating eddies (Biló & Johns, 2020). Such eddies are visible in the models velocity field (Movie S1), but their magnitude seems to be underestimated. At latitudes south of 24°N EKE values are in general higher and less confined to the western boundary (Figure 9d and Figure S2). Therefore, we argue that the model is able to simulate vigorous mesoscale variability in the deep STNA. It is this simulated mesoscale activity we study in the following sections. The noted differences must be kept in mind interpreting our results and are further discussed in Section 5.

3. Lagrangian Experiments

The Lagrangian analysis presented in the following sections is based on the ARIANE algorithm (Blanke & Raynaud, 1997) using the 5-day mean 3D output of VIKING20X. ARIANE solves the advection equation analytically, by assuming a stationary velocity field for 5-days. The calculation of trajectories with ARIANE using 5-day mean velocity fields is a well established method (e.g., Rühs et al., 2019). Following the argumentation of van Sebille et al. (2018) we interpret trajectories to represent pathways of small water volumes rather than single particles. Volume elements are automatically seeded along a predefined section based on the velocity field and tagged with a transport value at release. As this transport is conserved along

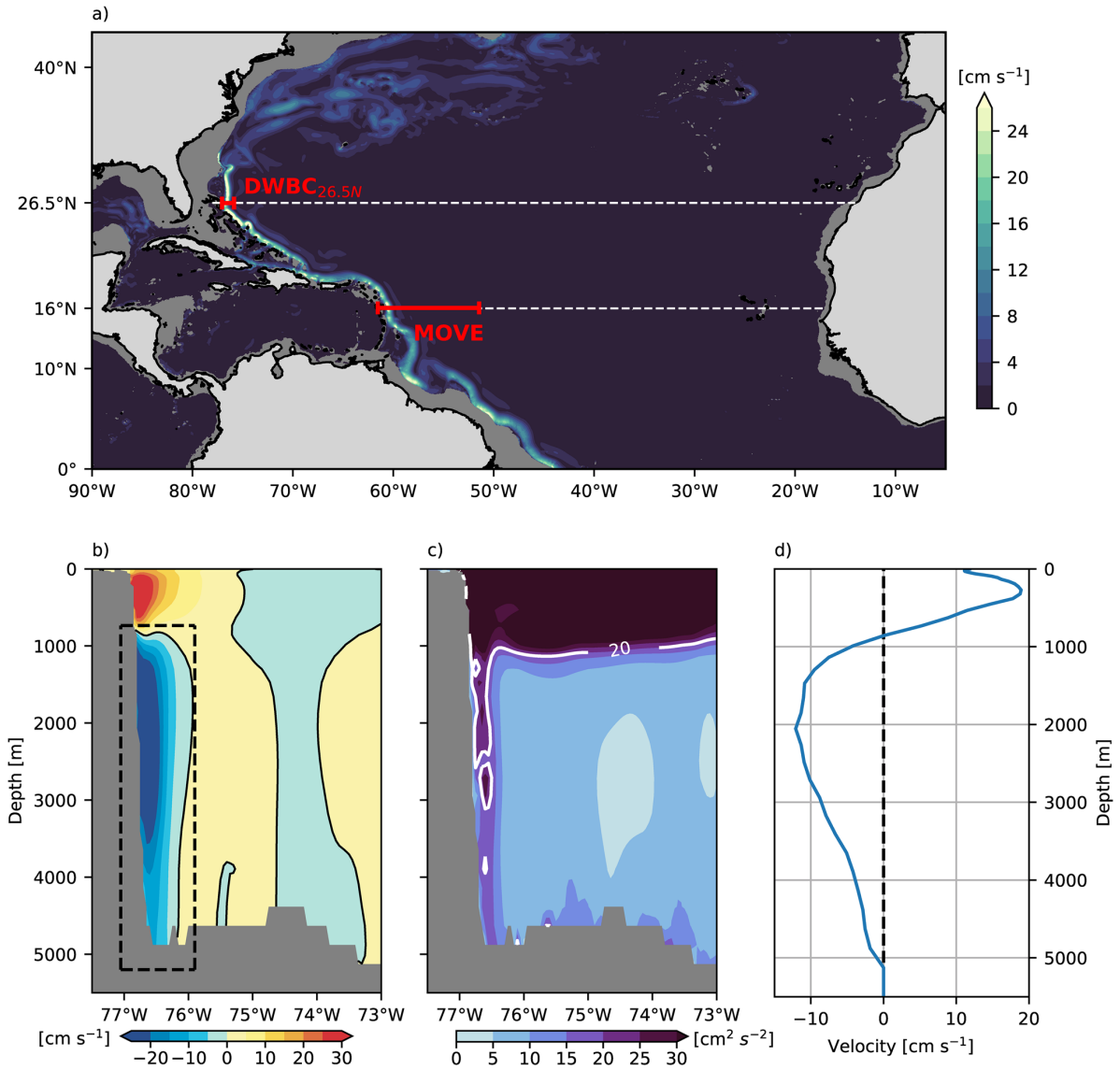

Figure 1. (a) Mean (1970–1999) speed between 1,000 and 3,500 m depth. Meridional velocity (b) and Eddy Kinetic Energy (EKE) (c) at 26.5°N. (d) Meridional velocity profile, zonally averaged within the zonal extend of the dashed box in (b). The box also indicates the ARIANE release section. Panels (b–d) show the 1990–1999 mean.

trajectories, they represent volume transport pathways. The maximum transport of a single water volume is limited to 0.1 Sv. A higher transport resolution (0.01 Sv) was tested, but does not change the results. Subsequently, ARIANE evaluates the transport across all sections of a closed domain and stores the integrated transport across all surfaces of the grid cells. This allows to obtain a two-dimensional representation of the flow field from individual trajectories by calculating the Lagrangian Stream function (LSF; Blanke et al., 1999). It is necessary to exclude the water volumes that do not exit the closed domain within the integration period. This is accomplished by restarting the ARIANE experiments with a subset of the initial release only containing water volumes that reach any section. Using the same method, it is possible to obtain the LSF of only those water volumes that reach the MOVE section or return to the release latitude.

In an initial set of experiments, water volumes were released every 5 days for each year between 1970 and 1999, resulting in 30 experiments (referred to as EXP_{var}). Here we use a zonal release section at 26.5°N, covering the longitudes from 77.05°W to 75.9°W (black line in Figure 3a) and all depth levels below 730 m. The southern boundary of the closed domain is located at 16°N and divided into multiple subsections. The MOVE section (cyan line in Figure 3a) covers the Atlantic from Guadeloupe (61.6°W) to 51.5°W. To avoid a dependence of the trajectory length on the release time step, the maximum length of all trajectories is 10 years. This experiment is thought to represent realistic conditions in the framework of the model. To assess the impact of variability, water volumes were released in the 30-year mean (1970–1999) velocity field and integrated forward in time for a maximum of 10 years in a second experiment (referred to as EXP_{mn}). This velocity field does not change throughout the entire calculation. By construction, temporal variability is excluded in EXP_{mn}. This second experiment represents a coherent DWBC, were temporally varying recirculations along the way to 16°N are excluded (see Section 4.3). The release section was chosen to fully capture the DWBC during the majority of time steps, but retain a comparable transport in the two experiments. Due to the seeding strategy of ARIANE, a too large release section would lead to a significantly increased transport in EXP_{var}. This additional transport is mostly related to Rossby waves or eddies and does not reflect an advective transport within the DWBC. The chosen release section fully contains the mean DWBC, as well as the region of highest variability (Figure 1). As a result, frequent offshore meanders that shift the DWBC out of the release box are not expected. This was verified by inspection of the 5-day mean velocity across the section. As we release particles in the variable flow field every 5 days for 30 years, a total of 2.7 million water volumes were released. EXP_{mn} is based on a single time step of the velocity field (the 30-year mean) and therefore water volumes are released at one time step only. This results in a lower number (700) of released water volumes.

The previously described experiments only trace water that originates from 26.5°N. We run a third experiment to test, if other sources of the DWBC at 16°N exist (referred to as EXP_{16N}). Therefore we release water volumes along a zonal section at 16°N (61.5°W–59.7°W). The width of this section is chosen to capture 90% of the transport arriving from 26.5°N in EXP_{var}. Again we release water volumes every 5 days for each year between 1970 and 1999, resulting in a total release of 2.4 million water volumes. As for EXP_{mn} and EXP_{var}, the integration is limited to 10 years and the boundaries of the closed domain are unchanged. However, we track water volumes backward in time to find their source region.

The three experiments were specifically designed to answer our main questions introduced in Section 1. While EXP_{var} alone is used to estimate the timescale and pathways of the DWBC in the STNA, a comparison with EXP_{mn} reveals the impact of temporal variability on the transit time distribution (TTD). These two forward experiments capture the flow of water transported in the DWBC at 26.5°N, but most likely not all water volumes that contribute to the DWBC at 16°N. EXP_{16N} allows to study the impact of other sources on the DWBC's variability at 16°N.

In order to further disentangle the impact of the TTD on the correlation of transport signals at different latitudes, we set up an idealized experiment using the PARCELS software package (Delandmeter & van Sebille, 2019). Here our attempt is not to reproduce realistic pathways, but to study the impact of different TTDs. Therefore we release particles at 39 discrete points along a section that represents 26.5°N for 2,190 time steps. This corresponds to a release every 5 days from 1970 to 1999. These particles are then advected purely in meridional direction until they reach a distant section. The velocity at each grid point is set to a certain value that is kept constant along the entire way to the southern boundary. Therefore, the release grid point is tied to a specific transit time from the release to the distant section. We define these transit times to match the bin centers of the TTD shown in Figure 3. By changing the number of particles released per grid point at different time steps, we can simulate a release timeseries. Here we simulate the DWBC transport timeseries at 26.5°N. Further it is possible to scale the number of released particles depending on their release grid point, or equivalently, depending on their transit time. This allows to simulate different TTDs and study their impact on the correlation between the timeseries of released particles and particles arriving at the distant section.

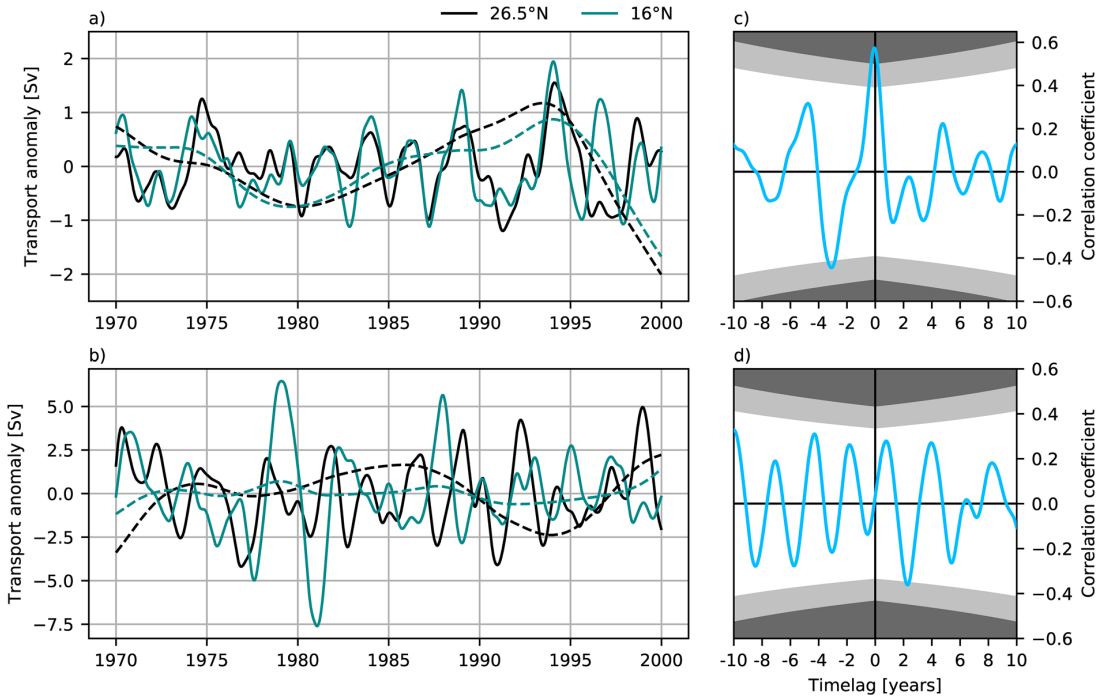

Figure 2. Low-pass filtered timeseries of the Atlantic Meridional Overturning Circulation (AMOC) (a) and Deep Western Boundary Current (DWBC) transports (b) at 26.5°N and 16°N. Solid (dashed) lines show interannual (decadal) anomalies. Cross-correlation of the interannual AMOC (c) and DWBC (d) timeseries at 26.5°N and 16°N. Gray shaded areas indicate significant correlation coefficients based on a confidence level of 95% and 99%. 26.5°N leads at positive lags.

4. Results

4.1. AMOC and DWBC Correlation

In agreement with studies by Biastoch et al. (2008) and Bingham et al. (2007) the AMOC at 26.5°N and 16°N shows coherent variability on interannual and decadal timescales (Figure 2). We define decadal changes as variations of the low-pass filtered timeseries, using a second-order butterworth filter with a cut-off frequency of 119 month. Interannual changes are studied using the 23-month low-pass filtered timeseries with the decadal signal subtracted. Before further analysis, we exclude half of the filtering period at the beginning and end and detrend the timeseries. Statistical significance is derived from a student t-test, where the effective degrees of freedom are calculated according to Emery and Thomson (2001). The correlation of the interannually filtered AMOC timeseries is significant based on a confidence level of 99% with 0.57. The maximum correlation is not exactly reached at timelag zero, but with 16°N leading by one month. Nevertheless, we describe the correlation to be instantaneous in the following. Also variations on decadal timescales are in phase with a significant instantaneous correlation of 0.95. In contrast to the AMOC, the correlation of the DWBC is strongly reduced on both timescales. The correlation does not exceed 0.33 for the interannual timeseries and is not statistically significant on the 95% level (Figure 2d). The DWBC correlation is higher with 0.76 on the decadal timescale and significant on the 95% confidence level. Here we define the DWBC transport as the southward transport across fixed boxes. These boxes correspond to the ARIANE release sections. To ensure that the lack of correlation is not just caused by the DWBC meandering to more offshore positions, we repeat the analysis defining the DWBC as the minimum of the cumulative transport below 1,000 m (Figure S3). Also with this alternative definition, there are no peaks in the cross-correlation that could be explained by advection. Additional to the lack of coherent variability in the DWBC, we find a 3–4 times enhanced interannual standard deviation of the DWBC transport compared to the AMOC.

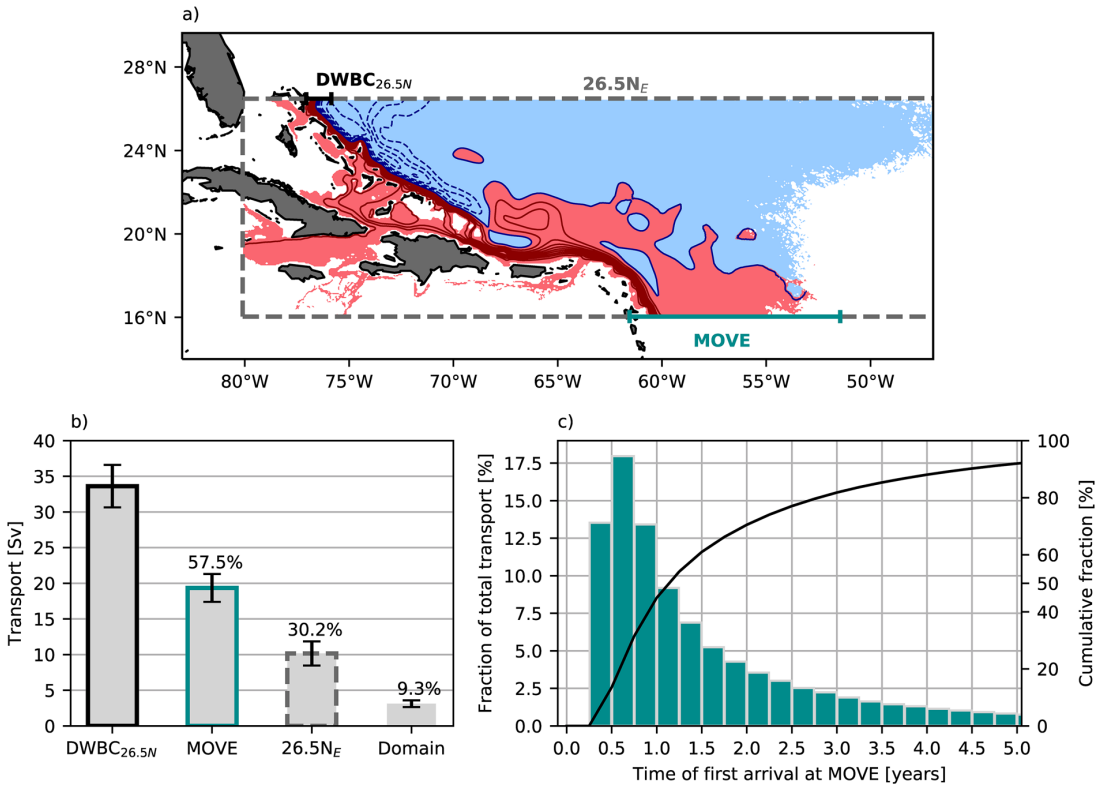

Figure 3. (a) Lagrangian Stream function (LSF) of all water volumes released in EXP_{var}. Contours are drawn with an interval of 2 Sv. The release section is colored black and the MOVE section cyan. All other sections of the closed domain are shown as dashed gray lines. (b) Transport across the boundaries of the closed domain. The mean transport of all 30 release years is shown together with the ensemble standard deviation (error bars). The transport fraction in % of the total release ($DWBC_{26.5N}$) is annotated. Domain refers to the transport that does not cross any section within 10 years after the release. (c) Transit time distribution (TTD) of the transport to MOVE. The line shows the cumulative fraction of the transport. The transport that has arrived after 10 years is defined as 100%.

Although previous studies find the flow of NADW to be concentrated in a narrow band along the western boundary, which is supported by the modeled velocity structure (Figure 1a), there is apparently no impact of this advection on the coherence of changes at both latitudes. This is true for the net transport across the whole Atlantic (the AMOC) and even for the southward transport close to the western boundary (the DWBC). In the following we test three hypothesis that could explain this observation:

1. There is no continuous pathway of NADW that connects both latitudes.
2. The timescale of advection in the DWBC is so long, that it's impact can not be seen in the 30-year long timeseries analyzed here.
3. The transport signal considerably changes between the latitudes of 26.5°N and 16°N.

4.2. Advective Pathways and Timescale

An average transport of 33.6 Sv per time step are released in EXP_{var} and subsequently advected in the full 5-day mean velocity field for 10 years. More than half of this transport (19.3 Sv) reaches 16°N (Figure 3b). The LSF shows that the majority of this transport follows the western boundary (Figure 3a). Interior southward pathways fed by the DWBC are not visible and all of the transport that reaches the southern domain boundary crosses 16°N close to the western boundary. These results already allow to falsify the first hypothesis, as a continuous DWBC is clearly existent in the model. Nevertheless, not all of the released transport reaches the MOVE latitude. A significant fraction of the transport released in the DWBC at 26.5°N is

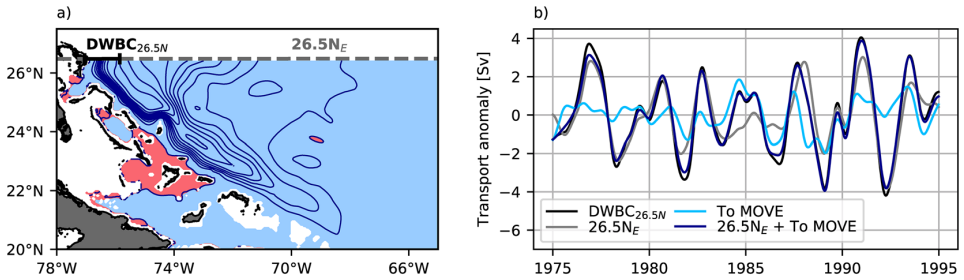

Figure 4. (a) Lagrangian Stream function (LSF) of only those water volumes that return to 26.5°N in EXP_{var}. Contours are drawn with an interval of 1 Sv. (b) Interannually filtered transport anomalies. $DWBC_{26.5N}$ (black) refers to the southward transport across the release section and equals the Eulerian definition of the Deep Western Boundary Current (DWBC). "To MOVE" (light blue) denotes the transport that ultimately reaches the MOVE section and $26.5N_E$ (gray) the transport that returns to the release latitude. The sum of both is shown in dark blue.

returned to the release latitude (30.2% or 10.2 Sv). Another 3.1 Sv do not reach any section of the closed domain within 10 years after the release. Additional analysis (not shown) shows that these water volumes are detrained from the DWBC and then trapped inside a closed circulation within the ocean interior. A small fraction of the transport enters the Caribbean Sea through the Windward and Anegada passages.

The fastest water volumes to reach the MOVE section need 96 days for the ~2,360 km long pathway along the western boundary. This corresponds to a velocity of nearly 30 cm s^{-1}, in line with Eulerian velocities in the DWBC core. The full TTD (Figure 3c) has a modal value between 0.5 and 0.75 years. The mean (1.9 years) and median (1.1 years) transit times are both well below 2 years. Accordingly, the mean southward spreading velocity of water that is advected from 26.5°N to 16°N is 4 cm s^{-1}. This is within the range of estimates directly derived from tracer observations (2.5 cm s^{-1}; Rhein et al., 2015) and theoretical models used to explain the observed tracer distributions (about 5 cm s^{-1}; Rhein, 1994; Waugh & Hall, 2005). Since the advective timescale is below 2 years, hypothesis 2 is not able to explain the lack of correlation in the DWBC transport at both latitudes.

4.3. Decorrelation of the Transport Timeseries

As hypotheses 1 and 2 are not able to explain the lack of correlation in the DWBC, we are now investigating how the transport timeseries is changed along the pathway to 16°N. As explained in the introduction, in a highly simplified ocean where the TTD can be approximated by a single peak, the maximum lagged cross-correlation would be one. In the real ocean however, deviations from these assumptions decrease the maximum cross-correlation. Here we follow the path of water transported in the DWBC from 26.5°N to 16°N and show three different mechanisms that ultimately result in an insignificant correlation of the DWBC transport timeseries at 16°N and 26.5°N on interannual timescales. At the same time we will investigate how the same mechanisms increase the DWBC's advective timescale, contributing to the spread between tracer and current-meter estimates.

4.3.1. Recirculation to 26.5°N

As already noted, not all of the transport released in the DWBC does reach the MOVE section. The return flow partly arises from a cyclonic recirculation north of San Salvador (24°N) and partly from mesoscale recirculation gyres seen along the DWBC pathway further south (Figure 4a).

Using ARIANE it is possible to split the timeseries of the DWBC at 26.5°N into individual transport timeseries based on the section where this transport leaves the closed domain (Figure 4b). Due to the seeding strategy in ARIANE, at any given time step the sum of all water volumes released equals the DWBC transport when defined as the southward transport across the release box. The interannual variability of the DWBC at 26.5°N is entirely explained by the combination of the timeseries reaching MOVE and the recirculating transport. The correlation between the sum of both timeseries (dark blue line) and the Eulerian DWBC timeseries (black line) is 0.99. Although the mean flow is dominated by water volumes that reach

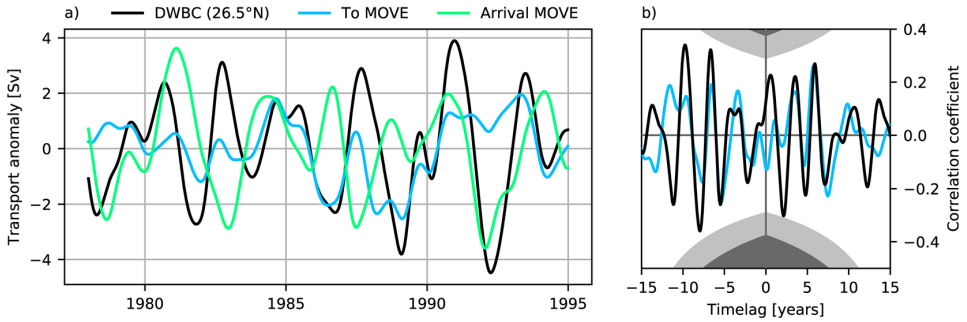

Figure 5. (a) Interannually filtered timeseries of the Eulerian Deep Western Boundary Current (DWBC) transport at 26.5°N and transport components derived from EXP_{var}. "To MOVE" denotes the transport of water volumes that ultimately reach 16°N sampled at the release section. "Arrival MOVE" shows the timeseries of the same water volumes, but sampled at arrival at 16°N. (b) Cross-correlation of the "Arrival MOVE" and "To MOVE" timeseries (blue), as well as "Arrival MOVE" and DWBC (26.5°N) timeseries (black). Timeseries showing a transport at 26.5°N lead at positive lags.

16°N, this is not true for the interannual variability. The flow to MOVE (light blue line) contributes about 20 Sv to the mean DWBC transport at this latitude and thus about twice as much as the recirculation to the $26.5N_E$ section (gray line). Nevertheless, the contribution to the interannual variability is larger for the recirculation component. Comparing the standard deviation, the recirculation (1.5 Sv) is more variable than the transport to 16°N (0.8 Sv). Also the correlation with the Eulerian DWBC is higher for the recirculation with a correlation coefficient of 0.9 compared to 0.55.

Although most of the water volumes that are released in the DWBC at 26.5°N reach 16°N, additional water volumes that are associated with an above average transport mostly return to the release section.

4.3.2. Variable pathway to 16°N

According to Section 4.2 water volumes are not advected to 16°N with a single transit time, but can take various different pathways that result in a rather broad distribution. Here we systematically assess how and why the transport signal changes from the release at 26.5°N to the arrival at 16°N.

To compare the two signals, at each time step we sample the transport of all water volumes when released at 26.5°N ("To MOVE") and during their arrival at 16°N ("Arrival MOVE"). Note that we exclude the first 3 years of the timeseries to allow a sufficient amount of water from the first release time steps to reach 16°N. In contrast to an idealized DWBC with a single transit time, the interannual transport signal is strongly changed along the pathway to 16°N (Figure 5a). As the advection of the signal is connected to a timelag, we do not expect a high instantaneous correlation and therefore calculate the cross-correlation (Figure 5b). The maximum cross-correlation at lags consistent with the TTD (between 1 and 2 years) is smaller than 0.2. Slightly higher values can be seen for longer timelags, but none of them are statistically significant different from zero. Consistently, there is also no significant correlation of the DWBC at 26.5°N and the transport arriving at MOVE. This change of the signal along the pathway therefore strongly contributes to the decorrelation of the interannual DWBC transport changes at 26.5°N and 16°N. It reduces the maximum cross-correlation from 0.55 (see previous section) to insignificant values below 0.2.

After showing its importance for the transport timeseries, we now study what causes the TTD to deviate from a single peak. By comparing the release experiment using a variable velocity field (EXP_{var}) to a release in the climatological mean velocity field (EXP_{mn}), it is possible to derive the impact of temporal variability. The released transport in both experiments differs by less than 1 Sv, verifying an appropriate choice of the release section. The transport that reaches MOVE is about 3 Sv higher in EXP_{mn}, which is mainly compensated by a weaker return flow to 26.5°N. In both experiments the water volumes follow the DWBC along the shelf break (Figures 6a and 6b). However, in EXP_{mn} recirculations along the pathway are largely excluded, especially west of 68°W. Between 68°W and 60°W water volumes follow an anticyclonic meander in both experiments. Nevertheless, this meander is stronger and has a more complex structure in EXP_{var}. Overall,

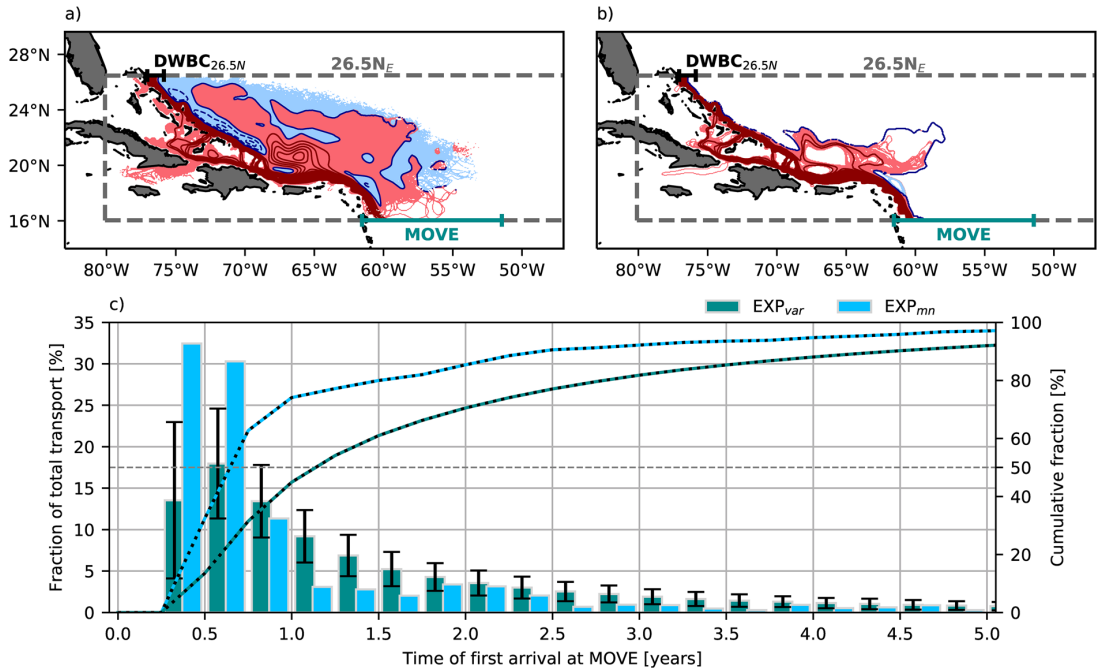

Figure 6. Lagrangian Stream function (LSF) of only those water volumes that reach the MOVE section in EXP_{var} (a) and EXP_{mn} (b). Contours are drawn with an interval of 1 Sv. (c) Transit time distribution (TTD) of the transport to MOVE from EXP_{mn} and EXP_{var} (as Figure 3c). Error bars show the standard deviation from calculating the TTD for each release time step in EXP_{var} individually.

we conclude that temporal variability introduces a variety of different pathways from 26.5°N to 16°N by allowing water volumes to follow recirculations but still reach the MOVE section. Note that the LSF of all water volumes is similar in EXP_{mn} (Figure S4) and EXP_{var}. However, in EXP_{mn} nearly all water volumes that follow these recirculations are returned to 26.5°N. Therefore we can use EXP_{mn} as a representation of a flow without recirculations along the way to 16°N. Estimated differences should be interpreted as a lower limit because not all recirculations are fully excluded.

The larger variety of pathways in EXP_{var} is also connected to a larger variety of transit times resulting in a broader TTD (Figure 6c). Especially, the advective peak is largely reduced in EXP_{var}. In EXP_{mn}, more than 30% of the total transport reaches the MOVE section between 0.25 and 0.5 years after the release More than 60% do so within the first 0.75 years and thus twice as much as in EXP_{var}. The more gradual increase of the cumulative distribution further illustrates the shift to longer transit times when temporal variability is considered. Along with the reduction of the advective peak the median (mean) of the distribution is shifted by 0.3 (0.4) years due to temporal variability of the flow. In contrast, the minimum transit time to reach the MOVE section is 10 days shorter in EXP_{var}. This is likely explained by water volumes that continuously follow the DWBC when it is stronger than average. Another important result is that even without temporal variability, the TTD can not be approximated by a single peak. Partly because the anticyclonic meander between 68°W and 60°W is not fully excluded and secondary pathways along the coast of Cuba and Puerto Rico exist. The more import reason, however, is the nonuniform velocity structure of the DWBC itself. The velocity is largest in a well defined core of the DWBC and gradually decreases away from the western boundary. The strong deviation of the real TTD from a single peak and the spread between tracer and current-meter estimates can be explained by two mechanisms. A nonuniform velocity structure of the DWBC and mesoscale recirculation gyres.

In a last step we combine the previous results of this section and show how different TTDs change the correlation of an advective signal at remote locations by studying idealized experiments (Section 3). The "To MOVE" timeseries (Figure 5a) is used to release particles along a section, which are then sampled at a

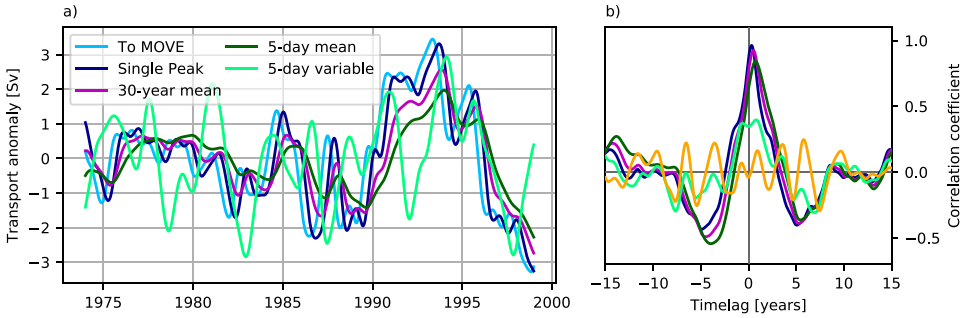

Figure 7. (a) 23-month low-pass filtered timeseries (decadal signal included) of the transport to MOVE (see Section 4.3) and the transport arriving at MOVE in idealized experiments with different transit time distributions (TTD). "Single Peak" refers to an experiment with a single transit time of 136 days. "30-year mean" and "5-day mean" are run with the TTDs shown in Figure 6. In "5-day variable" the TTD is derived from every release time step of EXP_{var} individually and therefore changes with time. (b) Cross-correlation of the timeseries (same color coding as in left panel) with the "To Move" timeseries. The orange line shows cross-correlation of "5-day variable" and "To Move", but with the decadal signal removed.

remote section, similar to our analysis of the ARIANE experiment. However, we do not exclude the decadal signal in this case, to also study the effect of different TTDs on this timescale. As expected, the signal is not changed when the TTD has a single peak (Figure 7). Release and arrival are cross-correlated with a maximum of 0.96 at the lag approximately corresponding to the transit time between the sections (136 days). The cross-correlation is not exactly 1 for two reasons. First, excluding the first three years is reasonable based on the TTD, but not enough to allow all water volumes from the first release time steps to reach the remote section. Second, the timelag is larger than 0 and therefore the cross-correlation is influenced by the zero-padding at the beginning and end of the timeseries. This is necessary because our timeseries are of finite length. Considering the DWBC's velocity structure by applying the TTD derived from EXP_{mn} reduces the correlation to 0.92 at a timelag of 185 days. The correlation is further decreased by adding the mean effect of temporal variability. For that we apply the TTD shown in Figure 3c derived from EXP_{var}. Even with the broader TTD, the maximum cross-correlation is still 0.84 at a timelag of 265 days. As the TTD gets broader, the correlation is only slightly reduced, but the maximum correlation is shifted to a longer lag time. The correlation drops to 0.4 at timelag 290 days, when it is also considered that the TTD itself is not constant, but depends on the release time step (see error bars in Figure 6c). Here the timelag is similar because the mean TTD is still the same, but the correlation is strongly reduced compared to the experiment with a broader TTD alone. Further, most of this correlation is caused by low frequency variability. Removing the decadal signal (119-month low-pass filtered), as for the ARIANE experiments, reduces the correlation from 0.4 to values below 0.25. The latter correlation is not statistically significant. Overall, this experiment is able to reproduce the timeseries at arrival in ARIANE to a large extend (correlation 0.99 with the decadal signal removed), despite its high simplicity. While the interannual signal is strongly altered along the pathway, the decadal signal is nearly unchanged by advection. This suggests that the change of the transport signal along the pathway is dependent on the timescale and almost negligible for decadal changes. However, our 30-year long timeseries is not long enough to make robust statements on this timescale.

Another interesting observation is the change of the signals amplitude (or its variability). A broad TTD causes the signal to be spread over a range of timescales, attenuating its amplitude. The releases using a temporally constant TTD show a lower variability of the arriving signal compared to the released signal. However, if the TTD depends on the release time step, the variability of the arriving signal is amplified. This matches the ARIANE experiment (Figure 5), where the arriving signal has a higher standard deviation.

4.3.3. Recirculation across 16°N

Integrating trajectories released in the DWBC at 16°N backwards in time (EXP_{16N}) reveals that not all these trajectories originate from 26.5°N (Figure 8). In agreement with the forward experiment (EXP_{var}) about 18 Sv of the DWBC at 16°N arise from a southward flow along the western boundary. This flow accounts for 61.2% of the DWBC transport across the MOVE section. Note that the "From 26.5°N" timeseries derived

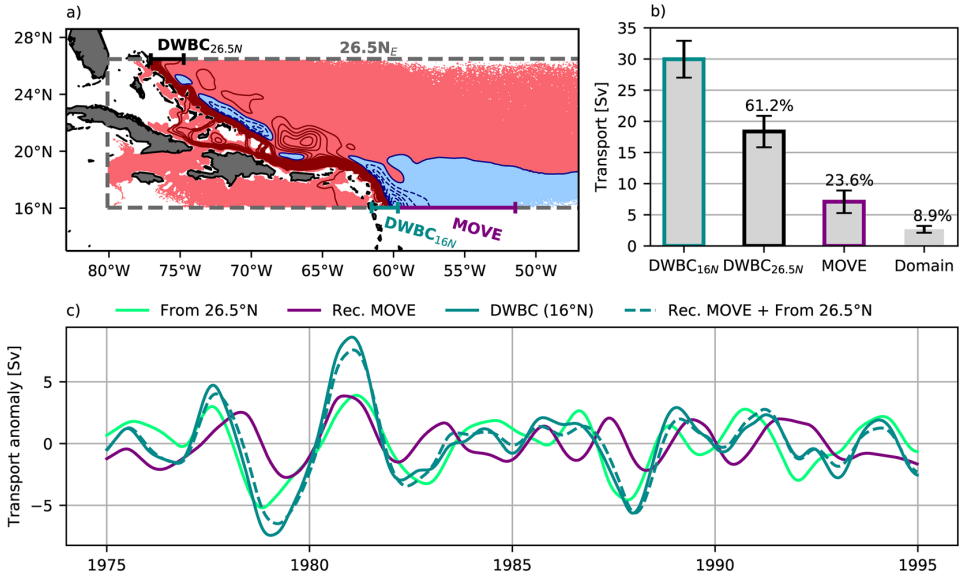

Figure 8. (a) Lagrangian Stream function (LSF) of all water volumes released in EXP_{16N} (backward tracking). Contours are drawn with an interval of 1 Sv. The release section ($DWBC_{16N}$) is shown in cyan. (b) Transport across the boundaries of the closed domain. The mean transport of all 30 release years is shown together with the ensemble standard deviation (error bars). Domain refers to the transport that does not cross any section within 10 years after the release. The transport fraction in % of the total release ($DWBC_{16N}$) is annotated. (c) Timeseries of the interannually filtered transport arriving at the release section in EXP_{16N} from the $DWBC_{26.5N}$ and MOVE sections. Additionally the sum of both is shown along with the Eulerian DWBC transport at 16°N.

from the backward experiment and the "Arrival MOVE" timeseries derived from the forward experiment (Figure 5) are closely related (correlation: 0.91) and represent the same water volumes. A nonnegligible contribution of 7 Sv is added by water that crosses 16°N in northward direction. This water is mostly entrained into the DWBC south of 20°N. These two components explain the majority of interannual variations of the DWBC at 16°N, as indicated by the similarity of the dashed and solid cyan lines in Figure 8. In contrast to 26.5°N, the recirculation component seems to be less dominant in controlling the DWBC's interannual variations. The recirculation component is slightly less variable than the transport from 26.5°N on interannual timescales and its correlation with the DWBC is lower (0.52 for the recirculation and 0.85 for the transport arriving from 26.5°N). A summary of all mentioned correlations related to the ARIANE experiments is provided in Table S1. The timeseries of the transport that arrives from 26.5°N is already not significantly correlated with the DWBC at 26.5°N (Section 4.3). Additionally, this transport does not fully provide the DWBC transport at 16°N. This can explain the lack of statistically significant peaks in the cross-correlation of the DWBC timeseries at 16°N and 26.5°N (Section 4.1).

4.4. Drivers of Mesoscale Recirculations

In the previous section we highlighted the importance of mesoscale recirculation gyres along the DWBC in the STNA. Therefore, we now turn our attention to the mechanisms driving these recirculations. Because the recirculations are visible in EXP_{mn}, they are present in the 30-year averaged flow field. Nevertheless, they are not caused by a steady flow following the bathymetry. The flow adjacent to the DWBC is highly variable (Movie S1). This is further illustrated by Hovmöller plots of the meridional velocity anomaly at 26.5°N, 20°N and 16°N (Figure 9). At all latitudes the flow in the interior ocean is characterized by anomalies propagating westward with ~ 4 cm s^{-1} (depending on the latitude). This speed is in agreement with the phase speed of first mode baroclinic Rossby waves in this latitude range (Gill, 1982). Close to the western boundary, velocity anomalies show a higher magnitude and have distinct characteristics. At 20°N the flow west of 60°W is characterized by northward anomalies that go along with southward anomalies to their east,

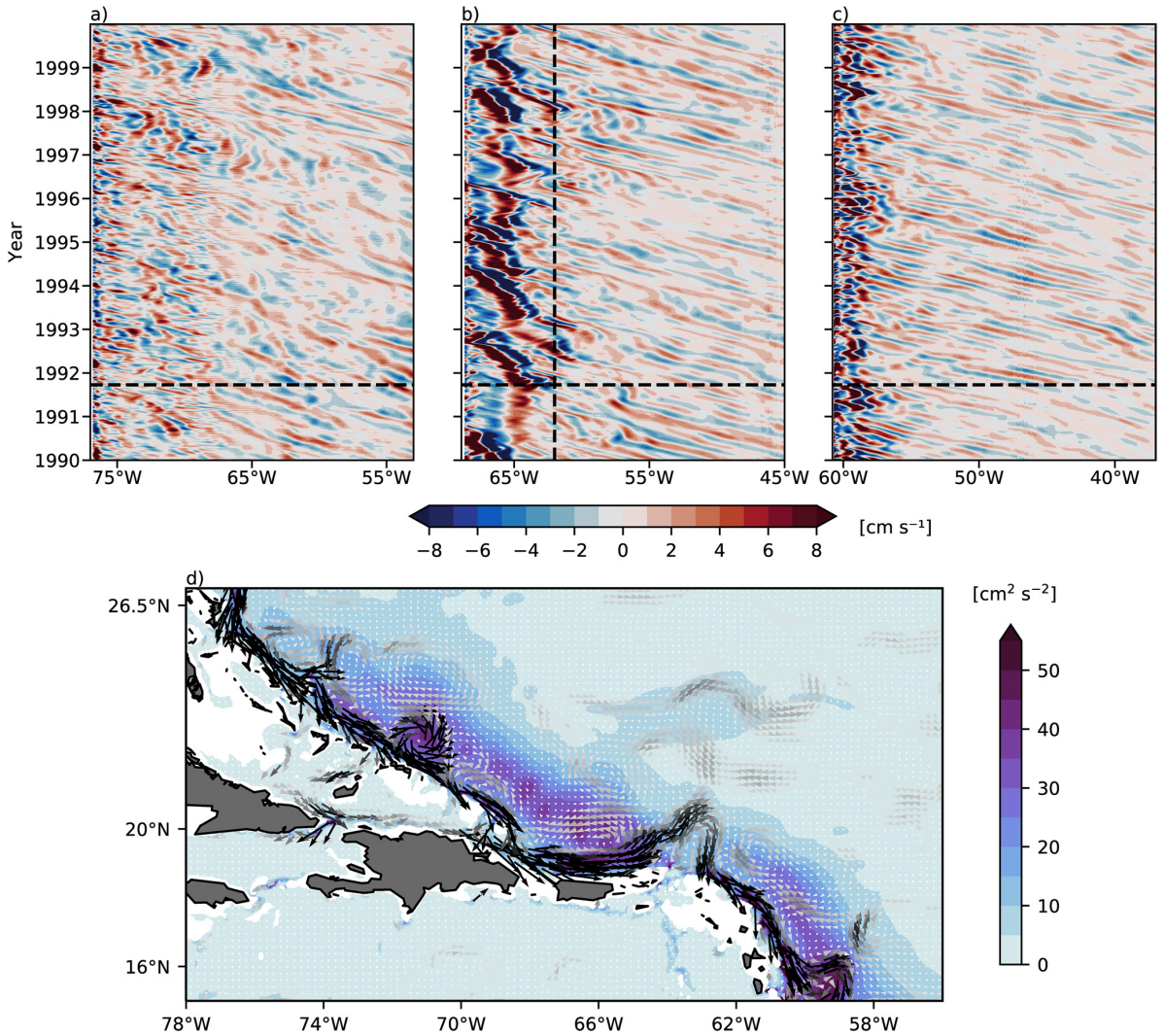

Figure 9. Hovmöller plots of the mean meridional velocity anomaly between 1,000 and 3,500 m depth at 26.5°N (a), 20°N (b) and 16°N (c). The horizontal dashed lines indicate the time step shown in (d). The edge of Lesser Antilles Arc at 20°N is marked with a vertical dashed line. (d) Mean Eddy Kinetic Energy (EKE) (1,000–3,500 m) calculated based on 5-day anomalies from annual means (1990–1999). Vectors show a snapshot (5-day mean) of the velocity field in the same depth range.

both exceeding 8 cm s^{-1} at many time steps. This longitude approximately corresponds to the eastern edge of the Lesser Antilles Arc. Note that the DWBC flows parallel to this section and is located further south. Meridional velocity anomalies west of 60°W are associated with meanders of the DWBC. This can be seen in Figure 9d, where vectors show the 5-day mean velocity field. The positive and negative velocity anomalies associated with the meander centered around 63°W are clearly visible in Figure 9b at the time of the snapshot (horizontal black line). As indicated by the slanting of the anomaly bands to the left, the meander propagates westward (upstream) with a speed around 1.3 cm s^{-1} until the end of 1992. A similar evolution of the flow can be seen for most of the time period shown in Figure 9b. Accordingly, the meander between 68°W and 60°W seen in the LSFs of all Lagrangian experiments is not a steady flow feature, but result of a repeating formation process. Similarly the meridional velocity at 16°N is characterized by strong variability close to the western boundary, showing the frequent existence of eddies at this latitude. At both latitudes, the western boundary regime is clearly separated from the interior ocean. The strong variability along the

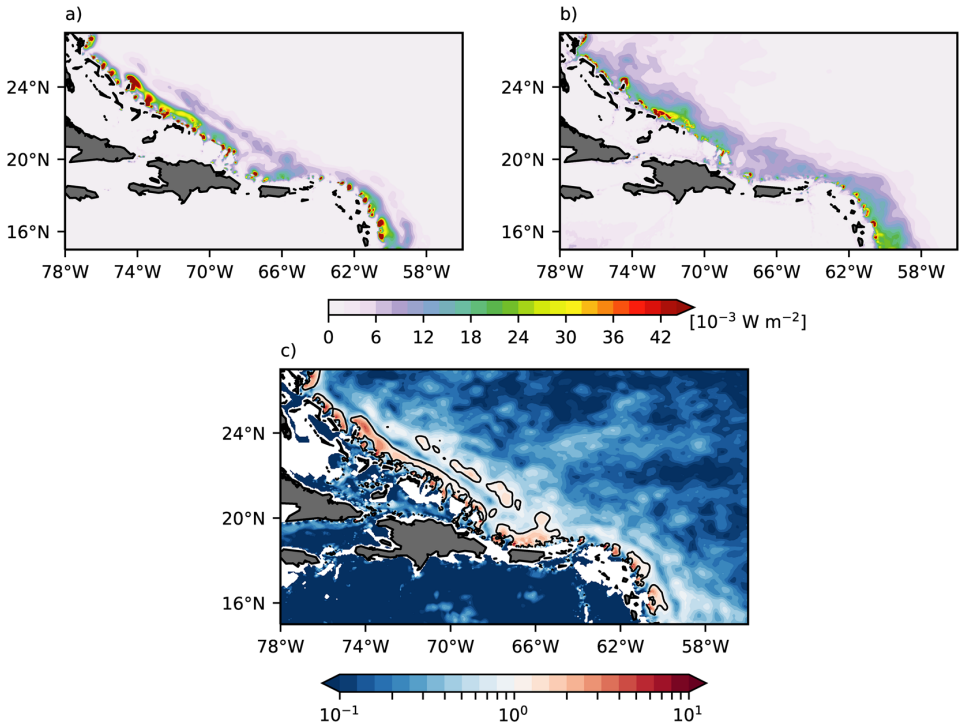

Figure 10. (a) Mean (1990–1999) Barotropic Instability Term $\langle BTI_+ \rangle$ and (b) Baroclinic Instability Term $\langle BCI_+ \rangle$. Both terms are calculated based on 5-day anomalies from annual mean fields and vertically integrated from 1,000 to 3,500 m depth. (c) shows the ratio $\langle BTI_+ \rangle / \langle BCI_+ \rangle$.

western boundary is therefore not directly caused by the arrival of Rossby waves. At 26.5°N this separation is less pronounced. Velocity anomalies are less intensified toward the DWBC. In agreement with Biló and Johns (2020), northward propagating eddies can be seen in the model (Movie S1), but their magnitude is weaker and their occurrence less frequent compared to the eddies and meanders further south. Therefore, the mechanisms driving variability at 26.5°N are different from those at 16°N. This is further supported by the deep EKE in this region (Figure 9d). Along most of the DWBC pathway, EKE is highly elevated compared to the interior ocean. However, north of San Salvador (24°N) EKE values remain low toward the DWBC. Overall, we can conclude that the recirculation gyres seen in the Lagrangian experiments are caused by transient mesoscale features, such as eddies or meanders of the DWBC. The only exception is the cyclonic circulation north of San Salvador that is partly responsible for the return of water to 26.5°N. In line with a description of Leaman and Vertes (1996) and the low EKE values this circulation is stationary.

To gain more information about the generation of eddies south of 24°N, we calculate the positive energy transfers due to barotropic instability (BTI_+) and due to baroclinic instability (BCI_+) following Schubert et al. (2018). Both terms represent local sources of EKE. The $\langle BTI_+ \rangle$ term, with $\langle\ \rangle$ denoting the 10-year average from 1990 to 1999 and vertical integral from 1,000 to 3,500 m, is close to zero in the interior ocean, but strongly enhanced along the western boundary (Figure 10). Especially from San Salvador (24°N) to about 20°N and along the Lesser Antilles Arc (60°W), a high transfer to EKE by barotropic instability can be seen. The baroclinic energy transfer term $\langle BCI_+ \rangle$ shows a similar spacial distribution. However, elevated values are less confined to the western boundary and maximum values are lower compared to $\langle BTI_+ \rangle$. The difference between both terms is more clearly visible in the ratio $\langle BTI_+ \rangle$ / $\langle BCI_+ \rangle$ (Figure 10c). While the interior ocean and Caribbean Sea are dominated by values smaller than one, indicating a dominance of baroclinic instability, the ratio is larger than one along most of the DWBC pathway. Accordingly, barotropic instability caused by a strong horizontal shear at the edge of the DWBC is the main local source of EKE close to the western boundary. Especially south of San Salvador and upstream of the anticyclonic meander

(68°W–60°W) $\langle BTI_+ \rangle$ is about one magnitude larger than $\langle BCI_+ \rangle$. Although Rossby waves are not directly responsible for the variability at the western boundary, they could be an important source of EKE as they reflect into short Rossby waves somewhat caught at the western boundary (Biló & Johns, 2020).

5. Summary and Discussion

In this study, deep flow variability and its implications for the advective spreading of deepwater and the coherence of transport changes at 26.5°N and 16°N were studied. While the AMOC was shown to be highly correlated on interannual to decadal timescales, the correlation of the DWBC transport across both latitudes is not statistically significant. This is in line with the missing impact of advection on coherent variability on annual to interannual timescales north of 38°N (Elipot et al., 2013). In contrast to these latitudes, the importance of slow interior pathways is not a possible explanation for this observation between 26.5°N and 16°N. After being released in the DWBC at 26.5°N, about 20 Sv follow a continuous pathway along the western boundary and reach 16°N. In the following we discuss the sources of temporal variability and differences at the latitudes of 26.5°N and 16°N. Thereafter we address the main questions raised in Section 1 by discussing the impact of mesoscale recirculations on the spreading of deepwater and coherent variability.

5.1. Sources of Temporal Variability in the STNA

The flow to 16°N is subject to strong exchange with the interior ocean caused by temporal variability, in agreement with observations (e.g., Leaman & Vertes, 1996; Rhein et al., 2004). There seems to be an important difference in the mechanism driving temporal variability north and south of San Salvador (24°N). Temporal variability on the northern side is weaker in the model, although this could be a bias of VIKING20X. According to a recent study by Biló and Johns (2020), temporal variability is mainly driven by southward (downstream) propagating meanders and (less frequent) northward propagating eddies, which is in agreement with our results. Temporal variability further south shows different patterns and is associated with southward propagating mesoscale eddies between 24°N and 20°N, and upstream propagating meanders (along the coast of Puerto Rico). At 16°N intense eddies may arrive from the north or south and are present at the vast majority of time steps analyzed here. Although the flow is not steady, a repeating formation process leads to an imprint of these features in the long term averaged velocity field. We find the dominant local source of EKE resulting from barotropic instability of the flow. Consistently, Xu et al. (2012) find mesoscale recirculations in the HYCOM model at very similar locations. Their robustness in both models supports the assumption, that their formation is associated with a strong horizontal shear of the flow at distinct locations. Especially, the Bahamas and Virgin Islands seem to trigger mesoscale recirculations.

5.2. Differences in the Recirculation Across 26.5°N and 16°N

Along with the different mechanisms generating temporal variability, we also find a notable difference between the volume transport recirculations across 26.5°N and 16°N. At 26.5°N the recirculation is supplied by the Abaco Gyre, a persistent cyclonic flow north of San Salvador. Lagrangian studies by Leaman and Vertes (1996) and Riser et al. (1978) show several floats turning north-eastward as they approach 24°N, following similar pathways as indicated by the LSFs shown here. Additionally, water that is detrained from the DWBC by eddies further south adds to the recirculation. A stronger DWBC is likely related to an enhancement through the Abaco Gyre. Also an increase in eddy activity south of San Salvador would be consistent with barotropic instability contributing to their generation. With increasing speed of the DWBC, the horizontal shear gets stronger. This could explain the strong dependence of the return flow on the DWBC strength seen in Section 4.3. Here it is important to consider the impact of a too low EKE at 26.5°N in VIKING20X. Biló and Johns (2020) show that variability on the timescales we consider here is dominated by eddies from south of 24°N. It is not trivial to state how their representation in VIKING20X affects our results. The direct impact of these very infrequent eddies on the volume transport to 26.5°N is likely small, but their reduced magnitude could lead to a stronger connection of the DWBC and Abaco Gyre strength. At 16°N we find the recirculation to be mainly associated with strong mesoscale eddies and there is no persistent recirculation equivalent to the Abaco Gyre. Although eddies can be also seen at 26.5°N they occur more frequently at 16°N, where the connection between DWBC strength and recirculation is weaker. This implies

that the presence of eddies is not directly related to the DWBC strength at 16°N. Extending our study to latitudes further south could show the origin of these eddies and help to understand this observation.

5.3. How does Temporal Variability Affect the Southward Spreading of Deepwater in the STNA?

Temporal variability driven by mesoscale activity in the STNA has a pronounced impact on the volume transport. Together with the nonuniform velocity structure of the DWBC, mesoscale recirculations contribute to the spread between tracer-based and current-meter estimates of the southward velocity in this region. Even long-term averages of the Eulerian velocity can exceed 30 cm s^{-1} in the DWBC core. The speed associated with the Lagrangian mean transit time is 5 cm s^{-1} in EXP_{mn}, mainly reflecting that not all the water that reaches 16°N is transported in the DWBC core, where velocities are highest. Adding recirculations further reduces the mean speed to 4 cm s^{-1}. This spread has important implications by extending the timelag of tracer concentration changes at remote locations and increasing the residence time of anthropogenic carbon dioxide in the deep ocean. Additionally, stirring by mesoscale eddies mixes tracers transported in the DWBC into the interior ocean in agreement with Rhein et al. (2004).

5.4. Can Advection in the DWBC Cause Coherent AMOC Changes in the STNA?

The recirculations lead to a decorrelation of the transport signals at 26.5°N and 16°N. Note that we only study the advective part of the signal propagation, so that decorrelation only refers to the advective component. Boundary waves and wind forcing as different processes to drive coherent changes are not taken into question. Based on our study of the DWBC's timescale these processes are clearly distinguishable based on the expected timelag (being much shorter for wave adjustment) and therefore do not interfere with our results. Recirculations are responsible for a northward return flow to 26.5°N. Bryden et al. (2005) derive a northward recirculation of 13 Sv, which matches our Lagrangian estimate of 10 Sv and shows that most of the northward flow in the vicinity of the western boundary is supplied by water detrained from the DWBC. The strength of the return flow is higher correlated with the DWBC than the component that reaches the MOVE section. Accordingly, additional water volumes associated with an above average DWBC transport are mostly returned to 26.5°N. As a result, the correlation between the DWBC transport and the transport that reaches 16°N is 0.55. Along the pathway to 16°N the transport signal is altered by a broad and variable TTD. The pure broadening of the TTD lengthens the advective timescale and shifts the maximum cross-correlation of the transport signal at release and arrival to longer transit times. However, the impact on the maximum correlation itself is small. In contrast, the correlation decreases when the temporal variability of the TTD itself is considered. Not only the added variety of pathways, but also the fact that trajectories released at different time steps will take different routes, reduces the correlation. This has important implications for observational studies using Lagrangian techniques. A TTD derived from a single float release (or very few release times) must not represent the mean distribution even without considering uncertainties from a limited spatial coverage of the DWBC. This also shows the importance of releasing virtual particles/water volumes over a time period as long as possible in modeling studies. To estimate the variability of the TTD is especially important when a study aims to infer changes of a signal along the pathway. As EKE in VIKING20X is lower than in observations at 26.5°N, the TTD may be even more variable and changes of the signal along the pathway even stronger in the real ocean. At 16°N the correlation of the transport arriving from 26.5°N and the DWBC at 26.5°N is already statistically insignificant. Additionally, the DWBC at 16°N is not fully supplied by water advected in the DWBC from 26.5°N. A local recirculation of 7 Sv further decouples the DWBC transport at both latitudes. As a consequence, advection in the DWBC does not play a role for the coherence of AMOC changes on interannual timescales, even though it is responsible for a strong mean flow between the latitudes with a timescale well below 2 years. Consistent with this result, the strong AMOC correlation is found at timelag zero without any significant peaks at timelags corresponding to the advective timescale. This may not be surprising based on modeling studies finding AMOC anomalies to propagate with Kelvin wave speed (Getzlaff et al., 2005; Zhang, 2010). Still the missing impact of advection on interannual timescales is not trivial, especially in the latitude range studied here. Our study provides information about mechanisms that decouple transport variations at remote sections, despite the existence of a strong, continuous mean current connecting them. Further, the existence of highly variable recirculations stresses the importance of trans-basin AMOC measurements. The southward DWBC transport does

not provide a good estimate of the total southward transport across the section. It is also not possible to simply include the recirculation to calculate a mean southward transport. Especially at 26.5°N the recirculation is rather broad with a variable extend and not connected to a clear maximum of the cumulative deep transport (from west to east) at many time steps. Note however, that the long term mean Lagrangian transport to the MOVE section (19.3 Sv) matches the mean AMOC of about 19 Sv in the STNA. This confirms that the main NADW pathway in this region is the DWBC.

Overall, our results are consistent with the conclusion of Frajka-Williams et al. (2018) that the different trends observed at MOVE and RAPID between 2004 and 2015 are caused by differences in the methodology of the transport calculation, not an actual difference in the transport tendency. First, the 119-months low-pass filtered AMOC timeseries in the model show a correlation of 0.95. As a result, different trends within a time span of around 10-years (filtering period), are not existent in the model. Second, our results suggest that the decorrelation of the (advective) transport signals at 16°N and 26.5°N is almost negligible on decadal timescales. Advection could therefore play an important role for the coherent, basin wide AMOC adjustment on decadal timescales described by Biastoch et al. (2008). However, our Lagrangian experiments only cover 30 years and are too short for robust results on this timescale. On interannual (and shorter) timescales, on the other hand, opposing anomalies are possible. At least advection in the DWBC does not determine the AMOC to show similar changes at 26.5°N and 16°N. This is apparent in the lower correlation of 0.57 for the 23-month low-pass filtered timeseries in the model. Nevertheless, this correlation is still significantly different from zero in agreement with Bingham et al. (2007). But instead of advection in the DWBC, wind forcing seems to be the driver of coherent interannual changes at MOVE and RAPID. Biastoch et al. (2008) and Zhao and Johns (2014) find interannual AMOC variations to be dominated by wind forcing in the STNA. Further, Elipot et al (2016) report on coherent changes across the STNA driven by a NAO-type wind pattern. Although the RAPID timeseries shows an inconsistent overturning response to this pattern compared to MOVE, Line W (39.8°N) and WAVE (42.58°N), this may only result from the very limited length of their timeseries. Here we took a first step in understanding processes that can impact the coherence of AMOC changes at remote locations. A detailed study of coherence driven by wind patterns or boundary waves is left for further research.

Data Availability Statement

Model computations and data analysis were performed at the North German Supercomputing Alliance (HLRN). The data is available at https://hdl.handle.net/20.500.12085/ec430a5c-1930-4a87-bb1f-973162c2a135. The MOVE transport time series used for model validation is available at http://www.oceansites.org/tma/move.html.

Acknowledgments
The study was supported by the cooperative program "RACE-Regional Atlantic Circulation and Global Change" (BMBF Grant 03F0729C) and the European Union's Horizon 2020 research and innovation programme under grant agreement No 818123 (iAtlantic).

References

Barnier, B., Madec, G., Penduff, T., Molines, J.-M., Treguier, A.-M., Le Sommer, J., & Cuevas, B. (2006). Impact of partial steps and momentum advection schemes in a global ocean circulation model at eddy-permitting resolution. *Ocean Dynamics*, *56*(5), 543–567. https://doi.org/10.1007/s10236-006-0082-1

Biastoch, A., Böning, C. W., Getzlaff, J., Molines, J.-M., & Madec, G. (2008). Causes of interannual-decadal variability in the meridional overturning circulation of the midlatitude North Atlantic Ocean. *Journal of Climate*, *21*(24), 6599–6615. https://doi.org/10.1175/2008JCLI2404.1

Biastoch, A., Schwarzkopf, F. U., Getzlaff, K., Rühs, S., Martin, T., Scheinert, M., et al. (2021). Regional imprints of changes in the Atlantic meridional overturning circulation in the eddy-rich ocean model VIKING20X. *Ocean Science*, 1–52. https://doi.org/10.5194/os-2021-37

Biló, T. C., & Johns, W. E. (2020). The deep western boundary current and adjacent interior circulation at 24°-30°N: Mean structure and mesoscale variability. *Journal of Physical Oceanography*, *50*(9), 2735–2758. https://doi.org/10.1175/JPO-D-20-0094.1

Bingham, R. J., Hughes, C. W., Roussenov, V., & Williams, R. G. (2007). Meridional coherence of the North Atlantic meridional overturning circulation. *Geophysical Research Letters*, *34*, L23606. https://doi.org/10.1029/2007GL031731

Blanke, B., Arhan, M., Madec, G., & Roche, S. (1999). Warm water paths in the equatorial Atlantic as diagnosed with a general circulation model. *Journal of Physical Oceanography*, *29*(11), 2753–2768. https://doi.org/10.1175/1520-0485(1999)029<2753:wwpite>2.0.co;2

Blanke, B., & Raynaud, S. (1997). Kinematics of the pacific equatorial undercurrent: An Eulerian and Lagrangian approach from GCM Results. *Journal of Physical Oceanography*, *27*(6), 1038–1053. https://doi.org/10.1175/1520-0485(1997)027<1038:kotpeu>2.0.co;2

Böning, C. W., Behrens, E., Biastoch, A., Getzlaff, K., & Bamber, J. L. (2016). Emerging impact of Greenland meltwater on deepwater formation in the North Atlantic Ocean. *Nature Geoscience*, *9*(7), 523–527. https://doi.org/10.1038/ngeo2740

Bower, A. S., Lozier, M. S., Gary, S. F., & Böning, C. W. (2009). Interior pathways of the North Atlantic meridional overturning circulation. *Nature*, *459*(7244), 243–247. https://doi.org/10.1038/nature07979

Bryden, H. L., Johns, W. E., & Saunders, P. M. (2005). Deep western boundary current east of Abaco: Mean structure and transport. *Journal of Marine Research*, *63*(1), 35–57. https://doi.org/10.1357/0022240053693806

Debreu, L., Vouland, C., & Blayo, E. (2008). AGRIF: Adaptive grid refinement in Fortran. *Computers & Geosciences*, *34*(1), 8–13. https://doi.org/10.1016/j.cageo.2007.01.009

Delandmeter, P., & van Sebille, E. (2019). The parcels v2.0 lagrangian framework: New field interpolation schemes. *Geoscientific Model Development*, *12*(8), 3571–3584. https://doi.org/10.5194/gmd-12-3571-2019

Elipot, S., Frajka-Williams, E., Hughes, C. W., Olhede, S., & Lankhorst, M. (2016). Observed basin-scale response of the North Atlantic meridional overturning circulation to wind stress forcing. *Journal of Climate*, *30*(6), 2029–2054. https://doi.org/10.1175/JCLI-D-16-0664.1

Elipot, S., Hughes, C., Olhede, S., & Toole, J. (2013). Coherence of western boundary pressure at the RAPID WAVE array: Boundary wave adjustments or deep western boundary current advection? *Journal of Physical Oceanography*, *43*(4), 744–765. https://doi.org/10.1175/JPO-D-12-067.1

Emery, W. J., & Thomson, R. E. (2001). Time-series analysis methods. In W. J. Emery & R. E. Thomson (Eds.), *Data analysis methods in physical oceanography* (pp. 371–567). Amsterdam. Elsevier Science. https://doi.org/10.1016/B978-044450756-3/50006-X

Frajka-Williams, E., Lankhorst, M., Koelling, J., & Send, U. (2018). Coherent circulation changes in the deep North Atlantic from 16°N and 26°N transport arrays. *Journal of Geophysical Research: Oceans*, *123*, 3427–3443. https://doi.org/10.1029/2018JC013949

Gary, S. F., Susan Lozier, M., Böning, C. W., & Biastoch, A. (2011). Deciphering the pathways for the deep limb of the meridional overturning circulation. *Deep Sea Research Part II: Topical Studies in Oceanography*, *58*(17–18), 1781–1797. https://doi.org/10.1016/j.dsr2.2010.10.059

Getzlaff, J., Böning, C. W., Eden, C., & Biastoch, A. (2005). Signal propagation related to the North Atlantic overturning. *Geophysical Research Letters*, *32*, L09602. https://doi.org/10.1029/2004GL021002

Gill, A. (1982). *Atmosphere-ocean dynamics* (1st ed). New York. Academic Press.

Johns, W. E., Kanzow, T., & Zantopp, R. (2005). Estimating ocean transports with dynamic height moorings: An application in the Atlantic deep western boundary current at 26°N. *Deep Sea Research Part I: Oceanographic Research Papers*, *52*(8), 1542–1567. https://doi.org/10.1016/j.dsr.2005.02.002

Kanzow, T., Send, U., & McCartney, M. (2008). On the variability of the deep meridional transports in the tropical North Atlantic. *Deep Sea Research Part I: Oceanographic Research Papers*, *55*(12), 1601–1623. https://doi.org/10.1016/j.dsr.2008.07.011

Kanzow, T., Send, U., Zenk, W., Chave, A. D., & Rhein, M. (2006). Monitoring the integrated deep meridional flow in the tropical North Atlantic: Long-term performance of a geostrophic array. *Deep Sea Research Part I: Oceanographic Research Papers*, *53*(3), 528–546. https://doi.org/10.1016/j.dsr.2005.12.007

Large, W. G., & Yeager, S. G. (2009). The global climatology of an interannually varying air-sea flux data set. *Climate Dynamics*, *33*(2), 341–364. https://doi.org/10.1007/s00382-008-0441-3

Leaman, K. D., & Vertes, P. S. (1996). Topographic influences on recirculation in the deep western boundary current: Results from RAFOS float trajectories between the Blake-Bahama outer ridge and the San Salvador "Gate". *Journal of Physical Oceanography*, *26*(6), 941–961. https://doi.org/10.1175/1520-0485(1996)026<0941:tiorit>2.0.co;2

Lee, T. N., Johns, W., Zantopp, R., & Schott, F. (1990). Western boundary current structure and variability east of Abaco, Bahamas at 26.5°N. *Journal of Physical Oceanography*, *20*(3), 446–466. https://doi.org/10.1175/1520-0485(1990)020<0446:wbcsav>2.0.co;2

Lee, T. N., Johns, W. E., Zantopp, R. J., & Fillenbaum, E. R. (1996). Moored observations of western boundary current variability and thermohaline circulation at 26.5° in the subtropical North Atlantic. *Journal of Physical Oceanography*, *26*(6), 962–983. https://doi.org/10.1175/1520-0485(1996)026<0962:moowbc>2.0.co;2

Lüschow, V., Storch, J.-S. V., & Marotzke, J. (2019). Diagnosing the influence of mesoscale eddy fluxes on the deep western boundary current in the 1/10° STORM/NCEP simulation. *Journal of Physical Oceanography*, *49*(3), 751–764. https://doi.org/10.1175/JPO-D-18-0103.1

Madec, G. (2016). *Nemo ocean engine. Note du Pôle de modélisation*, France. Institut Pierre-Simon Laplace (IPSL). No 27, ISSN No 1288-1619

Pickart, R. S., Hogg, N. G., & Smethie, W. M. (1989). Determining the strength of the deep western boundary current using the chlorofluoromethane ratio. *Journal of Physical Oceanography*, *19*(7), 940–951. https://doi.org/10.1175/1520-0485(1989)019<0940:dtsotd>2.0.co;2

Rhein, M. (1994). The deep western boundary current: Tracers and velocities. *Deep Sea Research Part I: Oceanographic Research Papers*, *41*(2), 263–281. https://doi.org/10.1016/0967-0637(94)90003-5

Rhein, M., Kieke, D., & Steinfeldt, R. (2015). Advection of North Atlantic deep water from the Labrador Sea to the southern hemisphere. *Journal of Geophysical Research: Oceans*, *120*, 2471–2487. https://doi.org/10.1002/2014JC010605

Rhein, M., Walter, M., Mertens, C., Steinfeldt, R., & Kieke, D. (2004). The circulation of North Atlantic deep water at 16°N, 2000-2003. *Geophysical Research Letters*, *31*, L14305. https://doi.org/10.1029/2004GL019993

Rieck, J. K., Böning, C. W., & Getzlaff, K. (2019). The nature of eddy kinetic energy in the Labrador Sea: Different types of mesoscale eddies, their temporal variability, and impact on deep convection. *Journal of Physical Oceanography*, *49*(8), 2075–2094. https://doi.org/10.1175/JPO-D-18-0243.1

Riser, S. C., Freeland, H., & Rossby, H. T. (1978). Mesoscale motions near the deep western boundary of the North Atlantic. *Deep Sea Research*, *25*(12), 1179–1191. https://doi.org/10.1016/0146-6291(78)90012-7

Rühs, S., Schwarzkopf, F. U., Speich, S., & Biastoch, A. (2019). Cold vs. warm water route - Sources for the upper limb of the Atlantic meridional overturning circulation revisited in a high-resolution ocean model. *Ocean Science*, *15*(3), 489–512. https://doi.org/10.5194/os-15-489-2019

Sabine, C. L., Feely, R. A., Gruber, N., Key, R. M., Lee, K., Bullister, J. L., & Rios, A. F. (2004). The oceanic sink for anthropogenic CO_2. *Science*, *305*(5682), 367–371. https://doi.org/10.1126/science.1097403

Schubert, R., Biastoch, A., Cronin, M. F., & Greatbatch, R. J. (2018). Instability-driven benthic storms below the separated gulf stream and the North Atlantic Current in a high-resolution ocean model. *Journal of Physical Oceanography*, *48*(10), 2283–2303. https://doi.org/10.1175/JPO-D-17-0261.1

Send, U., Lankhorst, M., & Kanzow, T. (2011). Observation of decadal change in the Atlantic meridional overturning circulation using 10 years of continuous transport data. *Geophysical Research Letters*, *38*, L24606. https://doi.org/10.1029/2011GL049801

Smeed, D. A., McCarthy, G. D., Cunningham, S. A., Frajka-Williams, E., Rayner, D., Johns, W. E., et al. (2014). Observed decline of the Atlantic meridional overturning circulation 2004-2012. *Ocean Science*, *10*(1), 29–38. https://doi.org/10.5194/os-10-29-2014

Srokosz, M. A., & Bryden, H. L. (2015). Observing the Atlantic meridional overturning circulation yields a decade of inevitable surprises. *Science*, *348*(6241), 1255575. https://doi.org/10.1126/science.1255575

van Sebille, E., Griffies, S. M., Abernathey, R., Adams, T. P., Berloff, P., Biastoch, A., et al. (2018). Lagrangian ocean analysis: Fundamentals and practices. *Ocean Modelling*, *121*, 49–75. https://doi.org/10.1016/j.ocemod.2017.11.008

Waugh, D. W., & Hall, T. M. (2005). Propagation of Tracer signals in boundary currents. *Journal of Physical Oceanography*, *35*(9), 1538–1552. https://doi.org/10.1175/JPO2779.1

Xu, X., Schmitz, W. J., Jr, Hurlburt, H. E., & Hogan, P. J. (2012). Mean Atlantic meridional overturning circulation across 26.5°N from eddy-resolving simulations compared to observations. *Journal of Geophysical Research*, *117*, C03042. https://doi.org/10.1029/2011JC007586

Zhang, R. (2010). Latitudinal dependence of Atlantic meridional overturning circulation (AMOC) variations. *Geophysical Research Letters*, *37*, L16703. https://doi.org/10.1029/2010GL044474

Zhao, J., & Johns, W. (2014). Wind-forced interannual variability of the Atlantic meridional overturning circulation at 26.5°N. *Journal of Geophysical Research: Oceans*, *119*, 2403–2419. https://doi.org/10.1002/2013JC009407

Journal of Geophysical Research: Oceans

Supporting Information for

On the variability of the DWBC transport between 26.5°N and 16°N in an eddy-rich ocean model

T. Schulzki[1], K. Getzlaff[1] and A. Biastoch[1,2]

[1]GEOMAR Helmholtz Centre for Ocean Research, Düsternbrooker Weg 20, 24105 Kiel, Germany

[2]Kiel University, Christian-Albrechts-Platz 4, 24118 Kiel, Germany

Contents of this file

Additional Supporting Information (Files uploaded separately)

Introduction

This file contains additional figures on the AMOC in VIKING20X, flow variability close to the western boundary and the ARIANE experiment EXP_{mn}. Additionally, it is verified that the lack of DWBC correlation seen in the model is not caused by our definition of the DWBC. Also, we provide a table summarizing the mentioned correlation-coefficients of the different timeseries derived from the ARIANE experiments (section 4.3). All figures and a movie are based on the same data as described in section 2 of the main publication.

The data is available at:
https://hdl.handle.net/20.500.12085/ec430a5c-1930-4a87-bb1f-973162c2a135
Additional information on the VIKING20X model run used in this paper will be available at:
https://git.geomar.de/NEMO/EXP/VIKING20X.L46-KKG36013H

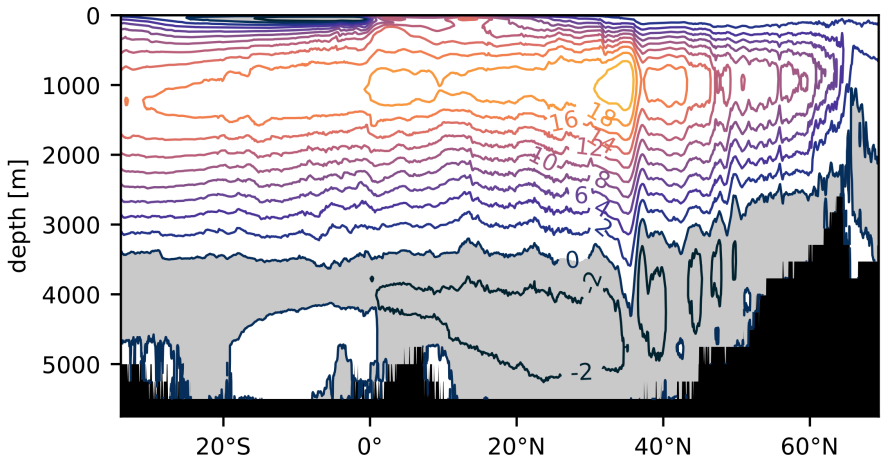

Figure S1. Mean (1970-2000) Meridional Overturning Streamfunction in the Atlantic Ocean. Contours are drawn every 2 Sv. Negative values are shaded grey.

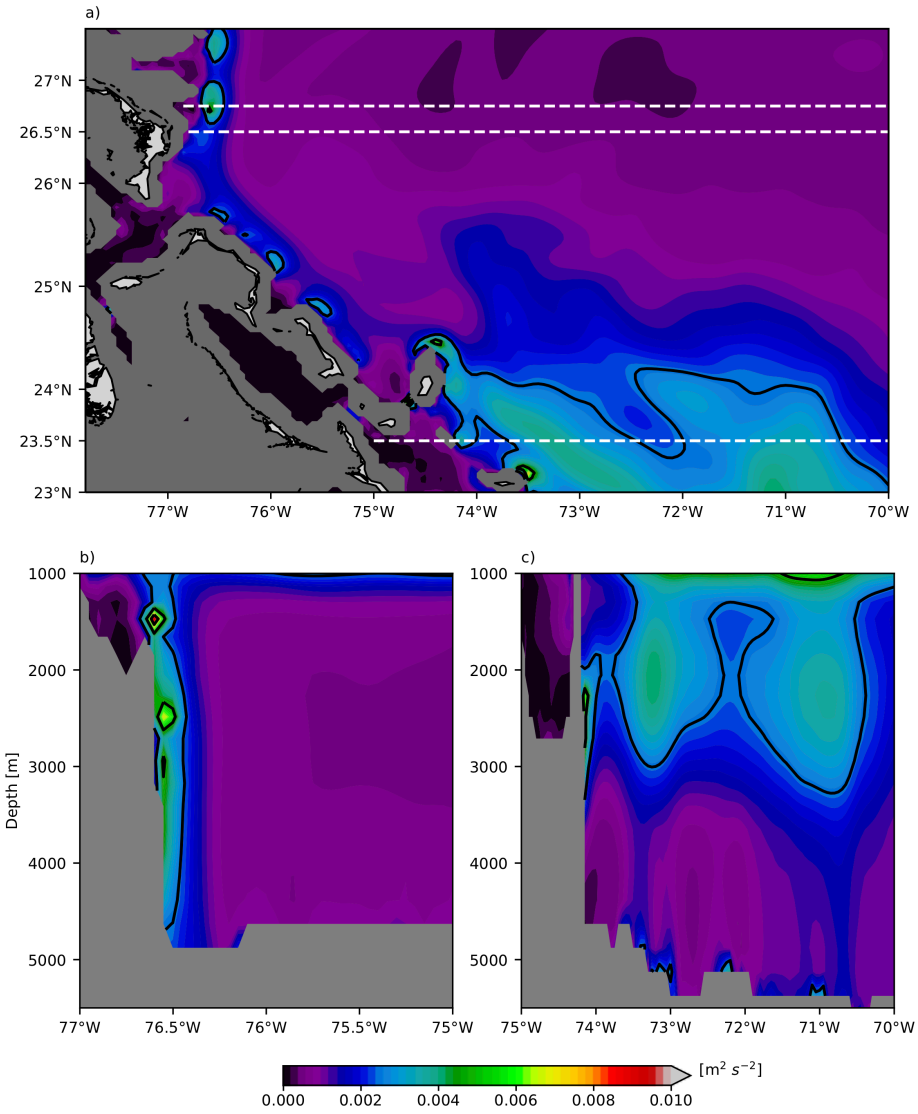

Figure S2. Mean (1990-1999) Eddy Kinetic Energy (EKE). a) Map of the vertically averaged EKE between 1500 and 2500 m depth. This is the depth range, where observations and the model used in *Biló et al. (2020)* show consistently high values. EKE sections at 26.75°N (b) and 23.5°N (c). Contours are drawn at 0.0025, 0.005 and 0.0075 m^2 s^{-2} in all panels. Dashed lines indicate the latitudes of the sections in b), c) and Figure 1c) of the main text.

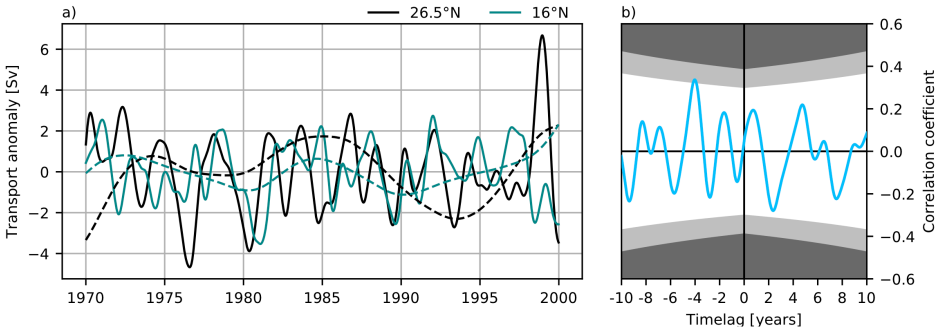

Figure S3. a) Low-pass filtered timeseries of the DWBC transports at 26.5°N and 16°N. Solid (dashed) lines show interannual (decadal) anomalies. b) Cross-correlation of the interannual DWBC timeseries at 26.5°N and 16°N. Grey shaded areas indicate significant correlation coefficients based on a confidence level of 95% and 99%. 26.5°N leads at positive lags. In contrast to Figure 2 of the main text, the DWBC is defined as the minimum of the cumulative transport (from west to east) below 1000 m.

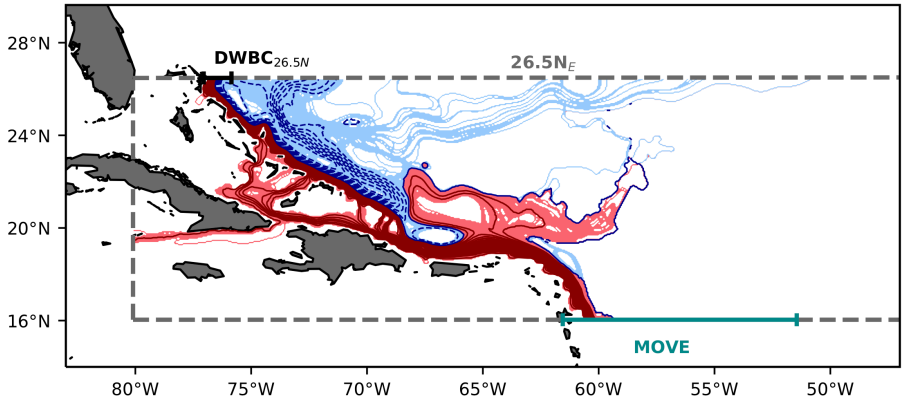

Figure S4. Lagrangian Streamfunction of all water volumes released in EXP_{mn}. Contours are drawn with an interval of 1 Sv.

Timeseries 1	Timeseries 2	Correlation coefficient
$26.5N_E$ (EXP_{var})	DWBC 26.5°N	0.90
To MOVE (EXP_{var})	DWBC 26.5°N	0.55
$26.5N_E$ + To MOVE (EXP_{var})	DWBC 26.5°N	0.99
To MOVE (EXP_{var})	Arrival MOVE (EXP_{var})	< 0.2
Arrival MOVE (EXP_{var})	From 26.5°N (EXP_{16N})	0.91
Rec. MOVE (EXP_{16N})	DWBC 16°N	0.52
From 26.5°N (EXP_{16N})	DWBC 16°N	0.85

Table S1. Summary of correlation coefficients and maximum cross-correlation coefficients related to the ARIANE experiments. See main text (section 4.3) for a definition of the timeseries mentioned here. All timeseries are derived from ARIANE, except the DWBC transport at 26.5°N and 16°N, which are calculated from the Eulerian velocity field. The corresponding ARIANE experiments are written in brackets.

Movie S1. Animation of the 5-day mean velocity field between 1000 and 3500 m depth for the time period 1990 - 1999. The grey line indicates the 1000 m depth contour.

CHAPTER 6

Ecosystem Connectivity in the Northwest Atlantic Shaped by Eddy-Current Interactions

Biophysical connectivity on regional scales:

The last chapter revealed how the interaction of the DWBC with mesoscale eddies is linked to the coherence of AMOC variability. In an interdisciplinary context, the interaction of important AMOC pathways, and in particular of the DWBC, with mesoscale eddies is also highly relevant for biophysical connectivity. The interplay of currents, mesoscale eddies and complex bathymetry strongly impacts the connectivity of remote ecosystems. This is demonstrated in this chapter by investigating the connectivity of deep-sea octocoral populations along the Northwest Atlantic continental slope, including a population on the wreck of RMS Titanic. It is shown that velocity anomalies, associated with overlying eddies, can strongly enhance the mean flow, or cause a reversal of the flow direction even at the Titanic wreck site at almost 4 km depth. Guided by the bathymetry, this results in two distinct dispersal pathways from the wreck. Eddies could further play an important role in connecting the Titanic to a natural occurring population of octocorals on the eastern slope of the Grand Banks. Larvae spawned at this location are rapidly advected southward in the Labrador Current and DWBC. At the Tail of the Grand Banks larvae continuously follow the continental slope to reach more downstream populations, or are deflected away from the boundary toward the wreck site in an interaction with eddies. Despite largely unknown larval characteristics, the results of this chapter suggest that the Titanic could be an important stepping stone for the dispersal of larvae and highlight the importance of high-resolution modelling to obtain realistic dispersal pathways.

Related manuscript:

Schulzki, T., Henry, L.-A., Roberts, J. M., Rakka, M., Ross, S. W. and Biastoch, A. (2023). Mesoscale ocean eddies determine dispersal and connectivity of corals at the RMS Titanic wreck site, submitted to Deep Sea Research Part I, under review.

Author contribution: The author was fully responsible for all Lagrangian experiments, all analysis and corresponding figures and wrote the manuscript, with exception of the biological background in the introduction section.

Mesoscale ocean eddies determine dispersal and connectivity of corals at the RMS *Titanic* wreck site

Tobias Schulzki[a,*], Lea-Anne Henry[b], J. Murray Roberts[b],

Maria Rakka[c,d] , Steve W. Ross[e], Arne Biastoch[a,f]

[a] GEOMAR Helmholtz Centre for Ocean Research, Kiel, Germany

[b]School of GeoSciences, University of Edinburgh, Edinburgh, UK

[c] Institute of Marine Sciences - Okeanos, University of the Azores, Horta, Portugal

[d] Oceanography Department, Dalhousie University, Halifax, NS, Canada

[e] Center for Marine Science, University of North Carolina at Wilmington, Wilmington, North Carolina, United States

[f] Kiel University, Kiel, Germany

*Corresponding author: Tobias Schulzki, Geomar Helmholtz Centre for Ocean Research, Düsternbrooker Weg 20, Kiel, Germany, tschulzki@geomar.de

Abstract

The sinking of the RMS *Titanic* on 15 April 1912 remains one of most iconic maritime disasters in history. Today, the wreck site lies in waters 3,800 m deep approximately 690 km south southeast of Newfoundland, Atlantic Canada. The wreck and debris field are colonized by various marine organisms, including the bathyal-abyssal octocoral *Chrysogorgia agassizii*. Because of the rapid deterioration of the *Titanic* and the vulnerability of natural deep-sea coral populations to environmental changes, it is vital to understand the role the *Titanic* as well as other such structures could play in connecting ecosystems along the North American slope. Based on Lagrangian experiments with more than one million virtual particles and different scenarios for larval behavior, given the uncertainties around the biology of *C. agassizii*, the dispersal of larvae spawned at the *Titanic* wreck is studied in a high-resolution numerical ocean model. While the large-scale bathymetry shields the *Titanic* from a strong mean flow, mesoscale ocean eddies can considerably affect the deep circulation and cause a significant speed up, or also a reversal, of the circulation. As a consequence, the position of upper and mid-ocean eddies in the model largely controls the direction and distance of larval dispersal, with the impact of eddies outweighing the importance of active larval swimming in our experiments. Although dependent on larval buoyancy and longevity, we find that the *Titanic* could be reached by larvae spawned on the upper slope east of the Grand Banks. Therefore, the *Titanic* could act as a stepping stone connecting the upper to the deep continental slope off Newfoundland. From the *Titanic*, larvae then spread into deep Canadian waters and areas beyond national jurisdiction.

Key Words

- RMS *Titanic*
- Deep-sea octocorals
- Lagrangian modeling
- Biophysical connectivity
- Mesoscale eddies
- *Chrysogorgia agassizii*

1. Introduction

The sinking of the RMS *Titanic* on 15 April 1912 was one of the deadliest and most iconic maritime disasters in history. As the ship sank, it split into two sections with the bow hitting the seafloor at approximately 56 km/hour, with her stern spiraling downwards and striking the seafloor at about 80 km/hour, roughly 600 m away from her bow. More than 1,500 people lost their lives, and today the wreckage site lies in waters 3,800 m deep approximately 690 km south southeast of Newfoundland in Atlantic Canada. The wreck site was discovered in 1985 by a joint French-US expedition, but it was not until 2012 that the site could be safeguarded by the UNESCO Convention on the Protection of Underwater Cultural Heritage, albeit this does not afford full site protection (Martin, 2018). The case could be made that the *Titanic* and its debris field are resting on the seafloor (the "Area") and more specifically in Areas Beyond National Jurisdication (ABNJ), but equally a case could be made that they actually rest on the outer edge of Canada's continental margin (Aznar and Varmer, 2013). Canada has filed to extend their seabed claim to include the site with the Commission on the Limits of the Continental Shelf (CLCS) in accordance with Article 76, paragraph 8 of the Law of the Sea Convention. Corrosion is rapidly degrading the *Titanic* (Salazar and Little, 2017). Much of the deterioration appears to be mediated by microbial communities leaching iron from the structure in an oxidative environment (Cullimore and Johnston, 2008). To further safeguard its protection and address other issues such as looting and unwanted salvage, a multilateral "Agreement Concerning the Shipwrecked Vessel RMS *Titanic*" came into force in 2019 after negotiations between Canada, the United Kingdom, France, and the United States.

Besides its monumental cultural legacy, more than a century of marine growth has accumulated and colonised the wreck and associated debris field, and these anthropogenic structures now support a biologically rich natural heritage. Few have observed this man-made ecosystem first hand, but exploration using deepwater submersible vehicles (DSVs) has helped reveal and document much of the *Titanic*'s legacy of natural heritage. Species richness of sessile fauna tends to be higher near or on the wreck itself, including numerous occurrences of cold-water corals and sponges.

The deep-sea bathyal-abyssal octocoral *Chrysogorgia agassizii* has been documented at various locations on the *Titanic* wreck based on visual identifications, including a quite prominent occurrence on the upper rail of the ship's bow (Vinogradov, 2000). Repeat surveys of the coral performed by the Russian DSVs *Mir-1* and *Mir-2* allowed detailed investigation of *C. agassizii* growth rates, showing relatively fast growth for a deep-sea coral (approximately 1 cm/year linear extension; Vinogradov, 2000). Recent accounts from DSV dives conducted by OceanGate Expeditions at the wreck site during 2021 and 2022 no longer document that specimen of *C. agassizii* on the upper rail of the bow (A. Gebruk, pers. comm.; SWR pers. obs.; Figure 1). However, the species remains a common member of *Titanic*'s sessile marine growth community on the ship's bow and elsewhere, and these occurrences offer an opportunity to explore how the natural heritage of the *Titanic* may confer a legacy connecting to marine ecosystems further afield.

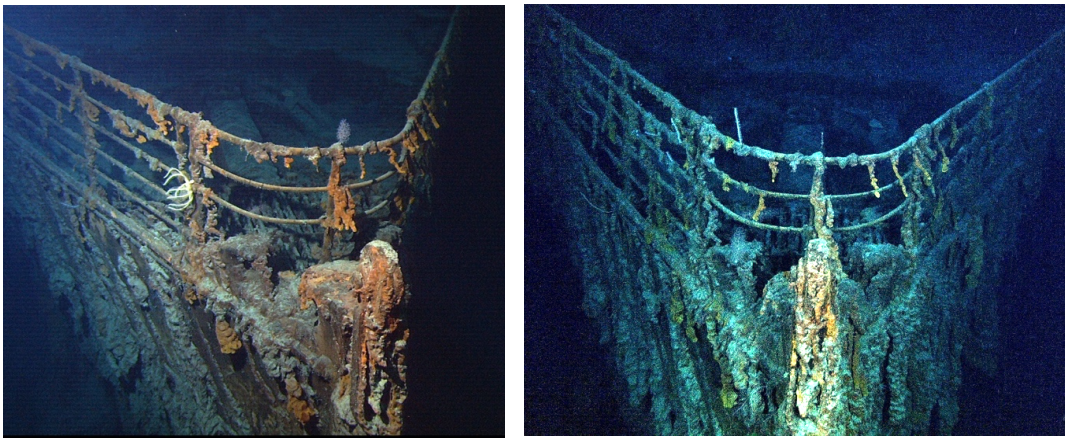

Figure 1: Photos of RMS *Titanic* bow. Left: photo from 2004 (credit NOAA Ocean Exploration and Research) with the putative *C. agassizii* in the center of the top rail. Right: photo from 2021 (credit Ocean Gate Expeditions), showing that most of that *C. agassizii* appears to be missing. Note, however, that there are other attached octocorals, some of which may be *Chrysogorgia* spp. and/or *Lepidisis* spp.

The role that shipwrecks play in facilitating ecological connectivity and the role of underwater cultural heritage more generally have gained significant global research interest over the last decade, (Meyer-Kaiser and Mires, 2022). Studies can identify important sources, sinks and the corridors used by organisms for dispersal: this knowledge can inform policy decisions about area-based management tools such as marine protected areas (MPAs) to halt or reverse loss of biodiversity and optimise ecosystem services such as fisheries benefits (Fontoura et al., 2022). As a new treaty on Biodiversity Beyond National Jurisdiction (BBNJ) is being negotiated, embracing the ecological connectivity concept can lead to improved High Seas and Areas Beyond National Jurisdiction (ABNJ) governance because the concept provides a firm rationale for enhancing cooperation and coordination among existing instruments, bodies, and frameworks that traditionally operate separately (Tessnow-von Wysocki and Vadrot, 2022). As isolated but abundant and globally distributed habitats on the seafloor, shipwrecks effectively reduce the distances that organisms must disperse from, or travel to, in order to be connected to upstream and downstream populations and habitats. This appears to be the case for a variety of marine organisms spanning microbiomes

(Hamdan et al., 2021) to sessile invertebrates (Gravina et al., 2021), or migratory sharks that use the same shipwrecks possibly in relation to their reproductive cycles (Paxton et al., 2019; Ross et al., 2016). Its location in ABNJ, protection under UNESCO and multilateral agreements, cultural significance, and natural heritage make the wreck site of the RMS *Titanic* a unique case study to launch an investigation into the role this structure plays in marine connectivity, and for *C. agassizii* populations more specifically.

High-resolution hydrodynamic modeling is employed to investigate population connectivity of cold-water corals, and these frameworks help to identify key sources, sinks, and corridors of coral larvae (reproductively produced propagules; Guy and Metaxas, 2022; Metaxas et al., 2019). For corals on the shelf and slope off Newfoundland and Labrador, these modelling approaches show that the strong Labrador Current underpins much of the potential connectivity from north to south along the shelf edge and make larval transport into the High Seas possible (Le Corre et al., 2018). Notably however, these approaches have also shown that the southern flanks of the Flemish Cap seem to experience faster currents at depth (1,000 m) than near the surface (100 m) due to the influence of the Gulf Stream and North Atlantic Current (NAC); these systems meander to the northeast in a region characterised by strong surface and sub-surface eddy activity (Kenchington et al., 2019; Schubert et al., 2018). Therefore, coral larvae dispersal to and from the *Titanic*, and thus the role the wreck plays in marine connectivity further afield, is likely a product of a complex interplay between various hydrographic features and ocean dynamics from the surface to the seafloor.

Biophysical hydrodynamic models that incorporate larval behavioural traits (e.g., timing of spawning, larval duration, vertical and horizontal swimming behaviours) provide idealised representations of potential larval dispersal pathways and thus, patterns of connectivity. But for most deep-sea corals including those found on the *Titanic*, such life history information is entirely absent, and this seriously limits the utility of modelling frameworks (Gary et al., 2020). It is not known whether *Chrysogorgia agassizii* is a broadcast spawner, an internal or an external brooder. Nothing is known of its reproductive cycle, let alone how long larvae live, whether they swim, or how long the planula larval phase lasts. Therefore, biophysical modelling requires experiments across multiple scenarios of larval biology based on what is known about other deep-sea octocorals, at least to set boundary constraints on, e.g., pelagic larval duration, swimming speeds, etc. The genus *Chrysogorgia* is an abundant and diverse octocoral taxon with 81 nominal species and worldwide distribution in waters 31–4,327 m deep (Untiedt et al., 2021). It has been hypothesised that shallow water *Chrysogorgia* spp. evolved from deep-water ancestors (Pante et al., 2012), but C*hrysogorgia agassizii* itself appears to have a wide North Atlantic distribution in deep waters below 600 m and extending well into the abyss (Cairns, 2001; Molodtsova et al., 2008). Thus, its larvae seem capable of widespread dispersal. We should note that the identifications of these corals relies on visual identifications from video or still photos, and thus there can be doubts concerning resolution to species. In fact, Molodtsova et al. (2008) noted that the coral identified by Vinogradov (2000) from the *Titanic* bow, appeared to actually be *C. campanula*. However, since there is no life history information for most *Chrysogorgia*, including the two species above, the exercise undertaken in this paper remains relevant, especially as related to the genus *Chrysogorgia*.

Multiple scenarios that experiment with different larval behaviors can help to establish levels of uncertainty but also a consensus view on the dispersal potential of corals from *Titanic*'s and its wider natural heritage legacy in terms of marine connectivity. Viewing dispersal models more as possible outcomes rather than true or actualised dispersal (Ross et al., 2020) can also help identify possible upstream sources of larvae arriving at the *Titanic* and whether slope to abyssal larval dispersal could be significant. It can also investigate the likelihood of the wreck site now acting as a stepping stone connecting to downstream populations. In doing so, these experiments can also inform future studies on the reproductive biology of *C. agassizii* by identifying which larval behaviour traits, if any, impart variability in connectivity patterns.

For more realistic representations of dispersal, biophysical models need to include the full spatio-temporal range of the underlying ocean circulation. Of particular importance is the mesoscale circulation at scales of 10–100 km that covers oceanic fronts, eddies and detailed boundary current structures. In addition to their importance for mixing water across fronts, eddies are also an important part of the large-scale circulation and are present in vast areas of the world oceans (Chelton et al., 2011, 2007). In the North Atlantic, individual eddies transport water over large distances, contributing to the transport of heat and freshwater (Müller et al., 2019). Experiments on the upper-ocean dispersal have shown that advective patterns and transfer time scales can be quite sensitive to the grid resolution of the physical ocean model (Blanke et al., 2012; Bonhommeau et al., 2009).

For the deeper ocean, grid resolution is important to correctly include topographic features like slopes, trenches, gaps or ridges. Seafloor bathymetry has a direct impact on the dispersal of benthic organisms by steering, or blocking, the flow and needs to be adequately represented (Breusing et al., 2016). As the underlying physical model, we use the high-resolution model VIKING20X that covers the Atlantic at 1/20° horizontal grid resolution. VIKING20X has been proven to realistically simulate various features of the Atlantic circulation from basin-scales down to the mesoscale (Biastoch et al., 2021; Rieck et al., 2019; Rühs et al., 2021) and is also often the basis for dispersal studies (e.g. Busch et al., 2021). Its predecessor VIKING20, restricted to the North Atlantic, has demonstrated its performance to simulate the deep circulation (Breusing et al., 2016; Schubert et al., 2018).

The rapid deterioration of the *Titanic* (Bright et al., 2005) and vulnerability of natural deep-sea coral populations to climate change (Morato et al., 2020) and human activities that fragment or degrade coral habitats (Ragnarsson et al., 2017) make it important we understand whether the *Titanic* and other shipwrecks could confer resilience to networks of marine populations. Given the importance of understanding population connectivity as part of Atlantic basin scale ecosystem assessment (Roberts et al., 2022) and the increasing amount of anthropogenic material in the deep ocean, including underwater cultural heritage such as shipwrecks (Meyer-Kaiser and Mires, 2022), experiments with virtual larvae released from shipwrecks will help us understand the dispersal potential of species from the *Titanic* and the natural heritage legacy this and other wrecks could play in terms of marine connectivity.

2. Methods

2.1 Model Configuration: VIKING20X

This study is based on a hindcast simulation of the global, nested VIKING20X ocean - sea-ice model configuration (Biastoch et al., 2021). The ocean component is provided by the NEMO v3.6 model and the sea-ice component by the Louvain la Neuve Ice Model (LIM2; Fichefet and Maqueda, 1997; Vancoppenolle et al., 2009). VIKING20X consists of a 1/20° nest grid, embedded within a global 1/4° grid. At the *Titanic* position this corresponds to a horizontal grid spacing of approximately 4 km.

The nest covers the Atlantic Ocean from the southern tip of Africa to approximately 65°N. Both grids exchange information via a 2-way coupling utilising the Adaptive Grid Refinement In Fortran (AGRIF) package (Debreu et al., 2008). The vertical grid consists of 46 z-levels with increasing spacing from 6 m at the surface to about 250 m at the deepest level (about 240 m at the *Titanic* depth). Partial steps are used for a better representation of bathymetric gradients (Barnier et al., 2006).

The momentum advection equation is discretised using the energy and enstrophy conserving (EEN; Arakawa and Hsu, 1990; Ducousso et al., 2017) scheme. Momentum diffusion is accomplished by application of a bi-Laplacian operator acting along geopotential surfaces with a viscosity of 15×10^{10} m^4s^{-1} (nest grid: 6×10^9 m^4s^{-1}). The tracer advection equation is discretised using the total variance dissipation scheme (TVD; Zalesak, 1979). Tracer diffusion is accomplished by a Laplacian operator along iso-neutral surfaces with an eddy diffusivity of 300 m^2s^{-1} (nest grid: 600 m^2s^{-1}).

On both grids free-slip lateral momentum boundary conditions are applied. Only on the nest grid, no-slip boundary conditions are applied around Cape Desolation to improve mesoscale activity to the west of Greenland (Rieck et al., 2019).

The model experiment used for this study is referred to as VIKING20X-JRA-SHORT (see Biastoch et al., 2021). This experiment is initialised in 1980 branching of from an experiment performed under the CORE2 (Griffies et al., 2009; Large and Yeager, 2009) surface forcing initialised in 1958 following a 30-year spin-up. VIKING20X-JRA-SHORT is then run until 2019 under the JRA55-do v1.4 (Tsujino et al., 2018) surface forcing. It uses a weak Sea Surface Salinity restoring with a timescale of 12.2 m yr^{-1} and no freshwater budget correction.

2.2 Lagrangian Experiments

To study the fate and potential source of *C. agassizii* larvae at the *Titanic*, we run a set of Lagrangian experiments, using the Parcels (version 2.2.1) Python package (Delandmeter and van Sebille, 2019).

Parcels solves the advection equation numerically. Here the fourth-order Runge-Kutta scheme, including vertical velocities, is applied with a numerical timestep of 10 minutes. No diffusion parameterisation scheme is used in the calculation of trajectories, a choice that is thoroughly discussed by Rühs et al. (2018). As input fields, the 5-day averaged output of VIKING20X on the nest grid is used. Within parcels these fields are linearly interpolated to the current time step.

We release 10,000 particles on the first day of each month from 2009 to 2018, resulting in 120 release experiments (1.2 million particles in total). The aim of this release strategy is to capture the impact of flow variability on timescales from months to years. It was verified that the number of released particles is sufficient by evaluating different sub-samples with reduced size. Metrics, such as the area that contains 95% of the particle occurrences, converge rapidly after 1,000-2,000 particles. All trajectories within the release experiment are integrated forward in time for 90 days.

The larval characteristics of *C. agassizii*, including larval longevity, are currently not known. Most octocoral larvae studied so far, including shallow tropical (Ben-David-Zaslow and Benayahu, 1998; Coelho and Lasker, 2016), temperate (Guizien et al., 2020), and deep-sea species (Rakka et al., 2021b; Sun et al., 2010) can survive without settling for 20-90 days and up to a year (Rakka, 2021a). Based on this information, we chose 90 days as our best estimate of larval longevity for *C. agassizii*. Although the chosen 90 days are considered realistic, deep-sea coral larvae can survive longer (e.g. Larsson et al., 2014), thus our results present a conservative estimate of the possible spreading.

All Lagrangian experiments analysed here are described below and summarised in table 1.

2.2.1 Releases from the Titanic

We seed particles horizontally around the *Titanic*'s position (coordinates of the bow section) according a random normal distribution with a standard deviation of 0.025° in latitude and $0.025/\cos(\phi)$° in longitude direction, where ϕ is the centre latitude of the release. This corresponds to a distance of 2.8 km in both cases. Experiments were focused on the bow section of the wreck site where most putative *C. agassizii* had been previously observed. Particles are initially placed 10 m above the actual depth at the *Titanic* site (at 3,810 m) to simulate this position on the bow. If the seafloor in the model is shallower than this depth, we release particles 10 m above the grid-cell floor.

In a first experiment, referred to as EXP_{pas}, particles are advected purely passive in the ocean currents as simulated by the model (20 exemplary trajectories are shown in figure 2). We use the full 4-dimensional output of the model, including depth, which was found to be important for the dispersal in a nearby area (Wang et al., 2020). In a second experiment, referred to as EXP_{act}, particles can actively swim in the vertical direction, a behaviour that has been reported for several deep-sea benthic species (Arellano, 2008; Beaulieu et al., 2015; Yahagi et al., 2017) including deep-sea corals (Larsson et al., 2014). Since there is currently no information on the larval traits of *C. agassizii*, in this experiment we use values for swimming speed and larval duration reported for larvae of *Viminella flagellum*, which is the only deep-sea octocoral with vertical swimming behaviour of its larvae known so far (Rakka, 2021a). The selected swimming speed is close to the highest speeds that have been reported for other octocoral species (e.g., Martínez-Quintana et al., 2015; Rakka et al., 2021b), serving the purpose of this experiment to provide an upper limit for the potential impact of active behaviour of the larvae on the dispersal. Based on very little information available, we assume a pelagic larval duration (PLD) of 6 days. Possible implications of a longer PLD are discussed later. Accordingly, larvae in EXP_{act} swim upward with a constant velocity of 1.5 mm/s for 6 days and then downward with the same constant velocity until they get closer than 10 m to the seafloor. After swimming terminates, particles passively drift until the end of the experiment.

2.2.2 Releases from natural occurring populations to the Titanic

In addition, we run three experiments to study population connectivity between the abyssal setting of the *Titanic* and sites in the Northwest Atlantic. Records of *C. agassizii* were obtained from a subset of data compiled from multiple sources (Ramiro-Sánchez et al., 2020). The general release strategy described in section 2.2.1 did not change, but only 12 release months are used (January - December 2009). This is sufficient, as the two previous experiments suggest interannual variability to be negligible compared to monthly variability.

A first experiment ($EXP_{P1\text{-}P2}$) is run to study the timescale of spreading from a known population of *C. agassizii* east of the Grand Banks (labeled as P1 in figure 2), to a population on the Nova Scotian Slope (labeled as P2 in figure 2). The purpose of this experiment is to answer questions on dispersal pathways along the upper continental slope and to identify possible locations, where larval particles could leave the boundary towards the *Titanic* position. Particles are passively advected without any active behaviour for 180 days. Especially because we are mainly interested in the advective timescale set by the ocean currents and there is little information about the larval biology, a passive experiment is the most appropriate choice and does not require any assumptions.

Motivated by the results of this experiment, a second experiment ($EXP_{P1\text{-}T}$) is conducted to study whether larvae from this known occurrence (P1) on the upper slope could reach the deeper lying *Titanic* wreck. Therefore, we set up an experiment where particles spread purely passive for 30 days and then sink with a constant velocity of 1.5 mm/s until they get closer than 100 m to the seafloor. Afterward, larvae can passively drift until an age of 90 days. We use the same speed as for EXP_{act}, as a fast downward motion increases the likelihood of connectivity, but at the same time the downward velocity should be achievable by the larvae. The onset of downward motion after 30 days is based on various short experiments showing that an onset of downward motion after 30 days makes a connection to the *Titanic* most likely. This experiment is therefore meant to provide information on the larval behaviour that is needed for a direct connectivity to exist, rather than an estimate of the true dispersal.

In a third experiment ($EXP_{T\text{-}P2}$) we assess, whether our results on connectivity from the *Titanic* to the downstream population (P2) of *C. agassizii* are changed by doubling the assumed larval longevity. Therefore, we repeat EXP_{PAS}, but with a runtime extended to 180 days.

Experiment	Release (position)	Release (time)	Runtime in days	Active motion	Motivation
EXP_{pas}	*Titanic*	monthly (2009 – 2018)	90	-	Dispersal from the *Titanic*
EXP_{act}	*Titanic*	monthly (2009 – 2018)	90	6 days upward swimming then sinking (1.5 mm/s)	Impact of swimming on dispersal from the *Titanic*
$EXP_{P1\text{-}P2}$	P1	monthly (2009)	180	-	Timescale of spreading along the upper slope (P1 to P2)
EXP_{P1_T}	P1	monthly (2009)	90	30 days passive then sinking (1.5 mm/s)	Larval characteristics needed for direct connectivity between P1 and the *Titanic*
EXP_{T_P2}	*Titanic*	monthly (2009)	180	-	Assess sensitivity of dispersal from the *Titanic* on larval longevity

Table 1: Overview of experiments. The Titanic is located at 41.73°N 49.95°W (3820 m), P1 is located at 46.07°N 47.61°W (400 m).

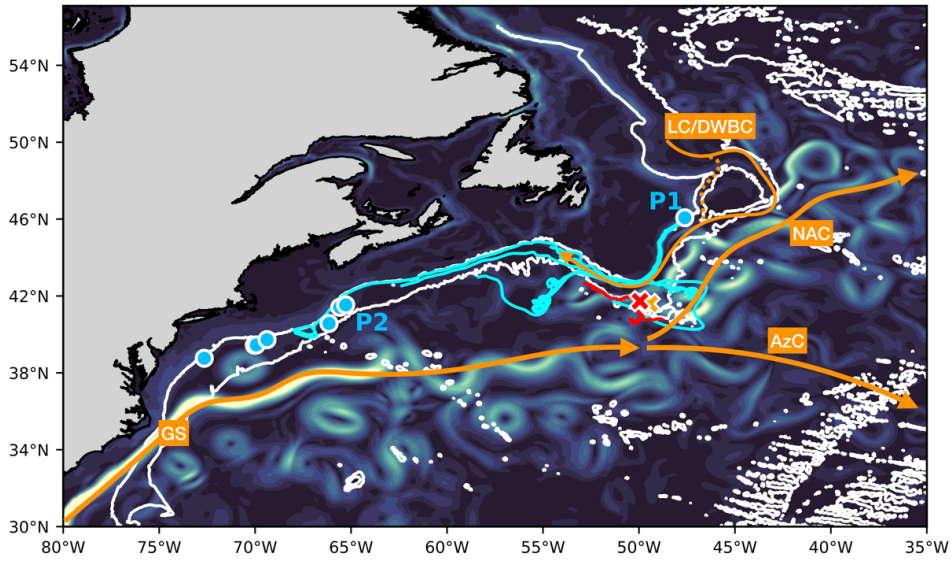

Figure 2: Surface velocity snapshot in VIKING20X (model day 15-10-2009). The red cross marks the *Titanic* position and blue dots indicate known positions of *C. agassizii*. The orange cross marks the Nargeolet-Fanning Ridge. The 1,000 and 3,500 m isobaths are shown in white. Exemplary trajectories from EXP_{pas} (red; length: 30 days) and $EXP_{P1\text{-}P2}$ (blue; length: 180 days). Major currents are indicated by arrows (GS: Gulf Stream, NAC: North Atlantic Current, AzC: Azores Current, LC: Labrador Current, DWBC: Deep Western Boundary Current).

3. Results

3.1 Oceanographic setting and model validation

Before we analyse and interpret the results of the Lagrangian experiments, we describe the general circulation in the region of interest and verify that it is reasonably represented in VIKING20X by comparing it to observational data. The *Titanic* wreck site is located in waters approximately 3,800 m deep, but direct (especially long term) measurements at this site are very sparse, or not available, at these depths. Therefore, we focus on the representation of major currents and mesoscale variability at the surface and mid-depth, that will be shown to strongly impact our results.

3.1.1 Gulf Stream and North Atlantic Current

The near surface circulation along the United States' east coast is dominated by the northward flowing Gulf Stream (GS) that separates from the coast near Cape Hatteras (35°N) and continues north-eastward. At the Tail of the Grand Banks the GS splits into the north-eastward North Atlantic Current (NAC) and an eastward branch called Azores Current (Daniault et al., 2016; Frazão et al., 2022). This general description also holds for the model as evident in Figure 2.

The mid-depth circulation, as derived from ARGO floats at a depth of approximately 1000 m (ANDRO dataset; Ollitrault et al., 2022), shows the GS centred around 39°N (Figure 3a). The modelled and observed mean velocity maxima are similar in magnitude at most longitudes, but cover a smaller latitude range and appear about 1.5° further south in the model (figure 3b). The reason, however, is not a shift of the whole current system. The position of the 15°C isotherm at 200 m depth, indicative

of the GS path, does match observations very well (Figure 3b; Seidov et al., 2019). The GS/NAC flow is characterised by strong meanders and mesoscale eddies known as Gulf Stream Rings (Ducet and Le Traon, 2001; Schubert et al., 2018). Eddies north of the main GS axis are predominantly anti-cyclonic, carry a positive temperature anomaly and are also known as Warm Core Rings (Brown et al., 1986; Saunders, 1971). The highest mean velocities being found too far south results from a too regular path of anti-cyclonic Warm Core Rings. Velocities are westward along the southern side of these eddies, which reduces the eastward velocities associated with the GS in the VIKING20X multi-year mean velocity field.

As a consequence, meanders of the NAC and Gulf Stream Rings do affect the circulation above the *Titanic*'s position in the model, although the current appears to be shifted south in the modelled mean velocity field. In agreement with observational Sea Surface Height (SSH) anomaly fields derived from satellite altimetry (AVSIO; Taburet and Pujol, 2022), the GS and NAC in the model are associated with strong eddy activity (Figure 3c,d). In both snapshots eddies are seen above the wreck site. However, eddies are in general associated with a stronger SSH anomaly in AVISO, especially west of the *Titanic* location. In addition to Gulf Stream Rings that are clearly visible at the surface, meanders of the GS/NAC can drive deep cyclogenesis, and these deep mesoscale features can cause benthic storms , i.e., strong velocity anomalies near the bottom, as evidenced by both ocean-based observations and the VIKING20X model (Schubert et al., 2018; Shay et al., 1995). Eddy Kinetic Energy (EKE), the kinetic energy contained in deviations from the time mean circulation (and in parts associated with mesoscale variability), at mid-depth is underestimated at the *Titanic* location compared to values from the ARGO-based ANDRO dataset (Figure 3a, b). Still, surface and mid-depth eddies associated with the GS/NAC current system are present in the model above the wreck site and EKE values at mid-depth are clearly higher than in the ocean interior (Figure 3a,b).

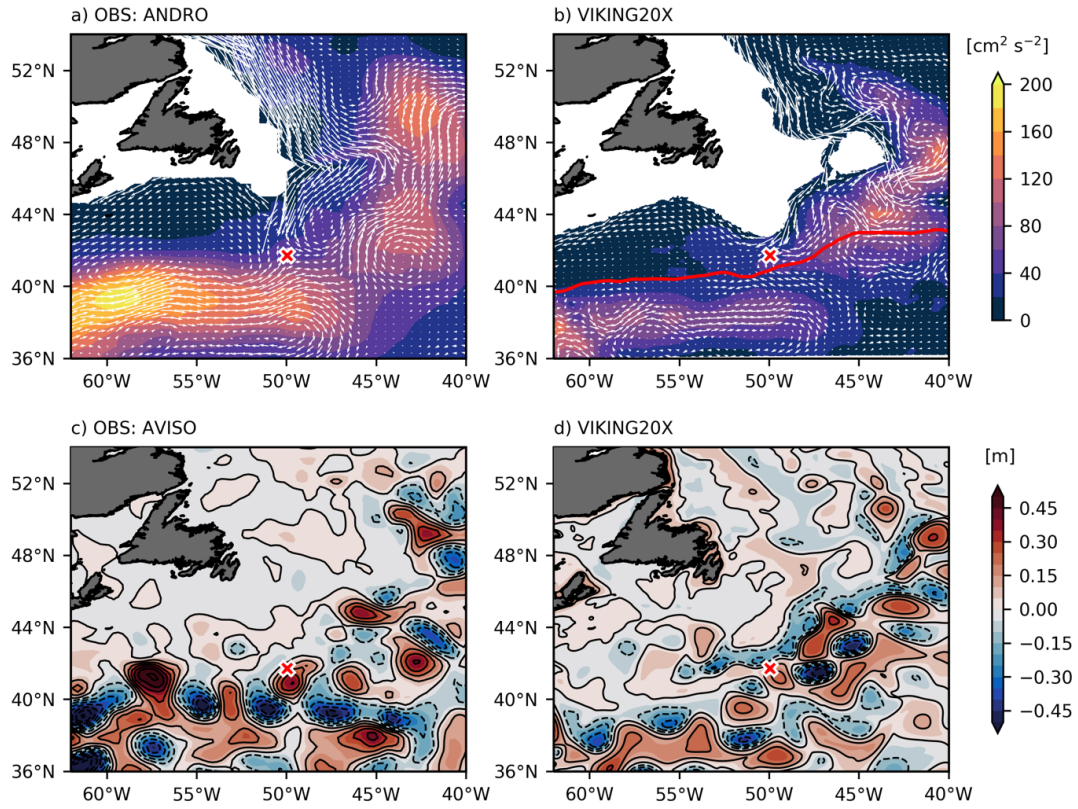

Figure 3: Eddy Kinetic Energy and mean currents at approximately 1,000 m depth based on the ARGO derived ANDRO dataset (a) and VIKING20X (b; 2009-2018). Snapshot (5-day mean) of spatially high-pass filtered SSH anomaly in AVISO (c, 05-08-2010) and VIKING20X (d,15-10-2009). The *Titanic* is marked with a red cross. The red contour in b) shows the mean position of the 15°C isotherm at 200 m depth (2009-2018) in VIKING20X.

3.1.2 Labrador Current and Deep Western Boundary Current

From the Labrador Sea, the Labrador Current transports water southward along the slope in the top 600 m (σ_0 < 27.68 kg m^{-3}). The Deep Western Boundary Current (DWBC) is responsible for a southward transport of more dense water (σ_0 > 27.68 kg m^{-3}) below the LC (New et al., 2021; Figure 2).

Since it is especially important for our study of connectivity, Figure 4a shows a velocity section on the eastern side of the Grand Banks, resembling the Grand Banks Mooring Array. The mooring array is described in Schott et al. (2004), and its position is shown in Figure 4b. The flow along the continental slope is southward with velocities between 5 and 15 cm/s in the top 1,500 m. A second deep core at densities larger than 27.88 kg m^{-3} is also visible in the model, but separated from the boundary by a small region of northward flow. In general, the southward flow is more confined to the boundary, but the mean velocity is in a reasonable range along the continental slope compared to the mooring observations (Schott et al., 2004).

The LC and DWBC turn west around the Tail of the Grand Banks, continuously following the continental slope (Schott et al., 2004; Figure 2). The main core of the DWBC at mid-depth (1,000 m) is located to the north of the *Titanic* (Figure 3a,b).

In addition to the aforementioned eddies associated with the GS/NAC current system, eddies above the *Titanic* wreck can also emerge from the LC/DWBC north of the wreck site. Eddies of subpolar origin, known as submesoscale coherent vortices, were shown to form south of the Grand Banks. They have a subsurface maximum and propagate west- or southward (Bower et al., 2013). Although VIKING20X does not resolve submesoscale dynamics, eddies with similar characteristics are present in the model (not shown). The modelled size of eddies is larger than estimated by Bower et al. (2013) and closer to the estimated size of eddies resulting from baroclinic instability of the Labrador Current (LC) close to Flemish Cap (Pickart et al., 1997). This suggests that the eddies found south of the Grand Banks in VIKING20X are generated by a similar formation process.

3.1.3 Mean flow at the Titanic depth

The *Titanic* itself, at a depth of 3,800 m, is shielded from a westward flow by the Newfoundland Ridge extending south from the Tail of the Grand Bank. North of approximately 42°N a coherent mean flow along the bathymetry is no longer present at a depth of 3,650 m (Figure 4b). This is probably a result of strong variability caused by the interaction between the DWBC and NAC (Schott et al., 2004). In addition, the interior flow at these latitudes is characterised by strong spatial variability consistent with a known high eddy activity (e.g., Bower et al., 2011). Further south, water flows around the Newfoundland Ridge and then diverts into a pathway that continuous westward and a secondary pathway that turns to the northwest towards the *Titanic*. The latter forms a weak current following the bathymetry (Figure 4b).

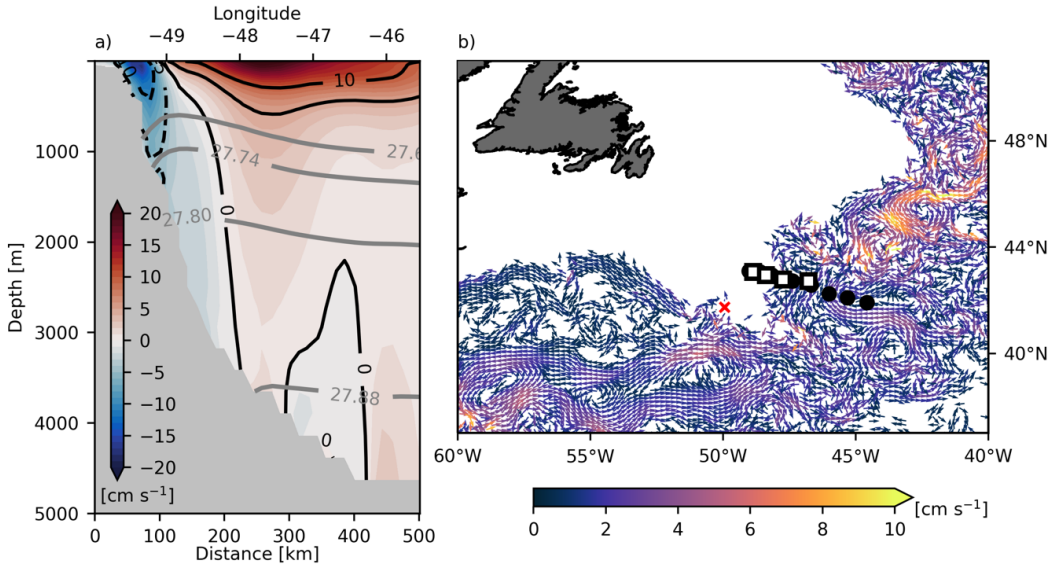

Figure 4: Mean velocity section (2009-2018) resembling the Grand Banks Mooring Array (a). σ_0 isopycnals are indicated by grey lines. The position of the mooring array is indicated by black dots and squares in panel (b) along with the mean velocity (2009-2018) at 3,650 m depth. The *Titanic* is marked with a red cross.

In summary, the model underestimates the energy contained in mesoscale variability near the surface and in mid-depth above the *Titanic*, compared to observational data. However, general features of the circulation (variability) that are deemed to be important for this study are reasonably well-represented. Although their energy is lower than in the observational estimate, mesoscale eddies of different origin are clearly present above the *Titanic,* and a coherent mean flow along continental slope with a mean velocity exceeding 5 cm/s above 1,500 m depth exists.

3.2 Larval dispersal from the RMS Titanic

When released in close proximity to the *Titanic*, passive Lagrangian particles follow two main pathways within the first 90 days after their release (Figure 5a). One pathway follows the 3,500 m isobath to the west. This pathway is diverted into a northern and a southern branch by a shallow (water depth 2,500 m) seamount. The second pathway is directed south and bounded approximately by the 3,500 and 4,000 m isobaths.

The probability distributions for each season (based on the month of release) individually reveal that the pathways itself do not change with seasons (Figure 5c-f). Thus, westward or southward spreading is not determined by seasonal variations of the deep circulation. The 95% contour extends similarly far west and south from the *Titanic* position in all seasons.

A comparison of figure 5a and b shows that including an active vertical movement does not lead to strong differences in the dispersal of larvae. The qualitative description of the pathways above is still valid for EXP_{act}. The 95% contour line extends further west, indicating that the distance larvae can reach from the *Titanic* slightly increases. In our experiments, larval particles can swim upward with 1.5 mm/s for 6 days (777 m in total) and thus reach a depth of about 3,000 m. As will be shown later, the circulation features that govern the dispersal do not have a strong velocity shear in this depth range. Therefore, the dispersal remains quite similar in the two experiments, and the swimming velocity that was defined in this experiment does not greatly impact the spreading in relation to the variability of ocean currents.

At the same time, the minor change in distance reached from the Titanic in EXP_{act} does allow for a considerable number of larval particles (indicated by the 95% contour) to reach the Canadian Exclusive Economic Zone (EEZ; EEZ boundaries were obtained from the Flanders Marine Institute (2019) Maritime Boundaries Geodatabase). In the passive dispersal scenario (EXP_{pas}), few particles can reach the EEZ, even under particularly strong circulation conditions (Figure 5a).

A direct dispersal from the *Titanic* to the aforementioned populations of *C. agassizii* (P1 and P2; figure 2) does not seem to be possible without additional stepping stones. There is no pathway to the north and larvae transported westward along the continental slope does not reach further than 55°W in any of the experiments. However, we do recognize that there are likely to be as yet undocumented habitats in the region that could be the stepping stones, which is further discussed in section 4.

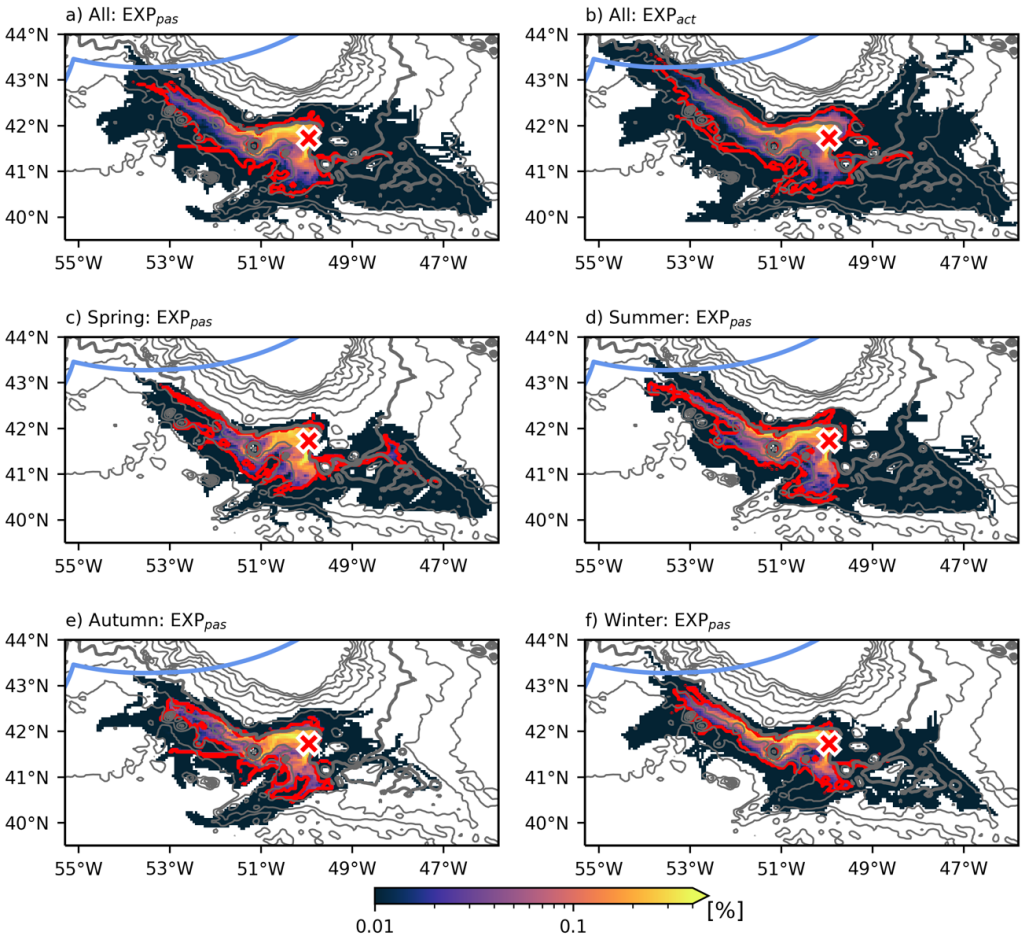

Figure 5: Probability of particles to be found within 0.05° x 0.05° bins within 90 days after release. Particles are only counted once per bin. a) All particles released in EXP$_{pas}$ and b) all particles released in EXP$_{act}$. c,d,e,f) particles released in EXP$_{pas}$ in the different seasons. The blue line in the top left corner indicates the Canadian Exclusive Economic Zone and grey contours the water depth (500 m interval, 3,500 m contour is drawn bold). The *Titanic* is marked with a red cross.

3.3 Circulation conditions controlling the spreading

As shown in the last section, there are two main pathways of particles released at the *Titanic.* We now study whether the relative importance of both pathways changes over time and what physical mechanisms causes particles to spread either to the west, or to the south. Therefore, we combine our Lagrangian experiments with a Eulerian analysis of the velocity field.

3.3.1 Velocity composites

We group all months by the dominant spreading direction in EXP$_{pas}$ and calculate the composite velocity field of the respective months. For each release, we calculate the centre of mass of all particles after 30 days. We chose to consider the position after 30 days, as we are interested in the

processes that determine the initial dispersal from the wreck after release. These positions are shown in Figure 6a. Subsequently, these positions are compared to the *Titanic* position. We group the release months according to the following equations:

WEST: $\mathrm{lon_p}(t_{rel}) < (\mathrm{lon_T} - x_{thr})$

SOUTH: $\mathrm{lat_p}(t_{rel}) < (\mathrm{lat_T} - y_{thr})$

$\mathrm{lon_p}(t_{rel})$ and $\mathrm{lat_p}(t_{rel})$ denote the coordinates of the centre of mass of all particles released at time t_{rel} 30 days after the release. $\mathrm{lon_T}$ and $\mathrm{lat_T}$ are the *Titanic* wreck's (bow section) coordinates. x_{thr} and y_{thr} are 80% percentiles of $\mathrm{lon_p}$ and $\mathrm{lat_p}$ for all release months. As a result, the WEST group contains all release months, where particles spread anomalously far towards the west (24 release months; marked blue in Figure 6a). The SOUTH group contains all months where particles spread anomalously far south (21 release months; marked purple in Figure 6a).

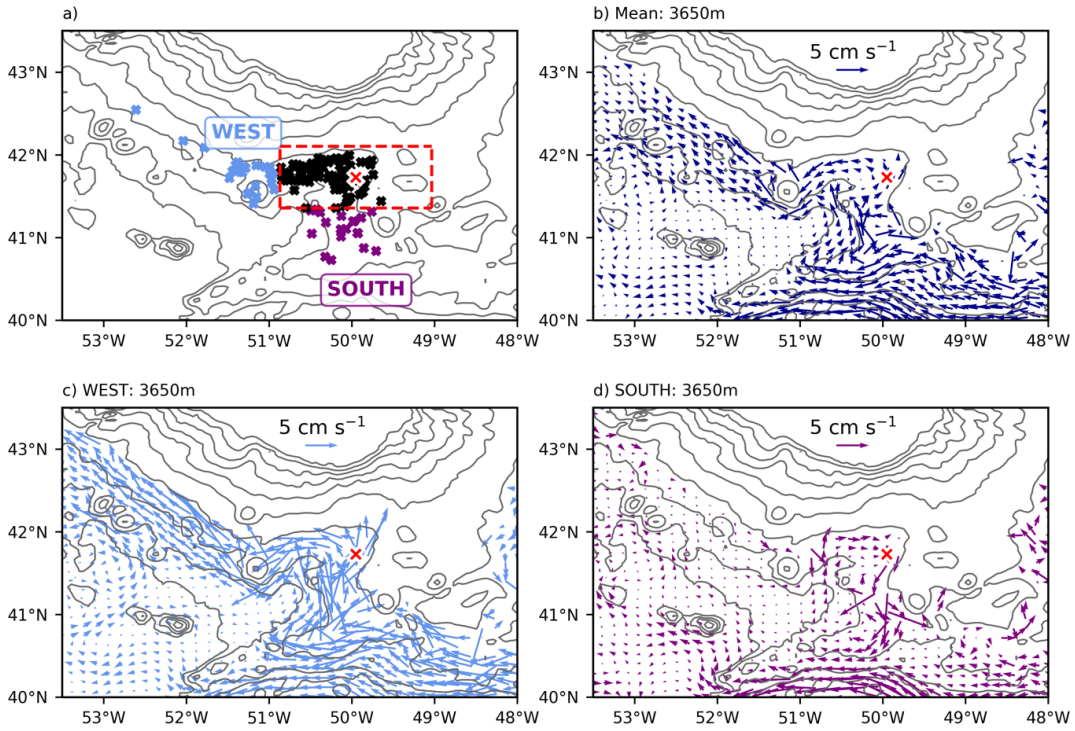

Figure 6: a) Centre of mass of all particles released in a particular month in EXP_{pas}, classified based on anomalously strong westward (WEST; blue), or southward (SOUTH; purple) spreading. The red cross marks the *Titanic* position and the boundaries used for classification are indicated with dashed red lines. b) Mean (2009-2018) velocity at 3,650 m depth. Composite velocity for subsets WEST (c) and SOUTH (d) at 3,650 m depth. In all subpanels grey contours show the water depth with an interval of 500 m.

Figure 6b shows the mean circulation around the *Titanic*. The wreck is located in an embayment about 80 km in diameter, bounded by the Grand Banks and the Newfoundland Ridge, shielding it from a large-scale eastward flow. Instead, it is characterised by a slow (< 3.5 cm/s) cyclonic circulation along the bathymetry. The mean velocity is directed northward directly at the *Titanic* and turns westward further north. The flow then continuously follows the bathymetry to the west.

During months of anomalous westward spreading the cyclonic circulation within the embayment is strongly enhanced (Figure 6c). The composite velocity can exceed 10 cm/s. In contrast, the circulation reverses to anticyclonic flow during phases of strong southward spreading along the 3,700 m isobath.

The composite of all months when spreading is neither anomalously west- nor southward, is nearly indistinguishable from the mean field (not shown). This is reasonable, since this group represents spreading under typical conditions. During normal conditions the particles tend to spread northwestward, but do not reach great distances from the *Titanic* (Figure 6a).

In the following, we investigate the mechanisms causing the cyclonic circulation at depth to speed up, or to reverse. Therefore, we analyse composites of months with strong westward and southward spreading at shallower depth levels.

The composite of all months with strong westward spreading shows the presences of an intense anticyclonic eddy located to the south-east of the *Titanic* at a depth of 1,000m (Figure 7a). The western side of the eddy with north-eastward velocities is located directly above the wreck.

Also, strong southward spreading is associated with an anticyclonic eddy at mid-depths (Figure 7b). However, the eddy is located to the southwest of the *Titanic* and therefore velocities above this position are directed south-eastward.

As described before, these eddies can be of different origin. Mooring observations (Richardson et al., 1979) suggest that Gulf Stream Rings possibly extend to the seafloor, affecting the dispersal of larvae released in abyssal ecosystems. However, based on the near-surface composites (Figure 7c,d), the circulation features affecting the dispersal must not have a clear surface signature. The near-surface circulation above the *Titanic* position is dominated by strong eastward velocities without a closed anticyclonic flow being visible in both cases. This suggests that in addition to Gulf Stream Rings, benthic storms driven by deep cyclogenesis and subsurface eddies of subpolar origin impact the spreading of larvae.

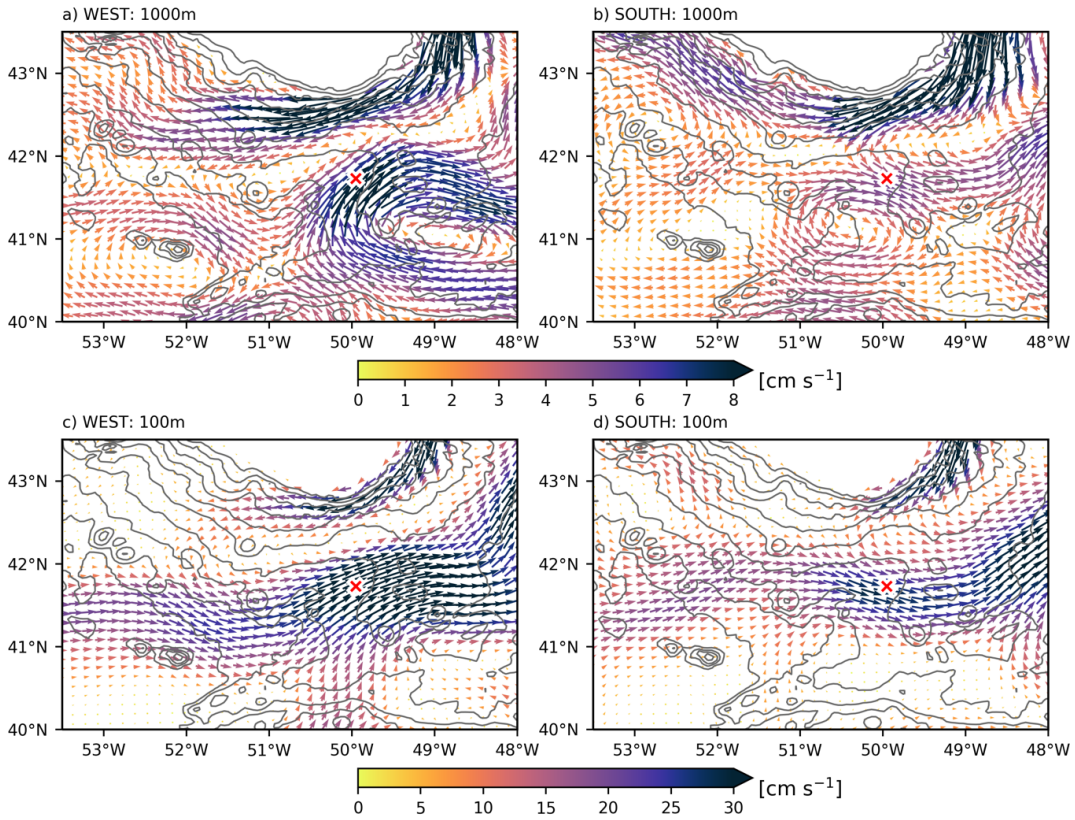

Figure 7: Composite mean velocity at 1,000 m depth based on all release month with strong westward (a) and southward (b) spreading. c), d) as a), b) but for 100 m depth. The *Titanic* is marked with a red cross. In all subpanels grey contours show the water depth with an interval of 500 m.

3.3.2 Characteristics of exemplary eddies

Composite means may not always represent true circulation, especially during extreme events. Therefore, we also provide the monthly mean velocity for the two release months with the strongest spreading in southward/westward direction. It is clearly visible in Figure 8a,b that both events are associated with a strong mesoscale eddy at mid-depths, and both eddies are anticyclonic. For westward spreading, the centre of the eddy is to the south-east of the *Titanic*, while it is to the south-west for southward spreading and therefore closely resembles the composite maps in Figure 7.

A section through both eddies shows that their depth structure differs in the upper water column. While for the eddy in October 2009 (Figure 8c) the strongest anomalies are found at the surface, the eddy in July 2011 is characterised by a subsurface maximum at 600 m depth (Figure 8d). Accordingly, only the first eddy shows a pronounced surface signature. The second eddy is associated with a very weak anticyclonic circulation close to the surface only and no clear SSH anomaly (not shown). This

suggests, in agreement with the composites, that not all eddies occurring south of the Grand Banks are Gulf Stream Rings with a detectable signature at the surface. This makes it difficult to verify the presence of such eddies, since they are not visible in e.g., satellite altimetry data.

Despite these differences, both eddies are associated with deep velocity anomalies extending to the seafloor. Therefore, eddies can alter the deep flow (below the main eddy core) and affect the spreading of larvae from the *Titanic*. The first eddy does increase the northward flow into the embayment. At the longitude of the *Titanic* (dashed grey line in Figure 8c) the velocity anomaly is positive and thus associated with stronger than average northward flow along the eastern side of the embayment. This anomalously strong northward flow into the embayment must turn westward as it approaches the northern boundary of the embayment at 3650 m depth. Therefore, the westward flow exiting the embayment is enhanced and particles from the *Titanic* can spread further to the west than under normal conditions. The second eddy is associated with an eastward velocity anomaly below 3,000 m. At the latitude of the *Titanic* (dashed grey line in Figure 8d) the eddy pushes water eastward into the embayment. An eastward flow along the northern boundary of the embayment must turn southward as it approaches the shallow bathymetry in the east. This southward flow is then responsible for carrying larvae away from the *Titanic* towards the south.

The rather small vertical gradients in the velocity anomaly below 2,500 m can also explain why active vertical movement does not strongly affect the spreading. Active swimming to shallower depths (in a realistic range) does not cause the particles to enter a different flow regime and thus does not greatly alter their pathways. In EXP_{act} particles reach a depth of about 3,000 m. This is still well below the eddy core of both exemplary eddies. Note that also the mean flow does not show significant vertical gradients in the depth range covered by the larvae.

The circulation in individual months with anomalously strong spreading not always exactly resembles the corresponding composite mean, or the two exemplary snapshots shown here. Still, in most cases the presence of mesoscale structures is visible in the vicinity of the *Titanic*, causing the flow to have a strong northward (for westward spreading), or south-eastward (for southward spreading) component at mid-depth.

Mesoscale features therefore play a major role, determining the direction and strength of the modelled spreading of larvae. However, particles are not entrained into and carried by the eddy itself. Instead, the abyssal circulation, strongly guided by the bathymetry, responds to the overlying eddy and causes the flow to be stronger than average in a westward direction, or to reverse. We find that all types of mesoscale features, deep cyclones generated below GS/NAC meanders, Gulf Stream Rings, and eddies of subpolar origin, may impact larval spreading. However, the subpolar origin eddies dominate in the model. Since these eddies were shown to be mostly anticyclonic (Bower et al., 2013; Pickart et al., 1997), this could explain the apparent dominance of anticyclonic eddies on larval trajectories. Additionally, Gulf Stream Rings north of the GS axis (Warm Core Rings) are anti-cyclonic (e.g., Brown et al., 1986).

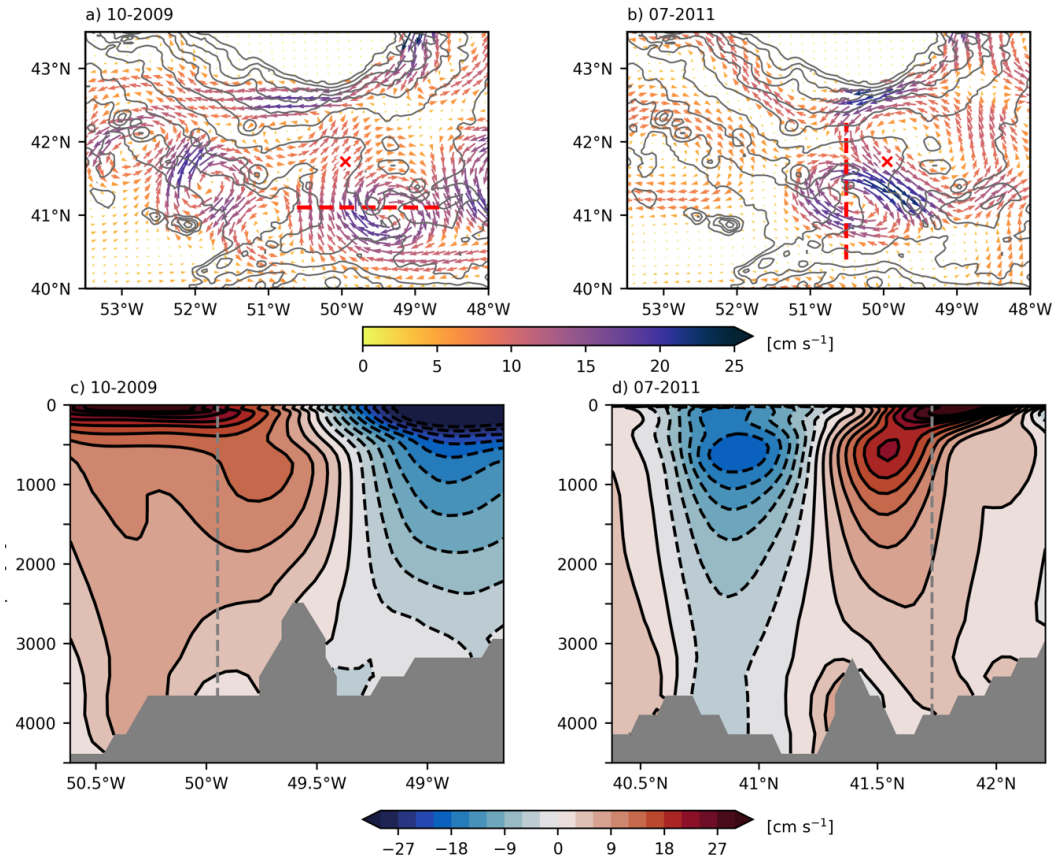

Figure 8: Monthly mean velocity at 1,000 m depth in the months of strongest westward spreading (10-2009; a) and strongest southward spreading (07-2011; b). The *Titanic* is marked with a red cross. Grey contours show the water depth with an interval of 500 m. c) Meridional velocity anomaly (10-2009) along the section shown in a). d) Zonal velocity anomaly (07-2011) along the section shown in b). The vertical grey lines indicate the latitude/longitude of the *Titanic*.

3.4 Ecosystem connectivity along the Northwest Atlantic continental slope

After studying the fate of larvae spawned at the *Titanic* wreck the question arises, whether the *Titanic* is connected to other known populations of *C. agassizii*. Known occurrences of *C. agassizii* at the present time are marked in Figure 9 (extracted from a subset of data compiled by Ramiro-Sánchez et al., 2020). As already mentioned, larvae cannot reach these locations directly assuming a maximum larval longevity of 90 days. Nevertheless, the more northerly occurrences could be sources for the *Titanic* population and downstream ecosystems off Nova Scotia may be reached with a reasonable number of stepping stones. Possibly the *Titanic* could be a stepping stone itself connecting these populations to the slopes and seamounts of the Northwest Atlantic and into the Canadian EEZ.

3.4.1 Connectivity between naturally occurring populations

To study whether such a connectivity is possible, we release particles at the position labelled as 'P1' (EXP_{P1-P2}) in Figure 9. Population 1 is located north of the *Titanic*, at a depth of approximately 400 m. This location is directly influenced by the strong mean flow of the LC and DWBC along the continental slope.

Most particles released continuously follow the bathymetry to the south. The distance reached from P1 is highly sensitive to the assumed larval longevity. Population 2 ('P2') is located downstream the DWBC. The fastest virtual particles do reach P2 within 120 days (Figure 9a). Thus, only one additional population along the pathway would be required, if a maximum larval longevity of 90 days is assumed. In close proximity to P2 and in the downstream DWBC direction there are several more known populations. A connection to P2 would therefore also connect P1 to all of these populations.

3.4.2 Connectivity between natural occurring populations and the Titanic

Not all larval particles remain in the LC/DWBC and eventually reach P2. As they encounter the Tail of the Grand Bank, a number of particles are diverted to the south towards the *Titanic*.

Although larvae can spread and reach the *Titanic* in a relatively short time (within 30 days), there is a large vertical gap between the particles at mid-depth and the *Titanic* at 3,800 m depth. Thus, for a connection between the populations to be realised, the larvae must sink due to negative buoyancy, or active downward swimming along the way.

To assess whether this could be possible, we conduct different experiments releasing virtual particles at P1. In these experiment particles can sink at 1.5 mm/s, if they are more than 100 m above the sea floor. Different scenarios were tested in which particles start to sink after a different duration of passive drift. In all scenarios that force particles to stay close to the seafloor very early, they are not advected in the fast LC or main DWBC core, but move with the much slower water at depth and need far longer than 90 days to reach the Tail of the Grand Bank (not shown).

In an experiment with passive drift for 30 days and sinking afterwards (EXP_{P1-T}), particles can reach the *Titanic*'s horizontal and vertical vicinity within 50 days. In two of the 12 release months, particles follow the LC/DWBC along the boundary and leave it in an eddying motion at the Tail of the Grand Bank. The velocity snapshot at the time particles leave the western boundary shows an anticylonic eddy at mid-depth centred at 50.6°W. Due to their added negative velocity, they spiral down the eddy and exactly reach the *Titanic* at approximately the correct depth (Figure 9c). This is a special case and the vast majority of particles continuously follow the LC/DWBC around the Tail of the Grand Bank, or are diverted into the interior ocean earlier.

Ontogenetic changes in larval buoyancy and behaviour are common in deep-sea species (Arellano, 2008; Larsson et al., 2014), but an onset of larval swimming after passive drift of 30 days is unlikely. However, one could also interpret this vertical profile, as larvae becoming negatively buoyant after a certain age and/or their negative buoyancy can be balanced by swimming up to a certain age. However, as mentioned before these experiments are not thought to be a realistic simulation of the true spreading, but help to answer the question, whether closing the vertical gap between the two populations is at least theoretically possible and what larval characteristics would be needed.

Since particles from the *Titanic* can spread westward, they eventually reach the vicinity of P2. However, velocities at depth are much lower and particles spread significantly slower. A release experiment from the *Titanic* with an extended run time ($EXP_{T\text{-}P2}$) shows that after 180 days, particles only reach about 57°W. Doubling the assumed larval longevity thus only allows larvae to reach 2° further west (compare Figure 5). This is caused by particularly slow mean velocities between 53°W and 60°W at depths below 3,000 m. Note that there are also no eddies present along the continental slope in this area, that could enhance the flow temporarily. After 300 days (not shown), larval particles can only reach 61°W. Even when larvae (with a large number of stepping stones) could reach 65°W, they arrive at a depth below 3,000 m and would need to swim more than 1,000 m upwards to reach P2. As a consequence, we conclude that an exchange between the *Titanic* and P2 is not impossible, but unlikely.

In summary, based on the known distribution of *C. agassizii*, from advection through ocean currents and realistic active swimming, there seems to be a main DWBC pathway that could connect P1 and P2 (with one stepping stone required). As larvae reach the Tail of the Grand Bank, they can be detrained from the LC/DWBC in eddies and reach the *Titanic*, possibly even without any additional stepping stones. The largest uncertainty, whether such a direct connectivity exists, is the vertical distance between the populations.

From the *Titanic*, the larvae spread westward in a 'deep DWBC' pathway and to the south towards the abyssal ocean. Therefore, the *Titanic* may be a stepping stone from P1 into the abyssal ocean, but likely not a stepping stone from P1 to P2, due to the slow velocities at depths below 3,000 m.

Acknowledging that the identification of *C. agassizii* on the wreck was challenged, Figure 9 also includes the position of known occurences of all *Chrysogorgia* species from the dataset compiled by Ramiro-Sánchez et al. (2020). However, no additional information about connectivity can be obtained. No additional populations are apparent that may be reached from the *Titanic*, or that could be a source of the *Titanic* population. Populations on the Corner Rise Seamounts at 35°N may be reached from P1 (within 150 days). However, the populations are at a depth of 2000 m and therefore again the larvae would need to bridge a large vertical gap. The southerly pathway away from the *Titanic* is too slow once larvae are advected away from the continental slope to reach the Corner Rise Seamounts within 180 days (Figure 9b).

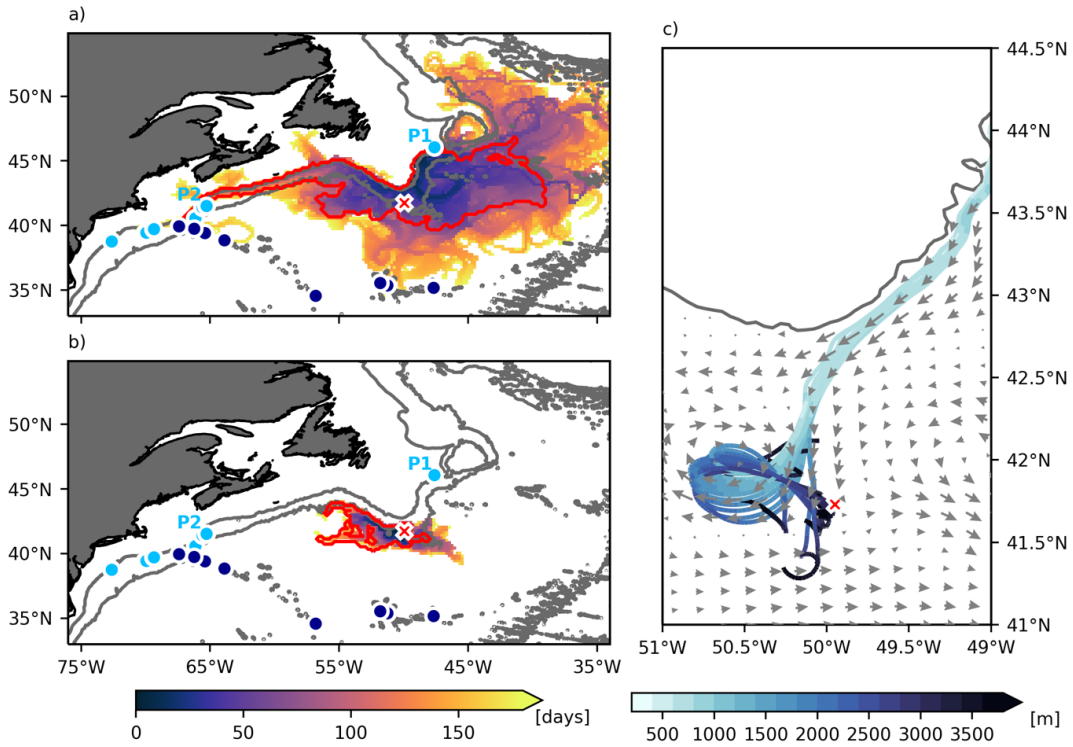

669

670 **Figure 9**: Minimum age of particles when first arriving in 0.2° x 0.2° bins in EXP_{P1-P2} (a). The red
671 contour shows the 95% contour based on a corresponding probability map. Light blue dots show
672 known populations of *Chrysogorgia agassizii* and dark blue contours known populations of other
673 *Chrysogorgia* species. Grey contours show the bathymetry. Same for EXP_{T-P2} (b). Grey contours
674 indicate a water depth of 1,000 and 3,500 m. c) Selected trajectories (length: 55 days) from EXP_{P1-T}
675 coloured with their depth and 500 m velocity snapshot (06-08-2009). The grey line indicates the 500
676 m isobath. The *Titanic* is marked with a red cross.

677

678 **4. Discussion**

679

680 In this study, we investigate whether the natural history legacy of the RMS *Titanic* in abyssal waters
681 depends on upstream connections to distant populations, and whether the *Titanic* herself could now
682 confer a resilience to the network of deep-sea coral populations in the North Atlantic. While high
683 mean velocities associated with the model's GS appear to be shifted south and the magnitude of EKE
684 is lower than in observations, general characteristics of the flow (variability) in the region around the
685 *Titanic* and the mean circulation along the continental slope are well represented. Thus, we are
686 confident the study identifies representative dispersal pathways to and from the *Titanic*, allowing us
687 to ascertain its importance in today's marine ecosystem connectivity. Below, we discuss the
688 importance of mesoscale eddies in abyssal and bathyal larval transport, the role of larval biology and
689 limitations in our knowledge, and the contributions the *Titanic* could play in deep-sea coral (as well
690 as other sessile biota) connectivity.

Mesoscale eddies control dispersal of larvae at the Titanic

In agreement with observations, the circulation above the wreck site in VIKING20X is associated with strong mesoscale eddy activity (Figure 3). We discover that the position of these mesoscale eddies exert significant control over the spreading of larvae to and from the RMS *Titanic*. Unexpectedly, effects of mesoscale eddies on dispersal far outweigh effects of either spawning or release season, or larval swimming behaviour as defined in our experiments. Instead, our study finds the spreading of *C. agassizii* to and from the RMS *Titanic* to be mainly determined by stochastic processes.

Experiments (EXP_{pas}, EXP_{act} and $EXP_{T\text{-}P2}$) show that larvae seeded at the *Titanic* are not entrained into and carried by the closed circulation of the eddies directly, but instead the abyssal circulation, strongly guided by the bathymetry, responds to the overlying eddies. Although the mean circulation is directed to the west (Figures 3,6), the presence of mesoscale activity associated with the GS/NAC and LC/DWBC does allow for a faster spreading at certain times, as well as considerable distances reached against the mean flow direction. For larvae spreading away from the *Titanic*, the existence of eddies is much more important than the mean flow (Figures 6,7). Spreading, not only in the westerly mean flow direction, but additionally to the south, is of particular importance, since it provides a pathway away from the continental slope into the abyssal ocean (Figure 5). Further, our results suggest that the interaction between eddies and the topography can cause very different spreading patterns than expected from the mean flow.

Because EKE and the strength of individual eddies at the *Titanic* position are underestimated compared to observations (Figure 3), the impact of mesoscale activity on the spreading of larvae could be even stronger in the real ocean than described here. Due to the bathymetric constraints a radically different spreading behaviour is unlikely, but distances reached from the wreck within 90 days may be larger. One would expect stronger eddies to generate larger anomalies of the circulation at depth that would carry the larvae further away within a given time.

Eddies are present nearly everywhere in the ocean (Chelton et al., 2011) and were shown to impact deeper water ecosystem processes including larval dispersal in deep-sea benthic ecosystems. They may help to retain and accumulate deep-sea larvae, or they may help to transport them over long distances. For example, eddy-driven impacts at the northern East Pacific Rise very likely extend beyond the upper ocean and main thermocline and can result in long-distance larval export from the hydrothermal vents (Adams et al., 2011). Here we show, that such an impact is not only possible in the upper ocean and mid-depth (e.g., Adams et al., 2011; Bracco et al., 2019), but also at the abyssal depths of the *Titanic*, nearly 4 km deep. Even if the near-surface flow in a given area may not be characterised by particularly strong mesoscale activity, the deep ocean may be (Schulzki et al., 2021). This highlights the need to perform Lagrangian dispersal experiments in high-resolution models so that simulations can explicitly represent mesoscale eddies and to achieve a more realistic representation of the bathymetry, especially close to the continental slope. Furthermore, eddies occurring at the *Titanic* position are not stationary. In agreement with observations (Bower et al., 2013; Chelton et al., 2011) eddies tend to propagate east, or south-westward, depending on their origin. The modelled velocity fields show that eddies remain above the *Titanic* position for periods shorter than a month. In most other regions of the ocean, eddies are not stationary, but propagate as well (Chelton et al., 2011), suggesting that dispersal studies should be carried out with a temporal resolution of the velocity field below one month to capture the impact of individual eddies.

The impact of larval behaviours on dispersal from the Titanic *wreck*

We do not find a significant dependency of season on the spreading distance or direction of larvae (Figure 5c-f). As mesoscale eddies above the *Titanic* position strongly control the spreading, more (or more intense) eddies would need to be present in different seasons to generate a seasonal cycle of the dispersal. A lack of a pronounced seasonal cycle in the modelled EKE is thus consistent with our result and in agreement with Schott et al. (2004), who do not find EKE east of the Grand Banks to show considerable seasonal variations. Whether C. *agassizii* is a seasonal spawner is therefore not expected to strongly affect its potential spreading from the wreck. Dispersal along the upper continental slope (e.g., from P1 to P2), that is mostly determined by coherent currents rather than stochastic eddy variability, could be more strongly affected by the season. The LC was shown to vary substantially between the seasons (Han et al., 2008).

As the vertical velocity shear of individual eddies at abyssal depths is very small (Figure 8), active swimming to shallower depths with the assumptions regarding duration and speed made in the present study does not greatly alter the dispersal patterns. Vertical swimming has been shown to be favourable for the dispersal of deep-sea species by allowing larvae to reach shallower waters where the circulation is usually faster. Nevertheless, short larval duration and early descent can counteract the advantages of vertical swimming (Gary et al., 2020). The larval duration used for the active experiments of this study is indeed low compared to that of other deep-sea species which display larval duration of several weeks (Hilário et al., 2015; Young et al., 2012), and this may have contributed to the limited role of larval swimming in our study system. On the other hand, some deep-sea species with longer larval duration have different larval characteristics compared to those expected for *C. agassizii.* The deep-sea scleractinian coral *Desmophyllum pertusum* (synonymous with *Lophelia pertusa*), for example, displays larval duration of 3-6 weeks (Larsson et al., 2014), but its larvae are planktotrophic while octocoral larvae are typically lecithotrophic (Watling et al., 2011). Since there is currently very little knowledge on the larval biology of deep-sea species, we based our experiments on the little information that is currently available for deep-sea octocorals, avoiding comparisons with other taxonomic groups that may display completely different larval traits.

The potential upper limit for the impact of swimming can be derived from $EXP_{P1\text{-}P2}$. If the PLD is sufficiently long for larvae to reach the main DWBC core with very high current speeds, then they can be transported rapidly towards the Nova Scotian slope (Figure 9). In this case, they would need to reach about 2,000 m depth and stay at this depth to become entrained into the strong DWBC flow.

Ecosystem connectivity along the Northwest Atlantic continental slope

Larvae released on the continental slope at the eastern side of the Grand Banks (position of population P1; Figure 2) are rapidly advected southward in the LC/DWBC. Most larvae follow the continental slope and eventually reach a known population off Nova Scotia with one additional stepping stone required (Figure 9). The larval longevity strongly determines the distance that larvae are transported within the LC/DWBC and thus the number of stepping stones required, highlighting that further studies on the larval biology of the species are essential.

However, not all virtual larvae continuously follow the LC/DWBC. Some larvae become detrained from the DWBC around the Tail of the Grand Bank and potentially reach the *Titanic* wreck (figure 9). Again, mesoscale ocean eddies seem to play a major role. Virtual larvae are diverted away from the western boundary by the interaction of eddies with the LC/DWBC. This in agreement with RAFOS

floats leaving the DWBC in eddying motion at nearly the same location, although the modelled eddies are larger than the described submesoscale vortices (Bower et al., 2013).

Still, there is considerable uncertainty, whether such a connection between P1 and the *Titanic* really exists, since larvae would need to bridge a large vertical gap. We were able to construct an experiment where larvae can reach the *Titanic* within 50 days after release. This experiment requires larvae to bridge the vertical gap by fast downward movement, which could be possible by downward swimming and/or a change in larval buoyancy. Octocoral larvae are typically lecithotrophic, i.e., non-feeding, (Watling et al., 2011) and usually contain large reserves in the form of lipids which are also important for larval buoyancy (Arai et al., 1993). During the pelagic phase, consumption of certain lipids like wax esters can indeed lead to a decrease in larval buoyancy (Harii et al., 2007). Regardless of the process, this scenario provides indications of ontogenetic changes in larval behaviour after a pelagic phase of at least 30 days, highlighting once again the need for more studies on the larval biology of this species.

Although the general circulation in this area provides a possible connection, the large vertical gap and slower spreading rate at depth make it more likely that connectivity between P1 and *Titanic* is reliant on an intermediary stepping stone with a larval longevity of 90 days. Results obtained by Riehl et al. (2020) and a recently discovered rocky ridge (proposed name “Nargeolet-Fanning (N-F) Ridge”) close to the *Titanic* in 2900 m (Ocean Gate Expeditions; J.M. Roberts and S.W. Ross, pers. obs.; Figure 2), suggest that such stepping stones are more frequent than expected. Larvae could reach the newly discovered N-F Ridge first, which is located about 1,000 m shallower than the *Titanic*. This would provide additional scenarios in which larvae could sink at a slower speed. Nevertheless, a much earlier onset of the downward velocity is unlikely for this scenario as well. Larvae would still need to be transported in the fast LC/DWBC towards the Tail of the Grand Bank, to reach the N-F Ridge within a time that does not require the larval longevity to more than twice our estimate of 90 days. Furthermore, the area is littered with glacial dropstones which are attachment sites for deep-sea sessile fauna, but which do not show up on most mapping systems. Such features could act as stepping stones adding a variety of pathways making connectivity even more likely.

It should be noted that the identification of *C. agassizii* on the wreck was challenged (Molodtsova et al., 2008), but considering known natural occurrences of all *Chrysogorgia* species does not allow to infer any other connectivity scenarios involving the *Titanic*.

While active swimming/buoyancy, as defined in our experiment, was found be of minor importance for the spreading from the *Titanic* itself, it could play a major role for possible sources of larvae at the *Titanic*. A more detailed knowledge of the larvae's buoyancy, swimming behaviour and larval longevity, would help to refine our results and better judge, whether the assumptions made here are realistic. Integrated approaches spanning genetics and experimental modelling would give even deeper insights into patterns of connectivity over different temporal and evolutionary timescales (Bracco et al., 2019).

As described before, from the *Titanic*, larvae may be exported along southern and westerly. pathways further into the abyss. While experiments indicated that the *Titanic* is unlikely a direct source of *C. agassizii* larvae for already known populations (Figures 5,9) along the Northwest Atlantic continental slope, the wreck possibly functions as a stepping stone, connecting coral populations from the slopes of the Grand Banks to abyssal populations in ABNJ along westerly and southerly circulation pathways.

With a slightly longer larval longevity than 90 days, or the ability of larvae to swim upwards, it is possible that larvae can directly reach the Canadian EEZ. Especially in combination with a longer PLD than 6 days, vertical swimming could greatly increase the number of living larvae that arrives in the EEZ. Furthermore, additional stepping stones in between would enhance the likeliness of larvae in the EEZ being supplied by the *Titanic*.

5. Conclusion: The Titanic's role in ecosystem connectivity and the importance of eddies

Depending on larval buoyancy, duration and the configuration of stepping stones, ocean circulation provides several possible pathways for larvae from a natural occurring population on the eastern slope of the Grand Banks to reach the *Titanic*, despite a large vertical gap. The interaction of eddies with the bathymetry generates two pathways away from the *Titanic*, allowing larvae to reach the Canadian EEZ along the deep continental slope, and to spread away from the slope into the abyssal North Atlantic. Therefore, the transboundary nature of coral dispersal to and from the *Titanic* is interesting on both geopolitical and ecological levels. Canada may in the future have jurisdictional rights over the *Titanic* through its claim to extend its EEZ, through which it could afford specific conservation measures, e.g., establishing a marine protected area to protect an important stepping stone for vulnerable deep-sea corals. Based on unknown larval characteristics and model uncertainties, there are different scenarios of this dispersal and the resulting connectivity in the Northwest Atlantic, but all converge on the role of Titanic as some sort of stepping stone. Our experiments also provide useful information, which biological and physical parameters must be known to narrow down the possible pathways from and to the *Titanic* discussed here. In any case and given the findings of the present study, it is unlikely that the *Titanic* is completely isolated from known or unknown populations of *C. agassizii*.

While our study was motivated by a specific case, the wreck of the RMS *Titanic*, our findings can be generalized. They support the importance of deep mesoscale eddies and fine-scale structures to understand the connectivity between deep ecosystems. Eddying structures can easily enhance or compensate the usually weaker mean flow, and in combination with bathymetry, lead to pronounced unidirectional dispersal patterns. High-resolution ocean modelling is required to correctly simulate the corresponding ocean dynamics. It can also provide answers on the importance of potentially unknown swimming or buoyancy motions of deep-sea organisms.

Acknowledgements

This study has received funding from the European Union's Horizon 2020 research and innovation programme under grant agreement No. 818123 for the iAtlantic project. This output reflects only the authors' views and the European Union cannot be held responsible for any use that may be made of the information contained therein. This research was supported in part through high-performance computing resources available at the Kiel University Computing Centre. The ocean model simulation was performed at the North-German Supercomputing Alliance (HLRN). We thank OceanGate Expeditions for providing access to recent (2021 and 2022) submersible observations and data about the *Titanic* site and N-F Ridge.

References

Adams, D.K., McGillicuddy, D.J., Zamudio, L., Thurnherr, A.M., Liang, X., Rouxel, O., German, C.R., Mullineaux, L.S., 2011. Surface-Generated Mesoscale Eddies Transport Deep-Sea Products from Hydrothermal Vents. Science 332, 580–583. https://doi.org/10.1126/science.1201066

Arai, I., Kato, M., Heyward, A., Ikeda, Y., Iizuka, T., Maruyama, T., 1993. Lipid composition of positively buoyant eggs of reef building corals. Coral Reefs 12, 71–75. https://doi.org/10.1007/BF00302104

Arakawa, A., Hsu, Y.-J.G., 1990. Energy Conserving and Potential-Enstrophy Dissipating Schemes for the Shallow Water Equations. Monthly Weather Review 118, 1960–1969. https://doi.org/10.1175/1520-0493(1990)118<1960:ECAPED>2.0.CO;2

Arellano, S.M., 2008. Embryology, larval ecology, and recruitment of "Bathymodiolus" childressi, a cold-seep mussel from the Gulf of Mexico (Ph.D. Thesis). University of Oregon.

Aznar, M.J., Varmer, O., 2013. The Titanic as Underwater Cultural Heritage: Challenges to its Legal International Protection. Ocean Development & International Law 44, 96–112. https://doi.org/10.1080/00908320.2013.750978

Barnier, B., Madec, G., Penduff, T., Molines, J.-M., Treguier, A.-M., Le Sommer, J., Beckmann, A., Biastoch, A., Böning, C., Dengg, J., Derval, C., Durand, E., Gulev, S., Remy, E., Talandier, C., Theetten, S., Maltrud, M., McClean, J., Cuevas, B., 2006. Impact of partial steps and momentum advection schemes in a global ocean circulation model at eddy-permitting resolution. Ocean Dynamics 56, 543–567. https://doi.org/10.1007/s10236-006-0082-1

Beaulieu, S.E., Sayre-McCord, R.T., Mills, S.W., Pradillon, F., Watanabe, H., 2015. Swimming speeds of polychaete larvae collected near deep-sea hydrothermal vents. Marine Ecology 36, 133–143. https://doi.org/10.1111/maec.12207

Ben-David-Zaslow, R., Benayahu, Y., 1998. Competence and longevity in planulae of several species of soft corals. Mar Ecol Prog Ser 163, 235–243.

Biastoch, A., Schwarzkopf, F.U., Getzlaff, K., Rühs, S., Martin, T., Scheinert, M., Schulzki, T., Handmann, P., Hummels, R., Böning, C.W., 2021. Regional Imprints of Changes in the Atlantic Meridional Overturning Circulation in the Eddy-rich Ocean Model VIKING20X. Ocean Sci. Discuss. 2021, 1–52. https://doi.org/10.5194/os-2021-37

Blanke, B., Bonhommeau, S., Grima, N., Drillet, Y., 2012. Sensitivity of advective transfer times across the North Atlantic Ocean to the temporal and spatial resolution of model velocity data: Implication for European eel larval transport. Dynamics of Atmospheres and Oceans 55–56, 22–44. https://doi.org/10.1016/j.dynatmoce.2012.04.003

Bonhommeau, S., Blanke, B., Tréguier, A.-M., Grima, N., Rivot, E., Vermard, Y., Greiner, E., Le Pape, O., 2009. How fast can the European eel (Anguilla anguilla) larvae cross the Atlantic Ocean? Fisheries Oceanography 18, 371–385. https://doi.org/10.1111/j.1365-2419.2009.00517.x

Bower, A., Lozier, S., Gary, S., 2011. Export of Labrador Sea Water from the subpolar North Atlantic: A Lagrangian perspective. Deep Sea Research Part II: Topical Studies in Oceanography 58, 1798–1818. https://doi.org/10.1016/j.dsr2.2010.10.060

Bower, A.S., Hendry, R.M., Amrhein, D.E., Lilly, J.M., 2013. Direct observations of formation and propagation of subpolar eddies into the Subtropical North Atlantic. Deep Sea Research Part II: Topical Studies in Oceanography 85, 15–41. https://doi.org/10.1016/j.dsr2.2012.07.029

Bracco, A., Liu, G., Galaska, M.P., Quattrini, A.M., Herrera, S., 2019. Integrating physical circulation models and genetic approaches to investigate population connectivity in deep-sea corals. Journal of Marine Systems 198, 103189. https://doi.org/10.1016/j.jmarsys.2019.103189

Breusing, C., Biastoch, A., Drews, A., Metaxas, A., Jollivet, D., Vrijenhoek, R.C., Bayer, T., Melzner, F., Sayavedra, L., Petersen, J.M., Dubilier, N., Schilhabel, M.B., Rosenstiel, P., Reusch, T.B.H., 2016. Biophysical and Population Genetic Models Predict the Presence of "Phantom" Stepping Stones Connecting Mid-Atlantic Ridge Vent Ecosystems. Current Biology 26, 2257–2267. https://doi.org/10.1016/j.cub.2016.06.062

913 Bright, D.A., Williams, R.M.L., McLare, A.S., 2005. Comparative photometric analysis of structural
914 degradation on the bow of RMS Titanic, in: Proceedings of OCEANS 2005 MTS/IEEE.
915 Presented at the Proceedings of OCEANS 2005 MTS/IEEE, pp. 106-110 Vol. 1.
916 https://doi.org/10.1109/OCEANS.2005.1639746
917 Brown, O.B., Cornillon, P.C., Emmerson, S.R., Carle, H.M., 1986. Gulf Stream warm rings: a statistical
918 study of their behavior. Deep Sea Research Part A. Oceanographic Research Papers 33,
919 1459–1473. https://doi.org/10.1016/0198-0149(86)90062-2
920 Busch, K., Taboada, S., Riesgo, A., Koutsouveli, V., Ríos, P., Cristobo, J., Franke, A., Getzlaff, K.,
921 Schmidt, C., Biastoch, A., Hentschel, U., 2021. Population connectivity of fan-shaped sponge
922 holobionts in the deep Cantabrian Sea. Deep Sea Research Part I: Oceanographic Research
923 Papers 167, 103427. https://doi.org/10.1016/j.dsr.2020.103427
924 Cairns, S.D., 2001. Studies on western Atlantic Octocorallia (Coelenterata: Anthozoa) Part 1: The
925 genus Chrysogorgia Duchassaing & Michelotti, 1864. Proceedings of the Biological Society of
926 Washington 114, 746–787.
927 Chelton, D.B., Schlax, M.G., Samelson, R.M., 2011. Global observations of nonlinear mesoscale
928 eddies. Progress in Oceanography 91, 167–216.
929 https://doi.org/10.1016/j.pocean.2011.01.002
930 Chelton, D.B., Schlax, M.G., Samelson, R.M., de Szoeke, R.A., 2007. Global observations of large
931 oceanic eddies. Geophysical Research Letters 34. https://doi.org/10.1029/2007GL030812
932 Coelho, M.A.G., Lasker, H.R., 2016. Larval behavior and settlement dynamics of a ubiquitous
933 Caribbean octocoral and its implications for dispersal. Mar Ecol Prog Ser 561, 109–121.
934 Cullimore, D.R., Johnston, L.A., 2008. Microbiology of Concretions, Sediments and Mechanisms
935 Influencing the Preservation of Submerged Archaeological Artifacts. International Journal of
936 Historical Archaeology 12, 120–132. https://doi.org/10.1007/s10761-008-0045-y
937 Daniault, N., Mercier, H., Lherminier, P., Sarafanov, A., Falina, A., Zunino, P., Pérez, F.F., Ríos, A.F.,
938 Ferron, B., Huck, T., Thierry, V., Gladyshev, S., 2016. The northern North Atlantic Ocean
939 mean circulation in the early 21st century. Progress in Oceanography 146, 142–158.
940 https://doi.org/10.1016/j.pocean.2016.06.007
941 Debreu, L., Vouland, C., Blayo, E., 2008. AGRIF: Adaptive grid refinement in Fortran. Computers &
942 Geosciences 34, 8–13. https://doi.org/10.1016/j.cageo.2007.01.009
943 Delandmeter, P., van Sebille, E., 2019. The Parcels v2.0 Lagrangian framework: new field
944 interpolation schemes. Geosci. Model Dev. 12, 3571–3584. https://doi.org/10.5194/gmd-12-
945 3571-2019
946 Ducet, N., Le Traon, P.-Y., 2001. A comparison of surface eddy kinetic energy and Reynolds stresses
947 in the Gulf Stream and the Kuroshio Current systems from merged TOPEX/Poseidon and
948 ERS-1/2 altimetric data. Journal of Geophysical Research: Oceans 106, 16603–16622.
949 https://doi.org/10.1029/2000JC000205
950 Ducousso, N., Le Sommer, J., Molines, J.-M., Bell, M., 2017. Impact of the “Symmetric Instability of
951 the Computational Kind” at mesoscale- and submesoscale-permitting resolutions. Ocean
952 Modelling 120, 18–26. https://doi.org/10.1016/j.ocemod.2017.10.006
953 Fichefet, T., Maqueda, M.A.M., 1997. Sensitivity of a global sea ice model to the treatment of ice
954 thermodynamics and dynamics. Journal of Geophysical Research: Oceans 102, 12609–12646.
955 https://doi.org/10.1029/97JC00480
956 Flanders Marine Institute, 2019. Maritime Boundaries Geodatabase version 11.
957 https://doi.org/10.14284/382
958 Fontoura, L., D’Agata, S., Gamoyo, M., Barneche, D.R., Luiz, O.J., Madin, E.M.P., Eggertsen, L., Maina,
959 J.M., 2022. Protecting connectivity promotes successful biodiversity and fisheries
960 conservation. Science 375, 336–340. https://doi.org/10.1126/science.abg4351
961 Frazão, H.C., Prien, R.D., Schulz-Bull, D.E., Seidov, D., Waniek, J.J., 2022. The Forgotten Azores
962 Current: A Long-Term Perspective. Frontiers in Marine Science 9.

963 Gary, S.F., Fox, A.D., Biastoch, A., Roberts, J.M., Cunningham, S.A., 2020. Larval behaviour, dispersal
964 and population connectivity in the deep sea. Scientific Reports 10, 10675.
965 https://doi.org/10.1038/s41598-020-67503-7
966 Gravina, M.F., Casoli, E., Donnarumma, L., Giampaoletti, J., Antonelli, F., Sacco Perasso, C., Ricci, S.,
967 2021. First Report on the Benthic Invertebrate Community Associated With a Bronze Naval
968 Ram From the First Punic War: A Proxy of Marine Biodiversity. Frontiers in Marine Science 8.
969 Griffies, S.M., Biastoch, A., Böning, C., Bryan, F., Danabasoglu, G., Chassignet, E.P., England, M.H.,
970 Gerdes, R., Haak, H., Hallberg, R.W., Hazeleger, W., Jungclaus, J., Large, W.G., Madec, G.,
971 Pirani, A., Samuels, B.L., Scheinert, M., Gupta, A.S., Severijns, C.A., Simmons, H.L., Treguier,
972 A.M., Winton, M., Yeager, S., Yin, J., 2009. Coordinated Ocean-ice Reference Experiments
973 (COREs). Ocean Modelling 26, 1–46. https://doi.org/10.1016/j.ocemod.2008.08.007
974 Guizien, K., Viladrich, N., Martínez-Quintana, Á., Bramanti, L., 2020. Survive or swim: different
975 relationships between migration potential and larval size in three sympatric Mediterranean
976 octocorals. Scientific Reports 10, 18096. https://doi.org/10.1038/s41598-020-75099-1
977 Guy, G., Metaxas, A., 2022. Recruitment of deep-water corals and sponges in the Northwest Atlantic
978 Ocean: implications for habitat distribution and population connectivity. Marine Biology 169.
979 https://doi.org/10.1007/s00227-022-04089-w
980 Hamdan, L.J., Hampel, J.J., Moseley, R.D., Mugge, Rachel.L., Ray, A., Salerno, J.L., Damour, M., 2021.
981 Deep-sea shipwrecks represent island-like ecosystems for marine microbiomes. The ISME
982 Journal 15, 2883–2891. https://doi.org/10.1038/s41396-021-00978-y
983 Han, G., Lu, Z., Wang, Z., Helbig, J., Chen, N., de Young, B., 2008. Seasonal variability of the Labrador
984 Current and shelf circulation off Newfoundland. Journal of Geophysical Research: Oceans
985 113. https://doi.org/10.1029/2007JC004376
986 Harii, S., Nadaoka, K., Yamamoto, M., Iwao K, 2007. Temporal changes in settlement, lipid content
987 and lipid composition of larvae of the spawning hermatypic coral Acropora tenuis. Mar Ecol
988 Prog Ser 346, 89–96.
989 Hilário, A., Metaxas, A., Gaudron, S.M., Howell, K.L., Mercier, A., Mestre, N.C., Ross, R.E., Thurnherr,
990 A.M., Young, C., 2015. Estimating dispersal distance in the deep sea: challenges and
991 applications to marine reserves. Frontiers in Marine Science 2.
992 Kenchington, E., Wang, Z., Lirette, C., Murillo, F.J., Guijarro, J., Yashayaev, I., Maldonado, M., 2019.
993 Connectivity modelling of areas closed to protect vulnerable marine ecosystems in the
994 northwest Atlantic. Deep Sea Research Part I: Oceanographic Research Papers 143, 85–103.
995 https://doi.org/10.1016/j.dsr.2018.11.007
996 Large, W.G., Yeager, S.G., 2009. The global climatology of an interannually varying air–sea flux data
997 set. Climate Dynamics 33, 341–364. https://doi.org/10.1007/s00382-008-0441-3
998 Larsson, A.I., Järnegren, J., Strömberg, S.M., Dahl, M.P., Lundälv, T., Brooke, S., 2014. Embryogenesis
999 and Larval Biology of the Cold-Water Coral Lophelia pertusa. PLOS ONE 9, e102222.
1000 https://doi.org/10.1371/journal.pone.0102222
1001 Le Corre, N., Pepin, P., Snelgrove, P., 2018. Connectivity of Bentho-Pelagic Species among Significant
1002 Benthic Areas off Newfoundland and Labrador. Zenodo.
1003 https://doi.org/10.5281/zenodo.1255743
1004 Martin, J.B., 2018. Protecting Outstanding Underwater Cultural Heritage through the World Heritage
1005 Convention: The Titanic and Lusitania as World Heritage Sites. The International Journal of
1006 Marine and Coastal Law 33, 116–165. https://doi.org/10.1163/15718085-13301069
1007 Martínez-Quintana, A., Bramanti, L., Viladrich, N., Rossi, S., Guizien, K., 2015. Quantification of larval
1008 traits driving connectivity: the case of Corallium rubrum (L. 1758). Marine Biology 162, 309–
1009 318. https://doi.org/10.1007/s00227-014-2599-z
1010 Metaxas, A., Lacharité, M., de Mendonça, S.N., 2019. Hydrodynamic Connectivity of Habitats of
1011 Deep-Water Corals in Corsair Canyon, Northwest Atlantic: A Case for Cross-Boundary
1012 Conservation. Frontiers in Marine Science. https://doi.org/10.3389/fmars.2019.00159

Meyer-Kaiser, K.S., Mires, C.H., 2022. Underwater cultural heritage is integral to marine ecosystems. Trends in Ecology & Evolution 37, 815–818. https://doi.org/10.1016/j.tree.2022.06.014

Molodtsova, T.N., Sanamyan, N.P., Keller, N.B., 2008. Anthozoa from the northern Mid-Atlantic Ridge and Charlie-Gibbs Fracture Zone. Marine Biology Research 4, 112–130. https://doi.org/10.1080/17451000701821744

Morato, T., González-Irusta, J.-M., Dominguez-Carrió, C., Wei, C.-L., Davies, A., Sweetman, A.K., Taranto, G.H., Beazley, L., García-Alegre, A., Grehan, A., Laffargue, P., Murillo, F.J., Sacau, M., Vaz, S., Kenchington, E., Arnaud-Haond, S., Callery, O., Chimienti, G., Cordes, E., Egilsdottir, H., Freiwald, A., Gasbarro, R., Gutiérrez-Zárate, C., Gianni, M., Gilkinson, K., Wareham Hayes, V.E., Hebbeln, D., Hedges, K., Henry, L.-A., Johnson, D., Koen-Alonso, M., Lirette, C., Mastrototaro, F., Menot, L., Molodtsova, T., Durán Muñoz, P., Orejas, C., Pennino, M.G., Puerta, P., Ragnarsson, S.Á., Ramiro-Sánchez, B., Rice, J., Rivera, J., Roberts, J.M., Ross, S.W., Rueda, J.L., Sampaio, Í., Snelgrove, P., Stirling, D., Treble, M.A., Urra, J., Vad, J., van Oevelen, D., Watling, L., Walkusz, W., Wienberg, C., Woillez, M., Levin, L.A., Carreiro-Silva, M., 2020. Climate-induced changes in the suitable habitat of cold-water corals and commercially important deep-sea fishes in the North Atlantic. Global Change Biology 26, 2181–2202. https://doi.org/10.1111/gcb.14996

Müller, V., Kieke, D., Myers, P.G., Pennelly, C., Steinfeldt, R., Stendardo, I., 2019. Heat and Freshwater Transport by Mesoscale Eddies in the Southern Subpolar North Atlantic. Journal of Geophysical Research: Oceans 124, 5565–5585. https://doi.org/10.1029/2018JC014697

New, A.L., Smeed, D.A., Czaja, A., Blaker, A.T., Mecking, J.V., Mathews, J.P., Sanchez-Franks, A., 2021. Labrador Slope Water connects the subarctic with the Gulf Stream. Environ. Res. Lett. 16, 084019. https://doi.org/10.1088/1748-9326/ac1293

Ollitrault, M., Rannou, P., Brion, E., Cabanes, C., Piron, A., Reverdin, G., Kolodziejczyk, N., 2022. ANDRO: An Argo-based deep displacement dataset. SEANOE. https://doi.org/10.17882/47077

Pante, E., France, S.C., Couloux, A., Cruaud, C., McFadden, C.S., Samadi, S., Watling, L., 2012. Deep-Sea Origin and In-Situ Diversification of Chrysogorgiid Octocorals. PLOS ONE 7, e38357. https://doi.org/10.1371/journal.pone.0038357

Paxton, A.B., Blair, E., Blawas, C., Fatzinger, M.H., Marens, M., Holmberg, J., Kingen, C., Houppermans, T., Keusenkothen, M., McCord, J., Silliman, B.R., Penfold, L.M., 2019. Citizen science reveals female sand tiger sharks (Carcharias taurus) exhibit signs of site fidelity on shipwrecks. Ecology 100, 1–4.

Pickart, R.S., Spall, M.A., Lazier, J.R.N., 1997. Mid-depth ventilation in the western boundary current system of the sub-polar gyre. Deep Sea Research Part I: Oceanographic Research Papers 44, 1025–1054. https://doi.org/10.1016/S0967-0637(96)00122-7

Ragnarsson, S.Á., Burgos, J.M., Kutti, T., van den Beld, I., Egilsdóttir, H., Arnaud-Haond, S., Grehan, A., 2017. The Impact of Anthropogenic Activity on Cold-Water Corals, in: Rossi, S., Bramanti, L., Gori, A., Orejas, C. (Eds.), Marine Animal Forests: The Ecology of Benthic Biodiversity Hotspots. Springer International Publishing, Cham, pp. 989–1023. https://doi.org/10.1007/978-3-319-21012-4_27

Rakka, M., 2021. Cold-water corals in a changing world: potential impacts of climate change across coral life history stages. PhD Dissertation, University of the Azores (Ph.D. Thesis). University of the Azores.

Rakka, M., Godinho, A., Orejas, C., Carreiro-Silva, M., 2021. Embryo and larval biology of the deep-sea octocoral Dentomuricea aff. meteor under different temperature regimes. PeerJ 9. https://doi.org/10.7717/peerj.11604

Ramiro-Sánchez, B., Henry, L.-A., Morato, T., Taranto, G., Cleland, J., Carreiro-Silva, M., Sampaio, Í., Domínguez-Carrió, C., Messing, C.G., Kenchington, E.L., Murton, B., Roberts, J.M., 2020. Compilation of records of vulnerable marine ecosystem indicator taxa in the North Atlantic. https://doi.org/10.1594/PANGAEA.920658

Richardson, P.L., Maillard, C., Stanford, T.B., 1979. The physical structure and life history of cyclonic Gulf Stream Ring Allen. Journal of Geophysical Research: Oceans 84, 7727–7741. https://doi.org/10.1029/JC084iC12p07727

Rieck, J.K., Böning, C.W., Getzlaff, K., 2019. The Nature of Eddy Kinetic Energy in the Labrador Sea: Different Types of Mesoscale Eddies, Their Temporal Variability, and Impact on Deep Convection. J. Phys. Oceanogr. 49, 2075–2094. https://doi.org/10.1175/JPO-D-18-0243.1

Riehl, T., Wölfl, A.-C., Augustin, N., Devey, C.W., Brandt, A., 2020. Discovery of widely available abyssal rock patches reveals overlooked habitat type and prompts rethinking deep-sea biodiversity. Proceedings of the National Academy of Sciences 117, 15450–15459. https://doi.org/10.1073/pnas.1920706117

Roberts, J.M., Devey, C.W., Biastoch, A., Carreiro-Silva, M., Dohna, T., Dorschel, B., Gunn, V., Al Huvenne, V., Johnson, D.E., Jollivet, D., Kenchington, E., Larkin, K., Matabos, M., Morato, T., Naumann, M.S., Orejas, C., Perez, J.A., Ragnarsson, S.A., Smit, A.J., Sweetman, A., Unger, S., Boteler, B., Henry, L.-A., 2022. A blueprint for integrating scientific approaches and international communities to assess basin-wide ocean ecosystem status. Nat. Commun. Earth Environ. in press.

Ross, R.E., Nimmo-Smith, W.A.M., Torres, R., Howell, K.L., 2020. Comparing Deep-Sea Larval Dispersal Models: A Cautionary Tale for Ecology and Conservation. Frontiers in Marine Science 7.

Ross, S.W., Rhode, M., Viada, S.T., Mather, R., 2016. Fish species associated with shipwreck and natural hard-bottom habitats from the middle to outer continental shelf of the Middle Atlantic Bight near Norfolk Canyon. Fishery Bulletin 114, 45–57. https://doi.org/10.7755/FB.114.1.4

Rühs, S., Oliver, E.C.J., Biastoch, A., Böning, C.W., Dowd, M., Getzlaff, K., Martin, T., Myers, P.G., 2021. Changing Spatial Patterns of Deep Convection in the Subpolar North Atlantic. Journal of Geophysical Research: Oceans 126, e2021JC017245. https://doi.org/10.1029/2021JC017245

Rühs, S., Zhurbas, V., Koszalka, I.M., Durgadoo, J.V., Biastoch, A., 2018. Eddy Diffusivity Estimates from Lagrangian Trajectories Simulated with Ocean Models and Surface Drifter Data—A Case Study for the Greater Agulhas System. Journal of Physical Oceanography 48, 175–196. https://doi.org/10.1175/JPO-D-17-0048.1

Salazar, M., Little, B., 2017. Review: Rusticle Formation on the RMS Titanic and the Potential Influence of Oceanography. Journal of Maritime Archaeology 12, 25–32. https://doi.org/10.1007/s11457-016-9168-1

Saunders, P.M., 1971. Anticyclonic eddies formed from shoreward meanders of the Gulf Stream. Deep Sea Research and Oceanographic Abstracts 18, 1207–1219. https://doi.org/10.1016/0011-7471(71)90027-1

Schott, F.A., Zantopp, R., Stramma, L., Dengler, M., Fischer, J., Wibaux, M., 2004. Circulation and Deep-Water Export at the Western Exit of the Subpolar North Atlantic. Journal of Physical Oceanography 34, 817–843. https://doi.org/10.1175/1520-0485(2004)034<0817:CADEAT>2.0.CO;2

Schubert, R., Biastoch, A., Cronin, M.F., Greatbatch, R.J., 2018. Instability-Driven Benthic Storms below the Separated Gulf Stream and the North Atlantic Current in a High-Resolution Ocean Model. J. Phys. Oceanogr. 48, 2283–2303. https://doi.org/10.1175/JPO-D-17-0261.1

Schulzki, T., Getzlaff, K., Biastoch, A., 2021. On the Variability of the DWBC Transport Between 26.5°N and 16°N in an Eddy-Rich Ocean Model. Journal of Geophysical Research: Oceans 126, e2021JC017372. https://doi.org/10.1029/2021JC017372

Seidov, D., Mishonov, A., Reagan, J., Parsons, R., 2019. Resilience of the Gulf Stream path on decadal and longer timescales. Scientific Reports 9, 11549. https://doi.org/10.1038/s41598-019-48011-9

Shay, T.J., Bane, J.M., Watts, D.R., Tracey, K.L., 1995. Gulf Stream flow field and events near 68°W. Journal of Geophysical Research: Oceans 100, 22565–22589. https://doi.org/10.1029/95JC02685

Sun, Z., Hamel, J.F., Mercier, A., 2010. Planulation periodicity, settlement preferences and growth of two deep-sea octocorals from the northwest Atlantic. Mar Ecol Prog Ser 410, 71–87.

Taburet, G., Pujol, M.-I., 2022. Global Ocean Gridded L 4 Sea Surface Heights And Derived Variables Reprocessed Copernicus Climate Service. Copernicus Climate Change Service. https://doi.org/10.48670/moi-00145

Tessnow-von Wysocki, I., Vadrot, A., 2022. Governing a Divided Ocean: The Transformative Power of Ecological Connectivity in the BBNJ negotiations. Politics and Governance 10, 14–28. https://doi.org/10.17645/pag.v10i3.5428

Tsujino, H., Urakawa, S., Nakano, H., Small, R.J., Kim, W.M., Yeager, S.G., Danabasoglu, G., Suzuki, T., Bamber, J.L., Bentsen, M., Böning, C.W., Bozec, A., Chassignet, E.P., Curchitser, E., Boeira Dias, F., Durack, P.J., Griffies, S.M., Harada, Y., Ilicak, M., Josey, S.A., Kobayashi, C., Kobayashi, S., Komuro, Y., Large, W.G., Le Sommer, J., Marsland, S.J., Masina, S., Scheinert, M., Tomita, H., Valdivieso, M., Yamazaki, D., 2018. JRA-55 based surface dataset for driving ocean–sea-ice models (JRA55-do). Ocean Modelling 130, 79–139. https://doi.org/10.1016/j.ocemod.2018.07.002

Untiedt, C.B., Quattrini, A.M., McFadden, C.S., Alderslade, P.A., Pante, E., Burridge, C.P., 2021. Phylogenetic Relationships Within Chrysogorgia (Alcyonacea: Octocorallia), a Morphologically Diverse Genus of Octocoral, Revealed Using a Target Enrichment Approach. Frontiers in Marine Science 7.

Vancoppenolle, M., Fichefet, T., Goosse, H., Bouillon, S., Madec, G., Maqueda, M.A.M., 2009. Simulating the mass balance and salinity of Arctic and Antarctic sea ice. 1. Model description and validation. Ocean Modelling 27, 33–53. https://doi.org/10.1016/j.ocemod.2008.10.005

Vinogradov, G.M., 2000. Growth rate of the colony of a deep-water gorgonarian Chrysogorgia agassizi: In situ observations. Ophelia 53, 101–103.

Wang, S., Kenchington, E.L., Wang, Z., Yashayaev, I., Davies, A.J., 2020. 3-D ocean particle tracking modeling reveals extensive vertical movement and downstream interdependence of closed areas in the northwest Atlantic. Scientific Reports 10, 21421. https://doi.org/10.1038/s41598-020-76617-x

Watling, L., France, S.C., Pante, E., Simpson, A., 2011. Biology of Deep-Water Octocorals, in: Lesser, M. (Ed.), Advances in Marine Biology. Academic Press, pp. 41–122. https://doi.org/10.1016/B978-0-12-385529-9.00002-0

Yahagi, T., Kayama Watanabe, H., Kojima, S., Kano, Y., 2017. Do larvae from deep-sea hydrothermal vents disperse in surface waters? Ecology 98, 1524–1534. https://doi.org/10.1002/ecy.1800

Young, C.M., He, R., Emlet, R.B., Li, Y., Qian, H., Arellano, S.M., Van Gaest, A., Bennett, K.C., Wolf, M., Smart, T.I., Rice, M.E., 2012. Dispersal of Deep-Sea Larvae from the Intra-American Seas: Simulations of Trajectories using Ocean Models. Integrative and Comparative Biology 52, 483–496. https://doi.org/10.1093/icb/ics090

Zalesak, S.T., 1979. Fully multidimensional flux-corrected transport algorithms for fluids. Journal of Computational Physics 31, 335–362. https://doi.org/10.1016/0021-9991(79)90051-2

CHAPTER 7

Synthesis and Outlook

The main goal of this thesis is to provide new insights on the connectivity and variability of the Atlantic Ocean circulation, based on series of high-resolution model experiments in conjunction with Lagrangian analysis techniques. Connectivity between remote regions has important implications on a range of spatial and temporal scales. It can affect global climate variability, the coherence of circulation changes on regional scales and the spreading of marine organisms.

A deeper insight into interhemispheric connectivity is relevant to advance the fundamental knowledge of the ocean circulation (variability), but also to assess future risks under global climate change. One of the main focuses of this thesis is the relative importance and interaction of changes in various key-regions across the hemispheres.

Necessary pre-requisites to improve our knowledge of locally and remotely forced circulation, and in particular AMOC, variability were the development of a new model configuration (FOCI-ATLAS10) and the joint implementation of procedures to apply a partial coupling and an online modification of the wind stress in the earth system model FOCI (see chapter 2). The unique model configuration FOCI-ATLAS10 covers the entire Atlantic at eddying (1/10°) resolution and is affordable enough to be run for several hundreds of years. FOCI-ATLAS10 realistically simulates several key features of the Atlantic Ocean circulation, including the mean AMOC and horizontal gyre transports (chapter 3).

Understanding past (wind-driven) variability (chapter 3) and interhemispheric AMOC connectivity (chapter 4) in more detail, has direct implications for the assessment of AMOC changes. It helps to decipher the sources of AMOC variability on different timescales and at different latitudes. Although various publications have argued that wind-driven processes dominate interannual variability (Biastoch et al., 2008a; Polo et al., 2014; Zhao & Johns, 2014), this has not been evaluated in a partially coupled model at eddying resolution. The question about possible feedbacks from interannual wind-driven variability on longer timescales, or the effect of connectivity (teleconnections) to the Pacific, could not have been addressed in a forced configuration. Furthermore, the developed and tested partial coupling mode can be useful for future projects and therefore contribute to an improved understanding of the ocean circulation in the Atlantic and beyond. This is by providing a set-up with improved timing of interannual variability along with a stable AMOC transport and more specifically a set-up that allows to study the impacts of interannual AMOC variability, e.g. the impact of the 2009/10 AMOC minimum, in a coupled model.

The nested FOCI-ATLAS10 configuration was specifically designed to study interhemispheric connectivity. Interhemispheric connectivity and in particular the impact of Southern Ocean wind stress and Agulhas leakage on the AMOC are especially relevant, since both have experienced an increase over recent decades (Agulhas leakage at least between the 1960s and 80s; Swart & Fyfe, 2012; Goyal et al., 2021; Rühs et al., 2022) and are projected continue increasing in the future (Goyal et al., 2021; Ivanciu et al., 2022a). An impact of increasing westerlies and Agulhas leakage could act to stabilise the AMOC by an increased production of deep water in the North Atlantic. The more than 100 years long ensemble experiment conducted here reveals such a connectivity, probably for the first time, in an eddying, coupled model (chapter 4). It provides a dynamical

consistent hypothesis, how temperature and salinity anomalies of South Atlantic origin can reach the subpolar North Atlantic. Additionally, the experiments provide new insights into fundamental processes that affect the AMOC strength, including the connection of sinking and water mass transformation in the North Atlantic.

Similar to the investigation of wind-driven variability and interhemispheric connectivity, a deeper knowledge of processes contributing to regional connectivity (chapter 5) results in a better understanding of AMOC changes. Regional connectivity is especially related the question, which processes determine the timescale on which variability measured at a specific section is representative for a larger range of latitudes. It is shown that although the advective timescale between two sections of long term measurements in the subtropical North Atlantic is shorter than 2-years, the presence of mesoscale variability strongly reduces the coherence of variability on interannual timescales. Thereby, it was possible to resolve an apparent contradiction (see chapter 1) between the dominance of wind-driven variability over advective signal propagation on this timescale, despite a strong and continuous current is connecting the sections.

Future changes of the Atlantic Ocean circulation are not only relevant for physical questions, but also highly important for interdisciplinary research. Deep-Sea species, such as the octocoral *C. agassizzii*, are vulnerable to changing environmental conditions (Morato et al., 2020) and it is necessary to better understand connectivity between remote ecosystems via the transport of larvae (chapter 6). Changing environmental conditions, as well as connectivity, are closely linked to the Atlantic circulation (Roberts et al., 2023). As an example, it is demonstrated in this thesis how the interaction of important AMOC pathways, such as the DWBC, with eddies impacts the connectivity of ecosystems along the Northwest Atlantic continental slope, including the wreck of RMS Titanic. This study provides insight on the role of the Titanic in connecting remote deep-sea coral populations with possible impacts on biodiversity and political measures to protect the wreck. At the same time, the oceanographic setting of the wreck site also results in a significance of this study for physical oceanography. The Titanic is under the influence of the Gulf Stream, North Atlantic Current, Labrador Current and Deep Western Boundary Current and strong temporal variability associated with the generation of mesoscale (and submesoscale) eddies. These eddies were shown to strongly influence the dispersal of larvae from the Titanic wreck and to provide possible pathways connecting the Titanic to known natural occurrences of deep-sea corals. Since the Lagrangian particles can be interpreted as larvae, but equivalently as any kind of tracer, the experiments do not only provide information about the dispersal of larvae, but also the spreading of subpolar water masses (including Labrador Sea Water). Although this was not explicitly discussed in chapter 6, the results support the conclusion of Bower et al. (2013) that the region south of the Grand Banks is important for an exchange between subpolar latitudes and the interior Subtropical Gyre.

7.1 Discussion: Connectivity of the Atlantic Ocean Circulation

In this chapter the main results of this thesis are discussed in the common context of connectivity through and of the Atlantic Ocean circulation.

Connectivity on Regional Scales and Sub-decadal Timescales

In a first step, a partial coupling procedure was jointly implemented and then applied in a newly developed high-resolution coupled model configuration (FOCI-ATLAS10) to investigate the ability of such experiments to reproduce past (AMOC) variability. In addition to independent advances in modelling, this allows to identify temporal and regional details of the impact of wind variability on the AMOC. It was shown in chapter 3 that the timing of AMOC variability is significantly improved compared to a fully coupled experiment on timescales up to 5-years. This is in line with previous studies that find variability on these timescales to be dominated by local wind-driven

processes, such as coastal upwelling, Ekman and Sverdrup transport (Zhao & Johns, 2014; Polo et al., 2014; Duchez et al., 2014).

Therefore, the results on partial coupling highlight the dominance of wind variability on interannual and shorter timescales, throughout the entire Atlantic. Investigating the impact of mesoscale variability on the coherence of DWBC and AMOC variability in chapter 5, yields the same result. It was shown that the AMOC at the RAPID (26.5°N) and MOVE (16°N) sections shows highly correlated variability, but this correlation is most likely attributed to large-scale wind patterns, rather than advection in the DWBC. Although this result itself is not necessarily unexpected based on previous studies (Elipot et al., 2013, 2016; Zhang, 2010), the detailed analysis of mechanisms that affect the advective propagation of transport anomalies provides a convincing hypothesis for the lack of coherent variability generated by the DWBC. It was shown that the DWBC connects the two latitudes with a mean transport of more than 20 Sv and an advective timescale shorter than 2 years. In principal, this transport could therefore be a source of coherent interannual variability. Nevertheless, the presence of mesoscale variability is found to decouple transport variations at 26.5°N and 16°N. Eddies and meanders result in temporal variability of the transit time distribution, which reduces the correlation of DWBC transport anomalies at both sections. Furthermore, they are responsible for strong recirculations across the latitudes of 26.5°N and 16°N. It was found that the recirculation across 26.5°N is highly correlated to the DWBC transport. Therefore, the recirculation compensates for a significant fraction of the additional transport that is associated with an above average DWBC transport. Eddies can also have another, more direct, impact on interannual AMOC variability. Although the interannual correlation between the partially coupled and forced simulation is significant, it is not (close to) 1, in particular in the South Atlantic and around 35°N. This is in agreement with Leroux et al. (2018) and Grégorio et al. (2015), who show that a significant fraction of variability can not be explained by local wind variability, but stochastic ocean variability, for example generated by eddies. This is another reason why the implementation of partial coupling in FOCI-ATLAS10 provides additional information over other studies on partial coupling (e.g. Thoma et al., 2015). It allows to study whether unforced variability in an eddying model could mask the wind-driven variability. Nevertheless, it should be noted that for a quantitative assessment of unforced variability an ensemble experiment is necessary. Overall, these results suggest that on interannual timescales, connectivity through advection is of minor importance, compared to the impact of local wind-driven variability and stochastic variability introduced by eddies and other mesoscale circulation features.

The impact of eddies was further shown to strongly influence the dispersal of marine organisms, even at a depth of 3800 m south of the Grand Banks (chapter 6). It is well known that the mesoscale is of major importance for the ocean circulation. But the studies presented in chapters 5 and 6 clearly show that this importance extends to regions, depths and processes that were initially not expected to be significantly impacted by mesoscale variability. For the coherence of AMOC variability in the subtropical North Atlantic, as well as larval dispersal from the Titanic wreck, it was initially assumed that the coherent flow of the DWBC would be the most important circulation feature. But it was shown that this is not true for the coherence of DWBC and AMOC variability, as described above, and neither for ecosystem connectivity along the Northwest Atlantic continental slope. Instead, the dispersal of larvae from the Titanic, as well as possible connectivity to natural occurring populations upstream the DWBC, are strongly affected by the presence of mesoscale eddies. These eddies cause a considerable speed-up of the mean circulation at the wreck site, allowing larvae to reach greater distances from the wreck. At the same time, eddies can cause a reversal of the mean flow direction, transporting larvae away from the continental slope into the abyssal North Atlantic. As a result, chapters 5 and 6 suggest that regional connectivity should be studied in eddy resolving models. Important pathways may be missed, if the impact of eddies is not explicitly considered. Future studies may show that submesoscale models are necessary to obtain even more realistic results. Especially for the Titanic wreck site, it was shown that submesoscale eddies exist in the vicinity (Bower et al., 2013).

Interhemispheric Connectivity and Connectivity on (Multi-) Decadal Timescales

The results on partial coupling further revealed a correlation between the partially coupled and forced experiments even on decadal timescales, caused by a direct impact of decadal Sverdrup transport variability (chapter 3). Although it was concluded that this impact is not sufficient to rely on partial coupling for studies on decadal AMOC variability, it shows that local wind forcing can affect AMOC variability even beyond interannual timescales in agreement with Duchez et al. (2014). However, there are no hints, or even evidence, that the interannual circulation variability could feed back on North Atlantic heat fluxes, or that teleconnections to the Pacific (e.g. ENSO) have a major impact on the timing of decadal heat flux variability in the North Atlantic. This does not necessarily mean that such impacts can not exist (see for example King et al., 2023), but their contribution to past variability in the North Atlantic was not of leading order and probably masked by other processes generating variability. Further, this result supports the hypothesis that heat fluxes in the North Atlantic are primarily controlled by the NAO and sea surface temperature variability (that does not result from wind-driven circulation changes) on decadal timescales (e.g. Eden & Jung, 2001a; Megann et al., 2021).

To separate the impact of local and remotely forced variability, interhemispheric connectivity needs to be studied on timescales of decades and longer. The partially coupled experiments (chapter 3) and other studies (e.g. Biastoch et al., 2008a; Leroux et al., 2018) suggest that on shorter timescales strong local wind-driven and stochastic variability would mask signals that may propagate across the hemispheres. Further, it was shown that the AMOC responds to changes in the same hemisphere much faster than to changes in the opposite hemisphere. This phenomena is known as the 'equatorial buffer' (Johnson & Marshall, 2002; Klinger & Cruz, 2009). Basin wide AMOC changes that allow to study its interhemispheric connectivity may be forced in both hemispheres (e.g. Swingedouw et al., 2013; Knorr & Lohmann, 2003). But the limited impact of wind stress variability on the timing of decadal variability in the subpolar North Atlantic found in chapter 3, contributed to the choice of applying a well defined wind stress anomaly in the southern hemisphere to study interhemispheric connectivity.

This anomaly is a 30% increase of the Southern Ocean wind stress. In chapter 4 it was possible to show a connection between the Southern Hemisphere westerly winds, Agulhas leakage and the AMOC in a coupled model at eddying resolution. Previous studies were either limited by coarse resolution, no interactive atmosphere, much shorter length of the experiments, or a combination of those (e.g. Weijer et al., 2002; Knorr & Lohmann, 2003; Webb et al., 2021). All these aspects were suggested to impact the results (e.g. Haarsma et al., 2011; Gent, 2016) and here verified to be of major importance for the adjustment of the Atlantic circulation to forced changes in the southern hemisphere. Different atmospheric adjustment were found to counteract or amplify the development of temperature, salinity and density anomalies. Eddies are especially important for the response of the Southern Ocean circulation to wind stress variability, but also for a more realistic representation of tracer mixing along the volume transport pathways. Furthermore, the results presented here highlight the need for experiments of at least 100 years length, since significant AMOC anomalies only start to develop after 60 years and become significant after 80 years. It is likely that even longer experiments are necessary to capture the full adjustment. Shorter experiments would not capture the impact of advective signal propagation at all.

In chapter 4 it was also possible to follow the pathways of anomalies originating from Agulhas leakage into the Nordic Seas and even back into the deep Subtropical Gyre. Thereby, many details of the propagation of anomalies in the upper limb of the AMOC were revealed. The results suggest that the timescale of connectivity must not match the advective timescale of water volumes. This is because volume transport pathways do not represent tracer pathways, as discussed in chapter 2 and van Sebille et al. (2018). The difference between volume and tracer pathways is especially important, if mixing counteracts anomalies spreading by volume advection. In chapter 4 it was shown that mixing of the anomalously warm and saline leakage water with anomalously fresh and cold water in the upper tropical Atlantic, caused by a southward shifting ITCZ, leads to pronounced difference in the development of tracer anomalies from expectations based on pure volume transport

pathways (see also Rühs et al., 2013, 2019; van Sebille et al., 2011).
Furthermore, chapter 4 provides evidence for an important impact of interhemispheric connectivity on the AMOC on climate (multi-decadal to centennial) and possibly even longer timescale. This is highly relevant for the interpretation of paleo climate records, in particular for the recovery of the AMOC from off to cold and warm states (likely linked to the Bipolar Climate/Ocean Seasaw BCS/BOS patterns) and possible evolution of the AMOC until the end of the century under rising greenhouse gas concentrations. The interhemispheric propagation of anomalies is related to the first part of the salt-advection feedback, but no direct evidence for the existence of this feedback. To prove its existence, it is necessary to show that the increase in AMOC transport further increases the import of salt via the southern boundary, which is not investigated here. Based on the results of chapter 4 and an increase of Agulhas leakage by roughly 3 Sv between the mid 1960s and 1980s (Rühs et al., 2022), one may expect an imprint of this change on the AMOC approximately by the mid of this century (overlaid by a long-term negative trend caused by rising greenhouse gas concentrations and decadal variability caused by the NAO). It is further interesting to note, that although the AMOC change here is initially forced by the Southern Ocean wind stress, the AMOC increase originates from increased water mass transformation and sinking in the North Atlantic. This must be considered when attributing AMOC changes to specific regions and yet again highlights the significance to understand connectivity.

The experiments also reveal a possible mechanism that connects the upper and deep AMOC limbs. The results suggest that increased water mass transformation associated with the AMOC strengthening takes place in the Rockall Through region, parts of the Iceland Basin and southern Nordic Seas. From here anomalously dense water circulates cyclonically around the Nordic Seas and returns as more dense overflow. This more dense overflow increases downward vertical velocities along the SPG boundary after crossing the overflow sills. This can explain how the AMOC in density and depth coordinates are linked. These results are consistent with results obtained by Desbruyères et al. (2019), Lozier et al. (2019) (both show that water mass transformation mostly takes place in the eastern SPG) and Katsman et al. (2018) (sinking occurs along the boundary of the SPG), but provide an additional link between the studies.

The results of chapter 4 are consistent with chapter 5. Although transport variability itself does not result in coherent AMOC changes on interannual timescales, the DWBC is the main conduit of deep water in the subtropical North Atlantic. It is visible in chapter 4 that anomalies at mid-depth first develop in the subpolar North Atlantic and then spread south via interior pathways north of 30°N, but solely along the western boundary south of 30°N. Furthermore, the net transport associated with the deep AMOC branch on decadal and longer timescales seems to be set by an imbalance between changes in the DWBC and the northward recirculation. This imbalance is much smaller than the DWBC transport anomaly itself. As the AMOC increases in the ensemble experiment conducted in chapter 4 after 60 years, so does the DWBC. The northward recirculation also increases, but not strong enough to fully compensate the DWBC transport, leaving a residual that corresponds to the AMOC increase. As a consequence, it not possible to derive a quantitative estimate of AMOC variability from measuring the DWBC alone, even on longer timescales. Considering the results of chapter 4 and chapter 5 together, it is likely that the volume transport changes in the DWBC related to a stronger AMOC on (multi-)decadal timescales are more coherent across the subtropical North Atlantic. Hence, connectivity through advection could be more important on decadal timescales than it is on interannual timescales. Especially, because in chapter 5 it was mentioned that variability introduced by eddies and meanders mostly affects interannual timescales, while lower frequency variability is less altered along the pathway between remote sections.

The sensitivity of the AMOC to Southern Ocean wind stress changes found in chapter 4 supports the conclusion of chapter 3, that applying an anomaly forcing in partially coupled experiments, keeping the wind stress climatology of the coupled model, is the more advantageous choice. Especially, if the mean wind stress in the coupled model and reanalysis differ as strongly as over the Southern

Ocean in FOCI. The experiments presented in chapter 3 show a clear mismatch in the Southern Ocean wind stress between the JRA55-do forcing dataset and FOCI(-ATLAS10). The partially coupled experiment with lower wind stress (PCPL-L) does not show a particularly strong AMOC decline. But the experiment is shorter than 60 years and therefore shorter than the AMOC's response time to Southern Ocean wind stress changes seen in chapter 4. In an additional partially coupled experiment (PCPL-ERA) that is not shown here, wind stress anomalies were derived from the ERA20C reanalysis (Poli et al., 2016) covering the years 1900 to 2011, using the methodology of the PCPL-L experiment (see chapter 3). This experiment revealed a strong decline of the AMOC approximately 70-80 years after switching to partial coupling mode. Although the cause of this decline was not investigated in this experiment, it matches the results of chapter 4 and suggests that the decline was caused by a reduction in Southern Ocean wind stress.

Additionally, it was shown in chapter 4 that atmospheric circulation changes, in response to changes of the Southern Ocean wind stress and Agulhas leakage, throughout the entire Atlantic are important for the generation of strong anomalies. At least the wind stress related adjustments (in particular Ekman transport/pumping changes that are mentioned in chapter 4) are overwritten in partially coupled experiments, as PCPL-ERA. Therefore, the AMOC slow-down in PCPL-ERA supports the hypothesis that there is more than one mechanism responsible for the AMOC response seen in chapter 4. In addition to a southward shift of the northern hemisphere westerlies, this could be the advection of anomalies along the eastern boundary and/or an anomalous volume transport in the GS/NAC that compensates changes in the geostrophic upper mid-ocean transport. An important contribution from changes in GS/NAC via changes in the transport is further supported by the result obtained in chapter 3. A local reduction in the northern hemisphere wind stress (in the PCPL-L experiment) did not strongly affect the AMOC strength within 50 years. It can be hypothesised that the prescribed weakening of the northern hemisphere westerlies, which drives anomalous northward Ekman transport of warm and saline water into the SPG, could be balanced by a reduction in the NA STG transport caused by the same prescribed weaker wind stress. This would provide a consistent explanation for the weak AMOC response to lower North Atlantic wind stress in PCPL-L (chapter 3) and the results obtained in chapter 4. Note that in chapter 4, the northern hemisphere westerly winds are not strongly weakened, but mostly shifted south, while in PCPL-L the mean position of the westerlies is prescribed by the FOCI climatology and only their strength decreases. While both is connected to anomalous northward Ekman transport into the SPG, the former/latter is related to stronger/reduced wind stress curl over the central NA STG (see chapter 4/3). It is possible that very specific wind stress patterns can affect the AMOC in the subpolar North Atlantic on longer than sub-decadal timescales. But the limited success of partial coupling to reproduce variability on these timescales in subpolar latitudes shows that such wind patterns did not dominate variability over the recent decades.

7.2 Summary of the Main Results

In the following, the most important results with regard to the main scientific questions of this thesis are summarised:

Question 1 (Model development and sources of AMOC variability, chapter 3):

Is it possible to improve the representation of past AMOC variability in models by assimilating observed wind stress anomalies in coupled models at eddying resolution?
On which spatial and temporal scales does wind-variability contribute to AMOC variability?

- The coupled, nested FOCI-ATLAS10 configuration is able to simulate a realistic strength and structure of the AMOC and horizontal gyre circulation. With regional exceptions, the pattern of mesoscale activity is in agreement with satellite observations.
- Partially coupled experiments are able to maintain necessary ocean-atmosphere feedbacks to simulate a stable AMOC without an application of sea surface salinity restoring.

- A secondary spin-up, after switching to partial coupling mode, can be avoided by maintaining the coupled models wind stress climatology (applying an anomaly forcing).
- The magnitude of variability in the partially coupled experiments is comparable to fully coupled and forced experiments.
- A significant correlation between AMOC anomalies in forced and partially coupled models can be expected on timescales shorter than 5-years.
- Wind forcing can explain a large fraction of pentadal, interannual and sub-annual AMOC variability throughout the entire Atlantic.
- Decadal variability of the wind stress curl affects decadal AMOC variability through changes in the Sverdrup transport, but is probably masked by stronger buoyancy driven variability in most cases.
- The assimilation of wind stress anomalies does not significantly feed back onto the North Atlantic buoyancy fluxes, which limits the applicability of partial coupling on decadal (and longer) timescales.
- Partial coupling provides a useful set-up to study interannual (AMOC) variability, but modifications to the partial coupling procedure are needed to improve the representation of past AMOC variability on decadal and longer timescales.

Question 2 (Interhemispheric connectivity, chapter 4):

How do temperature, salinity and density anomalies forced by an increased Southern Ocean wind stress propagate into the North Atlantic in an eddying, coupled model and what is their impact on the AMOC?

- In the coupled, eddying model configuration FOCI-ATLAS10, a 30% increase of the Southern Ocean wind stress maximum causes a fast and sustained Agulhas leakage increase by 3.8 Sv (35%) and an AMOC increase by 1.2 Sv (7%) after 80 years.
- Heat flux damping and a southward shifting ITCZ strongly reduce and delay the development of near-surface anomalies.
- Below 500 m depth, anomalously saline and warm water reaches the subtropical North Atlantic across the entire width of the basin.
- Anomalies developing in the Gulf Stream are small (and mostly not attributed to the advection of anomalies from the South Atlantic). A continuous pathway for temperature and salinity anomalies along the western boundary into the SPG does not seem to exist.
- There are three hypotheses for the propagation of anomalies into the SPG, namely mean advection of anomalous temperature and salinity along the mid-depth eastern boundary, anomalous advection of mean temperature and salinity in the GS/NAC and a southward shift of the northern hemisphere westerlies. Possibly, all contribute to temperature, salinity and density anomalies in the SPG. After anomalies have developed initially, they may be reinforced by a response of the AMOC.
- While salinity anomalies can enter the Nordic Seas, anomalous heat flux damping in the eastern SPG prevents temperature anomalies further north, causing an increase in density. This anomalously dense water returns as more dense overflow into the SPG.
- Consistent with the aforementioned result, increased water mass transformation is found north of OSNAP-East, not OSNAP-West.

- Enhanced sinking is found south of the overflow sills and along the boundary of the SPG, outside the SPG deep convection regions. The increase in overflow density is hypothesised to establish a link between the AMOC in density and depth coordinates.

Question 3 (Physical connectivity on regional scales, chapter 5):

What is the impact of mesoscale variability and advection in the DWBC on the coherence of AMOC variability in the subtropical North Atlantic?

- The Deep Western Boundary Current transports on average 34 Sv at 26.5°N. 58% (20 Sv) of this transport reaches the MOVE section at 16°N with an advective timescales of 1.1 years (median of the transit time distribution). Most of the remaining transport recirculates across 26.5°N (RAPID section).
- The recirculation is fed by water that is detrained from the DWBC in the Abaco Gyre (north of San Salvador) and eddy-driven recirculations adjacent to the western boundary between 24°N and 20°N. The strength of the recirculation is highly correlated with the DWBC transport.
- The recirculation across 16°N (MOVE section) is less strongly correlated to the local DWBC transport, which points to an important difference in the mechanisms that generate circulation variability at the MOVE and RAPID sections.
- Eddies and meanders form along the western boundary with an important contribution from barotropic energy transfer. Especially rough bathymetric features, such as the island of San Salvador, or the shallow plateau surrounding the Virgin Islands, seem important for the generation of eddies and large meanders.
- The non-uniform velocity structure of the DWBC itself and eddy-driven recirculations introduce a variety of different pathways, broadening the transit time distribution and extending the advective timescale.
- The pathways taken by water volumes depend on the release timestep and thus, the transit time distribution is not constant in time, which strongly decorrelates DWBC transport anomalies at 26.5°N and 16°N. This mechanism was found to affect interannual transport variations, but suggested to have a smaller impact on decadal variability.
- As a consequence of variable recirculations across 26.5°N, 16°N and along the entire western boundary in between, the DWBC transport at the MOVE and RAPID sections is not correlated (at any lag) on interannual timescales and does not contribute to coherent interannual AMOC variability.

Question 4 (Biophysical connectivity on regional scales, chapter 6):

What is the role of the DWBC and mesoscale eddies in connecting deep ecosystems along the Northwest Atlantic continental slope?

- Important pathways of the AMOC and their interaction with eddies can have large impacts on biophysical connectivity, as shown for ecosystems along the Northwest Atlantic continental slope. This is true for the shallow, but also the for the deep AMOC branch.
- The interaction of eddies with the bathymetry strongly influences the dispersal of larvae from the RMS Titanic wreck, providing a westward pathway into deep Canadian waters and a southward pathway into areas beyond national jurisdiction.
- Variability of the ocean circulation due to eddies outweighs the effect of active larval behaviour (at least with the assumptions made about the largely unknown swimming capabilities) and spawning season.
- The DWBC and Labrador Current provide fast pathways for larvae spawned on the continental slope east of the Grand Banks to other natural occurrences offshore Nova Scotia.

- Larvae can potentially reach the Titanic wreck after they are deflected from the western boundary in an interaction of eddies with the DWBC (and Labrador Current).
- Because of largely unknown larval characteristics, a variety of scenarios for ecosystem connectivity in the northwest Atlantic exist, but all point to the Titanic as a possible stepping stone connecting remote ecosystems.
- Eddies can significantly enhance the mean flow temporarily, or cause a reversal of the flow. This does not only apply to the Titanic wreck site, but various other locations as well. Therefore, connectivity studies in most regions need to utilise high-resolution models and sufficient temporal resolution. Otherwise, important pathways may be missed.

7.3 Outlook: Future Model Development and Analysis

The results and model developments presented in this thesis will be of future benefit for many other studies. Partial coupling is currently used in different projects at GEOMAR, across different research groups. An outlook to possible future projects building on this thesis are outlined in the following.

Increasing Oceanic and Atmospheric Resolution

It is well known that 1/10° resolution is not sufficient to simulate the entire mesoscale spectrum in subpolar latitudes (e.g. Hallberg, 2013; Martin & Biastoch, 2022). Thus FOCI-ATLAS10 is a significant improvement for basin-scale studies over other configurations available in FOCI, but its performance is still not comparable to the VIKING20X model configuration (only available in a forced set-up) used in this thesis. Although the results on partial coupling (chapter 3) are not expected to be strongly influenced by increasing the horizontal resolution, sensitivity experiments (chapter 4) could benefit from a more realistic distribution of temperature and salinity anomalies across the SPG in a 1/20° model. Therefore, future projects may aim to include a higher resolution ocean (for example a 0.25° global grid with a 1/20° 'ATLAS20' nest). However, increasing the ocean resolution, does increase the resolution gap between the atmosphere and ocean even further. One would need to strongly consider increasing the atmospheric resolution as well. In chapter 3 it was mentioned that the coarse atmospheric resolution of FOCI-ATLAS10 causes the Agulhas rings path to be unrealistically regular. Many other processes were shown to be better represented in coupled models with high resolution atmospheres, leading to an overall improved agreement between the coupled model and observations (Sakamoto et al., 2012; Tsartsali et al., 2022). Such a new configuration could strongly benefit from the experience gained with FOCI-ATLAS10, such that FOCI-ATLAS10 may be regarded as a first step towards an eddy-rich, coupled configuration of the whole Atlantic. Still, increasing oceanic and atmospheric resolution together results in a significant increase in computational resources needed. Thus, FOCI-ATLAS10 will also have a future role, whenever experiments need to cover timescales longer than a century, or several ensemble members are needed.

Modifications to the Partial Coupling Procedure

In the last section of chapter 3 the question was raised, whether partial coupling may be modified to improve the timing of decadal AMOC variability in the subpolar North Atlantic. Apparently feedbacks to the Pacific Ocean and a cumulative effect of the correctly timed interannual variability, are not sufficient to significantly improve the timing of decadal North Atlantic heat flux and AMOC variability. This supports the hypothesis that these heat fluxes are strongly tied to the North Atlantic Oscillation (e.g. Eden & Jung, 2001a; Megann et al., 2021). Therefore, any other modification to the surface momentum flux (i.e. the procedure of assimilating wind stress anomalies) does not seem promising. A first possible modification that affects the surface heat and freshwater fluxes is to replace the models own wind in the calculation of the surface heat and freshwater fluxes. In this case, the heat and freshwater flux would depend on the atmosphere models' 10 m

air temperature and humidity, but the reanalysis based wind speed. Such a procedure could be successful, for example, in the Irminger Sea, where the Greenland Tip Jets' strong velocity anomalies were shown to drive a strong heat loss (Doyle & Shapiro, 1999). Note that this is a rather small scale feature and would require to provide the reanalysed wind stress on a grid with sufficient horizontal resolution. In other regions, the mismatch between reanalysed wind speed and the atmosphere models' temperature and humidity is likely reducing the success of this method. As an example, the Labrador Sea may be considered. It was shown that deep convection is triggered under NAO+ conditions, when strong, cold winds blow over Canada and the ice-edge towards the central Labrador Sea (Marshall & Schott, 1999; Våge et al., 2009). Using the reanalysed wind speed to calculate turbulent heat and freshwater fluxes is probably not sufficient to reproduce the timing of deep convection variability. Processes, such as cold air advection, are not covered by this method. It is even more undesirable that a particularly strong wind stress in the reanalysis could coincide with an anomalously warm atmosphere in the model, which could counteract the effect of an increasing wind speed.

Processes, such as cold air advection, might be reproduced by assimilating the heat fluxes, or alternatively ocean-atmosphere temperature differences, themselves. A proposed method is to replace the wind in the atmosphere component, instead of the ocean component. Such a procedure was used by Roach et al. (2022), nudging the wind above the surface boundary layer to reanalysed winds. This does not only affected the momentum, but also the heat and freshwater fluxes. However, they note that nudging wind at latitudes south of 45°N leads to unrealistic model drift. A possible explanation for this result could be that, depending on the strength of the nudging, the strength of feedbacks that rely on an adjustment of the atmospheric circulation is reduced. Completely overwriting the wind instead of nudging would completely suppress these feedbacks. Another approach is to restore sea surface temperature and salinity to fields from a forced experiment (or reanalysis/observations), but leaving the wind free to adjust. This was shown to improve the timing of decadal AMOC variability (Zhang et al., 2022). However, combining this approach with the partial coupling procedure applied in this thesis would mean that wind stress is prescribed, while heat and freshwater fluxes are restored in the ocean component. Thus the coupling is mostly (depending on the strength of the restoring) overwritten, and the resulting experiment is comparable to a forced simulation. Most ocean-atmosphere feedbacks would be suppressed, but maintaining these feedbacks was the initial motivation to implement partial coupling.

A possible solution could be to modify the heat flux provided to the ocean on specific (e.g. decadal) timescales only, by applying a formulation based on the mean semi-prognostic method (Richard Greatbatch, pers. communication) described in Eden et al. (2004). It was mainly the heat flux that was found to generate decadal AMOC variability (e.g. Megann et al., 2021). It is likely that such an adjustment of the procedure would make partial coupling more successful in reproducing AMOC variability on decadal timescales. The major question is whether such a set-up can also maintain AMOC stability. This remains to be tested.

Additional Analysis on Connectivity and AMOC Variability

Although the described sensitivity experiments already yield important results on interhemispheric connectivity, they have the potential to be further exploited with very different motivations. Several regional details of the development of anomalies can be studied in more detail. In particular, this includes the relative importance of mean advection of anomalies, anomalous advection of mean temperature and salinity and atmospheric adjustments to generate strong anomalies in the SPG.

The AMOC response can be compared to changes in individual current systems similar to the approach of Biastoch et al. (2021). For the RAPID section at 26.5°N, this is already shown in chapter 4, but a similar analysis could be carried out for other sections as well. This may provide valuable information for AMOC monitoring arrays. In this context, it would also be highly interesting to extend the analysis in chapter 5 from interannual to decadal variability. Hints that variability of the DWBC is more coherent on decadal (and longer) timescales were already provided in chapters 4 and 5, but longer Lagrangian experiments would be needed to directly assess

the impact of the volume transport. Such experiments could provide evidence that indeed, long term variability of the AMOC is coherent due to the advective propagation of anomalies, which corresponds to the traditional description of the AMOC (see for example Lozier, 2010). Furthermore, it was visible that the anomalies at the end of the experiments have reached the tropical Atlantic in the DWBC. It is not likely that the oceanic state after 120 years reflects the full adjustment to the applied Southern Ocean wind stress changes. Therefore, extending the experiments could allow to assess the deep AMOC pathways in more detail, complementing the description of the shallow AMOC branch provided here. It could shed light on the mechanisms and locations that cause NADW to upwell in the South Atlantic and Southern Ocean to complete a full cycle. As mentioned before, it would be interesting to investigate whether the stronger AMOC does further increase salt import via Agulhas leakage, or the Drake Passage cold water route. Hence, whether the salt-advection feedback is present in FOCI-ATLAS10. The question remains, if the reappearance of anomalies in the South Atlantic feeds back on the southern hemisphere ocean and atmosphere circulation. In the experiments of chapter 4 there are already strong (locally forced) anomalies present in the South Atlantic and Southern Ocean. Additionally, the applied wind stress anomaly can not be switched off without introducing a variety of rapid changes. Therefore, a complementing experiment that forces changes initially in the North Atlantic would help to address this question.

At last, the study of larval dispersal from the RMS Titanic may benefit from a revision of the experiments in submesoscale resolving models. As mentioned before, Bower et al. (2013) found submesoscale eddies to spin-off at the Tail of the Grand Banks and although similar eddies exist in VIKING20X, they tend to be larger in the model than observed. Nevertheless, it is not very likely that a difference in eddy size has a major impact on the results. Therefore, the study would mainly benefit from advances in biology, not physics or modelling. Refined knowledge of the larval characteristics would allow to narrow down the possible connectivity scenarios. At the same time, the interaction between small scale bathymetry, currents and eddies is applicable to various other ocean regions. Although the idea of studying the impact of short-term, mesoscale, variability on marine organisms is not completely new (e.g. Adams et al., 2011; Steinle et al., 2015), the results obtained here may provide further motivation to apply similar analysis techniques for various other marine species and thereby contribute to a better understanding of ecosystem connectivity.

In conclusion, future model development and analysis building on this thesis can provide even deeper insights into connectivity and answers to fundamental questions about the Atlantic Ocean circulation.

References

Abernathey, R., Marshall, J. & Ferreira, D. (2011). The Dependence of Southern Ocean Meridional Overturning on Wind Stress. *Journal of Physical Oceanography*, *41*(12), 2261–2278. doi: 10.1175/JPO-D-11-023.1

Adams, D. K., McGillicuddy, D. J., Zamudio, L., Thurnherr, A. M., Liang, X., Rouxel, O., German, C. R. & Mullineaux, L. S. (2011). Surface-Generated Mesoscale Eddies Transport Deep-Sea Products from Hydrothermal Vents. *Science*, *332*(6029), 580–583. doi: 10.1126/science.1201066

Alheit, J., Gröger, J., Licandro, P., McQuinn, I. H., Pohlmann, T. & Tsikliras, A. C. (2019). What happened in the mid-1990s? The coupled ocean-atmosphere processes behind climate-induced ecosystem changes in the Northeast Atlantic and the Mediterranean. *Deep Sea Research Part II: Topical Studies in Oceanography*, *159*, 130–142. doi: 10.1016/j.dsr2.2018.11.011

Amante, C. & Eakins, B. (2009). ETOPO1 1 Arc-Minute Global Relief Model: Procedures. *NOAA Technical Memorandum NESDIS*, *NGDC-24*. doi: 10.7289/V5C8276M

Ansorge, I. J., Speich, S., Lutjeharms, J. R. E., Goni, G. J., Rautenbach, C. J. d. W., Froneman, P. W., Rouault, M. & Garzoli, S. L. (2005). Monitoring the oceanic flow between Africa and Antarctica: Report of the first GoodHope cruise. *South African Journal Of Science*, *101*, 29 – 35.

Arakawa, A. & Hsu, Y.-J. G. (1990). Energy Conserving and Potential-Enstrophy Dissipating Schemes for the Shallow Water Equations. *Monthly Weather Review*, *118*(10), 1960–1969. doi: 10.1175/1520-0493(1990)118<1960:ECAPED>2.0.CO;2

Arblaster, J. M. & Meehl, G. A. (2006). Contributions of External Forcings to Southern Annular Mode Trends. *Journal of Climate*, *19*(12), 2896–2905. doi: 10.1175/JCLI3774.1

Barnier, B., Madec, G., Penduff, T., Molines, J.-M., Treguier, A.-M., Le Sommer, J., Beckmann, A., Biastoch, A., Böning, C., Dengg, J., Derval, C., Durand, E., Gulev, S., Remy, E., Talandier, C., Theetten, S., Maltrud, M., McClean, J. & Cuevas, B. (2006). Impact of partial steps and momentum advection schemes in a global ocean circulation model at eddy-permitting resolution. *Ocean Dynamics*, *56*(5), 543–567. doi: 10.1007/s10236-006-0082-1

Beal, L. M., De Ruijter, W. P. M., Biastoch, A., Zahn, R., Cronin, M., Hermes, J., Lutjeharms, J., Quartly, G., Tozuka, T., Baker-Yeboah, S., Bornman, T., Cipollini, P., Dijkstra, H., Hall, I., Park, W., Peeters, F., Penven, P., Ridderinkhof, H., Zinke, J. & SCOR/WCRP/IAPSO Working Group 136. (2011). On the role of the Agulhas system in ocean circulation and climate. *Nature*, *472*(7344), 429–436. doi: 10.1038/nature09983

Behrens, E., Biastoch, A. & Böning, C. W. (2013). Spurious AMOC trends in global ocean sea-ice models related to subarctic freshwater forcing. *Ocean Modelling*, *69*, 39–49. doi: 10.1016/j.ocemod.2013.05.004

Berglund, S., Döös, K. & Nycander, J. (2017). Lagrangian tracing of the water–mass transformations in the Atlantic Ocean. *Tellus A*, *69*(1), 1306311. doi: 10.1080/16000870.2017.1306311

Biastoch, A., Böning, C. W., Getzlaff, J., Molines, J.-M. & Madec, G. (2008a). Causes of Interannual–Decadal Variability in the Meridional Overturning Circulation of the Midlatitude North Atlantic Ocean. *Journal of Climate*, *21*(24), 6599–6615. doi: 10.1175/2008JCLI2404.1

Biastoch, A., Böning, C. W. & Lutjeharms, J. R. E. (2008b). Agulhas leakage dynamics affects

decadal variability in Atlantic overturning circulation. *Nature*, *456*(7221), 489–492. doi: 10.1038/nature07426

Biastoch, A., Durgadoo, J. V., Morrison, A. K., van Sebille, E., Weijer, W. & Griffies, S. M. (2015). Atlantic multi-decadal oscillation covaries with Agulhas leakage. *Nature Communications*, *6*(1), 10082. doi: 10.1038/ncomms10082

Biastoch, A. & Krauss, W. (1999). The Role of Mesoscale Eddies in the Source Regions of the Agulhas Current. *Journal of Physical Oceanography*, *29*(9), 2303–2317. doi: 10.1175/1520-0485(1999)029<2303:TROMEI>2.0.CO;2

Biastoch, A., Schwarzkopf, F. U., Getzlaff, K., Rühs, S., Martin, T., Scheinert, M., Schulzki, T., Handmann, P., Hummels, R. & Böning, C. W. (2021). Regional imprints of changes in the Atlantic Meridional Overturning Circulation in the eddy-rich ocean model VIKING20X. *Ocean Science*, *17*(5), 1177–1211. doi: 10.5194/os-17-1177-2021

Biló, T. C. & Johns, W. E. (2019). Interior Pathways of Labrador Sea Water in the North Atlantic From the Argo Perspective. *Geophysical Research Letters*, *46*(6), 3340– 3348. doi: 10.1029/2018GL081439

Biló, T. C. & Johns, W. E. (2020). The Deep Western Boundary Current and Adjacent Interior Circulation at 24°–30°N: Mean Structure and Mesoscale Variability. *Journal of Physical Oceanography*, *50*(9), 2735–2758. doi: 10.1175/JPO-D-20-0094.1

Bingham, R. J., Hughes, C. W., Roussenov, V. & Williams, R. G. (2007). Meridional coherence of the North Atlantic meridional overturning circulation. *Geophysical Research Letters*, *34*(23), L23606. doi: 10.1029/2007GL031731

Bishop, S. P., Gent, P. R., Bryan, F. O., Thompson, A. F., Long, M. C. & Abernathey, R. (2016). Southern Ocean Overturning Compensation in an Eddy-Resolving Climate Simulation. *Journal of Physical Oceanography*, *46*(5), 1575–1592. doi: 10.1175/JPO-D-15-0177.1

Blaker, A. T., Hirschi, J. J.-M., Bell, M. J. & Bokota, A. (2021). Wind-Driven Oscillations in the Meridional Overturning Circulation near the equator. Part I: Numerical Models. *Journal of Physical Oceanography*, *51*(3), 645–661. doi: 10.1175/JPO-D-19-0296.1

Blanke, B., Arhan, M., Madec, G. & Roche, S. (1999). Warm Water Paths in the Equatorial Atlantic as Diagnosed with a General Circulation Model. *Journal of Physical Oceanography*, *29*(11), 2753–2768. doi: 10.1175/1520-0485(1999)029<2753:WWPITE>2.0.CO;2

Blanke, B. & Raynaud, S. (1997). Kinematics of the Pacific Equatorial Undercurrent: An Eulerian and Lagrangian Approach from GCM Results. *Journal of Physical Oceanography*, *27*(6), 1038–1053. doi: 10.1175/1520-0485(1997)027<1038:KOTPEU>2.0.CO;2

Blunier, T. & Brook, E. J. (2001). Timing of Millennial-Scale Climate Change in Antarctica and Greenland During the Last Glacial Period. *Science*, *291*(5501), 109–112. doi: 10.1126/science.291.5501.109

Boers, N. (2021). Observation-based early-warning signals for a collapse of the Atlantic Meridional Overturning Circulation. *Nature Climate Change*, *11*, 680–688. doi: 10.1038/s41558-021-01097-4

Bower, A. S., Hendry, R. M., Amrhein, D. E. & Lilly, M., Jonathan. (2013). Direct observations of formation and propagation of subpolar eddies into the Subtropical North Atlantic. *Deep Sea Research Part II: Topical Studies in Oceanography*, *85*, 15–41. doi: 10.1016/j.dsr2.2012.07.029

Bower, A. S., Lozier, M. S., Gary, S. F. & Böning, C. W. (2009). Interior pathways of the North Atlantic meridional overturning circulation. *Nature*, *459*(7244), 243–247. doi: 10.1038/nature07979

Bower, A. S., Lozier, S., Biastoch, A., Drouin, K., Foukal, N., Furey, H., Lankhorst, M., Rühs, S. & Zou, S. (2019). Lagrangian Views of the Pathways of the Atlantic Meridional Overturning Circulation. *Journal of Geophysical Research: Oceans*, *124*(8), 5313–5335. doi: 10.1029/2019JC015014

Brennecke, W. (1921). Die ozeanographischen arbeiten der deutschen antarktischen expedition 1911-1912. *Aus dem Archiv der Deutschen Seewarte*, *39*(1), 216.

Breusing, C., Biastoch, A., Drews, A., Metaxas, A., Jollivet, D., Vrijenhoek, R. C., Bayer, T., Melzner, F., Sayavedra, L., Petersen, J. M., Dubilier, N., Schilhabel, M. B., Rosenstiel, P. & Reusch, T. B. (2016). Biophysical and Population Genetic Models Predict the Presence

of “Phantom” Stepping Stones Connecting Mid-Atlantic Ridge Vent Ecosystems. *Current Biology*, *26*(17), 2257–2267. doi: 10.1016/j.cub.2016.06.062

Bright, D. A., Williams, R. M. L. & McLare, A. S. (2005). Comparative photometric analysis of structural degradation on the bow of RMS Titanic. In *Proceedings of OCEANS 2005 MTS/IEEE* (pp. 106–110 Vol. 1). doi: 10.1109/OCEANS.2005.1639746

Broecker, W. S. (1987). The biggest chill. *Natural History Magazine*, *97*, 74–82.

Broecker, W. S. (1991). The great ocean conveyor. *Oceanography*, *4*(2), 79–89. doi: 10.5670/oceanog.1991.07

Brovkin, V., Raddatz, T., Reick, C. H., Claussen, M. & Gayler, V. (2009). Global biogeophysical interactions between forest and climate. *Geophysical Research Letters*, *36*(7), L07405. doi: 10.1029/2009GL037543

Brown, O. B., Cornillon, P. C., Emmerson, S. R. & Carle, H. (1986). Gulf Stream warm rings: a statistical study of their behavior. *Deep Sea Research Part A. Oceanographic Research Papers*, *33*(11), 1459–1473. doi: 10.1016/0198-0149(86)90062-2

Bryden, H. L., Johns, W. E. & Saunders, P. M. (2005). Deep western boundary current east of Abaco: Mean structure and transport. *Journal of Marine Research*, *63*(1), 35–57. doi: 10.1357/0022240053693806

Buckley, M. W. & Marshall, J. (2016). Observations, inferences, and mechanisms of the Atlantic Meridional Overturning Circulation: A review. *Reviews of Geophysics*, *54*(1), 5–63. doi: 10.1002/2015RG000493

Burkholder, K. C. & Lozier, M. S. (2011). Subtropical to subpolar pathways in the North Atlantic: Deductions from Lagrangian trajectories. *Journal of Geophysical Research: Oceans*, *116*(C7), C07017. doi: 10.1029/2010JC006697

Burkholder, K. C. & Lozier, M. S. (2014). Tracing the pathways of the upper limb of the North Atlantic Meridional Overturning Circulation. *Geophysical Research Letters*, *41*(12), 4254–4260. doi: 10.1002/2014GL060226

Böning, C. W., Scheinert, M., Dengg, J., Biastoch, A. & Funk, A. (2006). Decadal variability of subpolar gyre transport and its reverberation in the North Atlantic overturning. *Geophysical Research Letters*, *33*(21), L21S01. doi: 10.1029/2006GL026906

Chafik, L. & Rossby, T. (2019). Volume, Heat, and Freshwater Divergences in the Subpolar North Atlantic Suggest the Nordic Seas as Key to the State of the Meridional Overturning Circulation. *Geophysical Research Letters*, *46*(9), 4799–4808. doi: 10.1029/2019GL082110

Chanut, J., Barnier, B., Large, W., Debreu, L., Penduff, T., Molines, J. M. & Mathiot, P. (2008). Mesoscale Eddies in the Labrador Sea and Their Contribution to Convection and Restratification. *Journal of Physical Oceanography*, *38*(8), 1617–1643. doi: 10.1175/2008JPO3485.1

Chassignet, E. P., Yeager, S. G., Fox-Kemper, B., Bozec, A., Castruccio, F., Danabasoglu, G., Horvat, C., Kim, W. M., Koldunov, N., Li, Y., Lin, P., Liu, H., Sein, D. V., Sidorenko, D., Wang, Q. & Xu, X. (2020). Impact of horizontal resolution on global ocean–sea ice model simulations based on the experimental protocols of the Ocean Model Intercomparison Project phase 2 (OMIP-2). *Geoscientific Model Development*, *13*(9), 4595–4637. doi: 10.5194/gmd-13-4595-2020

Chelton, D. B., Schlax, M. G. & Samelson, R. M. (2011). Global observations of nonlinear mesoscale eddies. *Progress in Oceanography*, *91*(2), 167–216. doi: 10.1016/j.pocean.2011.01.002

Chelton, D. B., Schlax, M. G., Samelson, R. M. & de Szoeke, R. A. (2007). Global observations of large oceanic eddies. *Geophysical Research Letters*, *34*(15), L15606. doi: 10.1029/2007GL030812

Cheng, W., Chiang, J. C. H. & Zhang, D. (2013). Atlantic Meridional Overturning Circulation (AMOC) in CMIP5 Models: RCP and Historical Simulations. *Journal of Climate*, *26*(18), 7187–7197. doi: 10.1175/JCLI-D-12-00496.1

Chylek, P., Folland, C. K., Lesins, G., Dubey, M. K. & Wang, M. (2009). Arctic air temperature change amplification and the Atlantic Multidecadal Oscillation. *Geophysical Research Letters*, *36*(14), L14801. doi: 10.1029/2009GL038777

Cowen, R. K. & Sponaugle, S. (2009). Larval Dispersal and Marine Population Connectivity. *Annual Review of Marine Science*, *1*(1), 443–466. doi: 10.1146/annurev.marine.010908.163757

Crowley, T. J. (1992). North Atlantic Deep Water cools the southern hemisphere. *Paleoceanography*, *7*(4), 489–497. doi: 10.1029/92PA01058

Cunningham, S. A., Kanzow, T., Rayner, D., Baringer, M. O., Johns, W. E., Marotzke, J., Longworth, H. R., Grant, E. M., Hirschi, J. J.-M., Beal, L. M., Meinen, C. S. & Bryden, H. L. (2007). Temporal Variability of the Atlantic Meridional Overturning Circulation at 26.5°N. *Science*, *317*(5840), 935–938. doi: 10.1126/science.1141304

Danabasoglu, G., Yeager, S. G., Bailey, D., Behrens, E., Bentsen, M., Bi, D., Biastoch, A., Böning, C., Bozec, A., Canuto, V. M., Cassou, C., Chassignet, E., Coward, A. C., Danilov, S., Diansky, N., Drange, H., Farneti, R., Fernandez, E., Fogli, P. G., Forget, G., Fujii, Y., Griffies, S. M., Gusev, A., Heimbach, P., Howard, A., Jung, T., Kelley, M., Large, W. G., Leboissetier, A., Lu, J., Madec, G., Marsland, S. J., Masina, S., Navarra, A., George Nurser, A., Pirani, A., y Mélia, D. S., Samuels, B. L., Scheinert, M., Sidorenko, D., Treguier, A.-M., Tsujino, H., Uotila, P., Valcke, S., Voldoire, A. & Wang, Q. (2014). North Atlantic simulations in Coordinated Ocean-ice Reference Experiments phase II (CORE-II). Part I: Mean states. *Ocean Modelling*, *73*, 76–107. doi: 10.1016/j.ocemod.2013.10.005

Daniault, N., Mercier, H., Lherminier, P., Sarafanov, A., Falina, A., Zunino, P., Pérez, F. F., Ríos, A. F., Ferron, B., Huck, T., Thierry, V. & Gladyshev, S. (2016). The northern North Atlantic Ocean mean circulation in the early 21st century. *Progress in Oceanography*, *146*, 142–158. doi: 10.1016/j.pocean.2016.06.007

Day, J. J., Hargreaves, J. C., Annan, J. D. & Abe-Ouchi, A. (2012). Sources of multi-decadal variability in Arctic sea ice extent. *Environmental Research Letters*, *7*(3), 034011. doi: 10.1088/1748-9326/7/3/034011

Debreu, L., Marchesiello, P., Penven, P. & Cambon, G. (2012). Two-way nesting in split-explicit ocean models: Algorithms, implementation and validation. *Ocean Modelling*, *49-50*, 1–21. doi: 10.1016/j.ocemod.2012.03.003

Debreu, L., Vouland, C. & Blayo, E. (2008). AGRIF: Adaptive grid refinement in Fortran. *Computers & Geosciences*, *34*(1), 8–13. doi: 10.1016/j.cageo.2007.01.009

de Jong, M. F., Oltmanns, M., Karstensen, J. & de Steur, L. (2018). Deep Convection in the Irminger Sea Observed with a Dense Mooring Array. *Oceanography*, *31*(1), 50–59. doi: 10.5670/oceanog.2018.109

Delandmeter, P. & van Sebille, E. (2019). The Parcels v2.0 Lagrangian framework: new field interpolation schemes. *Geoscientific Model Development*, *12*(8), 3571–3584. doi: 10.5194/gmd-12-3571-2019

Delworth, T. L. & Zeng, F. (2008). Simulated impact of altered Southern Hemisphere winds on the Atlantic Meridional Overturning Circulation. *Geophysical Research Letters*, *35*(20), L20708. doi: 10.1029/2008GL035166

Dengler, M., Schott, F. A., Eden, C., Brandt, P., Fischer, J. & Zantopp, R. J. (2004). Break-up of the Atlantic deep western boundary current into eddies at 8° S. *Nature*, *432*(7020), 1018–1020. doi: 10.1038/nature03134

Desbruyères, D. G., Mercier, H., Maze, G. & Daniault, N. (2019). Surface predictor of overturning circulation and heat content change in the subpolar North Atlantic. *Ocean Science*, *15*(3), 809–817. doi: 10.5194/os-15-809-2019

Dewar, W. K., Parfitt, R. & Wienders, N. (2022). Routine Reversal of the AMOC in an Ocean Model Ensemble. *Geophysical Research Letters*, *49*(24), e2022GL100117. doi: 10.1029/2022GL100117

Dickson, R. R. & Brown, J. (1994). The production of North Atlantic Deep Water: Sources, rates, and pathways. *Journal of Geophysical Research: Oceans*, *99*(C6), 12319–12341. doi: 10.1029/94JC00530

Dickson, R. R., Lazier, J., Meincke, J., Rhines, P. & Swift, J. (1996). Long-term coordinated changes in the convective activity of the North Atlantic. *Progress in Oceanography*, *38*(3), 241–295. doi: 10.1016/S0079-6611(97)00002-5

Dietz, S., Rising, J., Stoerk, T. & Wagner, G. (2021). Economic impacts of tipping points in the climate system. *Proceedings of the National Academy of Sciences*, *118*(34), e2103081118. doi: 10.1073/pnas.2103081118

Ding, H., Greatbatch, R. J., Latif, M., Park, W. & Gerdes, R. (2013). Hindcast of the 1976/77 and 1998/99 Climate Shifts in the Pacific. *Journal of Climate*, *26*(19), 7650–7661. doi: 10.1175/JCLI-D-12-00626.1

Doyle, J. D. & Shapiro, M. A. (1999). Flow response to large-scale topography:the Greenland tip jet. *Tellus A*, *51*(5), 728–748. doi: 10.1034/j.1600-0870.1996.00014.x

Drews, A. & Greatbatch, R. J. (2017). Evolution of the Atlantic Multidecadal Variability in a Model with an Improved North Atlantic Current. *Journal of Climate*, *30*(14), 5491–5512. doi: 10.1175/JCLI-D-16-0790.1

Duchez, A., Hirschi, J. J.-M., Cunningham, S. A., Blaker, A. T., Bryden, H. L., de Cuevas, B., Atkinson, C. P., McCarthy, G. D., Frajka-Williams, E., Rayner, D., Smeed, D. & Mizielinski, M. S. (2014). A New Index for the Atlantic Meridional Overturning Circulation at 26°N. *Journal of Climate*, *27*(17), 6439–6455. doi: 10.1175/JCLI-D-13-00052.1

Durgadoo, J. V., Loveday, B. R., Reason, C. J. C., Penven, P. & Biastoch, A. (2013). Agulhas Leakage Predominantly Responds to the Southern Hemisphere Westerlies. *Journal of Physical Oceanography*, *43*(10), 2113–2131. doi: 10.1175/JPO-D-13-047.1

Eady, E. T. (1949). Long Waves and Cyclone Waves. *Tellus*, *1*(3), 33–52. doi: 10.1111/j.2153-3490.1949.tb01265.x

Eden, C., Greatbatch, R. J. & Böning, C. W. (2004). Adiabatically Correcting an Eddy-Permitting Model Using Large-Scale Hydrographic Data: Application to the Gulf Stream and the North Atlantic Current. *Journal of Physical Oceanography*, *34*(4), 701–719. doi: 10.1175/1520-0485(2004)034<0701:ACAEMU>2.0.CO;2

Eden, C. & Jung, T. (2001a). North Atlantic Interdecadal Variability: Oceanic Response to the North Atlantic Oscillation (1865–1997). *Journal of Climate*, *14*(5), 676–691. doi: 10.1175/1520-0442(2001)014<0676:NAIVOR>2.0.CO;2

Eden, C. & Willebrand, J. (2001b). Mechanism of Interannual to Decadal Variability of the North Atlantic Circulation. *Journal of Climate*, *14*(10), 2266–2280. doi: 10.1175/1520-0442(2001)014<2266:MOITDV>2.0.CO;2

Ekman, V. W. (1905). On the influence of earth's rotation on ocean currents. *Arch. Math. Astron. Phys.*, *2*(11).

Elipot, S., Frajka-Williams, E., Hughes, C. W., Olhede, S. & Lankhorst, M. (2016). Observed Basin-Scale Response of the North Atlantic Meridional Overturning Circulation to Wind Stress Forcing. *Journal of Climate*, *30*(6), 2029–2054. doi: 10.1175/JCLI-D-16-0664.1

Elipot, S., Hughes, C., Olhede, S. & Toole, J. (2013). Coherence of Western Boundary Pressure at the RAPID WAVE Array: Boundary Wave Adjustments or Deep Western Boundary Current Advection? *Journal of Physical Oceanography*, *43*(4), 744–765. doi: 10.1175/JPO-D-12-067.1

Eyring, V., Bony, S., Meehl, G. A., Senior, C. A., Stevens, B., Stouffer, R. J. & Taylor, K. E. (2016). Overview of the Coupled Model Intercomparison Project Phase 6 (CMIP6) experimental design and organization. *Geoscientific Model Development*, *9*(5), 1937–1958. doi: 10.5194/gmd-9-1937-2016

Falkowski, P., Scholes, R. J., Boyle, E., Canadell, J., Canfield, D., Elser, J., Gruber, N., Hibbard, K., Högberg, P., Linder, S., Mackenzie, F. T., Moore III, B., Pedersen, T., Rosenthal, Y., Seitzinger, S., Smetacek, V. & Steffen, W. (2000). The Global Carbon Cycle: A Test of Our Knowledge of Earth as a System. *Science*, *290*(5490), 291–296. doi: 10.1126/science.290.5490.291

Farneti, R. & Delworth, T. L. (2010). The Role of Mesoscale Eddies in the Remote Oceanic Response to Altered Southern Hemisphere Winds. *Journal of Physical Oceanography*, *40*(10), 2348–2354. doi: 10.1175/2010JPO4480.1

Farrow, D. E. & Stevens, D. P. (1995). A New Tracer Advection Scheme for Bryan and Cox Type Ocean General Circulation Models. *Journal of Physical Oceanography*, *25*(7), 1731–1741. doi: 10.1175/1520-0485(1995)025<1731:ANTASF>2.0.CO;2

Ferrari, R., Nadeau, L.-P., Marshall, D. P., Allison, L. C. & Johnson, H. L. (2017). A Model of the Ocean Overturning Circulation with Two Closed Basins and a Reentrant Channel. *Journal of Physical Oceanography*, *47*(12), 2887–2906. doi: 10.1175/JPO-D-16-0223.1

Ferreira, D., Marshall, J. & Campin, J.-M. (2010). Localization of Deep Water Formation: Role of Atmospheric Moisture Transport and Geometrical Constraints on Ocean Circulation. *Journal*

of Climate, *23*(6), 1456–1476. doi: 10.1175/2009JCLI3197.1

Fichefet, T. & Maqueda, M. A. M. (1997). Sensitivity of a global sea ice model to the treatment of ice thermodynamics and dynamics. *Journal of Geophysical Research: Oceans*, *102*(C6), 12609–12646. doi: 10.1029/97JC00480

Flato, G., Marotzke, J., Abiodun, B., Braconnot, P., Chou, S. C., Collins, W., Cox, P., Driouech, F., Emori, S., Eyring, V., Forest, C., Gleckler, P., Guilyardi, E., Jakob, C., Kattsov, V., Reason, C. & Rummukainen, M. (2013). Evaluation of climate models. In T. F. Stocker et al. (Eds.), *Climate Change 2013: The Physical Science Basis. Contribution of Working Group I to the Fifth Assessment Report of the Intergovernmental Panel on Climate Change* (pp. 741–882). Cambridge, UK: Cambridge University Press. doi: 10.1017/CBO9781107415324.020

Foukal, N. P. & Lozier, M. S. (2016). No inter-gyre pathway for sea-surface temperature anomalies in the North Atlantic. *Nature Communications*, *7*(1), 11333. doi: 10.1038/ncomms11333

Frajka-Williams, E., Ansorge, I. J., Baehr, J., Bryden, H. L., Chidichimo, M. P., Cunningham, S. A., Danabasoglu, G., Dong, S., Donohue, K. A., Elipot, S., Heimbach, P., Holliday, N. P., Hummels, R., Jackson, L. C., Karstensen, J., Lankhorst, M., Le Bras, I. A., Lozier, M. S., McDonagh, E. L., Meinen, C. S., Mercier, H., Moat, B. I., Perez, R. C., Piecuch, C. G., Rhein, M., Srokosz, M. A., Trenberth, K. E., Bacon, S., Forget, G., Goni, G., Kieke, D., Koelling, J., Lamont, T., McCarthy, G. D., Mertens, C., Send, U., Smeed, D. A., Speich, S., van den Berg, M., Volkov, D. & Wilson, C. (2019). Atlantic Meridional Overturning Circulation: Observed Transport and Variability. *Frontiers in Marine Science*, *6*, 260. doi: 10.3389/fmars.2019.00260

Gary, S. F., Fox, A. D., Biastoch, A., Roberts, J. M. & Cunningham, S. A. (2020). Larval behaviour, dispersal and population connectivity in the deep sea. *Scientific Reports*, *10*(1), 10675. doi: 10.1038/s41598-020-67503-7

Gary, S. F., Susan Lozier, M., Böning, C. W. & Biastoch, A. (2011). Deciphering the pathways for the deep limb of the Meridional Overturning Circulation. *Deep Sea Research Part II: Topical Studies in Oceanography*, *58*(17-18), 1781–1797. doi: 10.1016/j.dsr2.2010.10.059

Garzoli, S. L., Dong, S., Fine, R., Meinen, C. S., Perez, R. C., Schmid, C., van Sebille, E. & Yao, Q. (2015). The fate of the Deep Western Boundary Current in the South Atlantic. *Deep Sea Research Part I: Oceanographic Research Papers*, *103*, 125–136. doi: 10.1016/j.dsr.2015.05.008

Garzoli, S. L., Ffield, A. & Yao, Q. (2003). North Brazil Current rings and the variability in the latitude of retroflection. In G. Goni & P. Malanotte-Rizzoli (Eds.), *Elsevier Oceanography Series* (Vol. 68, pp. 357–373). Elsevier. doi: 10.1016/S0422-9894(03)80154-X

Gent, P. R. (2016). Effects of Southern Hemisphere Wind Changes on the Meridional Overturning Circulation in Ocean Models. *Annual Review of Marine Science*, *8*(1), 79–94. doi: 10.1146/annurev-marine-122414-033929

Gent, P. R. & Danabasoglu, G. (2011). Response to Increasing Southern Hemisphere Winds in CCSM4. *Journal of Climate*, *24*(19), 4992–4998. doi: 10.1175/JCLI-D-10-05011.1

Gent, P. R. & McWilliams, J. C. (1990). Isopycnal Mixing in Ocean Circulation Models. *Journal of Physical Oceanography*, *20*(1), 150–155. doi: 10.1175/1520-0485(1990)020<0150:IMIOCM>2.0.CO;2

Getzlaff, J., Böning, C. W., Eden, C. & Biastoch, A. (2005). Signal propagation related to the North Atlantic overturning. *Geophysical Research Letters*, *32*(9), L09602. doi: 10.1029/2004GL021002

Getzlaff, K., Böning, C. W. & Dengg, J. (2006). Lagrangian perspectives of deep water export from the subpolar North Atlantic. *Geophysical Research Letters*, *33*(21), L21S08. doi: 10.1029/2006GL026470

Gill, A. (1982). *Atmosphere-Ocean Dynamics* (1st ed., Vol. 30). New York: Academic Press.

Goldsbrough, G. R. (1933). Ocean currents produced by evaporation and precipitation. *Proceedings of the Royal Society of London. Series A, Containing Papers of a Mathematical and Physical Character*, *141*(845), 512–517. doi: 10.1098/rspa.1933.0135

Gordon, A. L., Lutjeharms, J. R. & Gründlingh, M. L. (1987). Stratification and circulation at the Agulhas Retroflection. *Deep Sea Research Part A. Oceanographic Research Papers*, *34*(4), 565–599. doi: 10.1016/0198-0149(87)90006-9

Gordon, A. L., Weiss, R. F., Smethie Jr., W. M. & Warner, M. J. (1992). Thermocline and intermediate water communication between the south Atlantic and Indian oceans. *Journal of Geophysical Research: Oceans*, *97*(C5), 7223–7240. doi: 10.1029/92JC00485

Goyal, R., Sen Gupta, A., Jucker, M. & England, M. H. (2021). Historical and Projected Changes in the Southern Hemisphere Surface Westerlies. *Geophysical Research Letters*, *48*(4), e2020GL090849. doi: 10.1029/2020GL090849

Gregory, J. M., Dixon, K. W., Stouffer, R. J., Weaver, A. J., Driesschaert, E., Eby, M., Fichefet, T., Hasumi, H., Hu, A., Jungclaus, J. H., Kamenkovich, I. V., Levermann, A., Montoya, M., Murakami, S., Nawrath, S., Oka, A., Sokolov, A. P. & Thorpe, R. B. (2005). A model intercomparison of changes in the Atlantic thermohaline circulation in response to increasing atmospheric CO2 concentration. *Geophysical Research Letters*, *32*(12), L12703. doi: 10.1029/2005GL023209

Griffies, S. M., Biastoch, A., Böning, C., Bryan, F., Danabasoglu, G., Chassignet, E. P., England, M. H., Gerdes, R., Haak, H., Hallberg, R. W., Hazeleger, W., Jungclaus, J., Large, W. G., Madec, G., Pirani, A., Samuels, B. L., Scheinert, M., Gupta, A. S., Severijns, C. A., Simmons, H. L., Treguier, A. M., Winton, M., Yeager, S. & Yin, J. (2009). Coordinated Ocean-ice Reference Experiments (COREs). *Ocean Modelling*, *26*(1), 1–46. doi: 10.1016/j.ocemod.2008.08.007

Grégorio, S., Penduff, T., Sérazin, G., Molines, J.-M., Barnier, B. & Hirschi, J. (2015). Intrinsic Variability of the Atlantic Meridional Overturning Circulation at Interannual-to-Multidecadal Time Scales. *Journal of Physical Oceanography*, *45*(7), 1929–1946. doi: 10.1175/JPO-D-14-0163.1

Haarsma, R. J., Campos, E. J. D., Drijfhout, S., Hazeleger, W. & Severijns, C. (2011). Impacts of interruption of the Agulhas leakage on the tropical Atlantic in coupled ocean–atmosphere simulations. *Climate Dynamics*, *36*(5), 989–1003. doi: 10.1007/s00382-009-0692-7

Hagemann, S. & Gates, L. D. (2003). Improving a subgrid runoff parameterization scheme for climate models by the use of high resolution data derived from satellite observations. *Climate Dynamics*, *21*(3), 349–359. doi: 10.1007/s00382-003-0349-x

Hallberg, R. (2013). Using a resolution function to regulate parameterizations of oceanic mesoscale eddy effects. *Ocean Modelling*, *72*, 92–103. doi: 10.1016/j.ocemod.2013.08.007

Hallberg, R. & Gnanadesikan, A. (2006). The Role of Eddies in Determining the Structure and Response of the Wind-Driven Southern Hemisphere Overturning: Results from the Modeling Eddies in the Southern Ocean (MESO) Project. *Journal of Physical Oceanography*, *36*(12), 2232–2252. doi: 10.1175/JPO2980.1

Halliwell, G., Weisberg, R. & Mayer, D. (2003). A synthetic float analysis of upper-limb meridional overturning circulation interior ocean pathways in the tropical/subtropical Atlantic. In G. Goni & P. Malanotte-Rizzoli (Eds.), *Elsevier Oceanography Series* (Vol. 68, pp. 93–136). Elsevier. doi: 10.1016/S0422-9894(03)80144-7

Handmann, P., Fischer, J., Visbeck, M., Karstensen, J., Biastoch, A., Böning, C. & Patara, L. (2018). The Deep Western Boundary Current in the Labrador Sea From Observations and a High-Resolution Model. *Journal of Geophysical Research: Oceans*, *123*(4), 2829–2850. doi: 10.1002/2017JC013702

Hawkins, E., Smith, R. S., Allison, L. C., Gregory, J. M., Woollings, T. J., Pohlmann, H. & de Cuevas, B. (2011). Bistability of the Atlantic overturning circulation in a global climate model and links to ocean freshwater transport. *Geophysical Research Letters*, *38*(10), L10605. doi: 10.1029/2011GL047208

Herrford, J., Brandt, P., Kanzow, T., Hummels, R., Araujo, M. & Durgadoo, J. V. (2021). Seasonal variability of the Atlantic Meridional Overturning Circulation at 11°S inferred from bottom pressure measurements. *Ocean Science*, *17*(1), 265–284. doi: 10.5194/os-17-265-2021

Hirschi, J. J.-M., Barnier, B., Böning, C., Biastoch, A., Blaker, A. T., Coward, A., Danilov, S., Drijfhout, S., Getzlaff, K., Griffies, S. M., Hasumi, H., Hewitt, H., Iovino, D., Kawasaki, T., Kiss, A. E., Koldunov, N., Marzocchi, A., Mecking, J. V., Moat, B., Molines, J.-M., Myers, P. G., Penduff, T., Roberts, M., Treguier, A.-M., Sein, D. V., Sidorenko, D., Small, J., Spence, P., Thompson, L., Weijer, W. & Xu, X. (2020). The Atlantic Meridional Overturning

Circulation in High-Resolution Models. *Journal of Geophysical Research: Oceans*, *125*(4), e2019JC015522. doi: 10.1029/2019JC015522

Hogg, A. M. & Blundell, J. R. (2006). Interdecadal Variability of the Southern Ocean. *Journal of Physical Oceanography*, *36*(8), 1626–1645. doi: 10.1175/JPO2934.1

Hogg, A. M., Meredith, M. P., Blundell, J. R. & Wilson, C. (2008). Eddy Heat Flux in the Southern Ocean: Response to Variable Wind Forcing. *Journal of Climate*, *21*(4), 608–620. doi: 10.1175/2007JCLI1925.1

Hogg, A. M., Spence, P., Saenko, O. A. & Downes, S. M. (2017). The Energetics of Southern Ocean Upwelling. *Journal of Physical Oceanography*, *47*(1), 135–153. doi: 10.1175/JPO-D-16-0176.1

Huang, R. X. (1999). Mixing and Energetics of the Oceanic Thermohaline Circulation. *Journal of Physical Oceanography*, *29*(4), 727–746. doi: 10.1175/1520-0485(1999)029<0727:MAEOTO>2.0.CO;2

Hurrell, J. W. (1995). Decadal Trends in the North Atlantic Oscillation: Regional Temperatures and Precipitation. *Science*, *269*(5224), 676–679. doi: 10.1126/science.269.5224.676

Hurrell, J. W. & Deser, C. (2010). North Atlantic climate variability: The role of the North Atlantic Oscillation. *Journal of Marine Systems*, *79*(3), 231–244. doi: 10.1016/j.jmarsys.2009.11.002

Huss, M., Hock, R., Bauder, A. & Funk, M. (2010). 100-year mass changes in the Swiss Alps linked to the Atlantic Multidecadal Oscillation. *Geophysical Research Letters*, *37*(10), L10501. doi: 10.1029/2010GL042616

Ivanciu, I., Matthes, K., Biastoch, A., Wahl, S. & Harlaß, J. (2022a). Twenty-first-century Southern Hemisphere impacts of ozone recovery and climate change from the stratosphere to the ocean. *Weather and Climate Dynamics*, *3*(1), 139–171. doi: 10.5194/wcd-3-139-2022

Ivanciu, I., Ndarana, T., Matthes, K. & Wahl, S. (2022b). On the Ridging of the South Atlantic Anticyclone Over South Africa: The Impact of Rossby Wave Breaking and of Climate Change. *Geophysical Research Letters*, *49*(20), e2022GL099607. doi: 10.1029/2022GL099607

Jackson, L. C., Biastoch, A., Buckley, M. W., Desbruyères, D. G., Frajka-Williams, E., Moat, B. & Robson, J. (2022). The evolution of the North Atlantic Meridional Overturning Circulation since 1980. *Nature Reviews Earth & Environment*, *3*, 241—254. doi: 10.1038/s43017-022-00263-2

Jackson, L. C., Kahana, R., Graham, T., Ringer, M. A., Woollings, T., Mecking, J. V. & Wood, R. A. (2015). Global and European climate impacts of a slowdown of the AMOC in a high resolution GCM. *Climate Dynamics*, *45*(11-12), 3299 – 3316. doi: 10.1007/s00382-015-2540-2

Jackson, L. C., Roberts, M. J., Hewitt, H. T., Iovino, D., Koenigk, T., Meccia, V. L., Roberts, C. D., Ruprich-Robert, Y. & Wood, R. A. (2020). Impact of ocean resolution and mean state on the rate of AMOC weakening. *Climate Dynamics*, *55*(7), 1711–1732. doi: 10.1007/s00382-020-05345-9

Jochumsen, K., Moritz, M., Nunes, N., Quadfasel, D., Larsen, K. M. H., Hansen, B., Valdimarsson, H. & Jonsson, S. (2017). Revised transport estimates of the Denmark Strait overflow. *Journal of Geophysical Research: Oceans*, *122*(4), 3434–3450. doi: 10.1002/2017JC012803

Johnson, H. L. & Marshall, D. P. (2002). A Theory for the Surface Atlantic Response to Thermohaline Variability. *Journal of Physical Oceanography*, *32*(4), 1121–1132. doi: 10.1175/1520-0485(2002)032<1121:ATFTSA>2.0.CO;2

Kalnay, E., Kanamitsu, M., Kistler, R., Collins, W., Deaven, D., Gandin, L., Iredell, M., Saha, S., White, G., Woollen, J., Zhu, Y., Chelliah, M., Ebisuzaki, W., Higgins, W., Janowiak, J., Mo, K. C., Ropelewski, C., Wang, J., Leetmaa, A., Reynolds, R., Jenne, R. & Joseph, D. (1996). The NCEP/NCAR 40-Year Reanalysis Project. *Bulletin of the American Meteorological Society*, *77*(3), 437–472. doi: 10.1175/1520-0477(1996)077<0437:TNYRP>2.0.CO;2

Kanzow, T., Cunningham, S. A., Johns, W. E., Hirschi, J. J.-M., Marotzke, J., Baringer, M. O., Meinen, C. S., Chidichimo, M. P., Atkinson, C., Beal, L. M., Bryden, H. L. & Collins, J. (2010). Seasonal Variability of the Atlantic Meridional Overturning Circulation at 26.5°N. *Journal of Climate*, *23*(21), 5678–5698. doi: 10.1175/2010JCLI3389.1

Kanzow, T., Send, U. & McCartney, M. (2008). On the variability of the deep meridional transports in the tropical North Atlantic. *Deep Sea Research Part I: Oceanographic Research Papers*, *55*(12), 1601–1623. doi: 10.1016/j.dsr.2008.07.011

Katsman, C. A., Drijfhout, S. S., Dijkstra, H. A. & Spall, M. A. (2018). Sinking of Dense North Atlantic Waters in a Global Ocean Model: Location and Controls. *Journal of Geophysical Research: Oceans*, *123*(5), 3563–3576. doi: 10.1029/2017JC013329

King, M. P., Keenlyside, N. & Li, C. (2023). ENSO teleconnections in terms of non-NAO and NAO atmospheric variability. *Climate Dynamics*. doi: 10.1007/s00382-023-06697-8

Klinger, B. A. & Cruz, C. (2009). Decadal Response of Global Circulation to Southern Ocean Zonal Wind Stress Perturbation. *Journal of Physical Oceanography*, *39*(8), 1888–1904. doi: 10.1175/2009JPO4070.1

Knorr, G. & Lohmann, G. (2003). Southern Ocean origin for the resumption of Atlantic thermohaline circulation during deglaciation. *Nature*, *424*(6948), 532–536. doi: 10.1038/nature01855

Kuhlbrodt, T., Griesel, A., Montoya, M., Levermann, A., Hofmann, M. & Rahmstorf, S. (2007). On the driving processes of the Atlantic meridional overturning circulation. *Reviews of Geophysics*, *45*(2), RG2001. doi: 10.1029/2004RG000166

Large, W. G. & Yeager, S. G. (2009). The global climatology of an interannually varying air–sea flux data set. *Climate Dynamics*, *33*(2), 341–364. doi: 10.1007/s00382-008-0441-3

Lavender, K. L., Davis, R. E. & Owens, W. B. (2000). Mid-depth recirculation observed in the interior Labrador and Irminger seas by direct velocity measurements. *Nature*, *407*(6800), 66–69. doi: 10.1038/35024048

Leaman, K. D. & Harris, J. E. (1990). On the Average Absolute Transport of the Deep Western Boundary Currents East of Abaco Island, the Bahamas. *Journal of Physical Oceanography*, *20*(3), 467–475. doi: 10.1175/1520-0485(1990)020<0467:OTAATO>2.0.CO;2

Leaman, K. D. & Vertes, P. S. (1996). Topographic Influences on Recirculation in the Deep Western Boundary Current: Results from RAFOS Float Trajectories between the Blake–Bahama Outer Ridge and the San Salvador "Gate". *Journal of Physical Oceanography*, *26*(6), 941–961. doi: 10.1175/1520-0485(1996)026<0941:TIORIT>2.0.CO;2

Lemarié, F. (2006). *NEMO/AGRIF Nesting tools, User's Guide (30 January 2006)*. Retrieved from `https://forge.ipsl.jussieu.fr/nemo/wiki/Users/SetupNewConfiguration/AGRIF-nesting-tool`

Leroux, S., Penduff, T., Bessières, L., Molines, J.-M., Brankart, J.-M., Sérazin, G., Barnier, B. & Terray, L. (2018). Intrinsic and Atmospherically Forced Variability of the AMOC: Insights from a Large-Ensemble Ocean Hindcast. *Journal of Climate*, *31*(3), 1183–1203. doi: 10.1175/JCLI-D-17-0168.1

Link, P. M. & Tol, R. S. J. (2004). Possible economic impacts of a shutdown of the thermohaline circulation: an application of FUND. *Portuguese Economic Journal*, *3*(2), 99–114. doi: 10.1007/s10258-004-0033-z

Liu, W., Xie, S.-P., Liu, Z. & Zhu, J. (2017). Overlooked possibility of a collapsed Atlantic Meridional Overturning Circulation in warming climate. *Science Advances*, *3*(1), e1601666. doi: 10.1126/sciadv.1601666

Locarnini, R. A., Mishonov, A. V., Antonov, J. I., Boyer, T. P., Garcia, H. E., Baranova, O. K., Zweng, M. M., Paver, C. R., Reagan, J. R., Johnson, D. R., Hamilton, M., Seidov, D. & Levitus, S. (2013). World ocean atlas 2013. Volume 1, Temperature. *NOAA atlas NESDIS ; 73*. doi: 10.7289/V55X26VD

Lozier, M. S. (1997). Evidence for Large-Scale Eddy-Driven Gyres in the North Atlantic. *Science*, *277*(5324), 361–364. doi: 10.1126/science.277.5324.361

Lozier, M. S. (2010). Deconstructing the Conveyor Belt. *Science*, *328*(5985), 1507–1511. doi: 10.1126/science.1189250

Lozier, M. S. (2012). Overturning in the North Atlantic. *Annual Review of Marine Science*, *4*(1), 291–315. doi: 10.1146/annurev-marine-120710-100740

Lozier, M. S., Bacon, S., Bower, A. S., Cunningham, S. A., Femke de Jong, M., de Steur, L., deYoung, B., Fischer, J., Gary, S. F., Greenan, B. J. W., Heimbach, P., Holliday, N. P., Houpert, L., Inall, M. E., Johns, W. E., Johnson, H. L., Karstensen, J., Li, F., Lin, X., Mackay, N., Marshall, D. P., Mercier, H., Myers, P. G., Pickart, R. S., Pillar, H. R., Straneo, F., Thierry, V., Weller, R. A., Williams, R. G., Wilson, C., Yang, J., Zhao, J. & Zika, J. D. (2017). Overturning in the Subpolar North Atlantic Program: A New International Ocean

Observing System. *Bulletin of the American Meteorological Society*, *98*(4), 737–752. doi: 10.1175/BAMS-D-16-0057.1

Lozier, M. S., Bower, A. S., Furey, H. H., Drouin, K. L., Xu, X. & Zou, S. (2022). Overflow water pathways in the North Atlantic. *Progress in Oceanography*, *208*, 102874. doi: 10.1016/j.pocean.2022.102874

Lozier, M. S., Li, F., Bacon, S., Bahr, F., Bower, A. S., Cunningham, S. A., de Jong, M. F., de Steur, L., deYoung, B., Fischer, J., Gary, S. F., Greenan, B. J. W., Holliday, N. P., Houk, A., Houpert, L., Inall, M. E., Johns, W. E., Johnson, H. L., Johnson, C., Karstensen, J., Koman, G., Le Bras, I. A., Lin, X., Mackay, N., Marshall, D. P., Mercier, H., Oltmanns, M., Pickart, R. S., Ramsey, A. L., Rayner, D., Straneo, F., Thierry, V., Torres, D. J., Williams, R. G., Wilson, C., Yang, J., Yashayaev, I. & Zhao, J. (2019). A sea change in our view of overturning in the subpolar North Atlantic. *Science*, *363*(6426), 516–521. doi: 10.1126/science.aau6592

Lutjeharms, J. & Cooper, J. (1996). Interbasin leakage through Agulhas current filaments. *Deep Sea Research Part I: Oceanographic Research Papers*, *43*(2), 213–238. doi: 10.1016/0967-0637(96)00002-7

Lutjeharms, J. R. E. & Roberts, H. R. (1988). The Natal pulse: An extreme transient on the Agulhas Current. *Journal of Geophysical Research: Oceans*, *93*(C1), 631–645. doi: 10.1029/JC093iC01p00631

Madec, G. (2016). *NEMO ocean engine.* Note du Pôle de modélisation, Institut Pierre-Simon Laplace (IPSL), France, No 27, ISSN No 1288-1619.

Marshall, G. J. (2003). Trends in the Southern Annular Mode from Observations and Reanalyses. *Journal of Climate*, *16*(24), 4134–4143. doi: 10.1175/1520-0442(2003)016<4134:TITSAM>2.0.CO;2

Marshall, J. & Plumb, A. (2007). *Atmosphere, Ocean and Climate Dynamics - An Introductory Text* (1st Edition ed.). Academic Press.

Marshall, J. & Schott, F. (1999). Open-ocean convection: Observations, theory, and models. *Reviews of Geophysics*, *37*(1), 1–64. doi: 10.1029/98RG02739

Martin, T. (2021). *Runoff remapping for ocean model forcing.* Kiel, Germany. Retrieved from `https://git.geomar.de/open-source/runoff_remapping` doi: 10.3289/SW_2_2021

Martin, T. & Biastoch, A. (2022). On the ocean's response to enhanced Greenland runoff in model experiments: relevance of mesoscale dynamics and atmospheric coupling. *EGUsphere*, *2022*, 1–39. doi: 10.5194/egusphere-2022-869

Martin, T., Park, W. & Latif, M. (2015). Southern Ocean forcing of the North Atlantic at multi-centennial time scales in the Kiel Climate Model. *Deep Sea Research Part II: Topical Studies in Oceanography*, *114*, 39–48. doi: 10.1016/j.dsr2.2014.01.018

Matthes, K., Biastoch, A., Wahl, S., Harlaß, J., Martin, T., Brücher, T., Drews, A., Ehlert, D., Getzlaff, K., Krüger, F., Rath, W., Scheinert, M., Schwarzkopf, F. U., Bayr, T., Schmidt, H. & Park, W. (2020). The Flexible Ocean and Climate Infrastructure version 1 (FOCI1): mean state and variability. *Geoscientific Model Development*, *13*(6), 2533–2568. doi: 10.5194/gmd-13-2533-2020

McCabe, G. J., Palecki, M. A. & Betancourt, J. L. (2004). Pacific and Atlantic Ocean influences on multidecadal drought frequency in the United States. *Proceedings of the National Academy of Sciences*, *101*(12), 4136–4141. doi: 10.1073/pnas.0306738101

McCarthy, G., Smeed, D., Johns, W., Frajka-Williams, E., Moat, B., Rayner, D., Baringer, M., Meinen, C., Collins, J. & Bryden, H. (2015). Measuring the Atlantic Meridional Overturning Circulation at 26°N. *Progress in Oceanography*, *130*, 91–111. doi: 10.1016/j.pocean.2014.10.006

Megann, A., Blaker, A., Josey, S., New, A. & Sinha, B. (2021). Mechanisms for Late 20th and Early 21st Century Decadal AMOC Variability. *Journal of Geophysical Research: Oceans*, *126*(12), e2021JC017865. doi: 10.1029/2021JC017865

Meinen, C. S., Baringer, M. O. & Garcia, R. F. (2010). Florida Current transport variability: An analysis of annual and longer-period signals. *Deep Sea Research Part I: Oceanographic Research Papers*, *57*(7), 835–846. doi: 10.1016/j.dsr.2010.04.001

Meinen, C. S., Speich, S., Perez, R. C., Dong, S., Piola, A. R., Garzoli, S. L., Baringer, M. O., Gladyshev, S. & Campos, E. J. D. (2013). Temporal variability of the meridional overturning circulation at 34.5°S: Results from two pilot boundary arrays in the South Atlantic. *Journal of Geophysical Research: Oceans*, *118*(12), 6461–6478. doi: 10.1002/2013JC009228

Meinen, C. S., Speich, S., Piola, A. R., Ansorge, I., Campos, E., Kersalé, M., Terre, T., Chidichimo, M. P., Lamont, T., Sato, O. T., Perez, R. C., Valla, D., van den Berg, M., Le Hénaff, M., Dong, S. & Garzoli, S. L. (2018). Meridional Overturning Circulation Transport Variability at 34.5°S During 2009–2017: Baroclinic and Barotropic Flows and the Dueling Influence of the Boundaries. *Geophysical Research Letters*, *45*(9), 4180–4188. doi: 10.1029/2018GL077408

Menary, M. B., Hodson, D. L. R., Robson, J. I., Sutton, R. T. & Wood, R. A. (2015). A Mechanism of Internal Decadal Atlantic Ocean Variability in a High-Resolution Coupled Climate Model. *Journal of Climate*, *28*(19), 7764–7785. doi: 10.1175/JCLI-D-15-0106.1

Menary, M. B., Jackson, L. C. & Lozier, M. S. (2020). Reconciling the Relationship Between the AMOC and Labrador Sea in OSNAP Observations and Climate Models. *Geophysical Research Letters*, *47*(18), e2020GL089793. doi: 10.1029/2020GL089793

Menary, M. B., Kuhlbrodt, T., Ridley, J., Andrews, M. B., Dimdore-Miles, O. B., Deshayes, J., Eade, R., Gray, L., Ineson, S., Mignot, J., Roberts, C. D., Robson, J., Wood, R. A. & Xavier, P. (2018). Preindustrial Control Simulations With HadGEM3-GC3.1 for CMIP6. *Journal of Advances in Modeling Earth Systems*, *10*(12), 3049–3075. doi: 10.1029/2018MS001495

Meredith, M. P. & Hogg, A. M. (2006). Circumpolar response of Southern Ocean eddy activity to a change in the Southern Annular Mode. *Geophysical Research Letters*, *33*(16), L16608. doi: 10.1029/2006GL026499

Meyer-Kaiser, K. S. & Mires, C. H. (2022). Underwater cultural heritage is integral to marine ecosystems. *Trends in Ecology & Evolution*, *37*(10), 815–818. doi: 10.1016/j.tree.2022.06.014

Mielke, C., Frajka-Williams, E. & Baehr, J. (2013). Observed and simulated variability of the AMOC at 26°N and 41°N. *Geophysical Research Letters*, *40*(6), 1159–1164. doi: 10.1002/grl.50233

Mikolajewicz, U. & Voss, R. (2000). The role of the individual air-sea flux components in CO2-induced changes of the ocean's circulation and climate. *Climate Dynamics*, *16*(8), 627–642. doi: 10.1007/s003820000066

Moat, B. I., Smeed, D. A., Frajka-Williams, E., Desbruyères, D. G., Beaulieu, C., Johns, W. E., Rayner, D., Sanchez-Franks, A., Baringer, M. O., Volkov, D., Jackson, L. C. & Bryden, H. L. (2020). Pending recovery in the strength of the meridional overturning circulation at 26°N. *Ocean Science*, *16*(4), 863–874. doi: 10.5194/os-16-863-2020

Molines, J. M., Barnier, B., Penduff, T. & Brodeau, L. (2006). Definition of the global 1/2° experiment with CORE interannual forcing, ORCA05-G50. *LEGI report November 2006, LEGI-DRA-1-11-2006*.

Morato, T., González-Irusta, J.-M., Dominguez-Carrió, C., Wei, C.-L., Davies, A., Sweetman, A. K., Taranto, G. H., Beazley, L., García-Alegre, A., Grehan, A., Laffargue, P., Murillo, F. J., Sacau, M., Vaz, S., Kenchington, E., Arnaud-Haond, S., Callery, O., Chimienti, G., Cordes, E., Egilsdottir, H., Freiwald, A., Gasbarro, R., Gutiérrez-Zárate, C., Gianni, M., Gilkinson, K., Wareham Hayes, V. E., Hebbeln, D., Hedges, K., Henry, L.-A., Johnson, D., Koen-Alonso, M., Lirette, C., Mastrototaro, F., Menot, L., Molodtsova, T., Durán Muñoz, P., Orejas, C., Pennino, M. G., Puerta, P., Ragnarsson, S. , Ramiro-Sánchez, B., Rice, J., Rivera, J., Roberts, J. M., Ross, S. W., Rueda, J. L., Sampaio, , Snelgrove, P., Stirling, D., Treble, M. A., Urra, J., Vad, J., van Oevelen, D., Watling, L., Walkusz, W., Wienberg, C., Woillez, M., Levin, L. A. & Carreiro-Silva, M. (2020). Climate-induced changes in the suitable habitat of cold-water corals and commercially important deep-sea fishes in the North Atlantic. *Global Change Biology*, *26*(4), 2181–2202. doi: 10.1111/gcb.14996

Munday, D. R., Johnson, H. L. & Marshall, D. P. (2013). Eddy Saturation of Equilibrated Circumpolar Currents. *Journal of Physical Oceanography*, *43*(3), 507–532. doi: 10.1175/JPO-D-12-095.1

Munk, W. H. (1950). ON THE WIND-DRIVEN OCEAN CIRCULATION. *Journal of Atmospheric Sciences*, *7*(2), 80–93. doi: 10.1175/1520-0469(1950)007<0080:OTWDOC>2.0.CO;2

Munk, W. H. & Wunsch, C. (1998). Abyssal recipes II: energetics of tidal and wind mixing.

Deep Sea Research Part I: Oceanographic Research Papers, *45*(12), 1977–2010. doi: 10.1016/S0967-0637(98)00070-3

Ménesguen, C., Delpech, A., Marin, F., Cravatte, S., Schopp, R. & Morel, Y. (2019). Observations and Mechanisms for the Formation of Deep Equatorial and Tropical Circulation. *Earth and Space Science*, *6*(3), 370–386. doi: 10.1029/2018EA000438

Müller, V., Kieke, D., Myers, P. G., Pennelly, C., Steinfeldt, R. & Stendardo, I. (2019). Heat and Freshwater Transport by Mesoscale Eddies in the Southern Subpolar North Atlantic. *Journal of Geophysical Research: Oceans*, *124*(8), 5565–5585. doi: 10.1029/2018JC014697

Müller, W. A., Jungclaus, J. H., Mauritsen, T., Baehr, J., Bittner, M., Budich, R., Bunzel, F., Esch, M., Ghosh, R., Haak, H., Ilyina, T., Kleine, T., Kornblueh, L., Li, H., Modali, K., Notz, D., Pohlmann, H., Roeckner, E., Stemmler, I., Tian, F. & Marotzke, J. (2018). A Higher-resolution Version of the Max Planck Institute Earth System Model (MPI-ESM1.2-HR). *Journal of Advances in Modeling Earth Systems*, *10*(7), 1383–1413. doi: 10.1029/2017MS001217

NOAA National Geophysical Data Center. (2006). 2-minute Gridded Global Relief Data (ETOPO2) v2. *NOAA National Centers for Environmental Information*. doi: 10.7289/V5J1012Q

Orihuela-Pinto, B., England, M. H. & Taschetto, A. S. (2022). Interbasin and interhemispheric impacts of a collapsed Atlantic Overturning Circulation. *Nature Climate Change*, *12*(6), 558–565. doi: 10.1038/s41558-022-01380-y

Orsi, A. H., Johnson, G. & Bullister, J. (1999). Circulation, mixing, and production of Antarctic Bottom Water. *Progress in Oceanography*, *43*(1), 55–109. doi: 10.1016/S0079-6611(99)00004-X

Orsi, A. H., Whitworth, T. & Nowlin, W. D. (1995). On the meridional extent and fronts of the Antarctic Circumpolar Current. *Deep Sea Research Part I: Oceanographic Research Papers*, *42*(5), 641–673. doi: 10.1016/0967-0637(95)00021-W

Orvik, K. A., Skagseth, Ø. & Mork, M. (2001). Atlantic inflow to the Nordic Seas: current structure and volume fluxes from moored current meters, VM-ADCP and SeaSoar-CTD observations, 1995–1999. *Deep-Sea Research Part I*, *48*(4), 937–957. doi: 10.1016/S0967-0637(00)00038-8

Palter, J. B. (2015). The Role of the Gulf Stream in European Climate. *Annual Review of Marine Science*, *7*(1), 113–137. doi: 10.1146/annurev-marine-010814-015656

Penduff, T., Le Sommer, J., Barnier, B., Treguier, A.-M., Molines, J.-M. & Madec, G. (2007). Influence of numerical schemes on current-topography interactions in 1/4° global ocean simulations. *Ocean Science*, *3*(4), 509–524. doi: 10.5194/os-3-509-2007

Penven, P., Lutjeharms, J. R. E., Marchesiello, P., Roy, C. & Weeks, S. J. (2001). Generation of cyclonic eddies by the Agulhas Current in the Lee of the Agulhas Bank. *Geophysical Research Letters*, *28*(6), 1055–1058. doi: 10.1029/2000GL011760

Perez, F. F., Fontela, M., García-Ibáñez, M. I., Mercier, H., Velo, A., Lherminier, P., Zunino, P., de la Paz, M., Alonso-Pérez, F., Guallart, E. F. & Padin, X. A. (2018). Meridional overturning circulation conveys fast acidification to the deep Atlantic Ocean. *Nature*, *554*(7693), 515–518. doi: 10.1038/nature25493

Pershing, A. J., Alexander, M. A., Hernandez, C. M., Kerr, L. A., Le Bris, A., Mills, K. E., Nye, J. A., Record, N. R., Scannell, H. A., Scott, J. D., Sherwood, G. D. & Thomas, A. C. (2015). Slow adaptation in the face of rapid warming leads to collapse of the Gulf of Maine cod fishery. *Science*, *350*(6262), 809–812. doi: 10.1126/science.aac9819

Pickart, R. S., Spall, M. A. & Lazier, J. R. (1997). Mid-depth ventilation in the western boundary current system of the sub-polar gyre. *Deep Sea Research Part I: Oceanographic Research Papers*, *44*(6), 1025–1054. doi: 10.1016/S0967-0637(96)00122-7

Pickart, R. S., Spall, M. A., Ribergaard, M. H., Moore, G. W. K. & Milliff, R. F. (2003). Deep convection in the Irminger Sea forced by the Greenland tip jet. *Nature*, *424*(6945), 152–156. doi: 10.1038/nature01729

Poli, P., Hersbach, H., Dee, D. P., Berrisford, P., Simmons, A. J., Vitart, F., Laloyaux, P., Tan, D. G. H., Peubey, C., Thépaut, J.-N., Trémolet, Y., Hólm, E. V., Bonavita, M., Isaksen, L. & Fisher, M. (2016). ERA-20C: An Atmospheric Reanalysis of the Twentieth Century. *Journal of Climate*, *29*(11), 4083–4097. doi: 10.1175/JCLI-D-15-0556.1

Polo, I., Robson, J., Sutton, R. & Balmaseda, M. A. (2014). The Importance of Wind and Buoyancy Forcing for the Boundary Density Variations and the Geostrophic Component of the AMOC at 26°N. *Journal of Physical Oceanography*, *44*(9), 2387–2408. doi: 10.1175/JPO-D-13-0264.1

Rahmstorf, S. (2002). Ocean circulation and climate during the past 120,000 years. *Nature*, *419*(6903), 207–214. doi: 10.1038/nature01090

Rahmstorf, S., Crucifix, M., Ganopolski, A., Goosse, H., Kamenkovich, I., Knutti, R., Lohmann, G., Marsh, R., Mysak, L. A., Wang, Z. & Weaver, A. J. (2005). Thermohaline circulation hysteresis: A model intercomparison. *Geophysical Research Letters*, *32*(23), L23605. doi: 10.1029/2005GL023655

Rahmstorf, S. & England, M. H. (1997). Influence of Southern Hemisphere Winds on North Atlantic Deep Water Flow. *Journal of Physical Oceanography*, *27*(9), 2040–2054. doi: 10.1175/1520-0485(1997)027<2040:IOSHWO>2.0.CO;2

Rayner, D., Hirschi, J. J.-M., Kanzow, T., Johns, W. E., Wright, P. G., Frajka-Williams, E., Bryden, H. L., Meinen, C. S., Baringer, M. O., Marotzke, J., Beal, L. M. & Cunningham, S. A. (2011). Monitoring the Atlantic meridional overturning circulation. *Deep Sea Research Part II: Topical Studies in Oceanography*, *58*(17), 1744–1753. doi: 10.1016/j.dsr2.2010.10.056

Reick, C. H., Raddatz, T., Brovkin, V. & Gayler, V. (2013). Representation of natural and anthropogenic land cover change in MPI-ESM. *Journal of Advances in Modeling Earth Systems*, *5*(3), 459–482. doi: 10.1002/jame.20022

Reintges, A., Latif, M., Bordbar, M. H. & Park, W. (2020). Wind Stress-Induced Multiyear Predictability of Annual Extratropical North Atlantic Sea Surface Temperature Anomalies. *Geophysical Research Letters*, *47*(14), e2020GL087031. doi: 10.1029/2020GL087031

Ren, X. & Liu, W. (2021). The Role of a Weakened Atlantic Meridional Overturning Circulation in Modulating Marine Heatwaves in a Warming Climate. *Geophysical Research Letters*, *48*(23), e2021GL095941. doi: 10.1029/2021GL095941

Rennell, J. (1832). *An Investigation of the Currents of the Atlantic Ocean, and of Those Which Prevail between the Indian Ocean and the Atlantic*. London: J.G. & F. Rivington.

Rhein, M., Mertens, C. & Roessler, A. (2019). Observed Transport Decline at 47°N, Western Atlantic. *Journal of Geophysical Research: Oceans*, *124*(7), 4875–4890. doi: 10.1029/2019JC014993

Rhein, M., Walter, M., Mertens, C., Steinfeldt, R. & Kieke, D. (2004). The circulation of North Atlantic Deep Water at 16°N, 2000–2003. *Geophysical Research Letters*, *31*(14), L14305. doi: 10.1029/2004GL019993

Richardson, P. L. (2008). On the history of meridional overturning circulation schematic diagrams. *Progress in Oceanography*, *76*(4), 466–486. doi: 10.1016/j.pocean.2008.01.005

Rieck, J. K., Böning, C. W. & Getzlaff, K. (2019). The Nature of Eddy Kinetic Energy in the Labrador Sea: Different Types of Mesoscale Eddies, Their Temporal Variability, and Impact on Deep Convection. *Journal of Physical Oceanography*, *49*(8), 2075–2094. doi: 10.1175/JPO-D-18-0243.1

Roach, L. A., Blanchard-Wrigglesworth, E., Ragen, S., Cheng, W., Armour, K. C. & Bitz, C. M. (2022). The Impact of Winds on AMOC in a Fully-Coupled Climate Model. *Geophysical Research Letters*, *49*(24), e2022GL101203. doi: 10.1029/2022GL101203

Roberts, C. D., Waters, J., Peterson, K. A., Palmer, M. D., McCarthy, G. D., Frajka-Williams, E., Haines, K., Lea, D. J., Martin, M. J., Storkey, D., Blockley, E. W. & Zuo, H. (2013). Atmosphere drives recent interannual variability of the Atlantic meridional overturning circulation at 26.5°N. *Geophysical Research Letters*, *40*(19), 5164–5170. doi: 10.1002/grl.50930

Roberts, J. M., Devey, C. W., Biastoch, A., Carreiro-Silva, M., Dohna, T., Dorschel, B., Gunn, V., Huvenne, V. A. I., Johnson, D., Jollivet, D., Kenchington, E., Larkin, K., Matabos, M., Morato, T., Naumann, M. S., Orejas, C., Perez, J. A. A., Ragnarsson, S. , Smit, A. J., Sweetman, A., Unger, S., Boteler, B. & Henry, L.-A. (2023). A blueprint for integrating scientific approaches and international communities to assess basin-wide ocean ecosystem status. *Communications Earth & Environment*, *4*(1), 12. doi: 10.1038/s43247-022-00645-w

Roberts, M. J., Baker, A., Blockley, E. W., Calvert, D., Coward, A., Hewitt, H. T., Jackson, L. C., Kuhlbrodt, T., Mathiot, P., Roberts, C. D., Schiemann, R., Seddon, J., Vannière, B. & Vidale,

P. L. (2019). Description of the resolution hierarchy of the global coupled HadGEM3-GC3.1 model as used in CMIP6 HighResMIP experiments. *Geoscientific Model Development*, *12*(12), 4999–5028. doi: 10.5194/gmd-12-4999-2019

Robson, J., Sutton, R., Lohmann, K., Smith, D. & Palmer, M. D. (2012). Causes of the Rapid Warming of the North Atlantic Ocean in the Mid-1990s. *Journal of Climate*, *25*(12), 4116–4134. doi: 10.1175/JCLI-D-11-00443.1

Rouault, M., Reason, C. J. C., Lutjeharms, J. R. E. & Beljaars, A. C. M. (2003). Underestimation of Latent and Sensible Heat Fluxes above the Agulhas Current in NCEP and ECMWF Analyses. *Journal of Climate*, *16*(4), 776–782. doi: 10.1175/1520-0442(2003)016<0776:UOLASH>2.0.CO;2

Ruijter, W. D. (1982). Asymptotic Analysis of the Agulhas and Brazil Current Systems. *Journal of Physical Oceanography*, *12*(4), 361–373. doi: 10.1175/1520-0485(1982)012<0361:AAOTAA>2.0.CO;2

Rumford, B. (1798). Of the propagation of heat in fluids. In S. Brown (Ed.), *Collected works of count rumford (1968)* (Vol. 1 The Nature of Heat, pp. 117–284). Cambrige MA: Belknap Press of Harvard University Press.

Rühs, S., Durgadoo, J. V., Behrens, E. & Biastoch, A. (2013). Advective timescales and pathways of Agulhas leakage. *Geophysical Research Letters*, *40*(15), 3997–4000. doi: 10.1002/grl.50782

Rühs, S., Schmidt, C., Schubert, R., Schulzki, T. G., Schwarzkopf, F. U., Le Bars, D. & Biastoch, A. (2022). Robust estimates for the decadal evolution of Agulhas leakage from the 1960s to the 2010s. *Communications Earth & Environment*, *3*(1), 318. doi: 10.1038/s43247-022-00643-y

Rühs, S., Schwarzkopf, F. U., Speich, S. & Biastoch, A. (2019). Cold vs. warm water route – sources for the upper limb of the Atlantic Meridional Overturning Circulation revisited in a high-resolution ocean model. *Ocean Science*, *15*(3), 489–512. doi: 10.5194/os-15-489-2019

Sabine, C. L., Feely, R. A., Gruber, N., Key, R. M., Lee, K., Bullister, J. L., Wanninkhof, R., Wong, C. S., Wallace, D. W. R., Tilbrook, B., Millero, F. J., Peng, T.-H., Kozyr, A., Ono, T. & Rios, A. F. (2004). The Oceanic Sink for Anthropogenic CO_2. *Science*, *305*(5682), 367. doi: 10.1126/science.1097403

Sakamoto, T. T., Komuro, Y., Nishimura, T., Ishii, M., Tatebe, H., Shiogama, H., Hasegawa, A., Toyoda, T., Mori, M., Suzuki, T., Imada, Y., Nozawa, T., Takata, K., Mochizuki, T., Ogochi, K., Emori, S., Hasumi, H. & Kimoto, M. (2012). MIROC4h—A New High-Resolution Atmosphere-Ocean Coupled General Circulation Model. *Journal of the Meteorological Society of Japan. Ser. II*, *90*(3), 325–359. doi: 10.2151/jmsj.2012-301

Salazar, M. & Little, B. (2017). Review: Rusticle Formation on the RMS Titanic and the Potential Influence of Oceanography. *Journal of Maritime Archaeology*, *12*(1), 25–32. doi: 10.1007/s11457-016-9168-1

Sanström, J. W. (1908). Dynamische Versuche mit Meerwasser. *Ann. d. Hydr. u. Marit. Meterol.*, *36*, 6–23.

Schmidt, C., Schwarzkopf, F. U., Rühs, S. & Biastoch, A. (2021). Characteristics and robustness of Agulhas leakage estimates: an inter-comparison study of Lagrangian methods. *Ocean Science*, *17*(4), 1067–1080. doi: 10.5194/os-17-1067-2021

Schmittner, A., Saenko, O. & Weaver, A. (2003). Coupling of the hemispheres in observations and simulations of glacial climate change. *Quaternary Science Reviews*, *22*(5), 659–671. doi: 10.1016/S0277-3791(02)00184-1

Schott, F. A., Dengler, M., Zantopp, R., Stramma, L., Fischer, J. & Brandt, P. (2005). The Shallow and Deep Western Boundary Circulation of the South Atlantic at 5°–11°S. *Journal of Physical Oceanography*, *35*(11), 2031–2053. doi: 10.1175/JPO2813.1

Schott, F. A., Zantopp, R., Stramma, L., Dengler, M., Fischer, J. & Wibaux, M. (2004). Circulation and Deep-Water Export at the Western Exit of the Subpolar North Atlantic. *Journal of Physical Oceanography*, *34*(4), 817–843. doi: 10.1175/1520-0485(2004)034<0817:CADEAT>2.0.CO;2

Schouten, M. W., de Ruijter, W. P. M. & van Leeuwen, P. J. (2002). Upstream control of Agulhas Ring shedding. *Journal of Geophysical Research: Oceans*, *107*(C8). doi: 10.1029/2001JC000804

Schubert, R., Biastoch, A., Cronin, M. F. & Greatbatch, R. J. (2018). Instability-Driven Benthic Storms below the Separated Gulf Stream and the North Atlantic Current in a High-Resolution Ocean Model. *Journal of Physical Oceanography*, *48*(10), 2283–2303. doi: 10.1175/JPO-D-17-0261.1

Schubert, R., Gula, J. & Biastoch, A. (2021). Submesoscale flows impact Agulhas leakage in ocean simulations. *Communications Earth & Environment*, *2*(1), 197. doi: 10.1038/s43247-021-00271-y

Schubert, R., Schwarzkopf, F. U., Baschek, B. & Biastoch, A. (2019). Submesoscale Impacts on Mesoscale Agulhas Dynamics. *Journal of Advances in Modeling Earth Systems*, *11*(8), 2745–2767. doi: 10.1029/2019MS001724

Schulzki, T. (2019). *Pathways and timescales of the Deep Western Boundary Current in the Subtropical North Atlantic* (Master Thesis). Christian-Albrechts-Universität zu Kiel, Kiel.

Schulzki, T., Harlaß, J., Schwarzkopf, F. U. & Biastoch, A. (2022). Toward Ocean Hindcasts in Earth System Models: AMOC Variability in a Partially Coupled Model at Eddying Resolution. *Journal of Advances in Modeling Earth Systems*, *14*(12), e2022MS003200. doi: 10.1029/2022MS003200

Schwarzkopf, F. U., Biastoch, A., Böning, C. W., Chanut, J., Durgadoo, J. V., Getzlaff, K., Harlaß, J., Rieck, J. K., Roth, C., Scheinert, M. M. & Schubert, R. (2019). The INALT family – a set of high-resolution nests for the Agulhas Current system within global NEMO ocean/sea-ice configurations. *Geoscientific Model Development*, *12*(7), 3329–3355. doi: 10.5194/gmd-12-3329-2019

Seager, R., Battisti, D. S., Yin, J., Gordon, N., Naik, N., Clement, A. C. & Cane, M. A. (2002). Is the Gulf Stream responsible for Europe's mild winters? *Quarterly Journal of the Royal Meteorological Society*, *128*(586), 2563–2586. doi: 10.1256/qj.01.128

Send, U., Lankhorst, M. & Kanzow, T. (2011). Observation of decadal change in the Atlantic meridional overturning circulation using 10 years of continuous transport data. *Geophysical Research Letters*, *38*(24), L24606. doi: 10.1029/2011GL049801

Send, U. & Marshall, J. (1995). Integral Effects of Deep Convection. *Journal of Physical Oceanography*, *25*(5), 855–872. doi: 10.1175/1520-0485(1995)025<0855:IEODC>2.0.CO;2

Shay, T. J., Bane, J. M., Watts, D. R. & Tracey, K. L. (1995). Gulf Stream flow field and events near 68°W. *Journal of Geophysical Research: Oceans*, *100*(C11), 22565–22589. doi: 10.1029/95JC02685

Singleton, A. T. & Reason, C. J. C. (2006). Numerical simulations of a severe rainfall event over the Eastern Cape coast of South Africa: sensitivity to sea surface temperature and topography. *Tellus A*, *58*, 355-367. doi: 10.1111/j.1600-0870.2006.00180.x

Smeed, D. A., McCarthy, G. D., Cunningham, S. A., Frajka-Williams, E., Rayner, D., Johns, W. E., Meinen, C. S., Baringer, M. O., Moat, B. I., Duchez, A. & Bryden, H. L. (2014). Observed decline of the Atlantic meridional overturning circulation 2004–2012. *Ocean Science*, *10*(1), 29–38. doi: 10.5194/os-10-29-2014

Smith, R. D., Maltrud, M. E., Bryan, F. O. & Hecht, M. W. (2000). Numerical Simulation of the North Atlantic Ocean at 1/10°. *Journal of Physical Oceanography*, *30*(7), 1532–1561. doi: 10.1175/1520-0485(2000)030<1532:NSOTNA>2.0.CO;2

Spall, M. A. (2004). Boundary Currents and Watermass Transformation in Marginal Seas. *Journal of Physical Oceanography*, *34*(5), 1197–1213. doi: 10.1175/1520-0485(2004)034<1197:BCAWTI>2.0.CO;2

Steinle, L., Graves, C. A., Treude, T., Ferré, B., Biastoch, A., Bussmann, I., Berndt, C., Krastel, S., James, R. H., Behrens, E., Böning, C. W., Greinert, J., Sapart, C.-J., Scheinert, M., Sommer, S., Lehmann, M. F. & Niemann, H. (2015). Water column methanotrophy controlled by a rapid oceanographic switch. *Nature Geoscience*, *8*(5), 378–382. doi: 10.1038/ngeo2420

Stevens, B., Giorgetta, M., Esch, M., Mauritsen, T., Crueger, T., Rast, S., Salzmann, M., Schmidt, H., Bader, J., Block, K., Brokopf, R., Fast, I., Kinne, S., Kornblueh, L., Lohmann, U., Pincus, R., Reichler, T. & Roeckner, E. (2013). Atmospheric component of the MPI-M Earth System Model: ECHAM6. *Journal of Advances in Modeling Earth Systems*, *5*(2), 146–172. doi: 10.1002/jame.20015

Stocker, T. F. (1998). The Seesaw Effect. *Science*, *282*(5386), 61–62. doi: 10.1126/science.282.5386.61

Stocker, T. F. (2013). Chapter 1 - The Ocean as a Component of the Climate System. In G. Siedler, S. M. Griffies, J. Gould & J. A. Church (Eds.), *International Geophysics* (Vol. 103, pp. 3–30). Academic Press. doi: 10.1016/B978-0-12-391851-2.00001-5

Stommel, H. (1948). The westward intensification of wind-driven ocean currents. *Transactions American Geophysical Union*, *29*(2), 202–206. doi: 10.1029/TR029i002p00202

Stommel, H. (1958). The abyssal circulation. *Deep Sea Research*, *5*(1), 80–82. doi: 10.1016/S0146-6291(58)80014-4

Stommel, H. (1961). Thermohaline Convection with Two Stable Regimes of Flow. *Tellus*, *13*(2), 224–230. doi: 10.1111/j.2153-3490.1961.tb00079.x

Stommel, H. & Arons, A. (1959a). On the abyssal circulation of the world ocean — II. An idealized model of the circulation pattern and amplitude in oceanic basins. *Deep Sea Research*, *6*, 217–233. doi: 10.1016/0146-6313(59)90075-9

Stommel, H. & Arons, A. (1959b). On the abyssal circulation of the world ocean—I. Stationary planetary flow patterns on a sphere. *Deep Sea Research*, *6*, 140–154. doi: 10.1016/0146-6313(59)90065-6

Storkey, D., Blaker, A. T., Mathiot, P., Megann, A., Aksenov, Y., Blockley, E. W., Calvert, D., Graham, T., Hewitt, H. T., Hyder, P., Kuhlbrodt, T., Rae, J. G. L. & Sinha, B. (2018). UK Global Ocean GO6 and GO7: a traceable hierarchy of model resolutions. *Geoscientific Model Development*, *11*(8), 3187–3213. doi: 10.5194/gmd-11-3187-2018

Stouffer, R. J., Yin, J., Gregory, J. M., Dixon, K. W., Spelman, M. J., Hurlin, W., Weaver, A. J., Eby, M., Flato, G. M., Hasumi, H., Hu, A., Jungclaus, J. H., Kamenkovich, I. V., Levermann, A., Montoya, M., Murakami, S., Nawrath, S., Oka, A., Peltier, W. R., Robitaille, D. Y., Sokolov, A., Vettoretti, G. & Weber, S. L. (2006). Investigating the Causes of the Response of the Thermohaline Circulation to Past and Future Climate Changes. *Journal of Climate*, *19*(8), 1365–1387. doi: 10.1175/JCLI3689.1

Straneo, F. (2006). On the Connection between Dense Water Formation, Overturning, and Poleward Heat Transport in a Convective Basin. *Journal of Physical Oceanography*, *36*(9), 1822–1840. doi: 10.1175/JPO2932.1

Swallow, J. & Worthington, L. (1961). An observation of a deep countercurrent in the Western North Atlantic. *Deep Sea Research*, *8*(1), IN1–IN3. doi: 10.1016/0146-6313(61)90011-9

Swart, N. C. & Fyfe, J. C. (2012). Observed and simulated changes in the Southern Hemisphere surface westerly wind-stress. *Geophysical Research Letters*, *39*(16), L16711. doi: 10.1029/2012GL052810

Swingedouw, D., Fichefet, T., Goosse, H. & Loutre, M. F. (2009). Impact of transient freshwater releases in the Southern Ocean on the AMOC and climate. *Climate Dynamics*, *33*(2), 365–381. doi: 10.1007/s00382-008-0496-1

Swingedouw, D., Rodehacke, C. B., Behrens, E., Menary, M., Olsen, S. M., Gao, Y., Mikolajewicz, U., Mignot, J. & Biastoch, A. (2013). Decadal fingerprints of freshwater discharge around Greenland in a multi-model ensemble. *Climate Dynamics*, *41*(3), 695–720. doi: 10.1007/s00382-012-1479-9

Talley, L. D. & McCartney, M. S. (1982). Distribution and Circulation of Labrador Sea Water. *Journal of Physical Oceanography*, *12*(11), 1189–1205. doi: 10.1175/1520-0485(1982)012<1189:DACOLS>2.0.CO;2

Talley, L. D., Pickard, G. L., Emery, W. J. & Swift, J. H. (2011). *Descriptive Physical Oceanography An Introduction* (6th ed.). Academic Press. doi: 10.1016/C2009-0-24322-4

Thoma, M., Gerdes, R., Greatbatch, R. J. & Ding, H. (2015). Partially coupled spin-up of the MPI-ESM: implementation and first results. *Geoscientific Model Development*, *8*(1), 51–68. doi: 10.5194/gmd-8-51-2015

Thompson, D. W. J. & Solomon, S. (2002). Interpretation of Recent Southern Hemisphere Climate Change. *Science*, *296*(5569), 895–899. doi: 10.1126/science.1069270

Toggweiler, J. & Samuels, B. (1995). Effect of drake passage on the global thermohaline circulation. *Deep Sea Research Part I: Oceanographic Research Papers*, *42*(4), 477–500.

doi: 10.1016/0967-0637(95)00012-U

Treguier, A. M., Held, I. M. & Larichev, V. D. (1997). Parameterization of Quasigeostrophic Eddies in Primitive Equation Ocean Models. *Journal of Physical Oceanography*, *27*(4), 567–580. doi: 10.1175/1520-0485(1997)027<0567:POQEIP>2.0.CO;2

Trenberth, K. E. & Caron, J. M. (2001). Estimates of Meridional Atmosphere and Ocean Heat Transports. *Journal of Climate*, *14*(16), 3433–3443. doi: 10.1175/1520-0442(2001)014<3433:EOMAAO>2.0.CO;2

Tsartsali, E. E., Haarsma, R. J., Athanasiadis, P. J., Bellucci, A., de Vries, H., Drijfhout, S., de Vries, I. E., Putrahasan, D., Roberts, M. J., Sanchez–Gomez, E. & Roberts, C. D. (2022). Impact of resolution on the atmosphere–ocean coupling along the Gulf Stream in global high resolution models. *Climate Dynamics*, *58*(11), 3317–3333. doi: 10.1007/s00382-021-06098-9

Tsujino, H., Urakawa, L. S., Griffies, S. M., Danabasoglu, G., Adcroft, A. J., Amaral, A. E., Arsouze, T., Bentsen, M., Bernardello, R., Böning, C. W., Bozec, A., Chassignet, E. P., Danilov, S., Dussin, R., Exarchou, E., Fogli, P. G., Fox-Kemper, B., Guo, C., Ilicak, M., Iovino, D., Kim, W. M., Koldunov, N., Lapin, V., Li, Y., Lin, P., Lindsay, K., Liu, H., Long, M. C., Komuro, Y., Marsland, S. J., Masina, S., Nummelin, A., Rieck, J. K., Ruprich-Robert, Y., Scheinert, M., Sicardi, V., Sidorenko, D., Suzuki, T., Tatebe, H., Wang, Q., Yeager, S. G. & Yu, Z. (2020). Evaluation of global ocean–sea-ice model simulations based on the experimental protocols of the Ocean Model Intercomparison Project phase 2 (OMIP-2). *Geoscientific Model Development*, *13*(8), 3643–3708. doi: 10.5194/gmd-13-3643-2020

Tsujino, H., Urakawa, S., Nakano, H., Small, R. J., Kim, W. M., Yeager, S. G., Danabasoglu, G., Suzuki, T., Bamber, J. L., Bentsen, M., Böning, C. W., Bozec, A., Chassignet, E. P., Curchitser, E., Boeira Dias, F., Durack, P. J., Griffies, S. M., Harada, Y., Ilicak, M., Josey, S. A., Kobayashi, C., Kobayashi, S., Komuro, Y., Large, W. G., Le Sommer, J., Marsland, S. J., Masina, S., Scheinert, M., Tomita, H., Valdivieso, M. & Yamazaki, D. (2018). JRA-55 based surface dataset for driving ocean–sea-ice models (JRA55-do). *Ocean Modelling*, *130*, 79–139. doi: 10.1016/j.ocemod.2018.07.002

Våge, K., Pickart, R. S., Spall, M. A., Moore, G., Valdimarsson, H., Torres, D. J., Erofeeva, S. Y. & Nilsen, J. E. Ø. (2013). Revised circulation scheme north of the Denmark Strait. *Deep Sea Research Part I: Oceanographic Research Papers*, *79*, 20–39. doi: 10.1016/j.dsr.2013.05.007

Valcke, S. (2013). The OASIS3 coupler: a European climate modelling community software. *Geoscientific Model Development*, *6*(2), 373–388. doi: 10.5194/gmd-6-373-2013

Vancoppenolle, M., Fichefet, T., Goosse, H., Bouillon, S., Madec, G. & Maqueda, M. A. M. (2009). Simulating the mass balance and salinity of Arctic and Antarctic sea ice. 1. Model description and validation. *Ocean Modelling*, *27*(1), 33–53. doi: 10.1016/j.ocemod.2008.10.005

van Sebille, E., Beal, L. M. & Johns, W. E. (2011). Advective Time Scales of Agulhas Leakage to the North Atlantic in Surface Drifter Observations and the 3D OFES Model. *Journal of Physical Oceanography*, *41*(5), 1026–1034. doi: 10.1175/2011JPO4602.1

van Sebille, E., Griffies, S. M., Abernathey, R., Adams, T. P., Berloff, P., Biastoch, A., Blanke, B., Chassignet, E. P., Cheng, Y., Cotter, C. J., Deleersnijder, E., Döös, K., Drake, H. F., Drijfhout, S., Gary, S. F., Heemink, A. W., Kjellsson, J., Koszalka, I. M., Lange, M., Lique, C., MacGilchrist, G. A., Marsh, R., Mayorga Adame, C. G., McAdam, R., Nencioli, F., Paris, C. B., Piggott, M. D., Polton, J. A., Rühs, S., Shah, S. H., Thomas, M. D., Wang, J., Wolfram, P. J., Zanna, L. & Zika, J. D. (2018). Lagrangian ocean analysis: Fundamentals and practices. *Ocean Modelling*, *121*, 49–75. doi: 10.1016/j.ocemod.2017.11.008

Vellinga, M. & Wood, R. A. (2002). Global Climatic Impacts of a Collapse of the Atlantic Thermohaline Circulation. *Climatic Change*, *54*(3), 251–267. doi: 10.1023/A:1016168827653

Vinogradov, G. M. (2000). Growth rate of the colony of a deep-water gorgonarian Chrysogorgia agassizi: In situ observations. *Ophelia*, *53*(2), 101–103.

Våge, K., Pickart, R. S., Thierry, V., Reverdin, G., Lee, C. M., Petrie, B., Agnew, T. A., Wong, A. & Ribergaard, M. H. (2009). Surprising return of deep convection to the subpolar North Atlantic Ocean in winter 2007–2008. *Nature Geoscience*, *2*(1), 67–72. doi: 10.1038/ngeo382

Warren, B. A. (1983). Why is no deep water formed in the North Pacific? *Journal of Marine Research*, *41*, 327–347.

Weaver, A. J., Saenko, O. A., Clark, P. U. & Mitrovica, J. X. (2003). Meltwater pulse 1A from Antarctica as a trigger of the Bølling-Allerød warm interval. *Science*, *299*(5613), 1709–1713. doi: 10.1126/science.1081002

Weaver, A. J., Sedláček, J., Eby, M., Alexander, K., Crespin, E., Fichefet, T., Philippon-Berthier, G., Joos, F., Kawamiya, M., Matsumoto, K., Steinacher, M., Tachiiri, K., Tokos, K., Yoshimori, M. & Zickfeld, K. (2012). Stability of the Atlantic meridional overturning circulation: A model intercomparison. *Geophysical Research Letters*, *39*(20), L20709. doi: 10.1029/2012GL053763

Webb, D. J., Spence, P., Holmes, R. M. & England, M. H. (2021). Planetary-Wave-Induced Strengthening of the AMOC Forced by Poleward Intensified Southern Hemisphere Westerly Winds. *Journal of Climate*, *34*(17), 7073–7090. doi: 10.1175/JCLI-D-20-0858.1

Webb, D. J. & Suginohara, N. (2001). Vertical mixing in the ocean. *Nature*, *409*(6816), 37–37. doi: 10.1038/35051171

Wei, W., Lohmann, G. & Dima, M. (2012). Distinct Modes of Internal Variability in the Global Meridional Overturning Circulation Associated with the Southern Hemisphere Westerly Winds. *Journal of Physical Oceanography*, *42*(5), 785–801. doi: 10.1175/JPO-D-11-038.1

Weijer, W., Cheng, W., Drijfhout, S. S., Fedorov, A. V., Hu, A., Jackson, L. C., Liu, W., McDonagh, E. L., Mecking, J. V. & Zhang, J. (2019). Stability of the Atlantic Meridional Overturning Circulation: A Review and Synthesis. *Journal of Geophysical Research: Oceans*, *124*(8), 5336–5375. doi: 10.1029/2019JC015083

Weijer, W., Cheng, W., Garuba, O. A., Hu, A. & Nadiga, B. T. (2020). CMIP6 Models Predict Significant 21st Century Decline of the Atlantic Meridional Overturning Circulation. *Geophysical Research Letters*, *47*(12), e2019GL086075. doi: 10.1029/2019GL086075

Weijer, W., De Ruijter, W. P., Sterl, A. & Drijfhout, S. S. (2002). Response of the Atlantic overturning circulation to South Atlantic sources of buoyancy. *Global and Planetary Change*, *34*(3), 293–311. doi: 10.1016/S0921-8181(02)00121-2

Weijer, W., de Ruijter, W. P. M., Dijkstra, H. A. & van Leeuwen, P. J. (1999). Impact of Interbasin Exchange on the Atlantic Overturning Circulation. *Journal of Physical Oceanography*, *29*(9), 2266–2284. doi: 10.1175/1520-0485(1999)029<2266:IOIEOT>2.0.CO;2

Weijer, W. & van Sebille, E. (2014). Impact of Agulhas Leakage on the Atlantic Overturning Circulation in the CCSM4. *Journal of Climate*, *27*(1), 101–110. doi: 10.1175/JCLI-D-12-00714.1

Weijer, W., Zharkov, V., Nof, D., Dijkstra, H. A., de Ruijter, W. P. M., van Scheltinga, A. T. & Wubs, F. (2013). Agulhas ring formation as a barotropic instability of the retroflection. *Geophysical Research Letters*, *40*(20), 5435–5438. doi: 10.1002/2013GL057751

Wood, R. A., Vellinga, M. & Thorpe, R. (2003). Global Warming and Thermohaline Circulation Stability. *Philosophical Transactions: Mathematical, Physical and Engineering Sciences*, *361*(1810), 1961–1975. doi: 10.1098/rsta.2003.1245

Wyrtki, K., Magaard, L. & Hager, J. (1976). Eddy energy in the oceans. *Journal of Geophysical Research (1896-1977)*, *81*(15), 2641–2646. doi: 10.1029/JC081i015p02641

Xu, X., Rhines, P. B. & Chassignet, E. P. (2018). On Mapping the Diapycnal Water Mass Transformation of the Upper North Atlantic Ocean. *Journal of Physical Oceanography*, *48*(10), 2233–2258. doi: 10.1175/JPO-D-17-0223.1

Xu, X., Schmitz Jr., W. J., Hurlburt, H. E. & Hogan, P. J. (2012). Mean Atlantic meridional overturning circulation across 26.5°N from eddy-resolving simulations compared to observations. *Journal of Geophysical Research: Oceans*, *117*(C3), C03042. doi: 10.1029/2011JC007586

Yan, X., Zhang, R. & Knutson, T. R. (2017). The role of Atlantic overturning circulation in the recent decline of Atlantic major hurricane frequency. *Nature Communications*, *8*(1), 1695. doi: 10.1038/s41467-017-01377-8

Yeager, S. (2020). The abyssal origins of North Atlantic decadal predictability. *Climate Dynamics*, *55*(7), 2253–2271. doi: 10.1007/s00382-020-05382-4

Yeager, S., Castruccio, F., Chang, P., Danabasoglu, G., Maroon, E., Small, J., Wang, H., Wu, L. & Zhang, S. (2021). An outsized role for the Labrador Sea in the multidecadal

variability of the Atlantic overturning circulation. *Science Advances*, *7*(41), eabh3592. doi: 10.1126/sciadv.abh3592

Yeager, S. & Danabasoglu, G. (2014). The Origins of Late-Twentieth-Century Variations in the Large-Scale North Atlantic Circulation. *Journal of Climate*, *27*(9), 3222–3247. doi: 10.1175/JCLI-D-13-00125.1

Zalesak, S. T. (1979). Fully multidimensional flux-corrected transport algorithms for fluids. *Journal of Computational Physics*, *31*(3), 335–362. doi: 10.1016/0021-9991(79)90051-2

Zampieri, M., Scoccimarro, E. & Gualdi, S. (2013). Atlantic influence on spring snowfall over the Alps in the past 150 years. *Environmental Research Letters*, *8*(3), 034026. doi: 10.1088/1748-9326/8/3/034026

Zhang, Q., Chang, P., Yeager, S. G., Danabasoglu, G. & Zhang, S. (2022). Role of Sea-Surface Salinity in Simulating Historical Decadal Variations of Atlantic Meridional Overturning Circulation in a Coupled Climate Model. *Geophysical Research Letters*, *49*(4), e2021GL096922. doi: 10.1029/2021GL096922

Zhang, R. (2008). Coherent surface-subsurface fingerprint of the Atlantic meridional overturning circulation. *Geophysical Research Letters*, *35*(20), L20705. doi: 10.1029/2008GL035463

Zhang, R. (2010). Latitudinal dependence of Atlantic meridional overturning circulation (AMOC) variations. *Geophysical Research Letters*, *37*(16), L16703. doi: 10.1029/2010GL044474

Zhang, R. & Delworth, T. L. (2006). Impact of Atlantic multidecadal oscillations on India/Sahel rainfall and Atlantic hurricanes. *Geophysical Research Letters*, *33*(17), L17712. doi: 10.1029/2006GL026267

Zhang, R., Sutton, R., Danabasoglu, G., Kwon, Y.-O., Marsh, R., Yeager, S. G., Amrhein, D. E. & Little, C. M. (2019). A Review of the Role of the Atlantic Meridional Overturning Circulation in Atlantic Multidecadal Variability and Associated Climate Impacts. *Reviews of Geophysics*, *57*(2), 316–375. doi: 10.1029/2019RG000644

Zhang, R. & Thomas, M. (2021). Horizontal circulation across density surfaces contributes substantially to the long-term mean northern Atlantic Meridional Overturning Circulation. *Communications Earth & Environment*, *2*(1), 112. doi: 10.1038/s43247-021-00182-y

Zhao, J. & Johns, W. (2014). Wind-forced interannual variability of the Atlantic Meridional Overturning Circulation at 26.5°N. *Journal of Geophysical Research: Oceans*, *119*(4), 2403–2419. doi: 10.1002/2013JC009407

Zou, S. & Lozier, M. S. (2016). Breaking the Linkage Between Labrador Sea Water Production and Its Advective Export to the Subtropical Gyre. *Journal of Physical Oceanography*, *46*(7), 2169–2182. doi: 10.1175/JPO-D-15-0210.1

Zou, S., Lozier, M. S. & Buckley, M. (2019). How Is Meridional Coherence Maintained in the Lower Limb of the Atlantic Meridional Overturning Circulation? *Geophysical Research Letters*, *46*(1), 244–252. doi: 10.1029/2018GL080958

Zweng, M. M., Reagan, J. R., Antonov, J. I., Locarnini, R. A., Mishonov, A. V., Boyer, T. P., Garcia, H. E., Baranova, O. K., Johnson, D. R., Seidov, D., Biddle, M. M. & Levitus, S. (2013). World ocean atlas 2013. Volume 2, Salinity. *NOAA atlas NESDIS ; 74*. doi: 10.7289/V5251G4D

Acknowledgements

First, I would like to sincerely thank Prof. Dr. Arne Biastoch for his great supervision and for very constructive and helpful discussions. I highly appreciate his guidance, the time he took to talk through new ideas and results and also his very quick response to questions at all times. I am very thankful for all the opportunities he provided to share and discuss my science at various conferences and workshops.

I also thank Prof. Dr. Katja Matthes and Prof. Dr. Joakim Kjellsson for their constructive feedback and support of my thesis through the Integrated School of Ocean Sciences (ISOS).

I am very grateful for the support of all colleagues in the Ocean Dynamics department at GEOMAR. The collaborative environment in the department was extremely helpful during the whole doctorate. I especially thank Dr. Franziska Schwarzkopf for her great support in setting-up and running the nested (FOCI-)ATLAS10 configuration. Her deep knowledge of the NEMO model and her support in conducting experiments on high-performance computers was essential for the success of this thesis. Further, I thank Dr. Jan Harlaß and Dr. Sebastian Wahl for their support in running and modifying FOCI, which enabled me to perform new model experiments. I greatly appreciate the support of Dr. Willi Rath, Dr. Katharina Höflich and Dr. Siren Rühs in conducting and analysing large Lagrangian experiments. I also thank Dr. Torge Martin for sharing his knowledge of the North and South Atlantic circulation, as well as his experience in running nested model configurations in FOCI. Further, I would like to thank Dr. Klaus Getzlaff for his continuous assistance in analysing large model output since my time as a bachelor student. Thank you to Ilana Schiller-Weiß for her comments on my thesis and thank you to Prof. Dr. Richard Greatbatch for a long discussion about possible modifications to the partial coupling procedure on a trip to Lübeck.

I also thank Prof. Dr. Lea-Anne Henry, Prof. Dr. J. Murray Roberts, Dr. Maria Rakka and Prof. Dr. Steve Ross for their advice on the interdisciplinary part of this thesis and their effort to help me understand the details and significance of larval dispersal.

This work was supported by the European Horizon 2020 research and innovation program under grant agreement No. 818123 (iAtlantic). I highly appreciate the great environment for interdisciplinary collaborations provided by the iAtlantic project. Further, I acknowledge the Jülich Supercomputing Centre (JSC) for granting the computing time resources needed to perform new model experiments.

I am very grateful for the support of my parents Reinhard and Iris Schulzki and my sister Elisa Schulzki, not only during the doctorate, but my entire life. Finishing this thesis would not have been possible without Anika Mosebach and the great time we have spent together outside work. Furthermore, I thank Gabriel Ditzinger, Immo Petersen, Jan Ridderbusch and Philip Kreußler for being an important part of the path that ultimately led me pursuing the doctorate.

Erklärung

Hiermit erkläre ich, dass ich die vorliegende Dissertation, abgesehen von der Beratung durch die gennanten Betreuer, nach Inhalt und Form eigenständig und unter Einhaltung der Regeln guter wissenschaftlicher Praxis der Deutschen Forschungsgemeinschaft verfasst habe. Ich habe keine anderen als die angegebenen Hilfsmittel und Quellen verwendet. Diese Dissertation hat weder ganz noch in Teilen an einer anderen Stelle im Rahmen eines Prüfungsverfahrens vorgelegen. Diese Dissertation ist eine Mischform. Kapitel 3 wurde im "Journal of Advances in Modeling Earth Systems" veröffentlicht und Kapitel 5 im "Journal of Geophysical Research: Oceans". Kapitel 6 wurde eingereicht für die Veröffentlichung im Journal "Deep Sea Research Part I". Mir wurde kein akademischer Grad entzogen.

Kiel, 05.05.2023:

Tobias Gereon Schulzki